THE INFLUENCE OF ROTATING AND LOCKED MAGNETIC ISLANDS ON EDGE TRANSPORT IN TOKOLOSHE TOKAMAK

by

GARY WAYNE VAN VUUREN

Submitted in partial fulfilment of
the requirements for the degree of
Doctor of Philosophy
in the
Department of Physics,
University of Natal,
Durban.

PELINDABA
1993

The mediocre teacher tells.
The good teacher explains.
The superior teacher demonstrates.
The great teacher inspires.

—William Arthur Ward

Once again

for that great teacher:

Dorothy Sibson

Preface

Some of the theoretical work described in this thesis was carried out in the Department of Physics, University of Natal, Durban, under the supervision of Dr. M. J. Alport and Professor M. A. Hellberg.

All experimental and some theoretical work was performed at the Pelindaba site of the Atomic Energy Corporation in the Fusion Studies Group under the supervision of Dr. D. E. Roberts. The experimental data used in this thesis was acquired using the *Tokoloshe* tokamak from 1988 to 1992.

These studies represent the original work by the author and have not been submitted in any form to this or any other University. Where use was made of the work of others it has been duly acknowledged in the text. The work described in Chapter's 4 and 5 is in preparation for submission to *Nuclear Fusion* and *Plasma Physics and Controlled Fusion* respectively.

March 31, 1993

Acknowledgements

I acknowledge an enormous debt of gratitude to the many people who have contributed in some way or other to the completion of this thesis. In particular, I would like to thank:
Dr. Mike Alport, my supervisor, and Professor Manfred Hellberg, my UND co-supervisor, for their coordination of the project, valuable discussions and exhaustive proof reading,
Dr. Ted Roberts, my AEC co-supervisor, for his suggestions and guidance and, more importantly, for teaching me how to fish,
my parents, for the dream, desire and determination,
the FRD for financial support from 1986 to 1990 and the AEC for the opportunity to complete this project,
the *Tokoloshe* team: Ted Roberts, John Fletcher, Cathy Goosen, Dave Sherwell, Gawie Nothnagel, JAM de Villiers, Tony Joel, Willie McLoud, Jan Venter, John Venter, Bill Brown and Paul Kruger for practically everything,
Jeff and Lorna Adams and Fritz and Vera Kõnig for their limitless encouragement, support and confidence,
The Coffee-Club (Seonaid Hudson, Neil Peacock, Sam Mottram, Clinton Clarence, Harold Groothedde, Richard and Leonie Anderson, Shirley Dickson, Michael Knight, Leonie Anderson, John Hawkins, Sandy Yates, Paul and Timm Irvine-Smith, Haydn Rawlins, Simon Martens, Marcelle du Rand, Anton Groom, Kevin Talbot, Jock McKirdy, Mark Walker, Peter van Heerden) and other inmates of the Durban campus since 1983 for enthusiastic discussions, relentless activity and great coffee,
John and Lizelle Fletcher, for feeding all of my monkeys and silencing most of my Lambs and
a very special thanks to Dorothy Sibson, to whom I am deeply indebted indeed, for her unorthodox—but very effective—teaching methods. She has been for me a source of perpetual inspiration especially through the dark days and I hope this work serves as a fitting tribute to everything she has taught me.

Abstract

The turbulence and fluctuation induced transport in the edge plasma of the *Tokoloshe* tokamak was studied using a Langmuir probe array. In this thesis three separate experiments are presented, each of which examines a particular aspect of the edge plasma.

In the first experiment measurements of edge plasma parameters are presented. These include standard parameters (such as n_e, ϕ_p, T_e, etc.) as well as features such as the velocity shear, $\tilde{\Gamma}(t)$ during periods of both high and low Mirnov activity, $\tilde{T}_e/T_e$ and $\tilde{Q}$. These are compared with results from other machines as well as predictions of several turbulence theories. It was found that many of the results are very similar to those obtained on other machines and that, since the operating parameter space on *Tokoloshe* is well within the parameter space described by drift wave theories, resistivity-driven gradient driven turbulence theories do not describe the edge turbulence.

In the second experiment external windings are used to produce fields which can slow and lock magnetic islands in the toroidally rotating plasma. Edge parameters are again presented and these results compared with those from the so-called 'reference' plasmas, i.e. ones in which no locking occurred. During locking some parameters are dramatically altered, e.g. $\tilde{T}_e/T_e$. Standard transport theory ignores the effect of $\tilde{T}_e/T_e$ since they are usually small in reference discharges. During the locked phase, however, certain measurements used to deduce $\tilde{\Gamma}$ and $\tilde{Q}$ are greatly affected by increases in $\tilde{T}_e/T_e$. As a result, certain assumptions regarding these measurements are no longer valid. Comparison of results for different island positions (produced by different coils) indicates that the assumption of poloidal and toroidal symmetry of edge conditions is invalid.

The third experiment investigates the high frequency ($\sim 60\,\mathrm{kHz}$), low amplitude, magnetic oscillation which characterises the locked phase and which exhibits some small degree of correlation with the fluctuations observed on (e.g.) $\tilde{\phi}_f$. Since over 80% of the spectral power of $\tilde{T}_e/T_e$ lies below 70 kHz and since $\tilde{\phi}_f/T_e$ depends strongly on $\tilde{T}_e/T_e$, it is suggested that the magnetic mode and these large variations in T_e, may be due to a similar physical process.

Glossary of Symbols

Roman symbols

R	radius measured from major axis
R_o	major radius
r	radius measured from minor axis
a_L	limiter radius
a_W	wall radius
B_ϕ	toroidal magnetic field
B_θ	poloidal magnetic field
D	diffusion coefficient
j	current density
n	particle density
n_e	electron density
$\tilde{n}_e$	fluctuating electron density
$\overline{n}_e$	line average density
n_i	ion density
i_{sat}	saturated ion current
k_θ	poloidal wave vector
k_ϕ	toroidal wave vector
L_n	density $1/e$ decay length
L_{T_e}	temperature $1/e$ decay length
L_E	electric field scale length
q	safety factor
v_e	electron thermal velocity
v_i	ion thermal velocity
t_p	duration of discharge
m	poloidal mode number
n	toroidal mode number

Roman symbols (continued)

T_e, T_i	electron, ion temperature
$\tilde{T}_e$	fluctuating electron temperature
Z_{eff}	average ionic charge
V_{loop}	loop voltage
$q^{\tilde{E}}_{\text{conv}}$	electrostatic, fluctuation-induced, convected heat flux
$q^{\tilde{E}}_{\text{cond}}$	electrostatic, fluctuation-induced, conducted heat flux
I_p	plasma current
Q	rate of heat loss
$m_{e,i}$	electron, ion mass
W	thermal energy
L_{coher}	coherence length
r_s	ion gyroradius

Greek symbols

β	plasma pressure/magnetic pressure
$\gamma_{n\phi}$	coherence between $\tilde{i}_{\text{sat}}$ and $\tilde{\phi}_f$
$\tilde{\Gamma}$	fluctuation induced particle flux
$\tilde{Q}$	total, electrostatic fluctuation induced energy flux
θ	poloidal coordinate angle
ϕ	toroidal coordinate angle
$\alpha_{n\phi}$	phase angle between $\tilde{i}_{\text{sat}}$ and $\tilde{\phi}_f$
χ_e	electron thermal diffusivity coefficient
ρ	r/a
τ_c	correlation time
τ_E	energy confinement time
τ_p	particle confinement time
ϕ_p	plasma potential
ϕ_f	floating potential
$\tilde{\phi}_p$	fluctuating plasma potential
$\tilde{\phi}_f$	fluctuating floating potential
ω_{*e}	electron diamagnetic frequency
ω_{ci}	ion gyrofrequency
$\parallel$	parallel to magnetic field
$\perp$	perpendicular to magnetic field

Contents

Chapter 1

Introduction

1.1 Historical Backround

The present rate of world energy consumption ($\sim 3 \times 10^{20}$ J/annum) (WESSON (1987)) will exhaust current fossil fuel supplies within the next three hundred years. The continued use of fossil fuels as primary sources of energy is not only inefficient but has dangerous consequences for both the climatic and ecological balance of the earth. Renewable sources of energy such as wind, wave and solar power could make a potentially valuable contribution to our energy needs but they have yet to prove their large-scale economic viability. Nuclear fission is already established as a major energy source in most industrialised countries and fast breeder technology could provide supplies of fissionable material for many hundreds of years. However, the use of such material in nuclear weapons and the problems of the disposal of high level radio-active waste has resulted in considerable disapproval by the public.

Energy produced from the thermonuclear fusion of light elements is the most promising long-term alternative source. The process is potentially extremely safe, fuel supplies are essentially unlimited and, in comparison with fossil fuels, atmospheric pollution from the process is negligible. Despite significant advances in recent years e.g. JET in November 1991 (JET TEAM (1992)), fusion is notoriously difficult to achieve and it is almost certain that it will be many years before a power producing reactor proves to be a commercial success.

1.1.1 Thermonuclear Fusion

Fusion reactions between light nuclei are generally exothermic; the binding energy per nucleon increases up to a mass of $A \leq 50$. For the strong, short range nuclear forces to take effect and hence for fusion to occur, the nuclei involved must overcome the mutual (Coulomb) repulsion due to their positive charges. To do this, the ions require significant energy and this is provided by heating the reactants to high temperatures. The resulting quasi-neutral gas comprising electrons and fully ionized nuclei is called a plasma.

Reactions between the hydrogenic isotopes (H, D, T) and the lightest elements (e.g. He) are the only ones of any significance in practice. The most favoured reaction is that between deuterium and tritium in which

$$\begin{array}{ccccccc} {}^{2}_{1}\mathrm{D} & + & {}^{3}_{1}\mathrm{T} & \longrightarrow & {}^{4}_{2}\mathrm{He} & + & {}^{1}_{0}\mathrm{n} \\ & & & & \Downarrow & & \Downarrow \\ & & & & 3.5\mathrm{MeV} & + & 14.1\mathrm{MeV} = 17.6\mathrm{MeV} \end{array}$$

The energies indicated are the reaction products' kinetic energies. The fusion cross-section, σ, reaches a maximum for this reaction ($\sim 7 \times 10^{-28}\,\mathrm{m}^2$) for a deuteron energy of 100 keV on a stationary triton target.

1.1.2 The Lawson Criterion

The hope for the achievement of thermonuclear fusion for quasi-dc power generation lies at present with the magnetic confinement of deuterium-tritium plasma satisfying the Lawson criterion. If a thermonuclear reactor is to be a viable economic device, the power output must exceed the total power loss from the plasma. The Lawson criterion is a statement of this condition for the specific case of energy input from a source outside the plasma and may be written as

$$n\tau_E > 6 \times 10^{19}\,\mathrm{m}^{-3}\mathrm{s},$$

where n is the total ion density and τ_E is the energy confinement time (WESSON (1987)).

1.2 The Tokamak

In a tokamak, confinement of the plasma is achieved by the combination of magnetic fields by external current carrying coils and by the current flowing in the plasma itself,

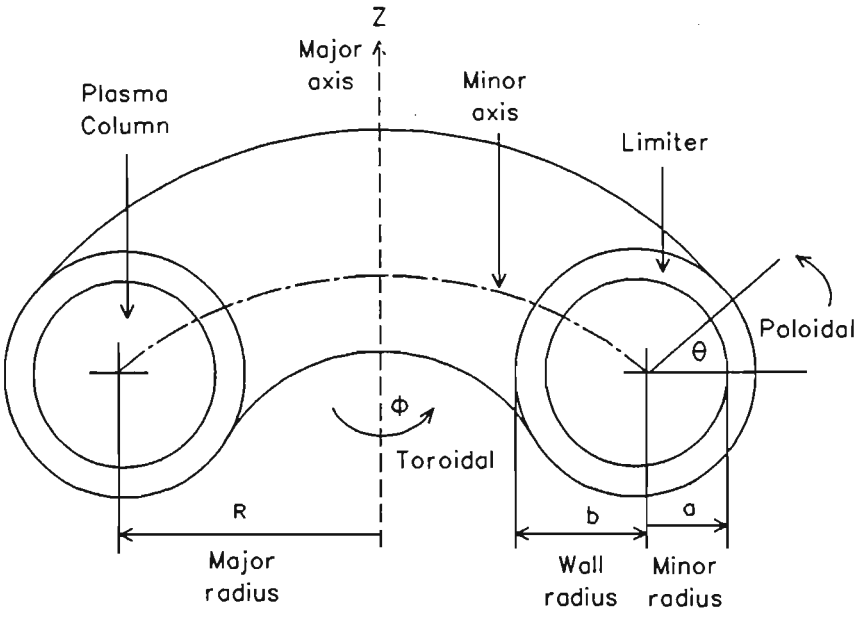

Figure 1.1: Tokamak coordinate system.

to produce a closed magnetic system. Figure 1.1 illustrates the basic coordinate system used in a standard tokamak.

The toroidal magnetic field, B_ϕ, is the main field component and is generated by a set of poloidally wound coils. This field alone cannot, however, provide the necessary equilibrium for a confined plasma. The field gradient results in the vertical (up/down) separation of the charges since the electron and ion guiding centres drift in opposite directions in the direction of $q\nabla\vec{B}_\phi \times \vec{B}_\phi$. This produces an electric field which then forces a $\vec{E}_r \times \vec{B}_\phi$ guiding center drift outwards in major radius. The addition of a poloidal magnetic field component gives a resultant helical field line structure and effectively eliminates this charge imbalance. This poloidal field, B_θ, is produced by a toroidal current induced in the plasma, I_p, by transformer action with the plasma as a single turn secondary. External toroidal windings produce a vertical magnetic field, required to counteract forces arising from the toroidal plasma and tending to expand the plasma ring. Figure 1.2 shows the basic tokamak magnetic field configuration.

1.2.1 Regions in the Tokamak

Three regions will be defined and referred to in this thesis. These are shown in Figure 1.3 and are outlined below. The limiter is an electrically conducting annulus usually made of stainless steel or molybdenum although more recently graphite has been used. The

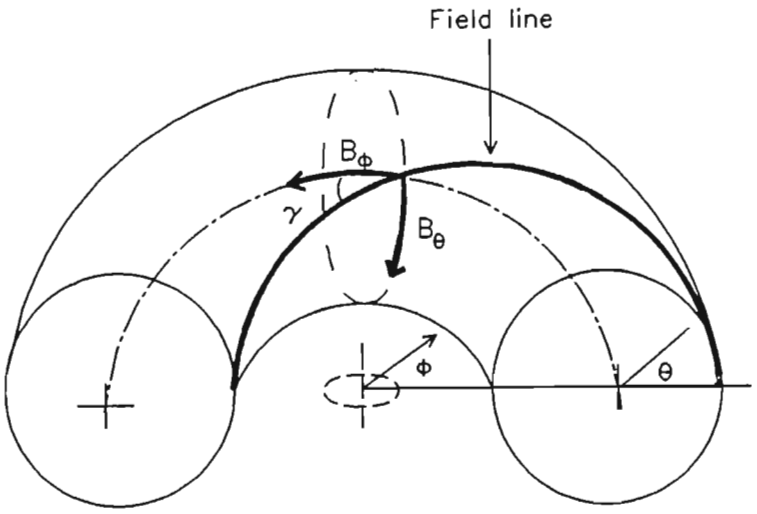

Figure 1.2: Tokamak magnetic field configuration.

limiter is fixed inside the vacuum vessel at a certain toroidal position to 'scrape-off' the plasma thus protecting the walls from high energy particles and disruptions. These are violently unstable discharges which result in a catastrophic loss of thermal and magnetic energy.

- THE SCRAPE-OFF LAYER. This is the outer region of the plasma, in contact with the vessel wall, which includes magnetic surfaces intercepted by the limiter. That is, where the field lines are 'open' and not 'closed' as in the plasma core region. In a magnetically confined plasma, the term 'edge plasma' refers to the outer regions of the discharge in which the effects of a material surface are felt. The physics of the edge plasma is differentiated from that of the core (or confined region) of the discharge by the need to include complex physical processes. These include recycling of particles, fast parallel transport to material surfaces, impurity release mechanisms and light impurity radiation. The physics of the boundary layer and mechanisms of plasma-surface interactions have been reviewed by McCracken (1979) and more recently by Stangeby *et al* (1990). The physics of the edge region may be complex but the investigation of the edge plasma parameters is simplified by the cooler temperatures and densities characteristic of the scrape-off layer. This region is accessible to material probes as well as other, less direct methods of measurement.

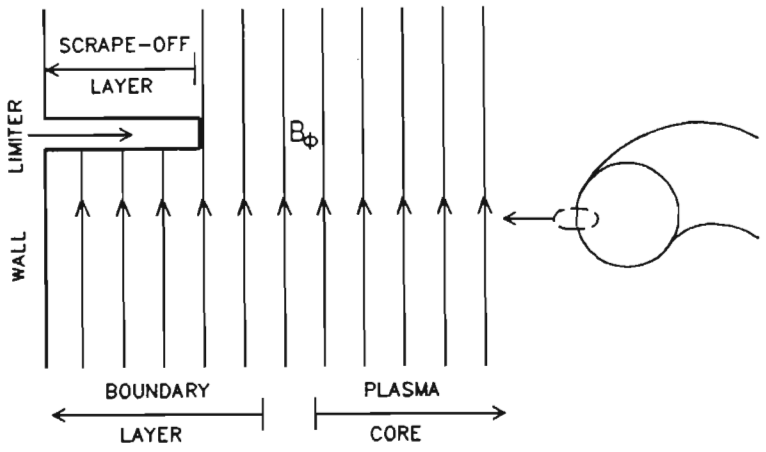

Figure 1.3: Regions in a tokamak plasma.

- THE BOUNDARY LAYER. That part of the plasma that is amenable to material probes is defined as the boundary layer. Materials inserted into the plasma more than a few centimetres melt, sputter, damage the probes and contaminate the plasma. Heat and particle fluxes to the limiter determine melting and sputtering rates and consequently the impurity content of the plasma. In many present tokamak experiments, metallic impurities from the limiter and walls are often responsible for significant energy losses. The heavy ions are not completely ionized by the low plasma temperatures in this region and hence emit strong line radiation. The boundary plasma suffers the highest levels of turbulence in the tokamak and MOTLEY (1981) has shown that the limiter itself may be a cause of some instabilities. This could be due to the electrical mismatch between the axisymmetric interior and the non-axisymmetric scrape off layer.

- THE PLASMA CORE. This region is characterised by high temperatures ($\sim$ keV), high densities (compared with the edge regions) and low turbulence. This region may only be studied by indirect methods of measurement (e.g. heavy ion beam probes, laser scattering, far infrared scattering, emmisivity of X-ray spectra, etc.)

1.3 Backround and Purpose of Study

It is well known that, in general, neoclassical transport theory (classical theory in toroidal geometry) inadequately describes the edge transport processes in tokamaks. Particle and energy losses from the edge regions are often much higher than those predicted by neoclassical theory and are termed 'anomalous'. Anomalous transport represents one of the most important problems in the field of fusion research. Despite almost twenty years of research and considerable work on the subject, there are relatively few detailed analyses of edge transport experiments and still little is known about the causes of anomalous transport. Low level backround fluctuations of apparent random nature are continuously observed in the time evolution of many plasma parameters, even when large amplitude, coherent instabilities are absent. These are widely regarded as responsible for the enhancement of energy and particle losses with good experimental evidence, especially for the case of electrostatic modes. Fluctuations in the edge density, temperature, electric and magnetic fields result in fluctuations in the particle's radial position and velocity, leading to transport of both particles and energy across the confining magnetic field.

The aims of this study were to investigate the nature of the fluctuations in density, potential and electron temperature which are observed, the estimation of their role in the confinement of energy and particles in the edge region and the comparison of these results with both the predictions of various theories and with results obtained on other tokamaks. In addition, the effects (if any) of mode locking on edge transport were investigated. This was of interest because changes in transport could, in principle, change the equilibrium temperature and current density profiles in such a way as to change the gross stability of the plasma.

1.4 Outline of Thesis

In the plasma edge detailed measurements of the quantities required to directly determine the fluctuation driven fluxes are available. The total and fluctuation driven fluxes can be compared and the results emphasise the importance of edge turbulence but no model adequately describes *all* the measured properties. In the confinement region experimental observations are presently restricted to measurements of density, electric potential, temperature and magnetic fluctuations and their correlations. Chapter 2 reviews some of the main theories to explain the edge transport processes.

The machine used for all experiments described in this thesis, *Tokoloshe,* is discussed in

Chapter 3 along with details of the construction and use of the 4-pin Langmuir probe array. To determine the fluctuation driven fluxes, several measurements are required. Chapter 3 examines the methods of data acquisition and isolation as well as the statistical techniques employed in the analysis of the data. Chapter 3 also examines the justification (or otherwise) for the use of Langmuir probes in the edge region to measure the fluctuating quantities. Since several assumptions are usually made in the interpretation of probe results—including the fact that the temperature fluctuations are negligible—this Chapter then details the technique of measuring the edge electron temperature and temperature fluctuations using the double probe technique and examines their relative importance. The so-called 'standard' or 'reference' shot is then presented in detail in Chapter 4, including measurements of most edge parameters. This Chapter serves as the control experiment with which the results from all other experiments are compared.

Saturated tearing modes are often observed to lock (i.e. stop rotating) shortly before a major disruption. An understanding of the effects of locking, including those of transport, are therefore of interest in the control of this serious instability. Externally applied, helical magnetic fields were used on *Tokoloshe* to study the effects of mode locking on particle and heat fluxes at the plasma edge. Fields with toroidal mode number $n = 1$ and poloidal mode numbers $m = 2$ or 3 were used. Chapter 5 presents results of measurements taken during periods when the $\ell = 2$ and $\ell = 3$ coils were used to lock the toroidally rotating plasma. The effect of locking the magnetic islands and stochastic fields on thermal and particle transport and other edge parameters is presented in this Chapter as well as the observation of a high frequency magnetic mode detected on *Tokoloshe* and its relevance (if any) to edge transport. A discussion of the results, a summary of the thesis and suggestions for future work, follows in Chapter 6.

Chapter 2

Theory

High levels of density and potential fluctuations have been observed in the edge plasma of all tokamaks and the nature of these turbulent fluctuations has received increased attention over the past decade or so. A detailed study of turbulence and transport is also motivated by the recent results on large tokamaks which show that pure extrapolation is not sufficient to safely project to next generation devices. Measurements of particle losses in the edge regions and comparison of these with total particle losses suggest that these fluctuations could play an important role in the determination of the global particle confinement since they result in significant cross-field transport. An understanding of the observed fluctuations and transport is also needed in order to optimize design of divertors and limiters. Also, the discovery of the ASDEX H-mode (WAGNER *et al*, (1982)) with accompanying improved confinement time and sensitivity to edge boundary conditions, and the correlation of the transition to H mode operation with edge related processes further emphasise the need to understand plasma edge turbulence. The edge plasma is easily accessible to probes and can be well diagnosed experimentally. This provides a wealth of data which may then be used for the development of realistic and comprehensive plasma turbulence models.

Measurements (e.g. ZWEBEN *et al*, (1981, 1983, 1987), LEVINSON *et al*, (1984), RUDYJ *et al*, (1990)) show the edge turbulence to be characterised by large fluctuations having $\tilde{n}_e/n_e \sim 0.1 \rightarrow 1.0$ in contrast to the center where 0.02 is typically measured. Both wavenumber and frequency spectra are broad with typical $\Delta\omega/\omega \approx \Delta k_\theta/k_\theta \approx 1.0$ indicating a strong state of turbulence. Strong non-adiabatic behavior of the density fluctuations is observed $\tilde{n}_e/n_e \neq \tilde{\phi}_p/T_e$ (but see e.g. ZWEBEN *et al*, (1982)) where T_e is in eV throughout the remainder of this thesis. Typical poloidal wavenumbers and frequencies are $k_\theta r_s \sim 0.1$ and $\omega \sim \omega_{*e}$ respectively. Large particle and energy losses also exist in the

edge plasma and have been attributed to turbulence-driven transport. Since these losses could have serious consequences for future reactor tokamaks, controlling these anomalous particle losses will directly impact on future reactor design. To date, the instability, free energy drive and damping mechanisms for the observed turbulence have not yet been identified.

2.1 Models of Edge Turbulence

The experimental observation of large levels of fluctuations and transport have motivated a large (and still growing) body of turbulence theory. Most models are non-linear and predict the magnitudes of the turbulence levels and the resulting transport. Many of these models predict simple relationships between fluctuation levels and the free energy drive. These include the density, temperature, pressure or resistivity gradients. The theories that are believed to be valid in the edge plasma region separate into four classes, viz., (1) drift wave turbulence, (2) resistivity-gradient driven turbulence, (3) impurity radiation driven turbulence and (4) the 'mixing length arguments' in which the fluctuation levels themselves are assumed to be the driving terms. All predict fluctuation levels and transport close to values observed experimentally in tokamak plasmas. In many of the cases presented below, only the main, pertinent results of the theory under investigation will be presented. In particularly complicated theories, only the *scaling* of certain quantities with parameters relevant to this thesis, will be presented. It should also be pointed out that the term 'diffusion coefficient' is often not strictly correct and should be applied only to those cases in which Fick's Law is obeyed. Most of the theories referred to in the following discussion, however, refer loosely to a 'diffusion coefficient'—even in cases where Fick's Law is clearly not obeyed. In this thesis, therefore, this convention has been retained.

2.1.1 Drift Wave Turbulence

Drift waves are usually understood as largely adiabatic fluctuations (i.e. $\tilde{n}_e/n_e \approx \tilde{\phi}_p/T_e$). Non-adiabatic departures, although small, are included since these give rise to a density gradient which provides the principle free energy driving mechanism in all versions of the drift wave turbulence theories. Damping terms and instability mechanisms are, however, different in the various versions. Temperature fluctuations are ignored in the turbulence dynamics, but they are needed in order to access the temperature gradient. In some drift

wave theories (e.g. TERRY *et al*, (1985)) the basic components of the turbulent state are considered as a mixture of waves and localised density fluctuation elements or 'blobs', experimentally relevant since they could explain the observations made by ZWEBEN *et al*, (1985) on the Caltech tokamak.

Hasegawa - Wakatini Model

In this model, mode-coupling equations for the resistive drift wave instability are derived and solved numerically (HASEGAWA *et al*, (1983)). The fluctuation levels predicted by this model are

$$\frac{\tilde{n}_e}{n_e} \simeq 3\sqrt{\frac{r_s}{L_n}},$$

$$\frac{\tilde{\phi}_p}{T_e} < \frac{\tilde{n}_e}{n_e}.$$

The particle flux is assumed to scale with edge electron density gradient and electron temperature and is given by

$$\tilde{\Gamma}_{n\phi} = \frac{T_e \nabla n_e}{B_\phi}.$$

The particle diffusion coefficient is given by

$$D_{\mathrm{HW}} = \frac{T_e}{B_\phi},$$

or 16 $\times D_{\mathrm{Bohm}}$. Collisional dephasing of the density and potential fluctuations gives rise to the instability and damping arises from parallel conductivity.

Terry - Diamond Model

The non-linear theory of resistive density-gradient driven turbulence of TERRY *et al*, (1985) predicts fluctuation levels

$$\frac{\tilde{n}_e}{n_e} \simeq \frac{\tilde{\phi}_p}{T_e}$$

and $\tilde{\phi}_p/T_e$ scales as $\beta(r_s/L_n)$, where the coefficient β varies between 2 and 7 depending on the turbulent regime. The magnitude of the particle flux is predicted to scale as

$$\tilde{\Gamma}_{n\phi} \sim \frac{T_e^{\frac{3}{2}}}{L_n^2 B_\phi},$$

with associated diffusion coefficient scaling as

$$D_{\mathrm{TD}} \sim \frac{n_e T_e^{\frac{3}{2}}}{L_n B_\phi}.$$

The average poloidal wavenumber is predicted to be

$$\overline{k}_\theta \simeq \frac{0.3}{r_s}.$$

In this model, electron density 'blobs' extract free energy from the density gradient and are torn apart by non-linear shear stresses from $\vec{E} \times \vec{B}$ convection and parallel collisional diffusion. These blobs have lifetimes a few times the average correlation time and may be thought of as eddies in a turbulent fluid rather than perturbations associated with linear waves. Damping in this model is provided by the parallel viscosity and Compton ion scattering.

Waltz - Dominguez Model

This model (WALTZ (1987)) uses the direct interaction approximation to numerically solve the equations describing plasma wave-wave and wave-particle interactions. The electrons are treated with a linear nearly Boltzmann response and the simple wave-wave non-linear coupling models in two dimensions is extended to more physical electrostatic models for drift waves in three dimensions. Fluctuation levels are predicted to be

$$\frac{\tilde{n}_e}{n_e} \simeq \frac{\tilde{\phi}_p}{T_e}$$

with $\tilde{\phi}_p$ scaling as $\beta(r_s/L_n)$, with β about $3-4$ in this model. The particle flux scales as

$$\tilde{\Gamma}_{n\phi} \sim c_s n_e \left(\frac{r_s}{L_n}\right)^2,$$

and the associated diffusion coefficient scales as

$$D_{\mathrm{WD}} \sim \frac{c_s r_s^2}{L_n}.$$

Average wavenumbers are

$$\bar{k}_\theta \sim \frac{0.3}{r_s}.$$

Damping is due to both magnetic shear and ion Landau damping.

Chiueh - Terry Model

This model is an extension of the density-gradient driven model, taking into account the effects of a radial electric field near the edge (CHIUEH *et al*, (1986)). Two driving mechanisms are considered, each taking effect in different regions. Near the maximum electric field shear, the electric field is the dominant driving mechanism and away from this mechanism, turbulence is driven by the density gradient. In the former regime the effect of magnetic shear on linear instabilities and on fully developed turbulence has been examined and, depending on the strength of this shear, two different sets of fluctuation levels are estimated at saturation. These are (i) weak magnetic shear (resulting in a nonlinear cascade process) and (ii) strong magnetic shear (resulting in a nonlinear broadened-mode-structure mechanism).

For a model shear-flow profile, $v_{\text{phase}}(r)$ has the form $V_0 \tanh r/L_e$ (see Section 4.2) with V_0 a characteristic velocity of order $10^5\,\text{ms}^{-1}$.
For (i), the following scaling laws apply:

$$\frac{\tilde{n}_e}{n_e} \sim \frac{L_E}{L_n},$$

$$\frac{\tilde{\phi}_p}{T_e} \sim \frac{1}{4\sqrt{3}k_0 L_E} \cdot \frac{V_0}{r_s c_s k_{\min}},$$

$$\frac{\tilde{b}_r}{B_0} \sim \frac{\pi}{\sqrt{3}} \cdot \frac{L_E V_0}{\eta k_{\min} c_s^2},$$

with k_0 and $k_{\min}$ the average and minimum wavenumbers respectively.
Similarly, for (ii), the scaling laws are:

$$\frac{\tilde{n}_e}{n_e} \sim \frac{L_E}{L_n} \cdot \left(\frac{1}{k_0 L_E R^2}\right)^{\frac{5}{16}},$$

$$\frac{\tilde{\phi}_p}{T_e} \sim \left(\frac{1}{k_0 L_E R^2}\right)^{\frac{15}{16}} \cdot \frac{V_0 L_E}{r_s c_s},$$

$$\frac{\tilde{b}_r}{B_0} \sim \left(\frac{1}{k_0 L_E R^2}\right)^{\frac{9}{16}} \cdot \frac{V_0^2 L_s}{V_A^2 L_E},$$

with V_A the Alfvén speed, R, the Reynolds number and L_s the magnetic shear length.

2.1.2 Resistivity Gradient Driven Turbulence

The free energy sources that drives the resistivity gradient driven turbulence are the temperature and impurity density gradients (∇T_e and ∇Z_{eff}) via fluctuations in the resistivity, η (HAHM *et al*, (1987)). This theory extends and expands on the linear theory of the rippling mode instability, which is due to a convection of η down the gradient of η (i.e. $\nabla\eta$) due to a $\vec{j} \times \vec{B}$ force. This model predicts the following scalings

$$\frac{\tilde{n}_e}{n_e} \sim \left(\frac{n_e}{B_\phi}\right)^{\frac{1}{3}} \cdot \frac{(1/L_\eta + 1/L_Z)V_{\text{loop}}}{L_n T_e^{\frac{5}{6}}},$$

$$\frac{\tilde{\phi}_p}{T_e} \sim \frac{V_{\text{loop}}(1/L_\eta + 1/L_Z)}{T_e},$$

where $L_\eta = (d\ln\eta/dr)^{-1}$ and $L_Z = (d\ln Z_{\text{eff}}/dr)^{-1}$ are the scale lengths for the resistivity and Z_{eff} respectively. For simplicity, only one impurity is assumed. The fluctuation levels depend strongly on the loop voltage and are not, in general, equal.

The particle flux is predicted to scale as

$$\tilde{\Gamma}_{n\phi} \sim \left(\frac{n_e V_{\rm loop}(1/L_\eta + 1/L_Z)}{B_\phi}\right)^{\frac{4}{3}} \cdot \frac{1}{T_e^{\frac{5}{6}}},$$

and the associated diffusion coefficient scales as

$$D \sim \left(\frac{V_{\rm loop}(1/L_\eta + 1/L_Z)}{B_\phi}\right)^{\frac{4}{3}} \cdot \frac{n_e^{\frac{1}{3}}}{T_e^{\frac{5}{6}}},$$

Parallel thermal conductivity and impurity ion drag provide the damping. Currentless devices (i.e. $V_{\rm loop} = 0$) also experience turbulence similar to that observed on tokamaks (ZUSHI *et al*, (1988)) and fluctuation levels independent of the loop voltage have been observed (KIM (1989a)). For these (and other) reasons, this model is believed not to apply to edge turbulence.

2.1.3 Impurity Radiation Driven Turbulence

This model is an extension of the $\nabla\eta$ model, described above. It assumes an enhancement of the turbulence due to a temperature instability and is driven by impurity radiation effects depending strongly on the local radiation rates and the density of impurities (THAYER *et al*, (1987)). This model results in non-linear algebraic equations for fluctuation levels and particle fluxes and can be evaluated easily only in certain limits. In the special case of large radiation rates and no impurity density gradient it predicts the following scaling laws

$$\frac{\tilde{n}_e}{n_e} \sim \frac{\tilde{\phi}_p^{\frac{1}{3}}}{L_n},$$

$$\frac{\tilde{\phi}_p}{T_e} \sim (n_e n_Z I_Z)^{\frac{3}{2}} T_e^{\frac{9}{4}} B_\phi,$$

where n_Z is the impurity density and I_Z the local radiation rate for the impurity. The particle flux is predicted to scale as

$$\tilde{\Gamma}_{n\phi} \sim \frac{(n_Z I_Z)^2 n_e}{L_n T_e^{\frac{5}{3}}},$$

and the associated diffusion coefficient scales as

$$D \sim \frac{(n_Z I_Z)^2}{T_e^{\frac{5}{3}}}.$$

In this case, both $\tilde{\Gamma}$ and D are independent of B_ϕ, $\tilde{\phi}_p/T_e \propto B_\phi$ and $\tilde{n}_e/n_e \neq \tilde{\phi}_p/T_e$. The fluctuations can be strongly enhanced by an impurity gradient, L_Z. The impurity

radiation driven turbulence theory is generally considered to be a good model to explain edge turbulence since it predicts $\tilde{\phi}_p/T_e > \tilde{n}_e/n_e$ (often observed on tokamaks). The physical origin of this result is that the non-linear structure responsible for the impurity radiation enhancement of both the potential and the density fluctuations described by THAYER *et al*, (1987), tends to force the potential fluctuation greater than the density fluctuation at saturation.

2.1.4 Mixing Length Arguments

Mixing length arguments use general assumptions about the free energy available to drive the turbulence and a knowledge of a linear instability in order to estimate the fluctuation levels and particle flux (DIAMOND (1987)). Damping and saturation mechanisms are not specified. If the free energy source is assumed to be the density gradient these arguments predict scaling laws similar to the drift wave models described above i.e. $\tilde{n}_e/n_e \sim 1/k_{\rm rms}L_n$ where $k_{\rm rms}$ is the rms value of a radial wavenumber of a linear mode. Three main difficulties arise with these arguments: (i) the lack of specific saturation conditions, (ii) the neglect of dissipation and (iii) the use of *linear* modes applied to strongly *non-linear* systems. Often, the mode widths themselves are amplitude dependent.

Nonetheless, in the absence of necessary information on the instabilities involved and saturation and dissipation mechanisms, these arguments are often used.

A model for the turbulence in the scrape off layer of tokamaks which used a fluid theory of electrostatic perturbations in the scrape off plasma has also been proposed by GARBET *et al*, (1990). The model takes into account the inhibition of stabilising currents by the intersection of field lines with the wall in the scrape off layer. RITZ *et al*, (1990b) compared results from TEXT and the ATF stellarator (since a velocity shear is present on both devices, both have substantial edge turbulence, and in both cases the fluctuation induced transport is enough to account for total particle transport). Edge characteristics were simulated with computer models assuming drift wave and resistive turbulence models including the impurity effects on turbulence. Impurity radiation enhanced rippling modes, drift waves and thermal instabilities were used by LEBOEUF *et al*, (1991) to model the far edge turbulence based on a realistic profile and parameter set from TEXT. The results agreed well with measured fluctuation characteristics.

2.2 Fluctuation Induced Transport

Fluctuations in the magnetic and electric fields of a tokamak lead to fluctuations in the particles velocities and positions. This could result in transport of both particles and heat across the confining magnetic field at rates in excess of the neoclassical binary Coulomb collisional models for which both $\tilde{E}_\theta$ and $\tilde{b}_r = 0$. This excess fluctuation-induced loss would therefore be contributory to anomalous loss.

The radial fluctuating velocity is given by the drift term $\tilde{E}_\theta/B_\phi$. The toroidal electric field and current fluctuations actually govern the electrostatic losses (BICKERTON (1973)) although an identical result is obtained. The radial fluctuating velocity will include parallel velocity flow components along perturbed magnetic field lines with a radial perturbation, $\tilde{b}_r$, giving

$$\tilde{v}_r = \frac{\tilde{E}_\theta}{B_\phi} + v_\parallel \frac{\tilde{b}_r}{B_\phi}. \tag{2.1}$$

The relative magnitudes of the two contributions to $\tilde{v}_r$ in Equation 2.1 differ by orders of magnitude. MANHEIMER (1979) showed that fluctuation losses, even in the presence of magnetic field fluctuations are ambipolar so $v_\parallel \sim v_i$ (ion thermal velocity). This means that ion inertia limits mass transport along the perturbed magnetic field lines. Experimentally $\tilde{E}_\theta/B_\phi \sim 10^5\,\mathrm{cm\,s^{-1}}$ and $v_\parallel \tilde{b}_r/B \sim 10^3\,\mathrm{cm\,s^{-1}}$ HOWLING (1986). The overall radial velocity is clearly dominated by the electrostatic (rather than the magnetic) contribution. Thus, these low-frequency, small-scale fluctuations are electrostatic in nature and the $v \times \tilde{b}_r$ terms will be ignored.

2.2.1 Electrostatic Turbulence

The macroscopic evolution of the plasma may be deduced by separating any fluctuating quantity, f, into an average (macroscopic part) evolving on a slow timescale of order τ_E and a rapidly varying microscopic part associated with the microturbulence. Hence

$$f = \langle F \rangle + \tilde{f},$$

where $\langle \tilde{f} \rangle = 0$ since the fluctuations are assumed to be random. The Vlasov equation may be averaged over the fluctuation timescale to yield

$$\left(\frac{\partial}{\partial t} + \vec{v} \cdot \frac{\partial}{\partial x} + \frac{q}{m}(\langle E \rangle + \vec{v} \times B_\phi) \frac{\partial}{\partial v} \right) \langle F \rangle + \frac{q}{m} \langle \tilde{E} \cdot \frac{\partial \tilde{F}}{\partial v} \rangle = \langle C(F) \rangle, \tag{2.2}$$

where F is the distribution function and the correlation term $\langle \tilde{E} \cdot \partial \tilde{F}/\partial v \rangle$ contains the effects of the electrostatic turbulence. The classical collision operator is denoted by

$\langle C(F)\rangle$. The velocity moments of Equation 2.2 yield the equations governing the evolution of the macroscopic plasma variables in the presence of the classical (and neoclassical) and turbulent processes.

In what follows, for the calculation of electrostatic fluctuation-induced losses from Equation 2.2, $\langle C(F)\rangle$, the classical term will be ignored on the understanding that all fluxes thus obtained are anomalous fluxes. Slab geometry is also assumed and normal toroidal coordinates r, θ, ϕ will be used with spatial variations allowed in r only. Both b and $\langle E\rangle$ are assumed to be poloidal, i.e. in the θ direction. The zeroth velocity moment of Equation 2.2 is the continuity equation given by

$$\frac{\partial}{\partial t}n + \frac{\partial}{\partial r}(nv_r) = 0.$$

The radial particle flux is $\Gamma_r = nv_r$ where v_r is the plasma radial fluid velocity. The toroidal (ϕ) component of the first velocity moment of Equation 2.2 becomes

$$\frac{q}{m}nv_rB - \frac{q}{m}\langle\tilde{n}_e\tilde{E}_\theta\rangle = 0.$$

The radial flux is then

$$\Gamma_r = nv_r = \frac{\langle\tilde{n}_e\tilde{E}_\theta\rangle}{B}, \tag{2.3}$$

with no assumptions of small amplitude fluctuations. LIEWER (1985) obtained the results for the heat flux. The derivation is much lengthier and is therefore not repeated here—only the result will be presented.

Electrons are considered since their thermal velocities greatly exceed their fluid velocities and, since the fluctuation frequency is low compared to the electron-electron collision frequency, isotropic pressure may be assumed. The total energy flux Q is often separated into a conducted heat flux and a convected heat flux

$$Q = q + \frac{5}{2}T_e\Gamma,$$

so that

$$\begin{aligned} Q_r &= \frac{3T_e\Gamma_r}{2B_\phi} + \frac{3n_e\langle\tilde{T}_e\tilde{E}_\theta\rangle}{2B_\phi}, \\ &= \frac{3T_e\langle\tilde{n}_e\tilde{E}_\theta\rangle}{2B_\phi} + \frac{3n_e\langle\tilde{T}_e\tilde{E}_\theta\rangle}{2B_\phi} \end{aligned} \tag{2.4}$$

There is disagreement in the literature as to whether the factor in the electrostatic convective component is 5/2 or 3/2: the difference is related to the contributions made by the turbulence to the energy source $\langle E_\perp j_\perp\rangle$ as shown by ROSS *et al*, (1987) and DÜCHS (1989). These fluxes must be studied experimentally and theoretically to discover whether anomalous transport is explicable in terms of fluctuations or not. Theoretical approaches are simplified by experimental evidence of $\tilde{n}_e$, $\tilde{E}_\theta$, $\tilde{b}_r$.

2.2.2 Magnetic Fluctuations

The effects of the magnetic field perturbations are ignored when considering the particle flux because they are small and dominated by large losses from the electrostatic contribution. The parallel classical heat conductivity is large and relatively small deviations of the field lines in the radial direction due to a radial field component result in a large net increase in the radial heat losses. Unlike mass diffusion, electron thermal transport is not inhibited by the inertia of the ions. The classical conductive heat flux may be written

$$Q = -K_{\|}\nabla_{\|}T - K_{\perp}\nabla_{\perp}T,$$

where $K_{\|}$ and $K_{\perp}$ are the classical conductivities parallel and perpendicular to the magnetic field respectively. HAAS (1981) showed that if a fluid approximation is used, fluctuations in magnetic field and temperature lead to a radial electron heat conductivity

$$K_r = K_{\|}e\frac{\langle|\tilde{b}_r^2|\rangle}{B^2} + K_{\|}\frac{\langle\tilde{b}_r(d\tilde{T}_e/dr)\rangle}{B}.$$

The radial thermal conduction resulting from microscopic field fluctuations can be written

$$Q_r = K_r(\tilde{b}_r)\frac{dT_e}{dr},$$

where K_r is some model-dependent anomalous thermal conductivity due to $\tilde{b}_r$.

The amplitude of $\tilde{b}_r/B_\phi$ is typically $\approx 10^{-4}$ to 10^{-5}, increasing towards smaller plasma radius. Both high (GENTLE *et al*, (1984), MALACARNE *et al*, (1987) and KIM *et al*, (1989)) and low (ZWEBEN *et al*, (1981)) correlation between the (edge) electrostatic and magnetic fluctuations has been found.

Quantitative calculations of the effects of the measured $\tilde{b}_r$ are difficult. Firstly the externally measured $\tilde{b}_r$ must be classified as an edge or interior phenomenon. Different conclusions have been reached concerning this point. Measured $\tilde{b}_r$ values need to be extrapolated to the value of $\tilde{b}_r$ at the resonant surfaces to check if island overlap has occurred. If so, a formula must be chosen to infer local electron heat transport (WOOTTON (1989)). Unless strong turbulence formulae are invoked (MALACARNE *et al*, (1987)) it is usually true that $\tilde{b}_r$ is too small to produce significant energy fluxes using existing models and formulae, except at high β values.

HEDEMANN (1981) found that using the quasi-linear estimate on the Caltech tokamak, $\tilde{b}_r$ was too small to be important to either particle or heat transport. ZWEBEN *et al*, (1979), (1981) showed that $\tilde{b}_r/B_\phi$ increases with decreasing r to 10^{-4} at $\rho = 0.6$. Using the quasi-linear expression this is too small to explain particle transport. WOOTTON

(1989) also found $\tilde{b}_r/B_\phi \sim 10^{-5}$ which is too small to explain particle transport. In the work presented here, no attempt was made to measure the magnetic fluctuations.

2.2.3 Mathematical Description of $\tilde{\Gamma}$

The original mathematical treatment of the problem of fluctuation induced transport was covered by POWERS (1974). In this paper, the digital implementation of spectral analysis techniques was utilized to investigate experimentally the relationship between plasma fluctuations and transport across confining magnetic fields. The salient points of the derivation are given below. Detailed descriptions may be found in POWERS *et al*, (1974).

Using Equation 2.3 the time averaged particle flux may be written as

$$\langle \tilde{n}_e \tilde{v}_r \rangle = \frac{1}{B_\phi} \langle \tilde{n}_e \tilde{E}_\theta \rangle = \frac{1}{B_\phi} \mathcal{C}_{nE}(0), \tag{2.5}$$

where $\mathcal{C}_{nE}(0)$ is the cross correlation function $\mathcal{C}_{nE}(\tau)$ between the density and electric field fluctuations evaluated for $\tau = 0$. $\mathcal{C}_{nE}(\tau)$ may be expressed as the Fourier transform of the cross power spectrum between density and electric field fluctuations $\mathcal{P}_{nE}(\omega)$

$$\mathcal{C}_{nE}(\tau) = \langle \tilde{n}_e(t) \tilde{E}_\theta(t+\tau) \rangle = \int_{-\infty}^{\infty} \mathcal{P}_{nE}(\omega) e^{-i\omega\tau} \, d\omega. \tag{2.6}$$

Symmetry properties of the cross-power spectrum allow Equation 2.6 to be written

$$\mathcal{C}_{nE}(\tau) = \langle \tilde{n}_e(t) \tilde{E}_\theta(t+\tau) \rangle = 2\Re \int_0^{\infty} \mathcal{P}_{nE}(\omega) e^{-i\omega\tau} \, d\omega. \tag{2.7}$$

Substituting Equation 2.7 into Equation 2.5, the time averaged flux in terms of the cross-power spectrum between the density and electric field fluctuations

$$\langle \tilde{n}_e \tilde{v}_r \rangle = \frac{1}{B_\phi} \langle \tilde{n}_e \tilde{E}_\theta \rangle = \frac{2}{B_\phi} \Re \int_0^{\infty} \mathcal{P}_{nE}(\omega) \, d\omega. \tag{2.8}$$

Practically, it is easier to measure $\tilde{\phi}_p$ than $\tilde{E}_\theta$ (where $\tilde{\phi}_p$ are the plasma potential fluctuations). Assuming that $\tilde{E}_\theta = -\nabla \tilde{\phi}_p$, the density and potential fluctuations may be represented by the following superposition

$$\tilde{n}_e(r,t) = \int_{-\infty}^{\infty} N_0(\omega) e^{i(k_\theta(\omega) r - \omega t)} \, d\omega, \tag{2.9}$$

$$\tilde{\phi}_p(r,t) = \int_{-\infty}^{\infty} \Phi_0(\omega) e^{i(k_\theta(\omega) r - \omega t)} \, d\omega, \tag{2.10}$$

$$\begin{aligned} \tilde{E}_\theta(r,t) &= -\nabla \tilde{\phi}_p(r,t) \\ &= -ik_\theta(\omega) \int_{-\infty}^{\infty} \Phi_0(\omega) e^{i(k_\theta(\omega) r - \omega t)} \, d\omega. \end{aligned} \tag{2.11}$$

The corresponding auto and cross power spectra are given by

$$\mathcal{P}_{nn}(\omega) = \mathcal{F}^{\star}[\tilde{n}_e]\mathcal{F}[\tilde{n}_e] = |N_0(\omega)|^2, \tag{2.12}$$

$$\mathcal{P}_{\phi\phi}(\omega) = \mathcal{F}^{\star}[\tilde{\phi}]\mathcal{F}[\tilde{\phi}] = |\Phi_0(\omega)|^2, \tag{2.13}$$

$$\mathcal{P}_{n\phi}(\omega) = \mathcal{F}^{\star}[\tilde{n}_e]\mathcal{F}[\tilde{\phi}] = N_0(\omega)\Phi_0(\omega) \tag{2.14}$$

$$= |\mathcal{P}_{n\phi}(\omega)| \exp(i\alpha_{n\phi}(\omega)), \tag{2.15}$$

$$\mathcal{P}_{nE}(\omega) = \mathcal{F}^{\star}[\tilde{n}_e]\mathcal{F}[\tilde{E}_\theta] = -ik_\theta(\omega)N_0(\omega)\Phi_0(\omega) \tag{2.16}$$

$$= -ik_\theta(\omega)\mathcal{P}_{n\phi}(\omega), \tag{2.17}$$

where $\mathcal{F}$ denotes a Fourier transform. The cross-power spectrum $\mathcal{P}_{nE}(\omega)$ is therefore the cross-power spectrum between the density and potential fluctuations $\mathcal{P}_{n\phi}(-ik_\theta(\omega))$. Substituting Equation 2.16 into Equation 2.8 the time averaged flux becomes

$$\langle \tilde{n}\tilde{v}_r \rangle = \frac{1}{B_\phi}\langle \tilde{n}_e \tilde{E}_\theta \rangle = -\frac{2}{B_\phi}\int_0^\infty ik_\theta(\omega)\mathcal{P}_{n\phi}(\omega)\, d\omega. \tag{2.18}$$

$\mathcal{P}_{n\phi}(\omega)$ may be written

$$\mathcal{P}_{n\phi}(\omega) = \mathcal{C}_{n\phi}(\omega) + i\mathcal{Q}_{n\phi}(\omega), \tag{2.19}$$

where $\mathcal{C}_{n\phi}$ is the co-spectrum and $\mathcal{Q}_{n\phi}$ is the quad-spectrum. Substituting Equation 2.19 into Equation 2.18 gives

$$\langle \tilde{n}\tilde{v}_r \rangle = \frac{1}{B_\phi}\langle \tilde{n}_e \tilde{E}_\theta \rangle = \frac{2}{B_\phi}\int_0^\infty k_\theta(\omega)\mathcal{Q}_{n\phi}(\omega)\, d\omega. \tag{2.20}$$

Equation 2.20 may now be written

$$\langle \tilde{n}\tilde{v}_r \rangle = \frac{1}{B_\phi}\langle \tilde{n}_e \tilde{E}_\theta \rangle = \int_0^\infty T(\omega)\, d\omega, \tag{2.21}$$

where

$$T(\omega) \equiv \frac{2k_\theta(\omega)\mathcal{Q}_{n\phi}}{B_\phi}.$$

The quantity $T(\omega)$ is a transport spectral density function, i.e. the number of particles per unit area per unit time per unit frequency interval. The transport due to a small spectral band of width $d\omega$ centered at ω is given by $T(\omega)\, d\omega$. The total particle flux due to spectral components between ω_a and ω_b is given by

$$\int_{\omega_a}^{\omega_b} T(\omega)\, d\omega.$$

If $\mathcal{P}_{n\phi}$ is expressed in terms of its absolute value $|\mathcal{P}_{n\phi}|$ and phase $\alpha_{n\phi}(\omega)$, Equation 2.18 becomes

$$\langle \tilde{n}\tilde{v}_r \rangle = \frac{1}{B_\phi}\langle \tilde{n}_e \tilde{E}_\theta \rangle = \frac{2}{B_\phi}\int_0^\infty k_\theta(\omega) \underbrace{|\mathcal{P}_{n\phi}(\omega)| \sin[\alpha_{n\phi}(\omega)]}_{\mathcal{Q}_{n\phi}(\omega)}\, d\omega,$$

where $\alpha_{n\phi}(\omega)$ is given by the phase of the potential fluctuations minus the phase of the density fluctuations at each frequency ω. Multiplying and dividing the integrand by $\sqrt{|\mathcal{P}_{nn}(\omega)\mathcal{P}_{\phi\phi}(\omega)|}$ gives

$$\langle \tilde{n}\tilde{v}_r \rangle = \frac{1}{B_\phi}\langle \tilde{n}_e \tilde{E}_\theta \rangle = \frac{2}{B_\phi}\int_0^\infty k_\theta(\omega)|\gamma_{n\phi}(\omega)|\sqrt{|\mathcal{P}_{nn}(\omega)\mathcal{P}_{\phi\phi}(\omega)|}\sin[\alpha_{n\phi}(\omega)]\,d\omega, \qquad (2.22)$$

where $|\gamma_{n\phi}(\omega)|$ is the coherency between the electron density and plasma potential fluctuations and is given by

$$|\gamma_{n\phi}(\omega)| = \frac{|\mathcal{P}_{n\phi}|}{\sqrt{\mathcal{P}_{nn}\mathcal{P}_{\phi\phi}}}.$$

The integral in Equation 2.22 indicates that all frequencies in the fluctuation spectrum may, in principle, contribute to the plasma transport. A small spectral band $\delta\omega$ centered at ω will contribute to the time averaged particle flux of this band by an amount

$$\langle \tilde{n}\tilde{v}_r \rangle_{\delta\omega} = \frac{k_\theta(\omega)}{B_\phi}|\gamma_{n\phi}(\omega)|\sin[\alpha_{n\phi}(\omega)]n_{\rm rms}\phi_{\rm rms}, \qquad (2.23)$$

where $n_{\rm rms}$ and $\phi_{\rm rms}$ denote the rms values of the density and potential fluctuations respectively due to the spectral components of width $\delta\omega$ centered at ω i.e.

$$n_{\rm rms} = \sqrt{2\mathcal{P}_{nn}(\omega)\delta\omega},$$

$$\phi_{\rm rms} = \sqrt{2\mathcal{P}_{\phi\phi}(\omega)\delta\omega}.$$

The contribution to the time averaged flux of a band of fluctuations $\delta\omega$ wide and centered at frequency ω is given by the product of

- $k_\theta(\omega)/B_\phi$
- rms values of n_e and ϕ_p in that spectral band
- the sine of the phase angle between the n_e and ϕ_p fluctuations
- the coherency between n_e and ϕ_p fluctuations within that spectral band,

giving finally

$$\tilde{\Gamma}(\omega) = \frac{\tilde{n}_e(\omega)\,\tilde{\phi}_p(\omega)\,\gamma_{n\phi}(\omega)\,k_\theta(\omega)\,\sin[\alpha_{n\phi}(\omega)]}{B_\phi}. \qquad (2.24)$$

Chapter 3

Tools and Procedures

3.1 The *Tokoloshe* Tokamak

The *Tokoloshe* tokamak is a medium sized, ohmically heated tokamak. The vacuum chamber is constructed from 3 mm thick 316L stainless steel with $R = 0.52$ m and $a_w = 0.28$ m. Figure 3.1 shows a plan view of *Tokoloshe* tokamak showing the positions of the major diagnostics and the convention of toroidal position measurement used throughout this thesis. The limiter arrangement on *Tokoloshe* consists of two, 180° segments of chromium plated stainless steel. It is therefore a fully poloidal, aperture or ring limiter mounted at $\phi = 112°$. It defines a plasma radius of 0.24 m which gives *Tokoloshe* the low aspect ratio of 2.17.

The machine has an air-core, ohmic heating transformer with a maximum volt-second rating of 0.25. The toroidal field on major axis has a maximum field strength of 1.2 T but all discharges studied here had $B_\phi = 0.6$ T on axis. Hydrogen was used as the fill gas at a pressure of 2.0×10^{-4} torr. The density is increased soon after the start of the discharge by strong gas puffing from gas inlet valves. Typical plasma discharges (which are referred to later as the "standard shot") terminate with a density disruption and exhibit the characteristics shown in Figure 4.1.

The low aspect ratio of *Tokoloshe* plasmas leads to strong toroidal effects such as the marked outward displacement of the flux surfaces. The vertical stabilising field is preprogrammed to maintain equilibrium. Peak plasma current is reached after about 8 ms into the discharge and the discharge is terminated by a major disruption during the current decay phase.

Wall conditioning before any experimental run is achieved with several hours of Taylor discharge cleaning (OREN *et al*, (1977)) combined with titanium gettering over close to 100% of the wall surface. To estimate Z_{eff}, it was assumed that $I_p = \int j(r) 2\pi r dr$ with $j(r)$ the current density. Also, $j(r)$ may be written $\sigma_{\|}(r)E$, assuming that $E = V_{\text{loop}}/2\pi R_0$ i.e. $E \neq E(r)$ and where $\sigma_{\|}(r)$ is the parallel Spitzer conductivity, proportional to $T_e^{\frac{3}{2}}/Z_{\text{eff}}$. Using these assumptions, Z_{eff} is estimated to be 2.2±0.5.

Standard diagnostics on *Tokoloshe* include two single soft X-ray scanners, a soft and hard X-ray spectrometer,, an eight diode soft X-ray array, a Thomson scattering apparatus, a neutral particle spectrometer, B_θ and B_r magnetic pickup coils, visible and H_α monitors, an HCN interferometer and both a single and 4-pin Langmuir probe. Thomson scattering measurements (ROBERTS *et al*, (1986)) indicate

$$T_e(r) \simeq T_e(0)\left(1 - \frac{r^2}{a^2}\right)^2.$$

Thomson scattering profile measurements of the electron density, $j(r)$, indicate

$$n_e(r) \simeq n_e(0)\left(1 - \frac{r^2}{a^2}\right).$$

The line averaged electron density through a centre chord is $\overline{n}_e \simeq 4 \times 10^{19}\text{m}^{-3}$. Using the power balance equation,

$$\frac{dW}{dt} = P_{\text{in}} - \frac{W}{\tau}$$

(where W is the electron thermal energy and P_{in} is the total power input) and assuming steady state conditions, the global electron energy confinement time, τ_{Ee} may be written as $\tau_{Ee} = \int_V W dV / \int_V P_{\text{in}} dV = \frac{3}{2}\int n_e T_e dV / V_{\text{loop}} I_p \simeq 4.7 \pm 1.5\,\text{ms}$. Using measured parameters from *Tokoloshe* in a free boundary equilibrium code, the best fit cylindrical q profile is

$$q(r) = 0.7 + 2.8\left(\frac{r}{a}\right)^2,$$

which gives good agreement with all general features of *Tokoloshe* standard equilibrium (NOTHNAGEL (1991)).

3.1.1 Helical Coils

Tokoloshe has three sets of fully toroidal, stellarator-like windings installed externally to the vacuum chamber. The helicity of the windings is $\ell(= m/n) = 3/1$, $2/1$ and $1/1$ and the current distribution due to these coils can be expressed by

$$I_k(\theta, \phi, r_s) = (-1)^{k-1} I_\ell \delta\left(\theta + \frac{m}{n}\phi - \delta_\ell \sin\theta + \frac{(k-1)\pi}{\ell}\right),$$

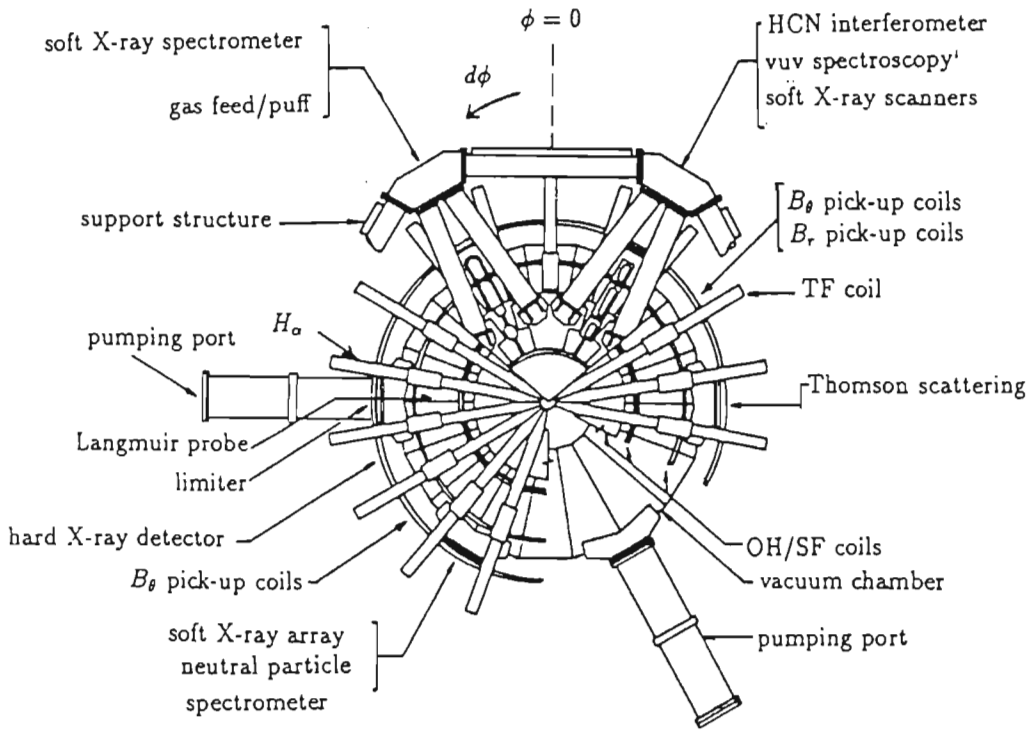

Figure 3.1: Plan view of *Tokoloshe* showing major diagnostics and toroidal coordinate system.

where $k = 1, 2$ or 3 and δ is used in the sense $\delta(A) = 1$ if $A = 0$ and $\delta(A) = 0$ if $A \neq 0$ (where A is an arbitrary quantity). δ_ℓ is a winding law parameter and has the values $\delta_1 = 40°$, $\delta_2 = 48°$ and $\delta_3 = 0°$ ROBERTS *et al* (1991a). Figure 3.2 shows a schematic representation of the $\ell = 1$ coil on a smooth torus (i.e. in the absence of viewing ports and other protrusions).

To a first approximation each winding is 'resonant' with a field line on the rational surfaces $q = 3/1$, $2/1$ and $1/1$ of interest. The toroidal field, B_ϕ, and plasma current, I_p, define the helicity of the field lines. The coils are wound such that they have the same helicity as these field lines ('resonant') or the opposite helicity (non-resonant). These two configurations may be obtained by chosing different directions of I_p or B_ϕ. The direction of I_p and I_ℓ determines the orientation of the coil induced magnetic islands. The field due to the windings does not give rise to pure helical islands of the required helicity. Higher order harmonics arise because of the toroidicity of the arrangement, the discreteness of the windings and the fact that the torus is not smooth so windings must deviate past viewing ports, etc.

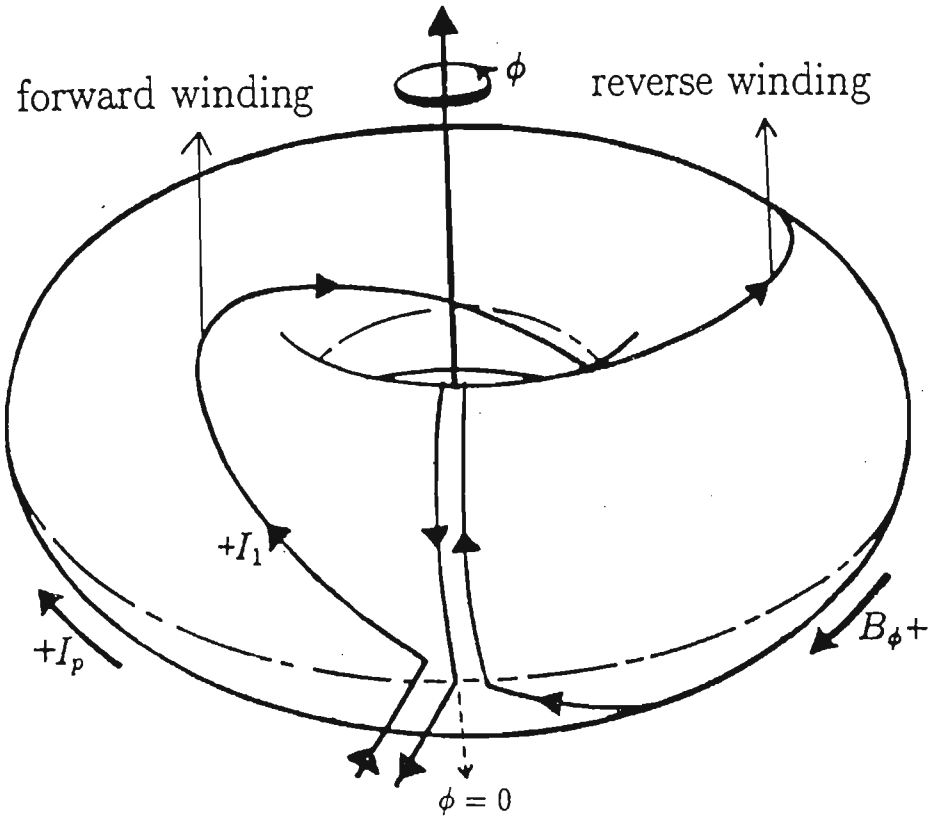

Figure 3.2: Position of the $\ell = 1$ coil on a smooth torus. The convention for positive and negative B_ϕ, I_p and $I_{\ell=1}$ and resonant and non-resonant combinations of current directions are also indicated.

3.2 Langmuir Probes

The complete experimental characterisation of a plasma would require the determination of all plasma parameters at each point as a function of time including the density, temperature and fluxes of particles and heat of each species, as well as the magnetic and electric fields and potential at every point. This would provide a complete database with which theoretical models could be compared provided the method of measurement did not perturb the plasma. The environment in the vacuum chamber, albeit transient, suffers sufficiently high temperatures that no solid materials can survive. Even if this were not the case, material probes well inside the plasma can significantly alter the parameters they measure. Consequently, data must be acquired from the analysis of radiation and particle emissions or by passing laser or ion beams through the plasma. These measurements are dominated by the plasma core and are unavoidably chord or volume averaged. Often important parameters, such as the plasma current density profile and diffusion coefficients, have to be inferred from other parameters such as the electron temperature profile. The fluctuations of interest in this thesis are known to be small scale so these data are of little value for direct information on fluctuation mechanisms. Also, fluctuation induced transport of particles and heat involves measurements of correlations between parameters at a point. These are not retrievable from chord/volume averaged data so they are of no value for gauging such losses. The edge plasma (where the 'edge' is defined as shown in Figure 1.3) on the other hand, is cooler, amenable to probes built from refractory materials and, with little perturbation to the local plasma, allows measurements of all the above plasma parameters. Material probes are relatively small so they can access the edge plasma a few centimetres either side of the limiter. Particle and heat flux have been found to be a maximum in this region and most fluctuation ratios are known to attain their largest values here. For these reasons the edge plasma is rich in information for the comparison of theory and experiment regarding the mechanisms and contribution to losses by fluctuations.

The current which flows in Langmuir probes when immersed in a plasma yields information on electron density, floating potential and, if properly configured, the electron temperature. In the last two decades, the Langmuir probe has been increasingly used by investigators of plasma turbulence. The probes must be constructed from material with a high melting point and thermal conductivity to withstand high temperature pulses. Secondary electron emission must be reduced to a minimum so the probes should also have a high work function. A high degree of purity is essential since arcs tend to form on impurity inclusions on the surface of a metal. Platinum is the best material for this

purpose, but tungsten also satisfies these requirements, is cheaper and easier to obtain. Spherical probes were chosen because the electric field surrounding a spherical probe decreases more rapidly with distance than for a plane probe. This tends to reduce the perturbative effect introduced by the probes.

3.2.1 Langmuir Probes on *Tokoloshe*

An array of four Langmuir probes, arranged in a square, 4 mm on edge, was used to measure the various properties of the *Tokoloshe* plasma. Each probe is a 0.8 mm diameter tungsten wire which terminates in a sphere of diameter 1.61 mm at the edge of a stainless steel head section shown schematically in Figure 3.3. The curved front section was introduced to reflect the curvature of *Tokoloshe* at the limiter radius. All four probe tips are, therefore, at the same radial position at the limiter. Although the curvature changes as the probe is moved radially, the tips are always within 2% of a 'mean' radial position—even at maximum insertion of 25 mm—since the change in curvature is very small. Figure 3.4 is a photograph of this arrangement. The flange which connects to the vacuum vessel is at left. Ceramic tubing protects the probe stems from the plasma, seen protruding beyond the head section of this component. The probe is installed 10 cm from the centre port in the port furthest from the centre of the torus, shown in Figure 3.5. A recessed ceramic tube provides insulation between the filament and the tube. Gold-tip connectors join the filaments to teflon-coated copper wires, covered with a coax braid sheath to reduce cross-talk between them. The wires pass through a macor block which is embedded in the head, reducing cross-talk in this region and ensuring that the wires do not touch. Hypodermic coupling connects this to the ceramic coated copper wire as shown in Figure 3.6.

The entire arrangement is located at the end of a stainless steel support tube to allow radial movement. The array was located 5° from the limiter in the ion drift direction and 90° from the $\phi = 0°$ position. The probes withstood insertion of up to 25 mm inside the limiter radius and gave rise to little perturbation to the plasma over this range. Insertion lengths beyond 25 mm resulted in an early plasma disruption. The tips are labelled **L1**, **S1**, **L2** and **S2** according to their length and orientation with respect to the plasma current direction. The '**L**' tips are the longer tips of the four, as shown in Figure 3.5 and the '**S**' tips the shorter. Although the electronics connected to the tips allowed either pair[1] to be configured to measure i_{sat} or ϕ_f, in most of the experiments in this experiment, **L1/S1** measured i_{sat} and **L2/S2**, ϕ_f.

[1](**L1** and **S1**) or (**L2** and **S2**).

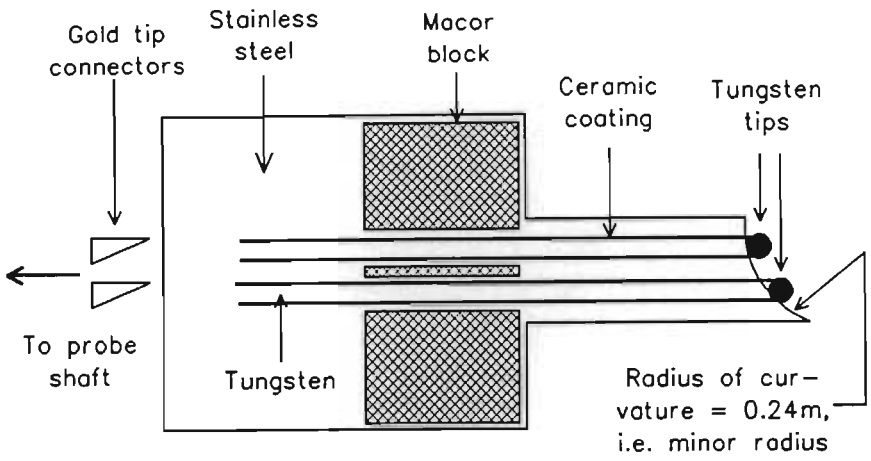

Figure 3.3: Schematic of the head section of the Langmuir probe array.

The tips were aligned such that the two L tips were both on a major radius, R. Using the equation of a field line,

$$r\frac{d\theta}{B_\theta} = R\frac{d\phi}{B_\phi}$$

with r the probe separation in this case, and using $q(a) \simeq 3.5$, it was found that, for the pitch of the edge magnetic field lines, the displacement of any given field line from tip to tip separated in the toroidal direction, was $\approx 0.5\,\mathrm{mm}$. With a diameter of 0.8 mm, it is therefore possible for one tip to shadow another 'downstream' from it. Measurements of n_e taken using both tips, however, gave very similar results, indicating that the shadow effect is not distorting parameters to a significant degree.

3.2.2 Langmuir Probe Theory

Single Probes

A Langmuir probe immersed in a plasma and biased strongly negative (i.e. $|V_{\mathrm{bias}}| > 3T_e$) will repel most of the electrons and the current in the probe will be due to i_{sat}, the ion saturation current. In a cold ion plasma ($T_i = 0$), simple plasma theory predicts (SWIFT (1970))

$$i_{\mathrm{sat}} = n_e e A \sqrt{\frac{eT_e}{m_i}}, \tag{3.1}$$

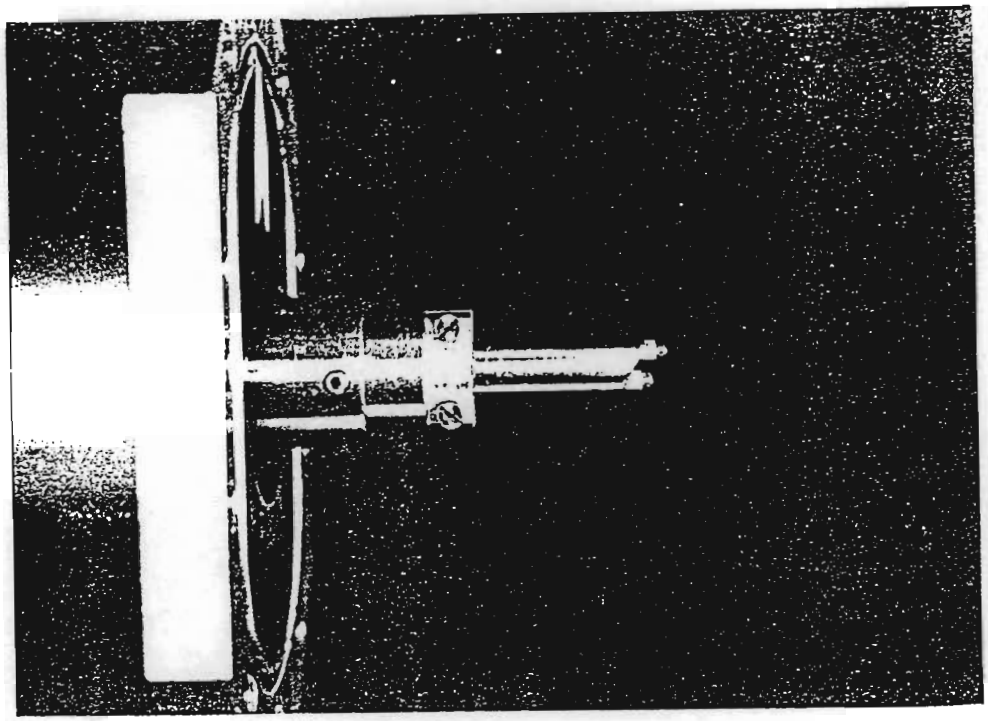

Figure 3.4: Photograph of head section of the Langmuir probe array.

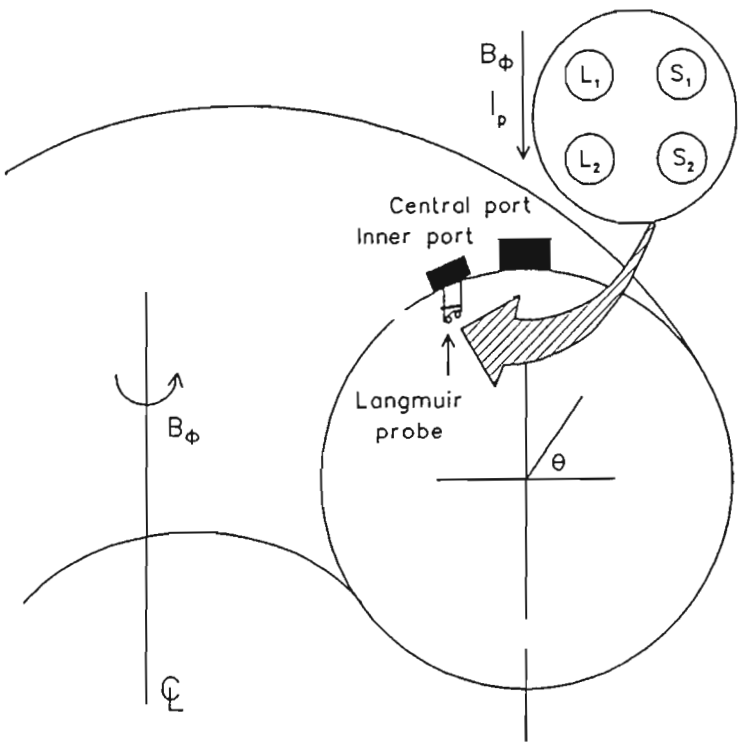

Figure 3.5: Schematic section of *Tokoloshe* showing the position of the probes and directions of I_p, the plasma current and B_ϕ, the toroidal field.

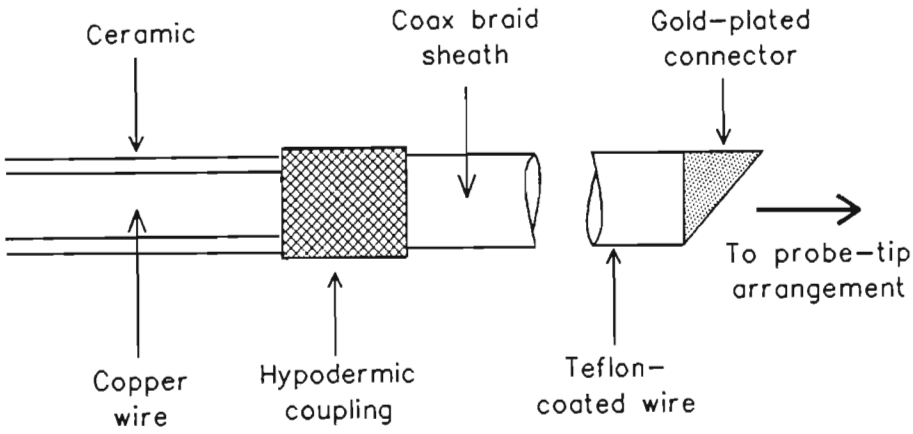

Figure 3.6: Detail of the connection in the head of the probe array.

where A is the probe area. The sheath potential reduces the thermal flux by a Boltzmann factor giving (for the net electron current i_e):

$$i_e = n_e e A \sqrt{\frac{eT_e}{2\pi m_e}} \exp\left(\frac{V - \phi_p}{T_e}\right), \tag{3.2}$$

with ϕ_p the plasma potential. Setting $V = \phi_f$ and equating the electron and ion currents gives ϕ_f, the floating potential,

$$\phi_f = \phi_p - \frac{T_e}{2} \ln\left(\frac{m_i}{2\pi m_e}\right). \tag{3.3}$$

Hence, if T_e is known, measurement of i_{sat} and ϕ_f allows the determination of electron density and plasma potential.

More sophisticated models account for non-zero T_i, secondary emission from the probe surface due to electron bombardment and density depression in the presheath (which modifies the ion flux) in a collisionless environment (EMMERT *et al*, (1980)). Allowing for a non-zero T_i the drift speed ($\sqrt{eT_e/m_i}$) in Equation 3.1 is replaced by the ion acoustic speed $(e(T_e + T_i)/m_i)^{\frac{1}{2}}$ using deductions from fluid models of ion flow. EMMERT *et al*, (1980) allowed for a density depression in the presheath which in turn modified the ion flux by a factor $f(\tau)$ (where $\tau = T_i/T_e$) lying between 0.5 and 0.8. Ion-induced electron and ion secondary emissions were ignored. Equation 3.1 then becomes

$$i_{\text{sat}} = f(\tau) e n_e A \sqrt{\frac{eT_e(1+\tau)}{m_i}}. \tag{3.4}$$

The net electron current, i_{en}, is the difference between the primary electron current, i_e, and the secondary electron current, $i_{es} = \gamma i_e$ where γ is the secondary emission coefficient of the probe surface. Equation 3.2 is now reduced by a factor $(1 - \gamma)$. Equating the adjusted values for i_{sat} and i_{en}, gives (STANGEBY (1984))

$$\phi_f = \phi_p - \frac{T_e}{2} \ln \left[\frac{m_i}{2\pi m_e} \frac{(1-\gamma)^2}{1+\tau} \right].$$

In Equation 3.4, $\tau \sim 1$ (i.e. $T_i \simeq T_e$) and $f(\tau) \sim 0.7$ giving the expression for $\tilde{i}_{sat}$ that will be used in this thesis (see e.g. HOWLING (1986)) namely

$$n_e = \frac{i_{sat}}{0.7eA} \sqrt{\frac{m_i}{2eT_e}}. \tag{3.5}$$

In this thesis, a pure hydrogen, Maxwellian, plasma was assumed to be present and the probe was assumed to be perfectly absorbing (hence secondary emission was ignored). The equation described by (CHEN (1965)) was used for $\tilde{\phi}_p$ (see also (e.g.) RHODES (1989) and LIN (1991))

$$\phi_p = \phi_f + 3.6T_e. \tag{3.6}$$

The saturated ion current is measured using the potential drop across a 100 Ω load and the floating potential is the potential between a floating probe and earth. The circuits used to measure these quantities is shown in Figure 3.8. The electron density and plasma potential can be measured within certain specified errors, but depend strongly on the accuracy of the measured value of T_e.

Double Probes

The accuracy of the measurement of plasma density and potential depends on the accuracy of the experimental determination of electron temperature. Similarly, $\tilde{i}_{sat}$ and $\tilde{\phi}_f$ require an estimate of $\tilde{T}_e$ before any information can be deduced from $\tilde{n}_e$ and $\tilde{\phi}_p$. For a complete estimate of heat transport, knowledge of the pressure or temperature fluctuations are needed. To understand the nature of the boundary plasma fluctuation mechanisms, knowledge of all three parameters ($\tilde{n}_e$, $\tilde{\phi}_p$ and $\tilde{T}_e$) is required. Despite this, few measurements of temperature fluctuations and their resulting effects on the energy transport have been made. Many authors correlate the ion saturation current and floating potential instead of the density and the plasma potential since $\tilde{T}_e$ is ignored. However, even a small fluctuation level of T_e invalidates these measurements. The primary difficulties in measuring temperature fluctuations are that the fluctuations are expected to be at the same frequency as density and potential fluctuations and it is technically difficult to make accurate measurements at a frequency of order 100 kHz.

The measurement of electron density and temperature using single Langmuir probes was first described by LANGMUIR *et al*, (1924). The double probe technique (i.e. with two Langmuir probes configured as shown in Figure 3.7) was first suggested by JOHNSON *et al*, (1950) and has several advantages:

- The current in the double probe circuit flows between the tips via the plasma and is thus a local measurement on a length scale of the probe tip separation. The current to a single probe, however, must flow by an undefined mechanism across the magnetic field lines to the vessel (the reference electrode).

- The probe potential should be defined with respect to the local plasma even though it may bear no simple relationship to the potential at any part of the system (e.g. the vessel used as a reference electrode for the single probe). As a result, plasma potential fluctuations will perturb the single probe current-voltage characteristic. The double probe, on the other hand, is floating (by Kirchoff's law) and it is only the *difference* in the plasma potential fluctuations at the tips that will perturb the effective probe bias. This represents a 2nd order perturbation compared with a 1st order perturbation in the single probe case.

- At plasma potential the electron current drawn by a single probe can be very large. This may be so large that it alters the parameters it is trying to measure. Fluctuation frequencies and edge densities have been observed to be appreciably altered as a function of bias and position of a single probe whilst no such disturbance was caused by a double probe. The current in a double probe circuit cannot exceed the ion saturation current.

Measurement of the electron temperature fluctuations at the edge may also be effected by a triple probe technique, first described by CHEN *et al* (1963) and later used on many machines (e.g. TSUI *et al*, (1991)). A new scheme was developed by TSUI (1992b) which extends the triple probe technique for the measurement of temperature fluctuations. Aimed at reducing the phase delay error, introduced by finite tip separations in the standard triple probe method, it provides a more reliable measurement of $\tilde{T}_e$. A comparison of the three different techniques was reviewed by LIN, (1992c). It was found that results from the double and extended triple probe methods agree within error limits. For this reason, in all of these experiments, only the double probe technique was used.

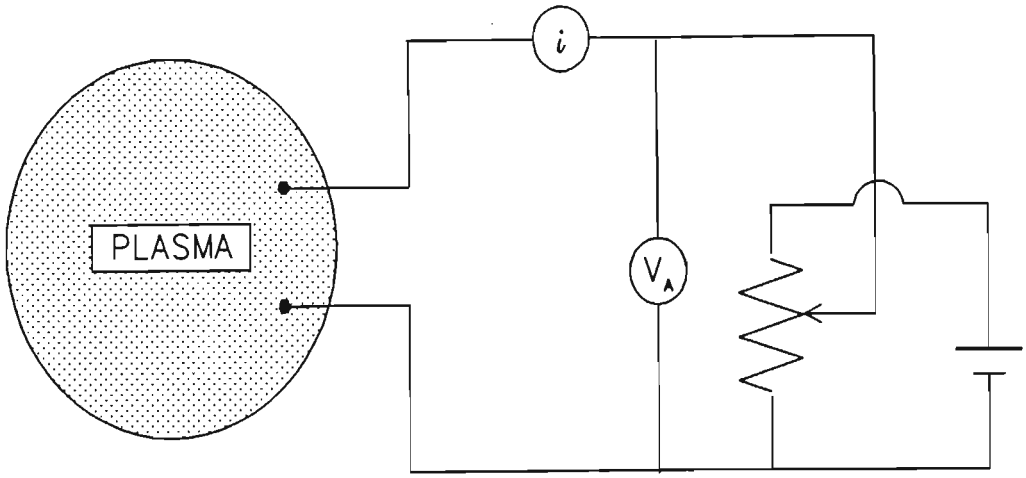

Figure 3.7: Floating double probe circuit. V_A is the differential voltage applied between the probes and i the current flowing in the circuit.

3.3 Data Acquisition

A transient, high voltage, high current experiment such as *Tokoloshe* is a noisy magnetic and electrical environment. This is particularly true for probe signals taken from within a hot ($\sim 25\,\mathrm{eV}$), current-carrying, turbulent plasma. Erroneous signals arise from electrostatic and magnetic pickup as well as circulating currents in earth loops. Care must be exercised to avoid these.

A flow chart of the process of data acquisition is shown in Figure 3.8. With the circuit(s) set up as shown, i_{sat} and ϕ_f may be measured in the plasma by the probes. The voltage drop across a $100\,\Omega$ load allows calculation of i_{sat} and the potential difference between the probe tip and earth measures ϕ_f.

Two Tektronix A6902B dual-channel, optical and transformer coupled voltage isolators were used, each comprising two independently isolated channels and a dc—20 MHz bandwidth. The A6902B acts as a buffer between the probes and the rest of the circuit and extends the range of the probes to 1500 V (dc plus peak ac). It allows grounded probes to make floating measurements at high sensitivity levels in the presence of large common-mode signals. Anti-aliasing filters ensure that frequencies above 500 kHz (f_{Nyquist}) are filtered out of the original signal. The signals were digitised by fast, 4 channel, 10-bit,

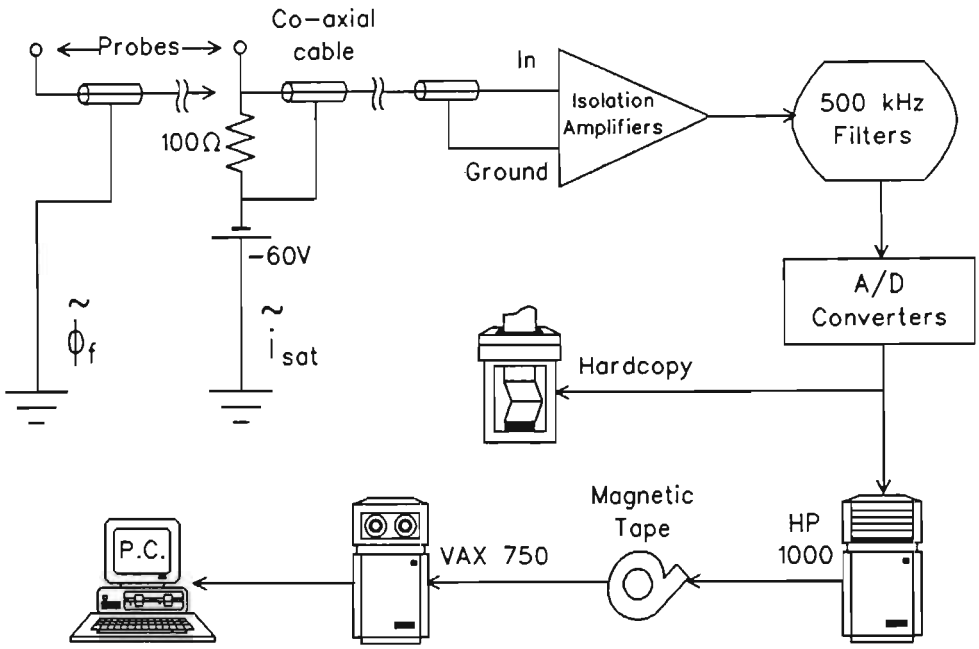

Figure 3.8: Flow chart of the data acquisition process.

1 MHz, Le-Croy, analog-to-digital convertors and stored temporarily in a 32 k word memory before transfer to the HP1000 computer. The transfer was effected via a CAMAC optical link driver and the data stored on magnetic disc and archived on tape. The data for each shot were stored in four separate files prefixed according to the probe label (e.g. **S1#.DAT**, **L1#.DAT**, **S2#.DAT**, **L2#.DAT** where # was the shot number). Each file comprised 32 000 numbers in ASCII format representing the 32 000 μs of digitized data. Unless otherwise specified in the text, the recording of signals of these data were effected about 7 ms from the start of the shot.

3.4 Data Processing

3.4.1 Single Probes

Spectral Analysis

Langmuir and floating potential probes are simultaneously sensitive to all frequencies within the bandwidth of their associated circuitry and data acquisition system. Fourier analysis of the time series contains information about the power level and phase of the component fluctuations. Two probe signals may be compared to give the phase relation between the parameters as a function of frequency and a knowledge of d, the

probe separation, and its orientation allows the wavenumber to be deduced. Valuable information on the phase, dispersion relations and coherency between localised plasma fluctuations is therefore attainable. These correlations must be made on small scale-lengths appropriate to plasma turbulence: no other diagnostic yields this information directly. The boundary plasma is therefore an important regime for the comparison of results with theoretical predictions on non-linearly saturated modes. Direct experimental measurements of density and potential fluctuations and a limited number of assumptions give the particle flux across magnetic field lines, Γ. The method is advantageous in that it is not necessary to know the detailed physical processes which give rise to the fluctuation spectra and it addresses the question of which parts of the fluctuation spectrum are most dangerous to the fluctuation-induced transport of particles and heat. Results are described in Chapter 4: this section is concerned with the important concepts of spectral analysis used in that Chapter.

Digital Fourier Analysis

The implementation of spectral analysis techniques with a digital data array requires the replacement of the continuous Fourier transform $\mathcal{F}[f(t)]$ of the data $f(t)$,

$$\mathcal{F}[f(t)] = \int_{-\infty}^{\infty} f(t) \exp(-i\,2\pi f t) dt, \tag{3.7}$$

with the discrete Fourier transform

$$\mathcal{F}[f_k(t_j)] = \frac{1}{N} \sum_{j=0}^{N-1} f(t_j) \exp \frac{-i\,2\pi jk}{N}, \tag{3.8}$$

where N is the number of data points sampled at intervals of time Δt apart, $t_j \equiv j\Delta t$ and $f_k \equiv k/N\Delta t$, $(j, k = 0, 1, 2, \ldots, N-1)$. The information of interest lies in the frequency interval $0 < f < f_s/2$ (where f_s is the sampling frequency $= 1/\Delta t$) due to the Nyquist criterion. The raw data is low pass filtered above $f_s/2$ to avoid aliasing errors. The sampling theorem states that if a continuous function is sampled at regular intervals the original function can be retrieved from the resultant discrete series provided that the signal bandwidth, B, is at most equal to $f_N = f_s/2$ where f_N is the Nyquist frequency, i.e. if $f_s \geq 2B$. Aliasing arises from violation of the sampling theorem, i.e. when $f_s < 2B$. The spectra overlap in the sampled signal when this occurs and frequency components *above* B appear *below* B in the sampled signal. In practice, the conditions required by the sampling theorem are generally ensured by filtering the original signal with a low-pass 'anti-aliasing' filter having a cut-off frequency $B_c < f_N$. Unless otherwise stated, all the data presented in this thesis were digitised at 1 MHz, resulting in a Nyquist frequency of 500 kHz.

The discrete Fourier transform makes use of the Fast Fourier Transform algorithm (COOLEY *et al*, (1967)). The distortion of the time spectrum by contamination of the pure frequencies with many neighboring frequencies, known as leakage, is a consequence of the finite-length data record and is minimised by applying one of several windows to the raw data. There are several different types of windows, $W(t)$, each satisfying the criteria that $W(t)$ is a smooth, continuous function and that $W(0) = W(T) = 0$, T being the duration of the data record. Data of finite duration may be viewed as a data record of indefinite duration multiplied by a rectangular window function. As a result, the Fourier transform of the finite record length equals the 'true' Fourier transform convolved with a sinc $(\sin(x)/x)$ function. Although the sinc function has a relatively narrow mainlobe, it does possess large sidelobes which allow contributions to the Fourier transform. To minimize leakage associated with the high sidelobes of the sinc function, various data windows can be used. It is well known from diffraction theory, that if the edges of the data windows are rounded, the resulting Fourier transform will have much smaller side lobes than the sinc function. This side lobe reduction takes place at the expense of broadening the main lobe. In essence, the various windows represent a compromise between reducing the side lobe on the one hand and broadening the main lobe on the other. The Hanning window was used in all cases for this project and is given by

$$W_{\text{Hanning}} = \frac{1}{2}\left(1 - \cos\frac{2\pi t}{T}\right), \quad 0 \leq t \leq T.$$

The Hanning window has the mathematical advantage that it can be equivalently implemented by a simple weighted averaging technique in the frequency domain (SMITH *et al*, (1974)).

Each transform, $\mathcal{F}_i(f)$, is in general complex and therefore may be written as $\mathcal{F}_i(f_k) = |\mathcal{F}_i(f_k)| \exp(i\theta_i(f_k))$. The power spectrum is obtained by multiplying the above by the complex conjugate, $\mathcal{F}_i^\star$, to obtain $\mathcal{P}_{ii} = |\mathcal{F}_i(f_k)|^2$. The cross power spectrum for two signals $f_1(t)$ and $f_2(t)$ is formed as $\mathcal{P}_{12}(f_k) = \mathcal{F}_1^\star(f_k)\mathcal{F}_2(f_k)$, which is again generally complex. The cross power can be written

$$\mathcal{P}_{12} = \mathcal{C}_{12} + i\mathcal{Q}_{12} \tag{3.9}$$

or

$$\mathcal{P}_{12} = |\mathcal{P}_{12}| \exp i(\theta_{12}), \tag{3.10}$$

where

$$
\begin{array}{lcll}
|\mathcal{P}_{12}| & = & \sqrt{(\mathcal{P}_{12} \star \mathcal{P}_{12})} & = & |\mathcal{F}_1^* \mathcal{F}_2| & \text{is the cross-amplitude} \\
\mathcal{C}_{12} & = & \Re(\mathcal{P}_{12}) & = & |\mathcal{P}_{12}| \cos(\theta_{12}) & \text{is the co-spectrum} \\
\mathcal{Q}_{12} & = & \Im(\mathcal{P}_{12}) & = & |\mathcal{P}_{12}| \sin(\theta_{12}) & \text{is the quadrature-spectrum and} \\
\theta_{12} & = & \theta_1 - \theta_2 & = & \tan^{-1}(\mathcal{Q}_{12}/\mathcal{C}_{12}) & \text{the phase difference.}
\end{array}
$$

The cross-power spectrum contains valuable phase information in the form of a phase difference, θ_{12}, between frequency components of the original two signals. The *relative* phase appears in the cross-power, not the absolute phase. Statistical errors may be reduced by averaging the cross-power values taken from different time periods within the same shot or from different shots taken under similar conditions.

The coherency, γ_{12}, is defined by

$$\gamma_{12} = \sqrt{\frac{|\overline{\mathcal{P}}_{12}|^2}{\overline{\mathcal{P}}_{11} \cdot \overline{\mathcal{P}}_{22}}}, \tag{3.11}$$

where the overline indicates an averaged quantity. The coherency is a measure of the degree of similarity between the two signals, $f_1(t)$ and $f_2(t)$, at each frequency with phase differences ignored and is identically 1.0 for monochromatic fluctuations. The coherency is reduced by averaging due to the phase factor which introduces a phase mixing effect as more spectral components are averaged. It can be shown using the Schwartz inequality that γ_{12} is bounded by 0 and 1. For two completely uncorrelated sources, γ_{12} is 0. It is important to note that if two signals are to be usefully related to each other, the probe separation must be less than a coherence length for the frequencies of interest. If this requirement is not met, the probes will yield an artificially low coherency because the probes will sample unconnected parts of the plasma. The same applies to spectral averaging which must not be too high otherwise it is possible that signals from independent mechanisms at different frequencies (and changes of the plasma conditions) will also reduce coherency. The smoothing interval must be less than the estimated spectral bandwidth of plasma fluctuations.

The probe separation, d, is used in the calculation of both the phase spectrum, $\alpha_{n\phi}(\omega)$, and the dispersion relation, $k_\theta(\omega)$. Two probes, measuring fluctuations in the plasma medium, have outputs $g_1(t)$ and $g_2(t)$ respectively. Although many waves propagate in the medium, a wave at a single frequency, ω, will undergo a phase shift, $\alpha_{12}(\omega)$, in propagating from probe 1 to probe 2. If the probe separation is d the phase shift is given by

$$\alpha_{12}(\omega) = k_\theta(\omega) d.$$

Since the phase shift is merely equal to the phase difference between the signals $g_1(t)$ and $g_2(t)$ at frequency ω, $\alpha_{12}(\omega)$ can be found by computing the phase spectrum correspond-

ing to the cross power spectrum. Because the cross-power spectrum preserves phase information in the form of a phase *difference*, the procedure for finding the wavenumber, $k_\theta(\omega)$, is to compute the power spectrum of $g_1(t)$ and $g_2(t)$, and from the phase spectrum, $\alpha_{12}(\omega)$, of the cross power spectrum, estimate $k_\theta(\omega)$ from

$$k_\theta(\omega) = \frac{\alpha_{12}(\omega)}{d}.$$

The maximum resolvable k_θ value is π/d, which is the point at which the phase difference of the two signals becomes π radians. However, the general trend of the phase spectrum may be used to compute k_θ values larger than this: if the phase is steadily increasing (or decreasing), an abrupt transition from π $(-\pi)$ to $-\pi$ $(+\pi)$ is unlikely. A measured phase difference of slightly less than $-\pi$ is therefore more likely to indicate a positive difference of slightly more than π. This phase can thus be 'unwrapped' to yield increasing k_θ values beyond π/d. Unless otherwise stated, all examples presented in this thesis were 'unwrapped'.

The analysis programs used in these experiments required ℓ data segments consisting of m data points in order to compute the fast Fourier transforms (FFT's), crosspower spectra, autocorrelation spectra, etc. The integer m must be chosen such that $m = 2^n$ (n, an integer) to satisfy requirements for the FFT. The maximum size sample chosen for this project is $n = 7$. Using $n = 6$ ($m = 64$) gave poor frequency resolution of the spectra. If $n = 8$ ($m = 256$) was used, ℓ was correspondingly reduced which resulted in less averaging of the spectra, and hence in irreproducible results. The number of segments of duration $m\,\mu$s, ℓ, must be chosen such that a reasonable time segment is analysed. If the segment is too small, little averaging will be performed and the final results will not be representative of the true spectra. If the segment is too large (≥ 5 ms), other plasma parameters (e.g. I_p), which are more or less constant over shorter (≤ 3 ms) time scales, will have changed. In such cases, conditions in the vacuum chamber can be considered to have changed too much over the duration of the analysis for the spectra to be considered reliable. In most of the results presented in this thesis, $\ell = 25$ (i.e. 3 200 points or 3.2 ms).

Summary of procedure and experimental applications

A summary of the steps outlined in the previous section is outlined below:

- From the ℓ samples of the signals $f_1(t)$ and $f_2(t)$ compute the Fourier spectra, $\mathcal{F}[f_1(t)]$ and $\mathcal{F}[f_2(t)]$ of each, apply the Hanning window using the FFT algorithm as for Equation 3.8 and average over all spectra from the ℓ samples.

- Calculate the cross-power spectra from the two sets of Fourier transforms giving the co- and quadrature-spectra (Equation 3.9).
- Average these spectra from data taken over time periods from shots considered to have closely similar conditions.
- From the smoothed spectra compute as required:
  1. The phase difference, $\alpha_{12} = \tan^{-1}(\overline{\mathcal{Q}}_{12}/\overline{\mathcal{C}}_{12})$. For two signals separated by a distance d with wavenumber k_θ, $k_\theta \cdot d = \alpha_{12}$, hence k_θ and the phase velocity $\omega/k_\theta = 2\pi f/k_\theta$ are found.
  2. The coherency $\gamma_{12} = \sqrt{(\overline{\mathcal{C}}_{12}^2 + \overline{\mathcal{Q}}_{12}^2)/(\overline{\mathcal{P}}_{11} \cdot \overline{\mathcal{P}}_{22})}$ from Equation 3.11 indicates the degree of correlation of the two signals as a function of frequency.
  3. The cross-power represents the signal power density in the frequency domain.

Noise Spikes

A low resolution graphical output is available after each shot so hard copies of the data could be viewed immediately. High frequency, high amplitude noise spikes were visible on all signals simultaneously, regularly spaced every 1.667 ms. The spikes were due to the rapid commutation of current between the thyristor legs of the ohmic heating rectifier which drives the vertical field coils during the shot.

Much of the data analysed on *Tokoloshe* does not require a high sampling rate of 1 μs; most are digitised every 10 μs. The duration of the spikes was between 15 and 35 points (i.e. 15 – 35 μs) long. For data sampled every 10 μs this represents one or at most two points; a trivial program easily locates and eliminates the spurious point(s) by setting it to a value equal to a local average value. For i_{sat} and ϕ_f data, where a sampling rate of 1 μs was used, the solution was not so straightforward.

$S(\omega, k_\theta)$ spectra, generated from data with a spike (of amplitude $\approx 5\times$ average amplitude of signals) and associated contour plots are shown in Figure 3.9(b)(i) and (ii). Results from the same data segment but without the spike present are shown for comparison in Figure 3.9(a) (i) and (ii). The spike produces a high amplitude, high frequency, narrow wavelength 'fin' centered around $k_\theta = 0$—with average amplitude about $\sim \frac{1}{2}$ that at low frequencies and wavelengths—in addition to the expected broadband spectra due to turbulence. This affects power, wavenumber and phase spectra as well as the dispersion relation and the coherency between the signals.

Simply removing the *spike* data points resulted in much 'cleaner' power spectra, with the power exponentially decreasing from the low frequencies to the high as observed in

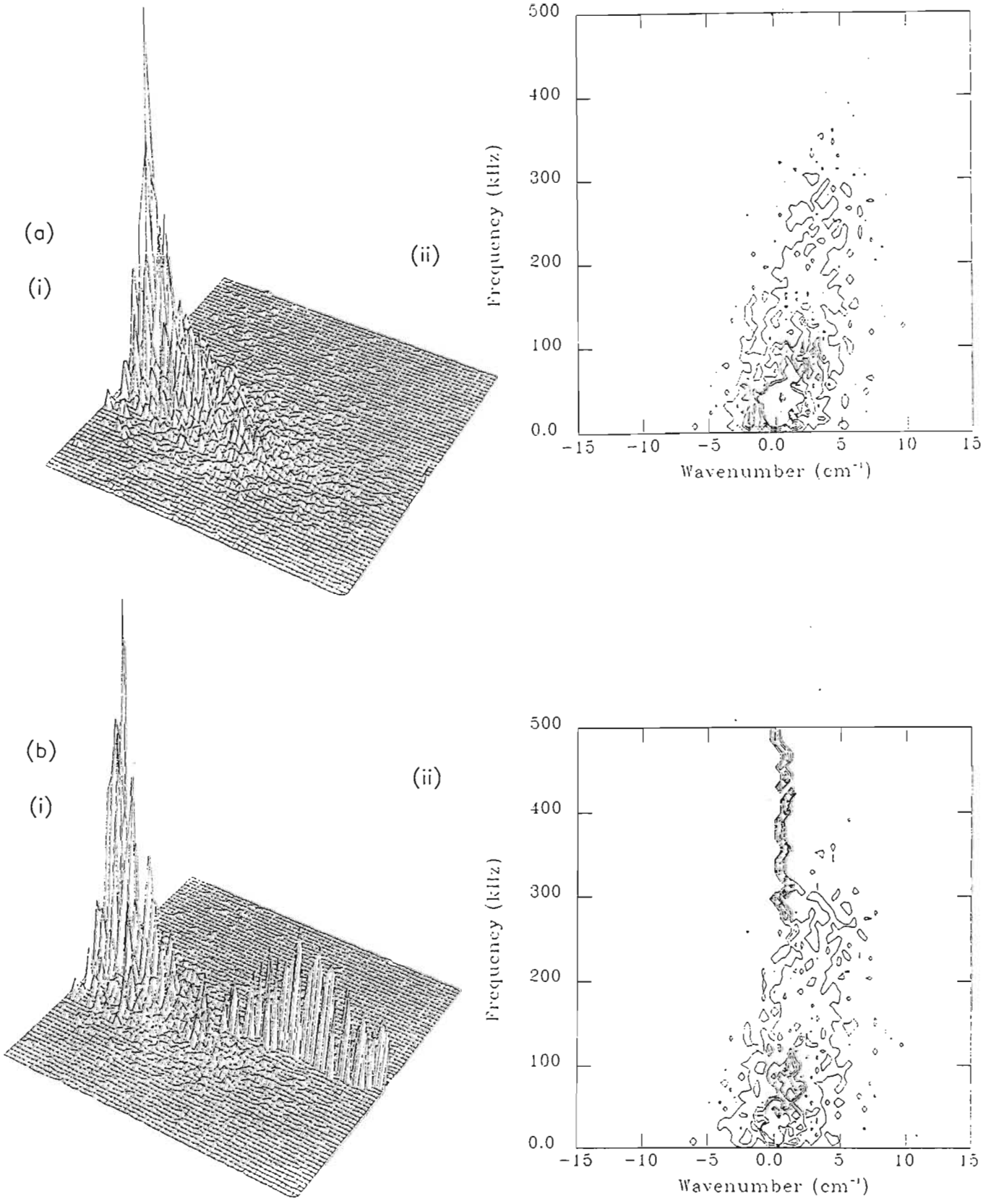

Figure 3.9: (i) $S(\omega, k_\theta)$ results and (ii) associated contour plots for data with (a) no noise spikes present and (b) one, 10 point spike in the data. The segments were both 3.072 ms in duration.

the unaffected spectrum. The coherency spectrum, however, shows a highly coherent peak at a frequency of between 450 and 500 kHz, a consequence of 'splicing' the data together on either side of the spike. This in turn affected both the dispersion relation and the phase spectrum. Eventually it was decided to remove the *entire* 128 point segment containing the spike so that any discontinuities in the data were *between* data segments and not *within* them. This method gave the most reliable and reproducible results and was therefore adopted.

3.4.2 Double Probes

The Double Probe Characteristic

SWIFT (1970) showed that the I/V double-probe characteristic may be given by

$$i = i_{\text{sat}} \tanh\left(\frac{V}{2T_e}\right), \tag{3.12}$$

with i_{sat} the ion saturation current, T_e the electron temperature (in eV) and V the total voltage between the electrodes.

Well developed probe theory exists for plasmas in which the ion temperature is much lower than the electron temperature and the magnetic fields are relatively weak. In the edge regions of tokamaks both conditions are violated since $T_i \approx T_e$ and $B_{\phi,\theta}$ are strong. The effect of strong magnetic fields on the double-probe characteristic has been examined by many authors (e.g. ROBINSON *et al*, (1969)) and it has been shown that they have little, if any, effect on the ion current given in Equation 3.12 above. Complex probe theories are therefore not usually considered and the ideal, non-magnetic theory is used instead. It is often found that the probe current does not saturate according to Equation 3.12 but rather exhibits a point of inflexion at $V \simeq 2T_e$. This is probably due to a different (changing) collection/sheath area since this is a function of probe bias. A simple algorithm for a linear departure from saturation is given by SWIFT *et al*, (1970), being a modified version of Equation 3.12,

$$i = i_{\text{sat}} \tanh\left(\frac{V}{2T_e}\right) + S \cdot \left(\frac{V}{2T_e}\right) + i_{\text{offset}}, \tag{3.13}$$

where $V = V_{\text{bias}} - V_{\text{offset}}$ and the parameters to be fitted are i_{sat}, T_e, V_{offset}, i_{offset} and the normalised slope, S. All double probe characteristics exhibit some degree of non-saturation and S, normalised to twice the electron temperature, reflects this. The plasma potential difference between the probe electrodes gives the intercept at zero bias (V_{offset}) and i_{offset} accounts for the amplifier offset or any other asymmetry after averaging. Both

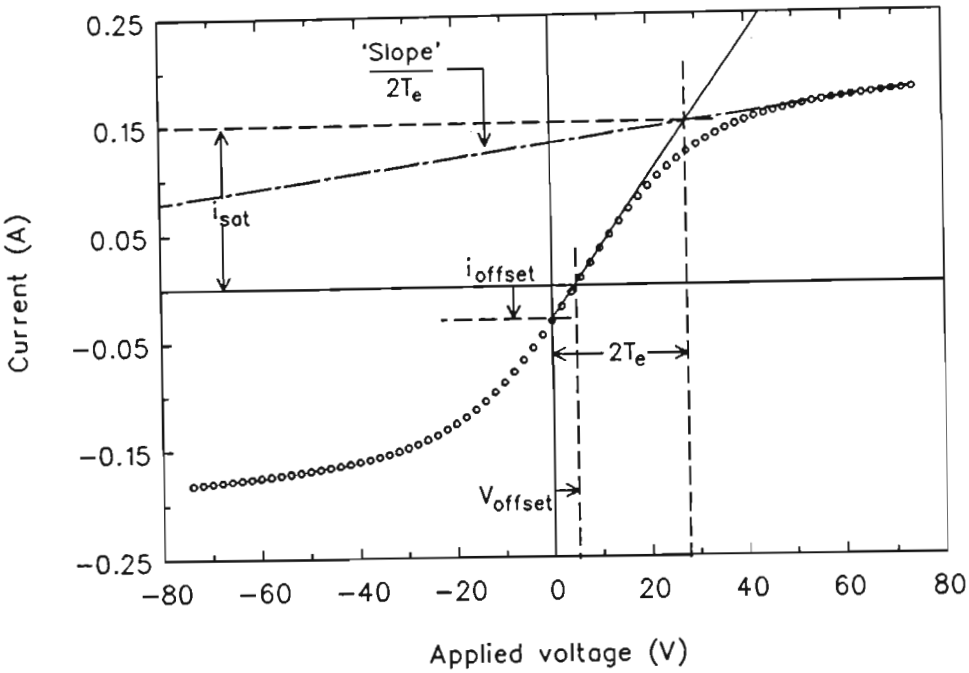

Figure 3.10: Standard curve for the deduction of T_e and other relevant parameters.

offsets are small but are nevertheless included. Figure 3.10 shows the standard curve produced by Equation 3.13 and the relevant parameters.

SWIFT *et al*, (1970) gives a correction to the electron temperature for the case of a non-zero slope in the saturation region. The expression for this correction is given by

$$T_e\,(\text{corrected}) = \mathrm{T_e}\frac{(\mathrm{i_{sat}}\,(\text{corrected}) - 0.85 \cdot \mathrm{S})}{(\mathrm{i_{sat}}\,(\text{corrected}) + 0.50 \cdot \mathrm{S})}$$

where $i_{\mathrm{sat}}\,(\text{corrected}) = \mathrm{i_{sat}} + \mathrm{S}$ is used since the true value of i_{sat} is given by the height of the 'knee' of the curve in Figure 3.10. These corrections are incorporated into the analysis given in the following Chapter.

Measurement of Temperature

The electron temperature may be deduced from Equation 3.13 by noting that the slope of the tangent to this curve at the origin is

$$\left.\frac{\partial i}{\partial V}\right|_0 = \frac{i_{\mathrm{sat}}}{2T_e}.$$

Many techniques claim good measurements of electron temperature, but no characteristics are displayed so it is difficult to judge how reliable they are (e.g. TODD (1979) who described a method of sweeping the probe with an AC voltage which only just produced current saturation. This also means that the deduction of T_e is even more indirect than the method described above.) A triangular voltage sweep, such as the one used on

TOSCA (HOWLING (1986)), produced a tanh curve directly which may be checked for quality and discarded if noise or spurious data is present. *Tokoloshe* has a short pulse length ($\sim 20 \rightarrow 30$ ms) so ideally, a high frequency sweep would be needed here. In the absence of the circuitry required, the curves produced in the following Chapters were generated by calculating the average value of i during a 5 ms period of the discharge in which gross plasma parameters remained approximately constant. This method has the disadvantage of being subject to potentially large errors due to the lack of sufficient averaging. To partially overcome this three shots were used at each value of probe bias and the results averaged over these three. This method has the advantage of taking shot-to-shot variations into account over an entire data run.

A FORTRAN program was used to sample and average several shots over a selected time interval. This yields a time-averaged characteristic which is now used as the data from which T_e may be extracted. The Gauss-Newton method of curve fitting to the data using the scientific environment ASYST was used. The program made use of a variation of the LEVENBERG-MARQUARDT method which has become the standard of nonlinear least-squares routines (PRESS (1986)).

Measurement of Temperature Fluctuations

The probe current fluctuations, $\tilde{i}$, are analysed as a function of probe bias in terms of contribution from density, electron temperature and potential fluctuations ($\tilde{n}_e$, $\tilde{T}_e$ and $\tilde{V}_d$ respectively). This technique was first presented by ROBINSON *et al*, (1969) for use in experiments on ZETA.

Using Equations 3.12 and 3.5 it can be shown that the current in an equal area double Langmuir probe in a plasma with a bias V is given by

$$i = cn_e eA\sqrt{\frac{2eT_e}{m_i}}\tanh\left[\frac{V - V_d}{2T_e}\right], \tag{3.14}$$

where V_d is the voltage due to floating potential differences across the probe tips, A is the probe surface area and c is a factor dependent on the probe geometry of order 1 (usually ≈ 0.7). It is clear from Equation 3.14 above, that, in a turbulent plasma, fluctuations in n_e, T_e, V_d, $\partial n_e/\partial x$ and $\partial T_e/\partial x$ (where x is the radial coordinate) will cause fluctuations in the probe current readings. Partially differentiating with respect to n_e, T_e, V_d and x and then squaring Equation 3.14 yields

$$\begin{aligned}\tilde{i}^2 \;=\; & f_1^2\tilde{n}_e^2 \;+\; f_2^2\tilde{T}_e^2 \;+\; f_3^2\tilde{V}_d^2 \;+\; f_4^2\nabla\tilde{n}_e^2 \;+\; f_5^2\nabla\tilde{T}_e^2 \\ & +\; 2f_1f_2\langle\tilde{n}_e\tilde{T}_e\rangle \;+\; 2f_1f_3\langle\tilde{n}_e\tilde{V}_d\rangle \;+\; 2f_1f_4\langle\tilde{n}_e\nabla\tilde{n}_e\rangle \;+\; 2f_1f_5\langle\tilde{n}_e\nabla\tilde{T}_e\rangle \\ & +\; 2f_2f_3\langle\tilde{T}_e\tilde{V}_d\rangle \;+\; 2f_2f_4\langle\tilde{T}_e\nabla\tilde{n}_e\rangle \;+\; 2f_2f_5\langle\tilde{T}_e\nabla\tilde{T}_e\rangle\end{aligned}$$

$$+ \; 2f_3f_4\langle\tilde{V}_d\nabla\tilde{n}_e\rangle \; + \; 2f_3f_5\langle\tilde{V}_d\nabla\tilde{T}_e\rangle$$
$$+ \; 2f_4f_5\langle\nabla\tilde{T}_e\nabla\tilde{n}_e\rangle, \tag{3.15}$$

giving 15 terms in total and where the non-dimensional forms of the f's are given by

$$f_1 : \left(\frac{\partial i}{\partial n_e}\right)\Bigg|_{T_e,\, V_d,\, \nabla T_e,\, \nabla n_e} = 2\tanh\Psi, \tag{3.16}$$

$$f_2 : \left(\frac{\partial i}{\partial T_e}\right)\Bigg|_{n_e,\, V_d,\, \nabla T_e,\, \nabla n_e} = \tanh\Psi - 2\Psi\mathrm{sech}^2\,\Psi, \tag{3.17}$$

$$f_3 : \left(\frac{\partial i}{\partial V_d}\right)\Bigg|_{n_e,\, T_e,\, \nabla T_e,\, \nabla n_e} = -\mathrm{sech}^2\,\Psi, \tag{3.18}$$

$$f_4 : \left(\frac{\partial i}{\partial x}\right)\Bigg|_{n_e,\, T_e,\, V_d,\, \nabla T_e} = \tanh\Psi, \tag{3.19}$$

$$f_5 : \left(\frac{\partial i}{\partial x}\right)\Bigg|_{n_e,\, T_e,\, V_d,\, \nabla n_e} = \frac{1}{2}\left[\tanh\Psi + (3-2\Psi)\mathrm{sech}^2\,\Psi\right], \tag{3.20}$$

with $\Psi = (V - V_d)/2T_e$.
The parameters of this equation have been normalised by setting

$$\tilde{i} = \frac{\tilde{i}}{i_{\mathrm{sat}}}, \quad \tilde{n}_e = \frac{\tilde{n}_e}{n_e}, \quad \tilde{T}_e = \frac{\tilde{T}_e}{T_e}, \quad \tilde{V}_d = \frac{\tilde{V}_d}{T_e}, \quad \nabla\tilde{n}_e = \frac{\nabla\tilde{n}_e}{n_e}, \quad \nabla\tilde{T}_e = \frac{\nabla\tilde{T}_e}{T_e}.$$

Curve fitting of $\tilde{i}_2$ to the model (Equation 3.15) allowed the above quantities to be estimated. This technique has been used on many tokamaks (e.g. HOWLING (1986, 1988), LIN(1989), BENGTSON *et al*, (1990) and VAYAKIS *et al*, (1990)). CARLSON *et al*, (1990), however, pointed out that the set of basis functions used in these experiments is incomplete. Since the data are not noise-free and many uncertainties and errors of measurement are present, any attempts to fit all of the above 15 functions to the double probe fluctuation level characteristic is unlikely to yield any important new results, a point noted by CARLSON *et al*, (1990). VAYAKIS *et al*, (1991) examined this problem of selecting an appropriate subset of functions to form the basis set for the fit. In this work, gradients in the fluctuating quantities were *not* considered; only 6 variational parameters were fitted to the data, viz., $\tilde{n}_e/n_e$, $\tilde{V}_d/T_e$, $\tilde{T}_e/T_e$, $\langle\tilde{n}_e\tilde{T}_e\rangle/n_eT_e$, $\langle\tilde{V}_d\tilde{T}_e\rangle/T_e^2$ and $\langle\tilde{n}_e\tilde{V}_d\rangle/n_eT_e$.

Current fluctuation data, $\tilde{i}$, were obtained by measuring the probe current as the bias was altered between shots. No two shots are ever identical: several shots at each value of V were needed to give a reasonable estimate of $\tilde{i}$. To obtain a representative set of data values, a wide range of bias voltage is required, usually $\pm$ 80 V. Three shots were taken at each bias voltage over a range of 160 V from -80 V to $+80$ V in steps of 10 V. The method is time consuming but has the advantage of not involving rapid sweep voltages

or multiple probe configurations. Also, there is no complex circuitry involved; a simple double probe circuit for measuring saturated current is all that is required. *Tokoloshe* is a small, high-repetition rate machine and is ideal for analysis of this type.

The Gauss-Newton method of curve fitting to the data using ASYST, referred to above, was used. The routine requires an input in the form of two arrays: one containing the bias voltage (x-data) and the other, $\tilde{i}^2$ (y-data). It then adjusts the six variational parameters to minimize the least squares difference between the model (Equation 3.15) and the data. The rms fractional values for the required fluctuating values are calculated and returned.

f_1^2, f_2^2, f_3^2 and $2f_1f_2$ are symmetric about $V = 0$ (e.g Figure 4.28(e)(i)) while $2f_2f_3$ and $2f_1f_3$ are asymmetric (e.g. Figure 4.28(e)(ii)). The correlation terms $\langle\tilde{n}_e\tilde{V}_d\rangle$ and $\langle\tilde{T}_e\tilde{V}_d\rangle$, which are responsible for particle and energy transport, therefore make the current fluctuations asymmetric with respect to inversion about $V = 0$. At $V = 0$, only $f_3(V)$ is non-zero so the only term contributing to $\tilde{i}^2$ is $\tilde{V}_d^2$. At large $|V|$ the dominant contribution to $\tilde{i}^2$ comes from $\tilde{n}_e$ plus a small but significant contribution from $\tilde{T}_e$ and the cross-term $\langle\tilde{n}_e\tilde{T}_e\rangle$.

Measurement of Heat Flux

The radial energy flux, $q_j(r)$, for species j can be written as a sum of the convected and conducted energy fluxes,

$$q_j = q_{\text{conv},j} + q_{\text{cond},j}.$$

The convected and conducted energy fluxes due to electrostatic fluctuations are given by (Ross *et al*, (1989)) as

$$q_{\text{conv}}^{\tilde{E}} = \frac{5}{2}T_e\Gamma, \tag{3.21}$$

$$q_{\text{cond}}^{\tilde{E}} = \frac{3}{2}n_e\frac{\langle\tilde{T}_e\tilde{E}_\theta\rangle}{B_\phi} - T_e\Gamma, \tag{3.22}$$

respectively, where B_ϕ is the toroidal magnetic field. The factor 5/2 results from the choice of the reference frame for the conducted energy flux moving with the velocity $v_i = \Gamma_j/n_j$ with Γ_j the particle flux of the jth species (Ritz *et al*, (1989)).

For double probes whose separation is much less than the coherence length and wavelength of the turbulence, V_d may be written as

$$V_d = E_\theta d$$

where E_θ is the poloidal electric field between the probe tips, separated by d (see e.g. Lin (1991)). This assumption will be used here since it will be shown that the coherence

length for the fluctuations below $f \leq 100\,\mathrm{kHz}$ is $L_{\mathrm{coher}} \approx 1.5 \pm 0.5\,\mathrm{cm}$ (Figure 4.13) and the wavelength of the turbulence at low frequencies is $\lambda_{|f\leq 100\,\mathrm{kHz}} = 2\pi/k_\theta \approx 1.26 \pm 0.3\,\mathrm{cm}$ (Figure 4.15). The fluctuation driven particle flux is related to the variational parameter $\langle \tilde{n}_e \tilde{E}_\theta \rangle$ through

$$\begin{aligned} \tilde{\Gamma} &= \frac{\langle \tilde{n}_e \tilde{E}_\theta \rangle}{B_\phi}, \\ &= \frac{\langle \tilde{n}_e \tilde{V}_d \rangle}{B_\phi d}. \end{aligned} \tag{3.23}$$

Thus, Equations 3.21 and 3.22 become

$$q^{\tilde{E}}_{\mathrm{conv}} = \frac{5}{2} T_e \frac{\langle \tilde{n}_e \tilde{V}_d \rangle}{B_\phi d}, \tag{3.24}$$

$$q^{\tilde{E}}_{\mathrm{cond}} = \frac{3}{2} n_e \frac{\langle \tilde{T}_e \tilde{V}_d \rangle}{B_\phi d} - T_e \frac{\langle \tilde{n}_e \tilde{V}_d \rangle}{B_\phi d}. \tag{3.25}$$

Knowledge of T_e and the cross correlation terms ($\langle \tilde{T}_e \tilde{V}_d \rangle$ and $\langle \tilde{n}_e \tilde{V}_d \rangle$) allows these quantities to be estimated.

3.4.3 Comparison of Techniques

Two methods of measuring the particle transport in *Tokoloshe* are employed in this thesis: the method of digital spectral analysis and that involving the technique described in this section. In the former, temperature fluctuations are ignored since they are considered negligible.

Both techniques require that all probes be located within a correlation volume. Since measurements obtained using the curve fitting technique are not time-resolved, they contain little spectral information as compared to the digital spectral analysis technique. The curve fitting technique also assumes an ideal probe characteristic of Equation 3.12, thus ignoring known effects such as sheath size, strong magnetic field effects, secondary electron emission etc. In addition, since electron distributions are known not to be Maxwellian (THAYER *et al*, (1987)) in a tokamak plasma, this may alter the probe current/voltage relation. Advantages of the curve-fitting technique are also that it allows the measurement of the level of temperature fluctuations, yields the correlation with density and electric field fluctuations and provides an estimate of energy flux due to electrostatic fluctuations.

Chapter 4

Reference Plasmas

The edge plasma region of tokamaks is characterised by large cross field particle and energy losses and it constitutes a strongly turbulent region of the plasma. A major obstacle to plasma confinement is the existence of instabilities, manifested through macroscopic distortions of the plasma column (MHD) and small scale, microscopic turbulence. Although the edge has been under study for more than two decades, this study has not been as intensive or as systematic as that of the core plasma (STANGEBY *et al*, (1990)).

Before an analysis of the edge plasma during locking can be understood, the so-called 'reference shot' must first be completely characterised. A systematic comparison between the results from these two cases can then be made in order to deduce the effects of locking on the turbulent edge region of the plasma. This Chapter deals with the characterisation of the edge plasma in *Tokoloshe* tokamak via measurements of both macro- and microscopic quantities.

4.1 Reference Discharges

A typical reference shot on *Tokoloshe* exhibits the characteristics shown in Table 4.1.

Typical traces from several diagnostics can be seen in Figure 4.1. The $\tilde{B}_\theta(m = 2)$ signal is characterised by a period of high Mirnov activity preceding a period of low Mirnov activity as shown in Figure 4.1(b). Such shots are fairly reproducible on *Tokoloshe* and cases which did not involve the type of Mirnov activity described above were discarded. A high Mirnov activity discharge is characterised by a large amplitude sinusoidal like signal from Fourier analysing coils which measure magnetic fluctuation components

Table 4.1: Reference shot parameters.

PARAMETER	VALUE
B_ϕ	0.6 T
I_p (maximum)	120 kA
V_{loop} (maximum)	2 V
$q(a)$ (sawtoothing plasma)	2.4 — 3.3
Z_{eff}	2.2 ± 0.5
$n_e(0) \rightarrow n_e(a)$	$2.5 \rightarrow 0.1 \times 10^{19}\,\text{m}^{-3}$
$T_e(0) \rightarrow T_e(a)$	$600 \rightarrow 15$ eV
τ_E, τ_p	4 ms
t_p	35 ms
$\dot{\tilde{B}}_\theta(m=2)/\tilde{B}_\theta$ ($t \simeq 4 \rightarrow 16$ ms)	$\sim 1\%$ (high)
$\dot{\tilde{B}}_\theta(m=2)/\tilde{B}_\theta$ ($t \simeq 16 \longrightarrow$)	$\sim 0.05\%$ (low)
f_{Mirnov}	$8 \rightarrow 15$ kHz

$\tilde{B}_\theta \lesssim 0.6\% B_\theta$. The dominant modes have been identified as the $m/n = 2/1$ mode and the smaller $m/n = 3/1$ mode by ROBERTS *et al*, (1986). The high Mirnov discharge was produced by suitably controlling the H_2 gas puff. The influx of this hydrogen results in a cooling of the edge plasma leading to a change in the $j(r)$ profile which results in an instability. This instability manifests itself in the plasma as large magnetic island structures near the $q = 2$ and $q = 3$ rational surfaces. Modulations in the probe ion saturation current and floating potential, associated with the Mirnov oscillations have been measured on *Tokoloshe*. Figure 4.2(a) shows the $\tilde{B}_\theta(m = 3)$ mode amplitude, (b) the $\tilde{B}_\theta(m = 2)$ mode amplitude, (c) the saturated ion current and (d) the floating potential signal during 1.2 ms of high Mirnov ($m = 2$) activity on *Tokoloshe*. There is no overall 'slowing down' of the modes (i.e. the Mirnov period remains approximately constant over the period indicated), but it is apparent that the mode *has been* slowed down, probably by a stray edge field. This is seen by the modulation of the mode velocity which manifests itself by the Mirnov signal being strongly distorted from a sinusoidal curve. This is happening throughout the interval indicated in the figure.

The Mirnov coils are situated on the inside of the vacuum chamber at $\rho \simeq 1.15$, close to the wall at $\phi = 55°$ (Figure 3.1). In Figure 4.2(c) and (d), the Langmuir probe array is situated at $\theta \simeq 105°$, $\phi = 90°$, $\rho = 0.91$ or 2 cm into the bulk plasma. Traces shown in this figure are absolute functions of time, i.e. no phase shifts have been introduced. Since

the probes are situated 35° 'downstream' (i.e. in the plasma current direction) from the Mirnov coils, a toroidal time delay of 26.8 μs between probe and magnetic coil signals (using the Mirnov frequency of 3.62 kHz at this time) is expected and observed as shown in the Figure. The width of the $m/n = 2/1$ island is about 4 cm, situated at $\rho = 0.71$ or about 7 cm from the limiter radius whilst the $m/n = 3/1$ have a smaller width of about 2 cm, situated at the $q = 3$ rational surface ($\rho = 0.79$, or 5 cm from the limiter radius) with a 60° phase shift between maxima as shown in Figures 4.2(a) and (b) (ROBERTS *et al*, (1992)). No time delay between Mirnov signals and probes is observed in the radial direction.

The plasma sometimes experienced a minor disruption, resulting in some loss of plasma current (typically $\Delta I_p/I_p \simeq 4\%$) accompanied by a rapid loss of particles to the wall. Such cases were also discarded but the effects of such disruptions on particle transport is discussed in Chapter 5. In most cases, several (~4–6) shots were analysed to statistically reduce errors.

Throughout the remainder of this thesis, the assumptions that $\tilde{n}_e/n_e \simeq 0.7\tilde{i}_{sat}/i_{sat}$ and $\tilde{\phi}_p/T_e \simeq \tilde{\phi}_f/T_e$ will *not* be used. It has been pointed out earlier that temperature fluctuations are often ignored in the calculation of these fluctuating quantities. Whilst this assumption is more or less valid for the reference case results (where $\tilde{T}_e/T_e$ and cross terms involving $\tilde{T}_e$ *are* small) it is *not* the case during the locked phase where these quantities are relatively large and can affect measurements by up to 100%. For consistency, then, the values of the actual fluctuating quantities will be stated throughout with no assumptions concerning the levels of $\tilde{T}_e/T_e$.

4.2 Results

4.2.1 Single Probe Results

Edge Density, Potential & Electric Field

The edge electron density ($n_e = i_{sat}\sqrt{m_i}/(Ae\sqrt{T_e})$ with A the probe surface area) as a function of time, measured at $\rho = 0.93$ or 1.5 cm into the bulk plasma, is shown in Figure 4.3. The linear increase is a result of strong gas puffing accompanied by recycling processes at the edge. The radial profile of the electron density is shown in Figure 4.4. These measurements are averages taken between $t = 10$ and 16 ms during part of the 'flat-top' period of the plasma current and when the density varies by about 25% over

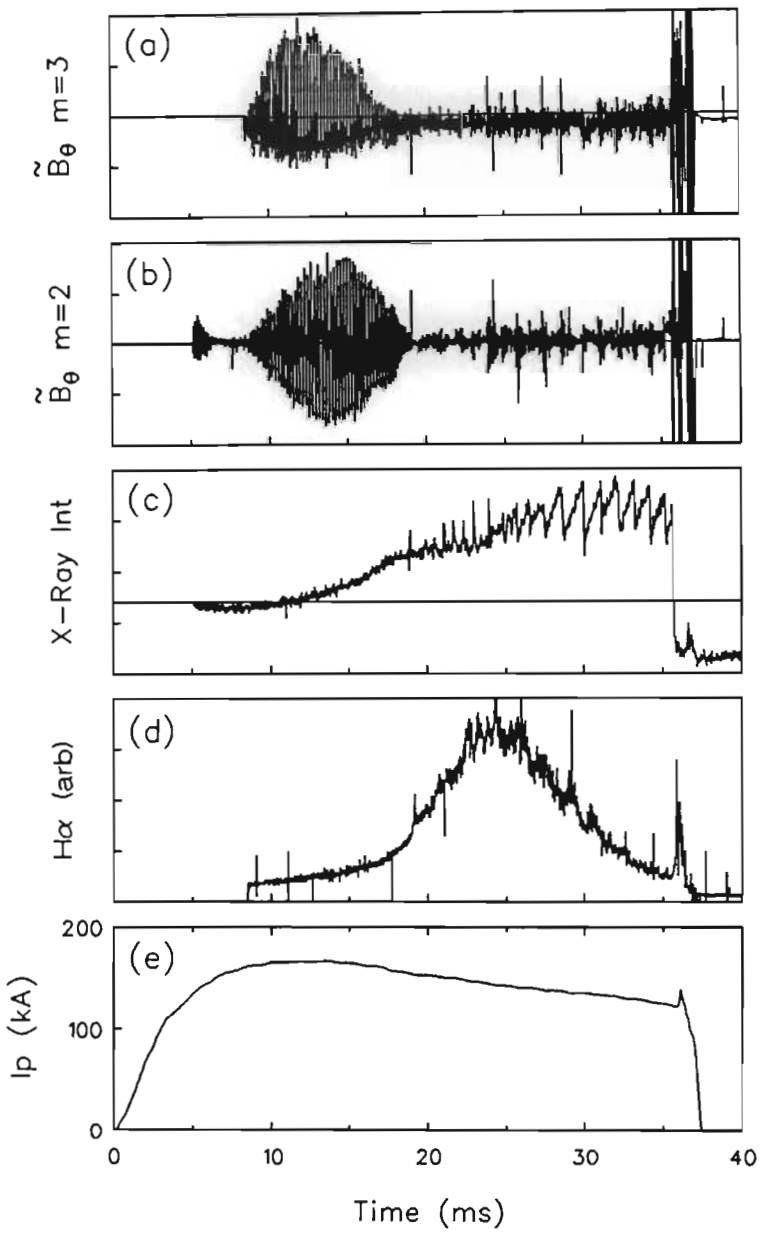

Figure 4.1: Typical traces from 5 diagnostics on *Tokoloshe*. (a) $\tilde{B}_\theta(m = 3)$, (b) $\tilde{B}_\theta(m = 2)$, (c) X-ray intensity profile showing sawtoothing after about 20 ms from the start of the discharge, (d) H_α intensity and (e) the plasma current, I_p, with maximum of ≈ 160 kA.

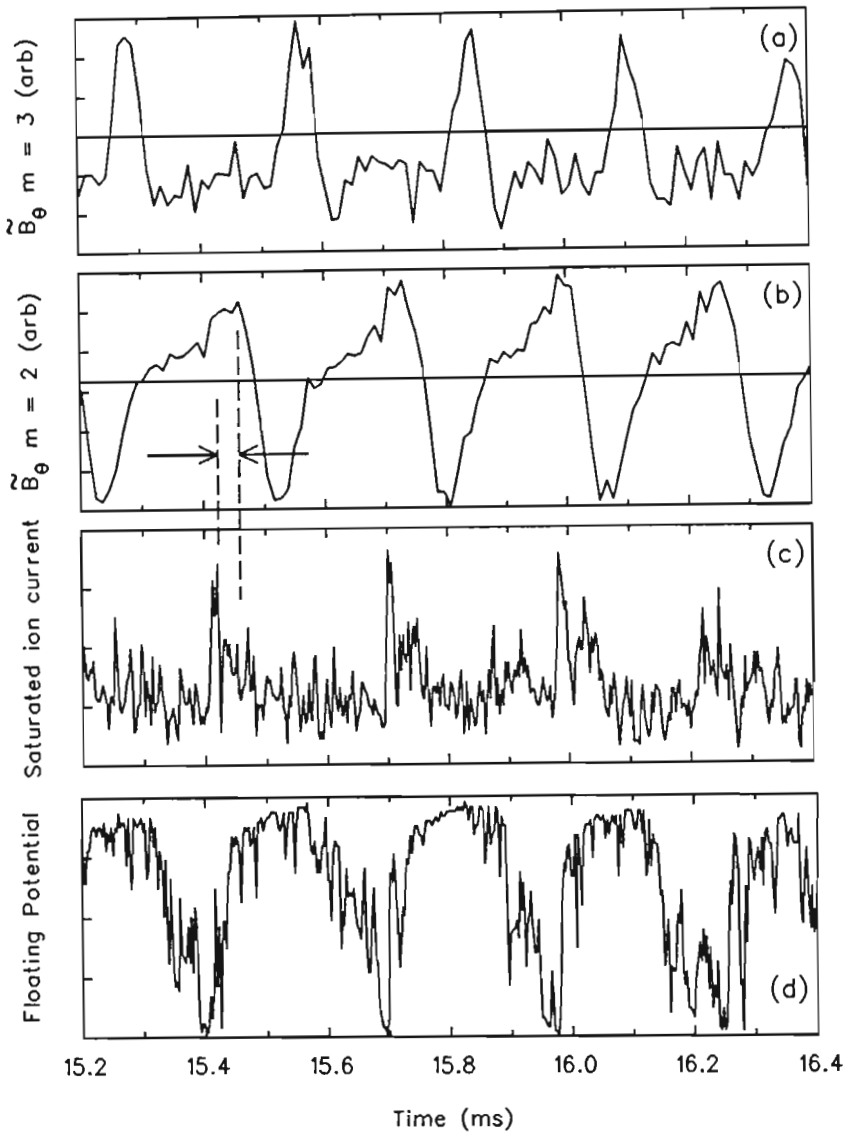

Figure 4.2: Mirnov (a) $m = 3$ and (b) $m = 2$ signals during a few ms of high Mirnov activity. The saturated ion current (c) and floating potential (d) are strongly modulated by these oscillations. The time delay of $\sim 27\,\mu$s between maxima of (e.g.) the saturated ion current and the $\dot{\tilde{B}}_\theta(m = 2)$ signals is also shown.

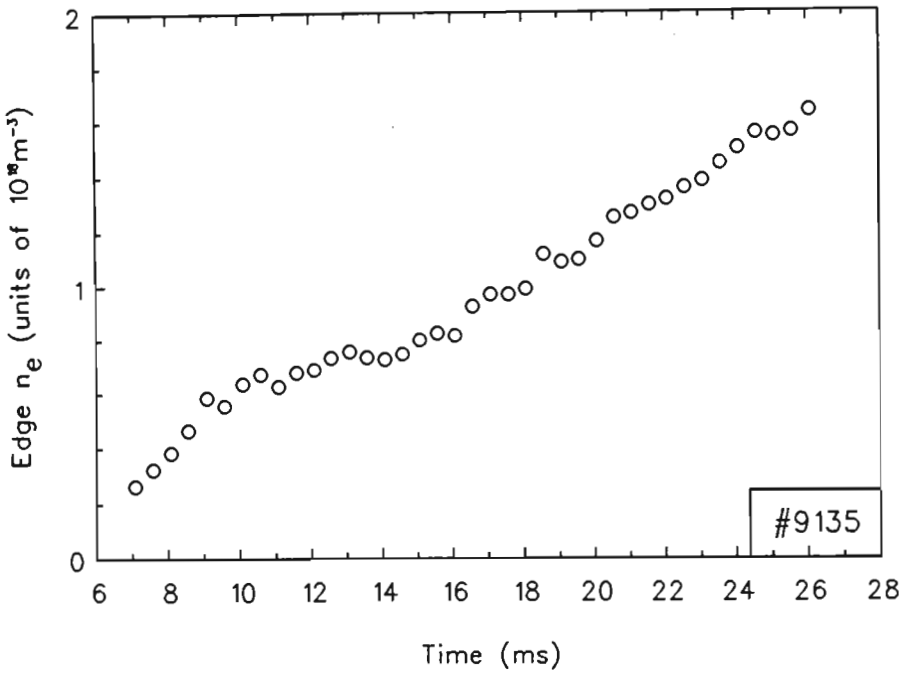

Figure 4.3: Edge electron density as a function of time (deduced from $n_e \simeq i_{sat}(m_i)^{1/2}/Ae(T_e)^{1/2}$) at $\rho = 0.93$.

this time. This is a fairly small variation compared with the variation of n_e over the full range of ρ investigated. The density decreases from bulk plasma to the limiter roughly linearly, the gradient increasing further out, closer to the limiter edge. The radial scale length in this region, L_n, also shown in Figure 4.4, increases towards about $\rho = 0.93$ and then decreases towards the limiter from $\approx 7 \rightarrow 1$ cm where $L_n = n_e/\nabla n_e$. At the limiter a local estimate gives $L_n \simeq 1.0$ cm. This value is constant within the error bars at all positions in the limiter shadow.

The floating potential for two different shots with different time dependence is shown in Figures 4.5(a) and (b) with the probe located at the same radius, 1.5 cm into the bulk plasma. $\dot{\tilde{B}}_\theta(m = 2)$ is also shown on the same timescale showing a clear correlation between these two quantities. Since $\dot{\tilde{B}}_\theta \propto \omega \tilde{B}_{\theta 0}$ and, in the absence of locking, ω varies by $\sim 2\times$ throughout the discharge, the main changes in $\dot{\tilde{B}}_\theta$ are due to changes in $\tilde{B}_\theta$. During the period of high Mirnov activity, ϕ_f is high and roughly constant at $\simeq 25$ V. At $t \simeq 12$ ms, however, the $m = 2$ amplitude rapidly decreases, signalling the onset of low Mirnov activity which then persists throughout the remainder of the shot up to the major disruption. About 0.5 ms before this, the floating potential also decreases rapidly (some $30 - 40$ V in ≈ 5 ms) to between 0 and -10 V and then slowly increases again to $\approx +8$ V after about another 5 ms. The degree to which ϕ_f decreases at the onset of low Mirnov activity is determined by both the radial position of the Langmuir probe and

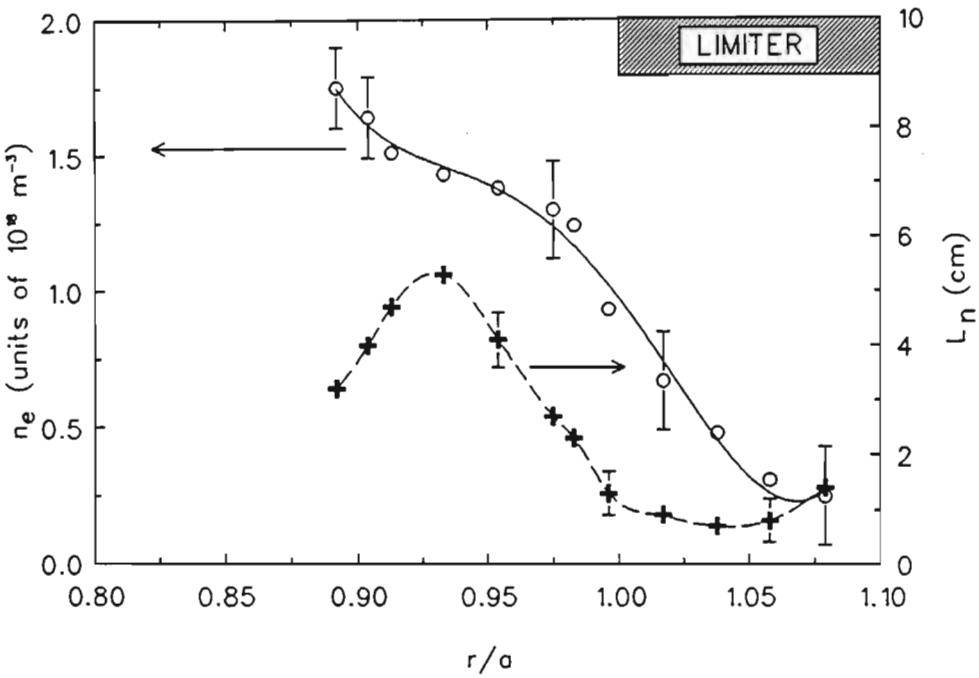

Figure 4.4: Edge electron density profile with points representing time averages of n_e from $t = 10$ — 16 ms during the 'flat-top' condition of the plasma current.

the Mirnov ($m = 2$) mode amplitude. When the amplitude is high—as in 4.5(b)—the potential decreases more steeply and by a greater amount than when the mode amplitude is lower, as in 4.5(a).

The modulation of the floating potential by the Mirnov $m = 2$ amplitude could be due to the high rate of diffusion of electrons across the magnetic islands situated close to the edge. When the $m = 2$ mode amplitude is high, the islands are large and could overlap the probe position. The diffusion of particles radially across an island is known to be rapid, relative to the radial transport in a stochastic region. In such a region any one particle may undergo several toroidal revolutions before traversing a substantial distance radially outwards. Hence, during high Mirnov activity, the amplitude of the $m = 2$ mode (or $m = 3$) is large and this enhances the cross field electron flow which maintains a high floating potential. As the amplitude decreases (low Mirnov activity) the edge becomes more stochastic and the radial rearrangement of particles decreases. Consequently, the probe floats to a lower potential and remains at this value until the major disruption.

Figure 4.6, shows ϕ_p as a function of ρ calculated using $\phi_p = \phi_f + 3.6T_e$. The floating potential values are the average ϕ_f measured between $t = 6$ and 12 ms, i.e. during high Mirnov activity. The electron temperature measurements were obtained using results from double probe analysis (see later). These measurements show a peaked profile with

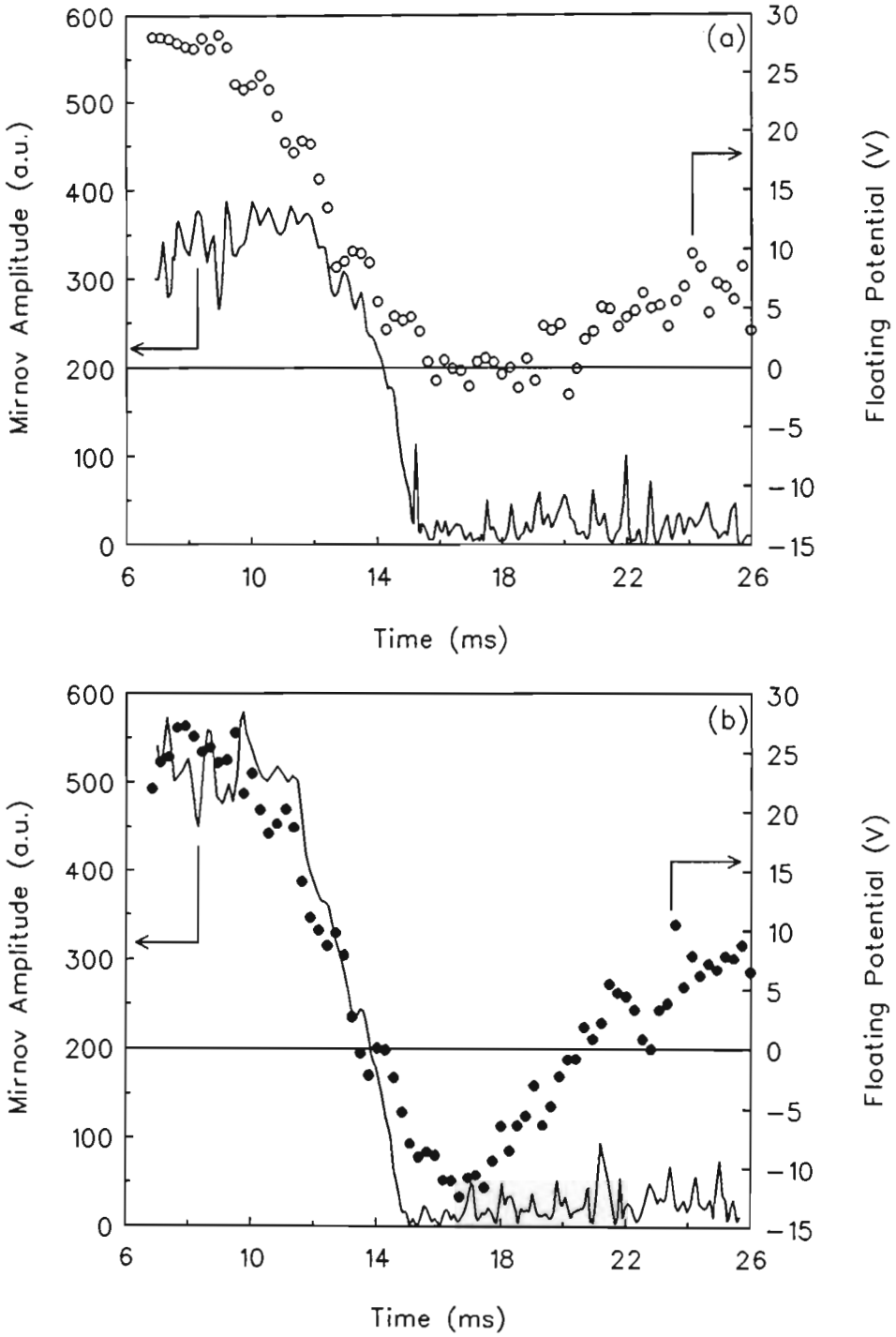

Figure 4.5: Edge $\phi_f(t)$ at $\rho = 0.93$ for shots (a) #9136 and (b) #9138. Also shown on the same time scale are Mirnov $m = 2$ mode amplitudes.

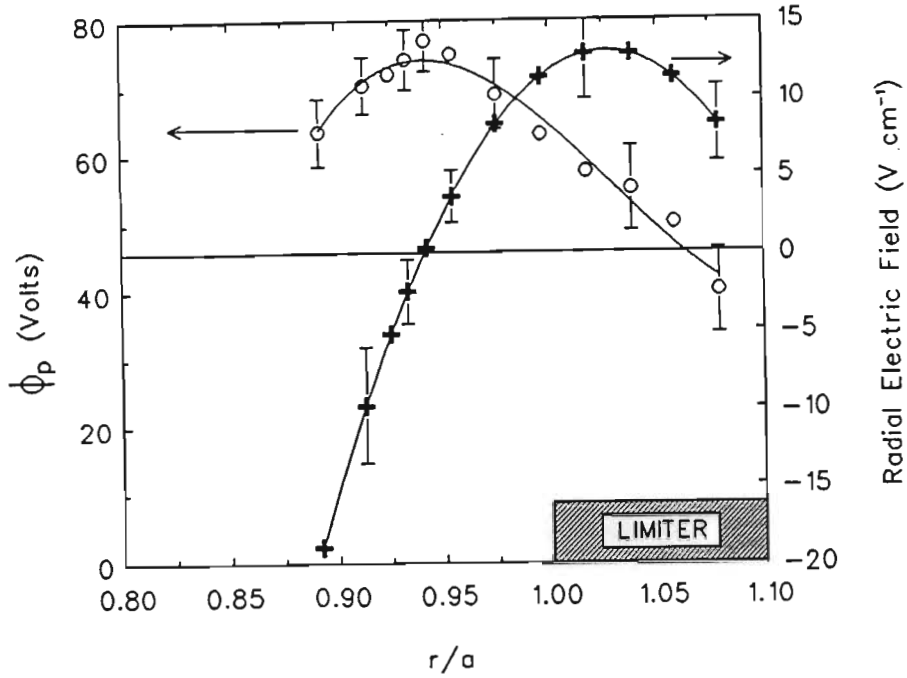

Figure 4.6: Radial edge profile of plasma potential. Points are time averages taken during high Mirnov activity ($t \approx 6$ — 12 ms). Also shown is the radial electric field, calculated from $\vec{E}_r = -\nabla\phi_p$.

a maximum at $\rho \simeq 0.94 \pm 0.02$ or between 0.9 and 1.9 cm into the bulk plasma measured from the limiter. The radial electric field is also shown in the figure with $\vec{E}_r = -\nabla\phi_p$ (or $-\partial\phi_p/\partial r$) at each radial position, changing sign at $\rho = 0.94$ and having a maximum $\vec{E}_r$ at $\rho = 1.03$ of $\simeq 12\,\mathrm{Vcm}^{-1}$. The value of L_E is about 1.4 cm and $L_E/r_s \approx 15$.

Fluctuation Levels

Figure 4.7 shows the relative fluctuation levels of the ion saturation current and floating potential as functions of time with the probe 1.5 cm into the bulk plasma at $\rho = 0.93$. The former were calculated from $\tilde{i}_{\mathrm{sat}}(t) = \langle\sum(i_{\mathrm{sat}}(t) - \bar{i}_{\mathrm{sat}})^2\rangle^{\frac{1}{2}}$ where $\bar{i}_{\mathrm{sat}}$ is the average ion saturation current and $\langle\ldots\rangle$ represents a time average over 2 ms. Both current and potential fluctuation levels increase until $t \simeq 13$ ms during the period in which the Mirnov ($m = 2$) amplitude is roughly constant. The current fluctuations then decrease from ≈ 0.35 at $t \simeq 13$ ms to ≈ 0.25 at $t \simeq 16$ ms coinciding with the sharp decrease in ($m = 2$) Mirnov amplitude during this time. These fluctuation levels then remain at this value (0.25) throughout the remainder of the discharge.

The potential fluctuations, on the other hand, remain at a constant, elevated level of

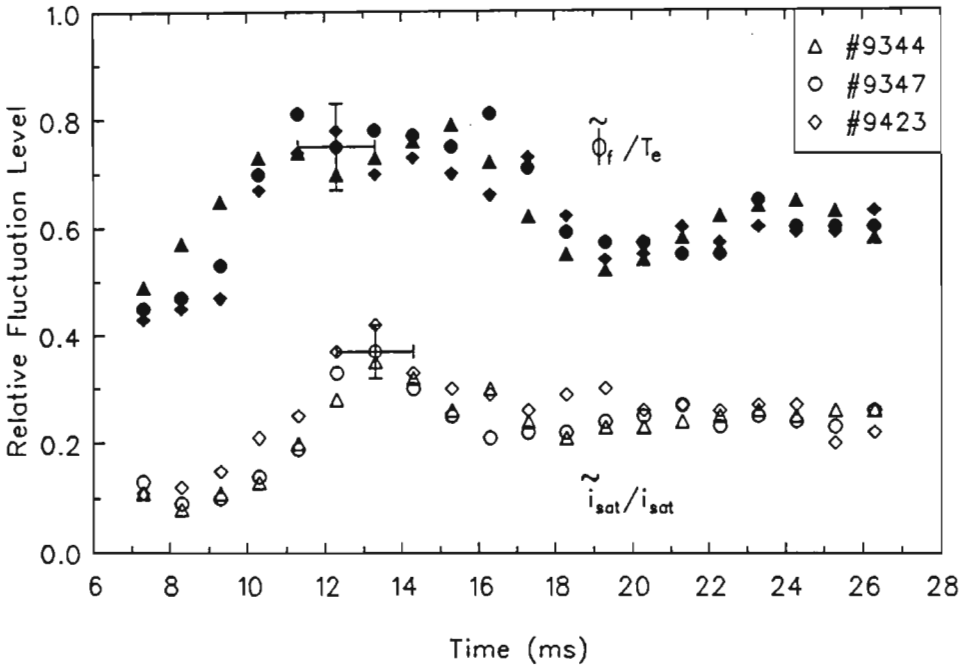

Figure 4.7: Levels of $\tilde{\phi}_f(t)/T_e$ and $\tilde{i}_{sat}(t)/i_{sat}$ at $\rho = 0.93$ with T_e from double probe results. Horizontal error bars are intervals over which data was averaged.

about 0.75 during the period in which the $m = 2$ mode amplitude (and floating potential) is decreasing, i.e. from $t \simeq 13$ ms to 16 ms. The level then decreases to about 0.6 during the period of low Mirnov activity.

Figure 4.8 shows the radial profile of the current and potential fluctuations. Because these quantities are also time dependent, these points represent averages of $\tilde{i}_{sat}/i_{sat}$ and $\tilde{\phi}_f/T_e$ between $t = 18$ ms and $t = 26$ ms. This period was chosen because of the small variation in these quantities during this time.

Current fluctuations increase monotonically from bulk plasma into limiter shadow from 0.1 to about 0.5 with no abrupt changes at the limiter edge. Potential fluctuations show a peaked profile with a maximum of ≈ 0.55 at $\rho \simeq 0.96 \pm 0.02$ or 1.0 ± 0.5 cm into the bulk plasma, although the shot-to-shot variations (from at least four shots at each position) are large, as indicated by the error bars.

Power Spectra

Figure 4.9 shows the power spectrum of $\tilde{\phi}_f$ during a period of high Mirnov activity (solid line) and then during the period of low Mirnov activity (dashed line). These spectra were obtained with the Langmuir probe again positioned 1.5 cm into the bulk

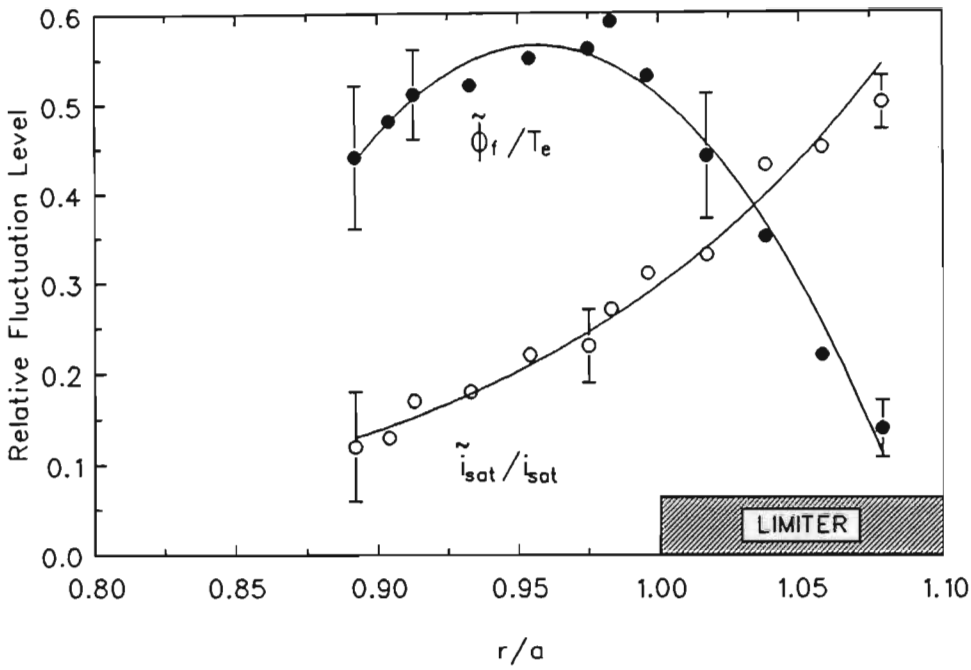

Figure 4.8: Radial profiles of $\tilde{\phi}_f/T_e$ and $\tilde{i}_{sat}/i_{sat}$, averaged over 5 ms (between $t = 7$ — 12 ms).

plasma. At this radial position, the floating potential is strongly modulated by the $m = 2$ mode amplitude as shown as an inset in Figure 4.9, hence the high amplitudes at and near the Mirnov frequency of $\approx 8 \rightarrow 15$ kHz. The spectra have a broadband, turbulent character, i.e. there are no reproducible or persistent peaks in them.

Poloidal correlation times, calculated using tips measuring $\tilde{\phi}_f$ separated in the poloidal direction, are short with $\tau_c = 2 \rightarrow 3\,\mu$s. Correlation times are shown in Figure 4.10(a) and (b) between poloidally and toroidally separated signals respectively, measured at $\rho = 0.93$. The poloidal correlation time is less than half that for the toroidal τ_c of $\approx$ 7 μs.

The toroidal phase velocity of the plasma is between $\simeq 25$ and 50×10^3 ms^{-1}, calculated using the range of Mirnov frequencies during the high Mirnov activity phase (i.e. between 8 and 15 kHz). These velocities are roughly a factor of 10 times greater than the measured poloidal phase velocity.

It could be speculated that a high velocity shear exists in the toroidal direction which results in a toroidal elongation of the 'blobs'[1] (mentioned in Section 2.1), since the high toroidal phase velocity *per se* could not cause this elongation. If the poloidal velocity

[1]Within which a high degree of correlation between fluctuating parameters exists.

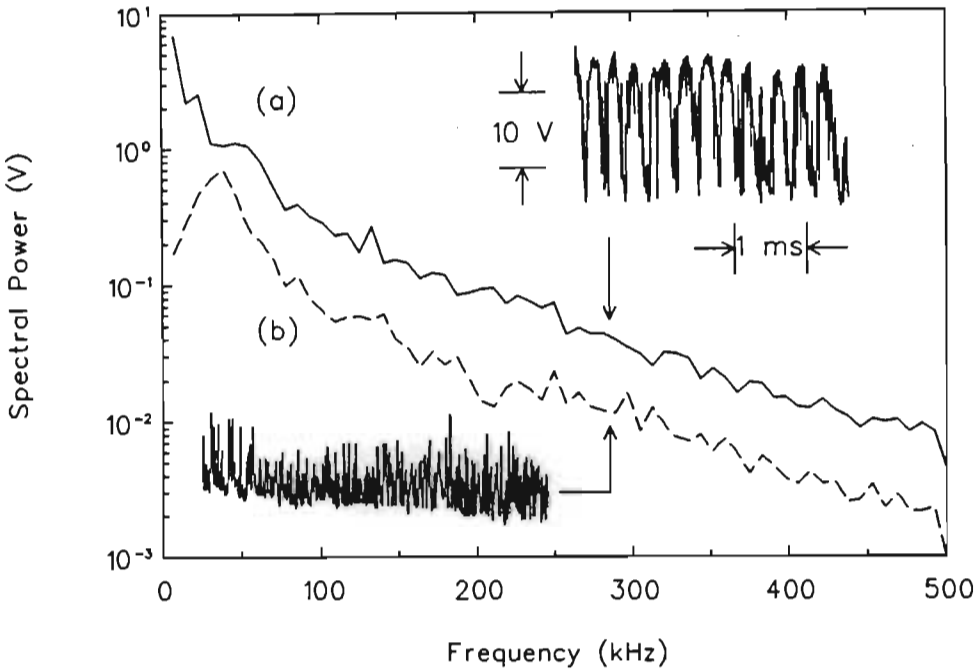

Figure 4.9: Power spectrum of $\tilde{\phi}_f$ during a period of (a) high and (b) low Mirnov activity at $\rho = 0.93$ with $\tilde{\phi}_f(t)$ traces during both these periods shown for comparison. Both time intervals sampled were ≈ 5 ms in duration.

shear was smaller than the toroidal case, this could lead to a correspondingly longer $\tau_{c,\mathrm{TOROIDAL}}$ and shorter $\tau_{c,\mathrm{POLOIDAL}}$, as observed.

The power spectrum of $\tilde{i}_{\mathrm{sat}}$ is very similar to that of $\tilde{\phi}_f$ and is therefore not presented here. There is a small peak at $f \approx 40$ kHz in the spectrum taken during low Mirnov activity. This peak and its correlation with other quantities is further discussed in Chapter 5. The power in the floating potential fluctuations is about 5× lower during low Mirnov activity since ϕ_f is high when the amplitude of the $m = 2$ mode is high and then later drops to low values as the Mirnov amplitude decreases. This is true at all radii and at all times during the discharge. In all cases the largest components of $\tilde{\phi}_f$ (and $\tilde{i}_{\mathrm{sat}}$) are at low frequencies ($f < 200$ kHz). The spectral power $P(f) \propto f^{-\xi}$ has $\xi \approx 2$ (i.e. $1.6 \leq \xi \leq 2.2$) for $f < 200$ kHz and $\xi \approx 3$ (i.e. $2.6 \leq \xi \leq 3.3$) for $200 < f < 500$ kHz, as shown in Figure 4.11 with the both axes on a logarithmic scale.

Coherency & Coherence Length

The coherency between $\tilde{i}_{\mathrm{sat}}$ and $\tilde{\phi}_f$ is shown in Figure 4.12 taken with the probe 1.5 cm into the bulk plasma during both high and low Mirnov activity. There is only partial

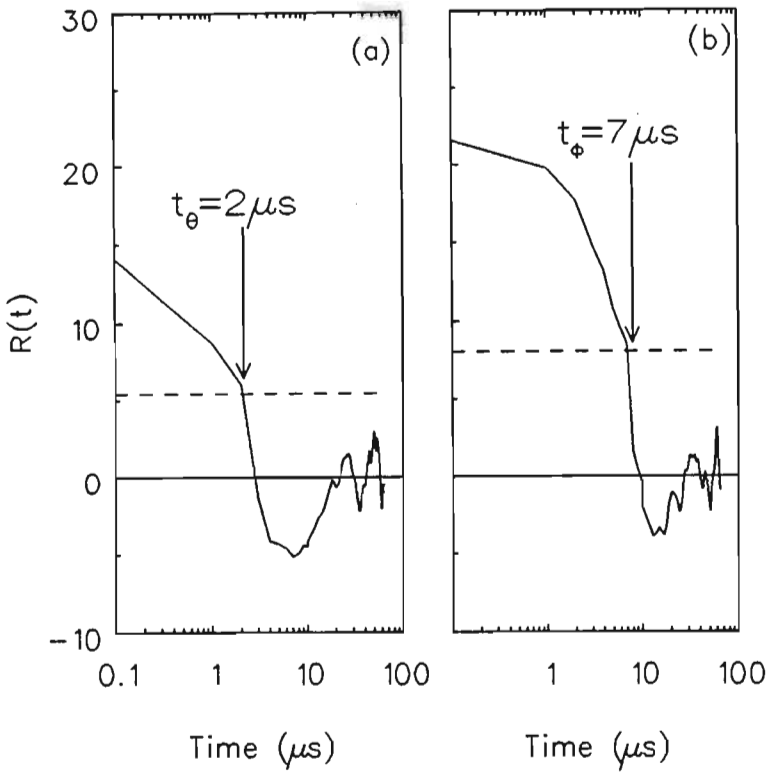

Figure 4.10: Correlation times between $\tilde{\phi}_f$ signals separated by 4 mm (probe separation) in the (a) poloidal direction and (b) toroidal direction during high Mirnov activity. Dashed lines are $1/e$ levels of $R(t)|_{\max}$.

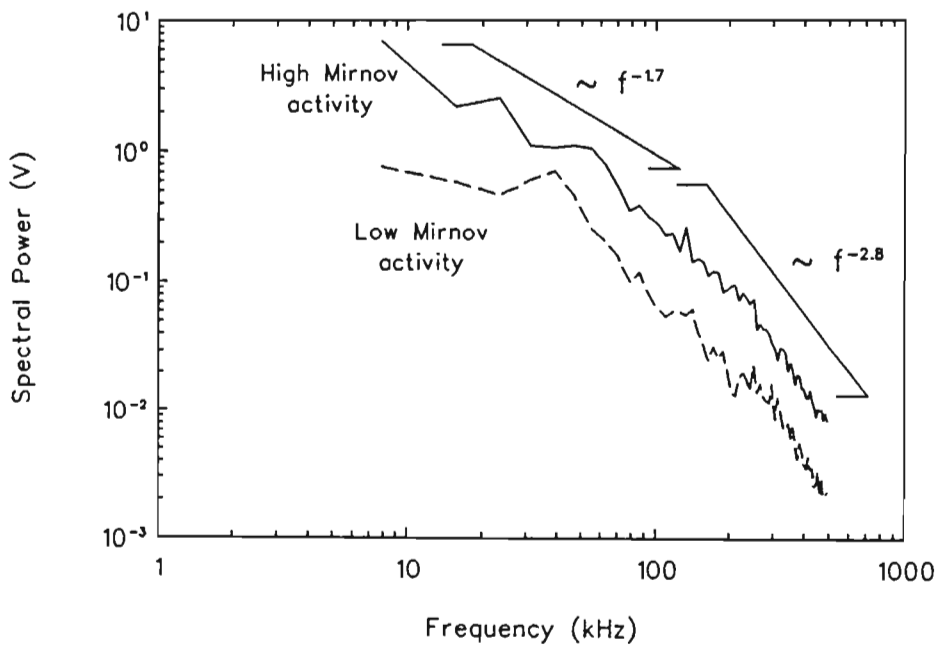

Figure 4.11: Power spectrum of $\tilde{\phi}_f$ during a period of high and low Mirnov activity at $\rho = 0.93$, with both axes on a logarithmic scale. The time interval was the same as that used in the previous Figure.

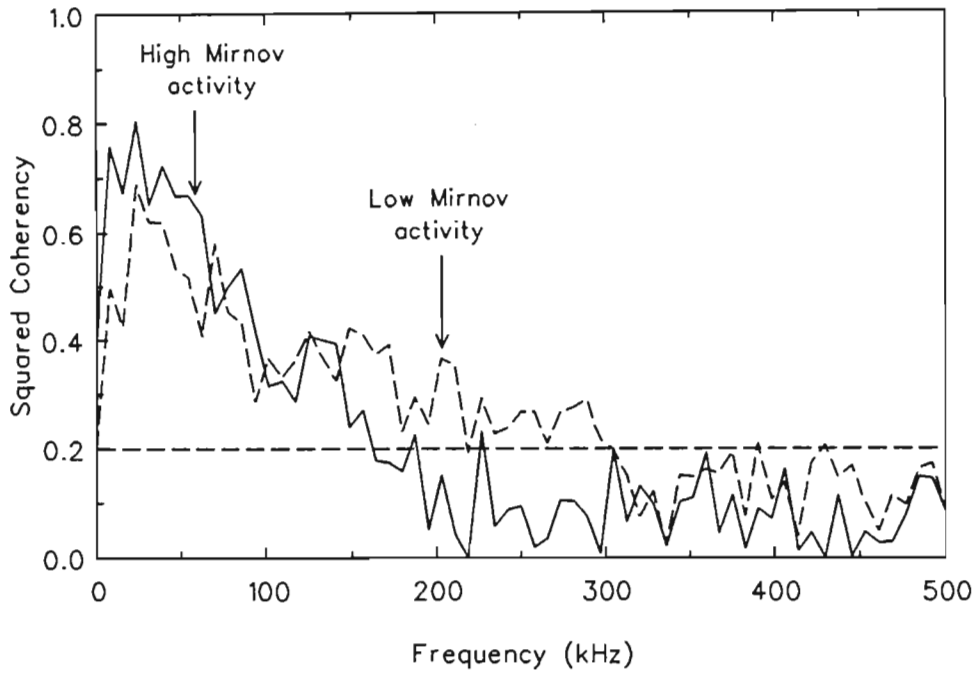

Figure 4.12: Coherency spectrum, $\gamma_{n\phi}$ (for poloidally separated probes) during high and low Mirnov activity for the times indicated in Figure 4.9. The dashed line indicates the significance level.

coherency between these quantities (i.e. less than 0.8) but this is large enough for the phase between the two to be well defined, at least for most of the range below $f < 200\,\mathrm{kHz}$. For frequencies above $\approx 200\,\mathrm{kHz}$ the coherency falls below the significance level indicated by the dashed line. The coherency increases slightly as the probe is moved further into the limiter shadow. The uncertainties in the coherency spectra are assumed to depend only on the size of the ensemble. The average value of the cross-coherence function is found by statistical analysis to be $(1/\sqrt{\ell})$ (where ℓ is the number of blocks in each ensemble) for any two independently-generated random data ensembles. Thus, the smallest value of coherence at any frequency that is believable is $1/\sqrt{\ell}$. For most of the data used here, $\ell = 25$ (i.e. $25 \times 128\,\mu\mathrm{s} \simeq 3.2\,\mathrm{ms}$) so $1/\sqrt{25} = 0.2$. The significance level was also independently computed between two sets of random data (comprising ℓ blocks) of similar amplitude to the real data and was found, at all frequencies, to be $\leq 1/\sqrt{\ell}$.

During high Mirnov activity the coherency between the fluctuating quantities is highest at low frequencies, i.e., $< 150\,\mathrm{kHz}$. At the Mirnov frequency the coherency is ≈ 0.8 and above 150 kHz it drops below the significance level. The coherency during the low Mirnov activity phase has high values around 50 kHz which decrease until $\approx 300\,\mathrm{kHz}$ and then fall below the significance level. No peaks are observed in the low ($< 30\,\mathrm{kHz}$)

frequency range.

The coherence length is defined as the $e-$folding length of $\gamma_{n\phi}$ and is given by $L_{\rm coher}(f) = d/(-\ln\gamma_{n\phi}(f))$, where d is the probe separation (GRAESSLE (1989)). This is derived from $\gamma_{n\phi}(f) = \exp^{-d/L_{\rm coher}(f)}$, but it is important to note that it is not necessarily true that $\gamma_{n\phi}(f) = 1$ if $d = 0$, i.e., zero separation. At small separations, the assumption of an exponential coherence function is physically incorrect and could, in certain circumstances lead to large overestimations of $L_{\rm coher}$, even if the above definition of $L_{\rm coher}$ were altered to involve the stricter criterion, i.e., that $L_{\rm coher}(f) = d/(-\ln\gamma_{nn}(f))$. This problem could be avoided by defining $\gamma_{n\phi}(f) = \gamma|_{d=0}\exp^{-d/L_{\rm coher}(f)}$. The definition would then allow

$$L_{\rm coher}(f) = \frac{-d}{\ln\gamma_{n\phi}(f) - \ln\gamma|_{d=0}}.$$

Since, in these experiments, $\gamma_{n\phi}|_{\rm max}(d = 4\,{\rm mm}) \approx 0.85$, it is not unreasonable to assume that $\gamma_{n\phi}|_{\rm max}(d = 0\,{\rm mm}) \approx 1.00$ (see also GREASSLE (1989)). For this reason, the original definition will be used, with the assumption that $\gamma|_{d=0} = 1$.

Scale lengths such as this one are useful in evaluating what theoretical approach might be appropriate to explain the presence (and to ascertain the consequences of) the turbulence. The uncertainty in the coherence length $L_{\rm coher}$ is also taken to be determined by ℓ. The coherency might always be smaller by an amount $1/\sqrt{\ell}$ so the uncertainty in $L_{\rm coher}$ is calculated by taking the difference between the value calculated from $L_{\rm coher}(f) = d/(-\ln(\gamma_{n\phi}(f)))$, with d the probe separation, and the value calculated from $L_{\rm coher}(f) = d/(-\ln(\gamma_{n\phi}(f) - 1/\sqrt{\ell}))$. Because no value of coherency below $1/\sqrt{\ell}$ should be accepted as real, the limit of resolution of $L_{\rm coher}$ is given by $L_{\rm limit} = d/(-\ln(1/\sqrt{\ell}))$.

The dashed line on the graph of the poloidal coherence lengths shown in Figure 4.13 is the limit of resolution of $L_{\rm coher}$. The coherence lengths are, in general, longer for the low frequencies (i.e. $< 150\,{\rm kHz}$) with high values at $f \simeq 25\,{\rm kHz}$ of about $1.5\ \pm 0.5\,{\rm cm}$. The short poloidal coherence lengths found for most of the high frequency turbulence make it impossible to determine its absolute poloidal mode structure. These results justify the probe tip separation of 4 mm.

Phase Angle & Dispersion Relation

Figure 4.14(a) through (c) shows the phase angle between $\tilde{i}_{\rm sat}$ and $\tilde{\phi}_f$, with the probe at three radial positions ($\rho = 0.95, 1.00$ and 1.04). In these cases, at the lowest frequencies, the phase between $\tilde{i}_{\rm sat}$ and $\tilde{\phi}_f$ is usually within $45° < \alpha_{n\phi} < 80°$ for measurements taken in the limiter shadow and $-90° < \alpha_{n\phi} < -135°$ for those taken in the bulk plasma. At

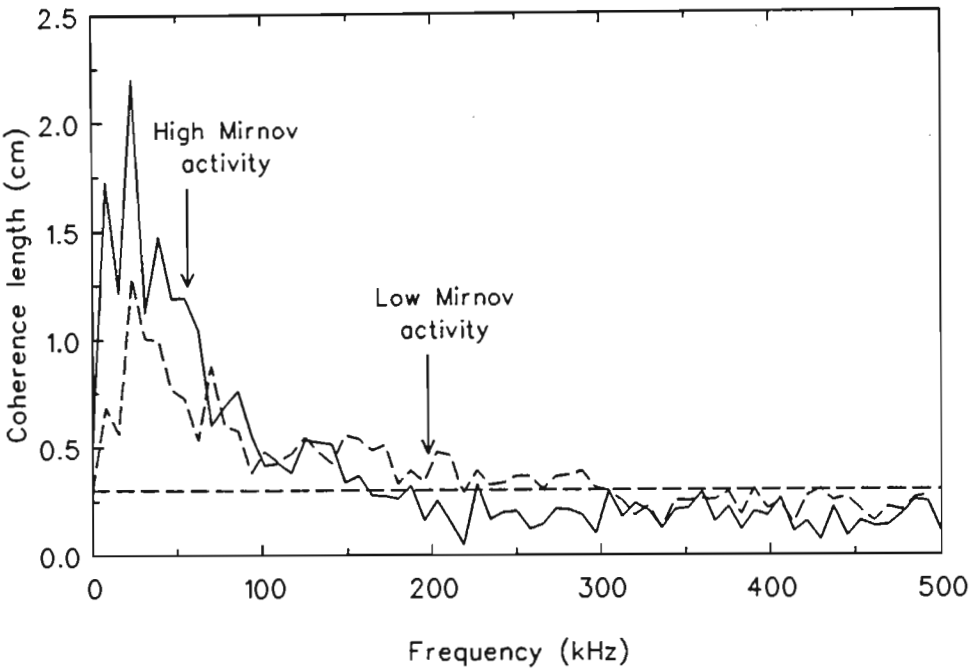

Figure 4.13: Poloidal coherence length spectrum between $\tilde{i}_{\rm sat}$ and $\tilde{\phi}_f$ during the two time intervals indicated in the previous Figure. The dashed line indicates the significance level below which the coherence length is meaningless.

the limiter, $\alpha_{n\phi}$ is positive and, for low frequencies ranges between $30° < \alpha_{n\phi} < 60°$.

The $k_\theta(f)$ spectrum of $\tilde{i}_{\rm sat}$ is shown in Figure 4.15 at the three radial positions indicated above. A distinct reversal in phase velocity is observed in passing from the bulk plasma to the limiter shadow with $v_{\rm phase} = -3.1 \times 10^3\,{\rm ms}^{-1}$ at $\rho = 0.95$, $+1.1 \times 10^3\,{\rm ms}^{-1}$ at the limiter and $+3.5 \times 10^3\,{\rm ms}^{-1}$ in the limiter shadow at $\rho = 1.04$. The coherency for these shots is low for $f > 200\,{\rm kHz}$ so $v_{\rm phase}$ is most reliably calculated for $f < 200\,{\rm kHz}$. It is worth noting that the phase angle changes sign when $k_\theta(f)$ changes sign, so the fluctuation induced transport is always outwards.

Phase Velocity

The power weighted phase velocity may be measured from the $S(\omega, k_\theta)$ spectrum via (RITZ *et al*, (1987a))

$$v_{\rm phase} = \frac{\sum_k (\omega/k_\theta) S(\omega, k_\theta)}{\sum_{\omega,k} S(\omega, k_\theta).}$$

Measurement of this quantity helps identify the turbulence as well as provide information on E_r, the radial electric field.

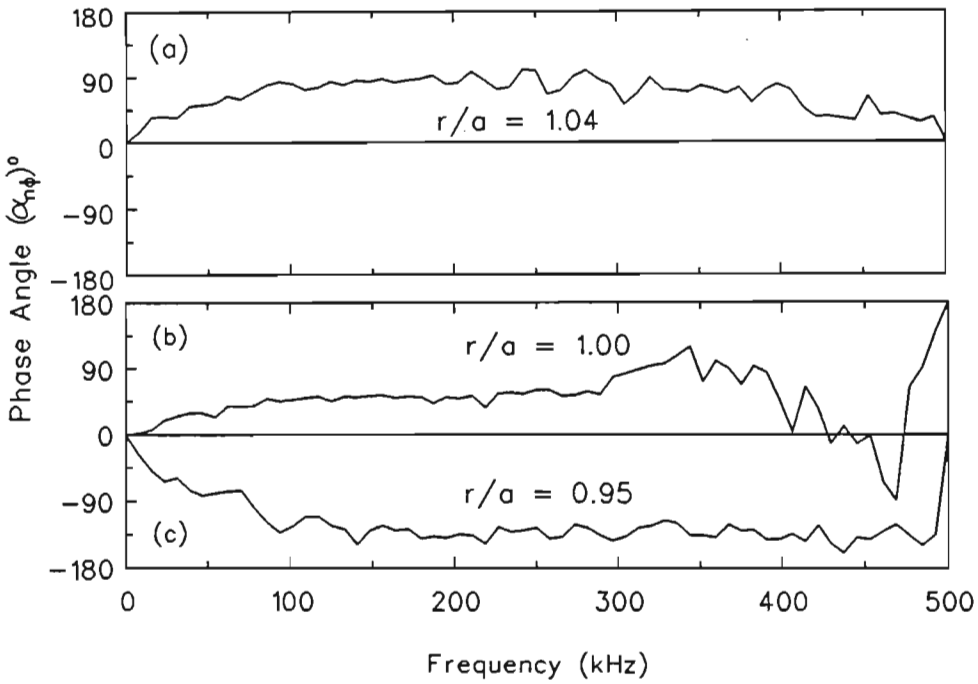

Figure 4.14: Poloidal phase angle between $\tilde{i}_{\rm sat}$ and $\tilde{\phi}_f$ as a function of frequency at three radial positions (a) $\rho = 1.04$, (b) $\rho = 1.00$ at the limiter radius and (c) $\rho = 0.95$ showing change of sign in the phase angle near the limiter.

Modes are expected to propagate in either the electron or the ion drift directions. Drift wave theories predict the drift wave velocity to be in the electron diamagnetic direction but this contradicts the observed propagation direction of the turbulent fluctuations in the outer edge (which, in some cases, propagate in the ion diamagnetic drift direction). A simple drift wave model, therefore, is insufficient to describe the measured propagation of the turbulence (RITZ *et al*, (1984)). Since observations are made in the laboratory frame, allowance must be made for Doppler shifts (WOOTTON (1991)). A radial electric field (HORTON *et al*, (1984), TERRY *et al*, (1984)) gives an $E_r \times B_\phi$ doppler shift which explains the observed change of direction of wave propagation. The phase velocity of the plasma measured in the laboratory frame, $v_{\rm phase}$ (lab), is then

$$v_{\rm phase}\,({\rm lab}) = v_{\rm phase}\,({\rm plasma}) + v_{E\times B}$$

where $v_{\rm phase}$ (plasma) is the phase velocity in the plasma frame or the diamagnetic drift velocity (given by $(T_e/B_\phi)(\nabla n_e/n_e)$) and $v_{E\times B}$ is the velocity of the plasma due to the radial electric field, given by $E_r \times B_\phi$, which results in a doppler shift of $v_{\rm phase}$ (plasma).

In order to determine $v_{E\times B}$, $E_r(= -\partial\phi_p/\partial r)$ must be calculated from a radial profile of ϕ_p. The non-uniform radial electric field is computed from the first derivative of a cubic spline fit to the plasma potential profile given in Figure 4.6. The resulting $E_r \times B_\phi$

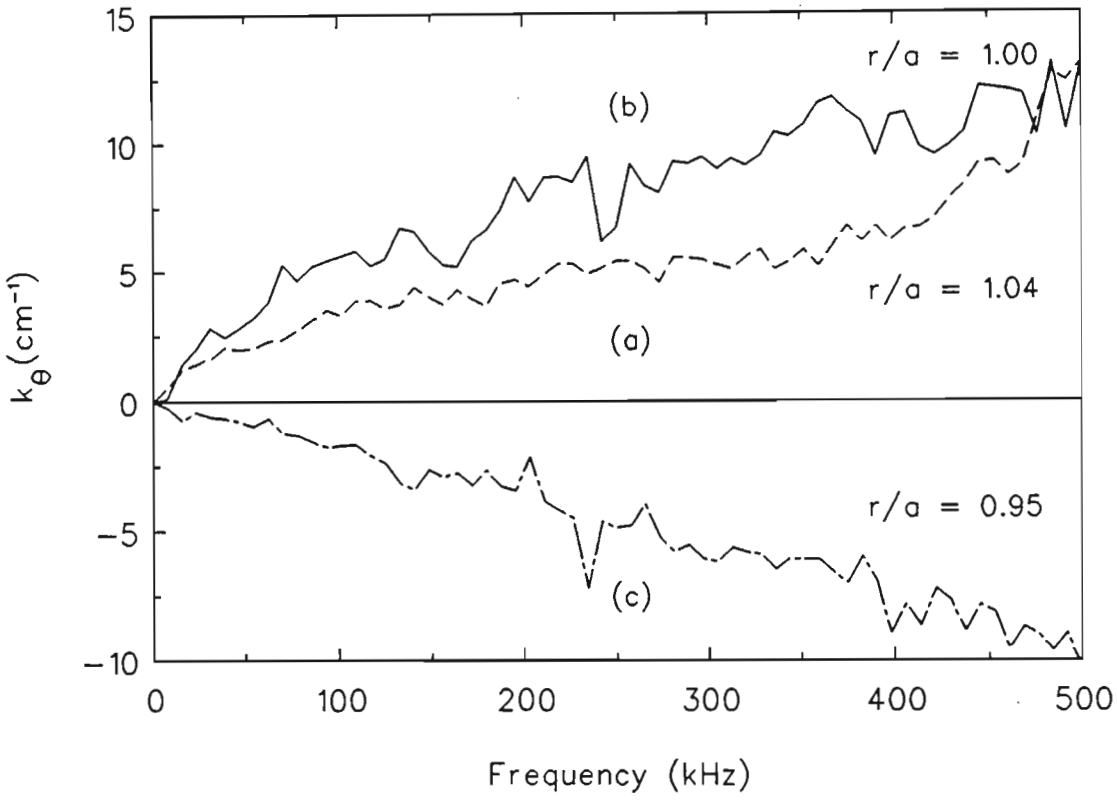

Figure 4.15: Dispersion relation between two poloidally separated probes measuring $\tilde{\phi}_f$ as a function of frequency. Measurements were taken at the same three radial positions indicated in the previous Figure, viz., (a) $\rho = 1.04$, (b) $\rho = 1.00$ and (c) $\rho = 0.95$, clearly showing the reversal of propagation direction from limiter shadow to bulk plasma.

velocity is added to the electron diamagnetic drift velocity to give the values as shown in Figure 4.16. The diamagnetic drift velocity does not change much over the five radial positions where the electron temperature was measured and, to obtain values of v_{drift} at positions other than those indicated, the curve was extrapolated roughly linearly in both directions. The dominant contribution to the change in measured phase velocity comes from the $E_r \times B_\phi$ velocity. Significant uncertainty is attached to the value of $v_{E\times B}$ since E_r is obtained from difference measurements of ϕ_p. Within the uncertainties of the measurements the measured phase velocity of the fluctuations is in agreement with the sum of the $E_r \times B_\phi$ velocity and pressure gradient driven velocity outside the limiter and in approximate agreement inside.

The radial profile of the measured poloidal phase velocity of $\tilde{\phi}_f$ is shown in Figure 4.16. These values were calculated by obtaining the best linear fit to k_θ over the frequency range where γ is high, i.e. $< 200\,\text{kHz}$. Up to 2.5 cm into the bulk plasma, the phase velocity is high and in the electron diamagnetic direction. Closer to the limiter, this value decreases rapidly from $\approx 4 \times 10^3\,\text{ms}^{-1}$ to ≈ 0 at $\rho = 0.98$. It then changes to the ion diamagnetic direction and increases again over a very short radial distance ($\approx 0.8\,\text{cm}$) to high values of $\approx 3.5 \times 10^3\,\text{ms}^{-1}$. Further into the limiter shadow, the velocity is approximately constant within the error bars.

The radial velocity shear, dv_{phase}/dr, is shown in Figure 4.17 with v_{phase} shown on the same radial scale. A velocity shear in the edge plasma has been observed on many tokamaks (e.g. RITZ *et al*, (1984), BURRELL (1989), and RUDYJ *et al*, (1989)) giving rise to a 'velocity shear layer' in the edge region accompanied by a reduction in the absolute turbulence in the region of maximum shear. On *Tokoloshe*, the results show an increase in both fluctuating quantities from the shadow region into bulk plasma. In the shear layer, both these quantities are reduced as shown in Figure 4.18. The width of the layer is $\approx 1.7\,\text{cm}$ with a maximum of $\approx 3.5 \times 10^5\text{s}^{-1}$ at $\rho \simeq 0.97$. This quantity (dv_{phase}/dr) should be indicative of the gradient in mass velocity since the change in the phase velocity is due mainly to the $E_r \times B_\phi$ velocity (RITZ *et al*, (1984)).

Several theories have been proposed to explain the observed strong velocity shear near the plasma edge. These are (1) turbulent drive (DIAMOND (1991)), (2) self-consistently calculated neoclassical drive (HINTON (1991)), (3) poloidal asymmetry drive (HASSAM *et al*, (1991)), (4) the spin up of the plasma due to orbit loss (**ion:** SHAING (1990), **electron:** HAZELTINE (1989) who showed that the peaking of the plasma potential just outside the outermost flux surface gives rise to a shear in the $E_r \times B_\phi$ drift which in turn gives rise to the observed phase velocity shear—the peaked plasma potential corresponds to a localised excess of $-$ve charge which results in a halo of ions surrounding

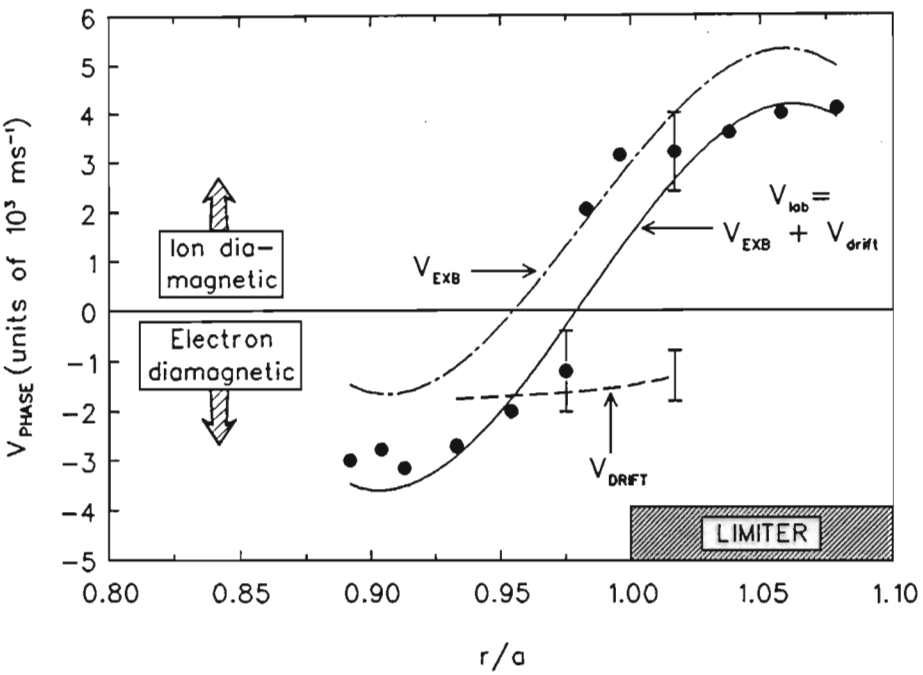

Figure 4.16: Measured, power weighted, poloidal phase velocity profile of $\tilde{\phi}_f$ (solid circles). The dashed line is v_{phase} (plasma), the diamagnetic drift velocity, the dot-dash line is v_{ExB} and the solid line, the sum of these quantities (= calculated value of v_{phase} (lab)).

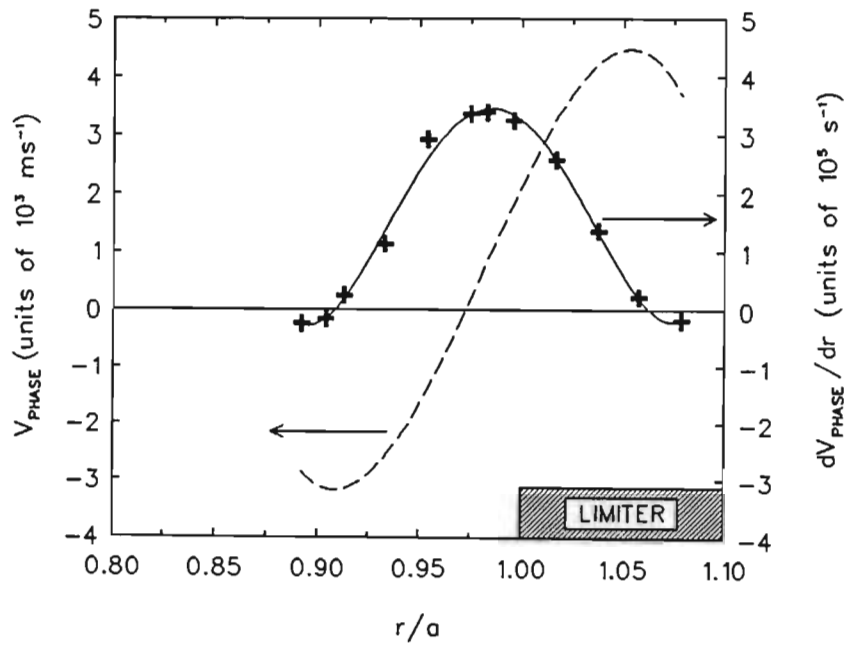

Figure 4.17: Velocity shear profile calculated from $-dv_{\text{phase}}/dr$. The phase velocity is also shown for comparison with the position of maximum shear.

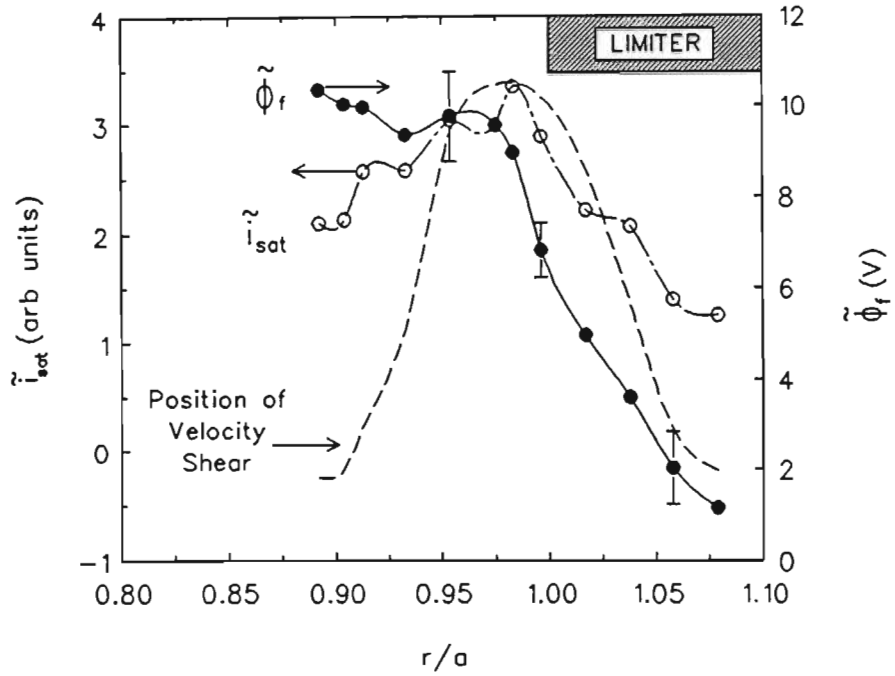

Figure 4.18: Absolute fluctuation levels of $\tilde{i}_{sat}(\rho)$ and $\tilde{\phi}_f(\rho)$ with the velocity shear layer shown as a dashed line.

the quasineutral plasma), and (5) the work of TSUI (1992) who showed that a velocity shear layer forms naturally from the radial potential profile created in the edge region of confined plasmas where field lines interact with material surfaces. The formation of this layer is accompanied by a finite momentum loss and an increase in the velocity shear leads to an improvement in momentum confinement. Evidence for a confinement improvement by velocity shear effects in the edge plasma of normal ohmic discharges in the TEXT tokamak was also reported by RITZ *et al*, (1990a). The effects of stochastic magnetic fields on the velocity shear layer was reported by RITZ *et al*, (1990b).

$S(\omega, k_\theta)$ Spectra

It is desirable to know the detailed form of the wavenumber spectrum, in order to compare the turbulent field with theory. BEALL *et al*, (1982) proposed that it is possible, under certain conditions, to extract $S(\omega, k_\theta)$ from two-point measurements. Such methods have since been applied to a number of experiments (see, e.g. RITZ *et al*, (1987a)). However, modelling and experimental evidence has recently shown that the method fails to reproduce $S(\omega, k_\theta)$ correctly (CARLSON *et al*, (1990)). CARLSON *et al*, (1989) also addressed the problem of the limitations of measurements of the local wavenumber using adjacent probe tips. It was shown that, while the power-weighted mean of phase

difference measurements accurately reflected the mean wavenumber of the fluctuations, no further information about the wavenumber spectrum could be obtained. More information of $S(\omega, k_\theta)$ is desirable and can in principle become available by the use of more tips. However, it is doubtful whether their perturbation to the plasma could be tolerated or whether they could be kept within a correlation volume. If detailed knowledge of the $k-$spectrum is required, a full measurement of the 2-D correlation function ($\gamma_{12}(d, t')$ as given by VAYAKIS (1991), where d is the probe separation and t' is the time delay between signals propagating from tip to tip) appears unavoidable. The results below were estimated from only two probe tips and they should be viewed in the light of this discussion.

The complete $S(\omega, k_\theta)$ spectra and associated contour plots for $\tilde{i}_{\rm sat}$ fluctuations are shown in Figure 4.20(a) through (c) at three different radial positions[2]. The dominant low wavenumber regions ($k_\theta < 5\,{\rm cm}^{-1}$) are characterised by broad, peaked spectra with $\Delta\omega/\omega \approx \Delta k_\theta/k_\theta \approx 0.6$. The contour plots also indicate that the fluctuating power above $k_\theta = 5\,{\rm cm}^{-1}$ is small. The $S(k_\theta)$ spectra exhibit a broad peak at $k_\theta \approx 2-4\,{\rm cm}^{-1}(k_\theta r_s \simeq 0.27)$ with a fall off proportional to $k_\theta^{-6\pm1}$ for larger wavenumbers as shown in Figure 4.19. The contour plots show a clear change in the propagation direction from the ion diamagnetic direction in the outer edge of the plasma behind the limiter ($\rho > 1.00$) to the electron diamagnetic direction inside the limiter. In the intermediate region ($\rho \approx 1.00$) the spectrum is much broader ($\Delta k_\theta \simeq 4.5\,{\rm cm}^{-1}$) than it is 1 cm on either side of the limiter where the spectra are relatively narrow ($\Delta k_\theta \lesssim 3\,{\rm cm}^{-1}$). In contrast, using two probe tips separated in the toroidal direction, a narrow spectrum ($\Delta k_\phi < 0.8\,{\rm cm}^{-1}$) and relatively high propagation velocity ($\simeq 12.6 \times 10^3\,{\rm ms}^{-1}$) is found (see Figure 4.21).

The effective ion gyroradius, r_s, (given by v_{T_i}/ω_{ci}, where T_i is assumed to be $\approx T_e$) at $\rho = 0.93$ is ≈ 0.12 cm and, in the limiter shadow at $\rho = 1.02$, $r_s \approx 0.09$ cm. The poloidal wavenumber spectrum shows that k_θ does not vary much over the radial range under investigation, being $\simeq 2\,{\rm cm}^{-1}$ at all radii between $0.89 \leq \rho \leq 1.05$ giving the range $0.15 \gtrsim \overline{k}_\theta r_s \gtrsim 0.25$. Using this range of values of k_θ, the range of m, the poloidal mode number, is between 20 and 40, using $a\,k_\theta = m$.

Radial Particle Flux

The frequency resolved, fluctuation induced, particle flux is shown in Figure 4.22 at $\rho = 0.93$ during both high (i.e. from $t \simeq 6$ ms $\rightarrow t \simeq 15$ ms) and low (i.e. $t \simeq 16$ ms

[2]The $S(\omega, k_\theta)$ spectra for the potential fluctuations are practically identical to that for the density fluctuations.

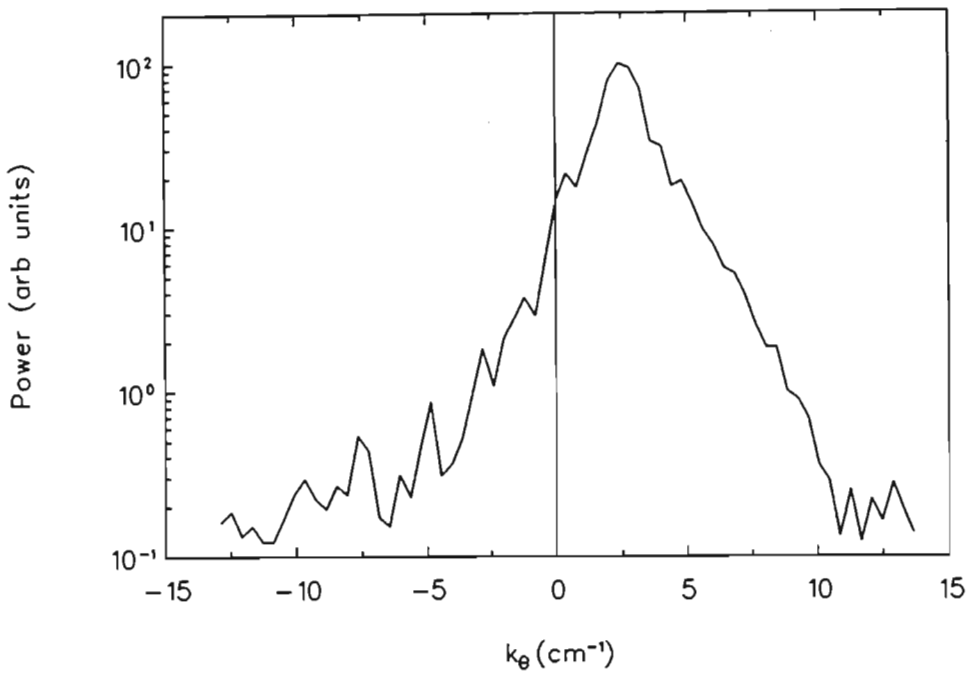

Figure 4.19: Power spectrum as a function of wavenumber, $S(k_\theta)$, for $\tilde{\phi}_f$ measured at $\rho = 0.93$ during about 5 ms of high Mirnov activity.

$\rightarrow t \simeq 28$ ms) Mirnov activity. The data segments used comprised 39 ensembles, each 128 μs long (hence a total duration of ≈ 5.0 ms). The frequency resolution is 7.81 kHz and the Nyquist frequency 500 kHz.

Comparison of the spectrally resolved fluctuating flux during high and low Mirnov activity shows that they are both positive (i.e. outward) at all frequencies, both are very small for frequencies above 100 kHz and both have high values of flux in the frequency range from 0 to 100 kHz. The peak is at low frequencies ($\lesssim 30$ kHz) in the high Mirnov case and, during the transition from high Mirnov activity to low Mirnov activity this peak shifts to higher frequencies (≈ 60 kHz). During this transition, the width of the peak also broadens considerably (by up to 3 times the width during high Mirnov activity). At low frequencies, below 30 kHz, there is relatively little flux. This interesting feature of these results has not been reported on other tokamaks and is currently the subject of further investigation.

The temporal evolution of $\tilde{\Gamma}$ is shown in Figure 4.23 at the radial position of peak particle flux, i.e. $\rho = 0.93$. No minor disruptions were present at any stage during the discharge. Each point was obtained by using a time duration of 25 ensembles each 128 μs long (i.e. 3.2 ms) as a window which was moved a fixed time for each point on the graph. The flux increases almost linearly throughout the duration of the discharge in the presence

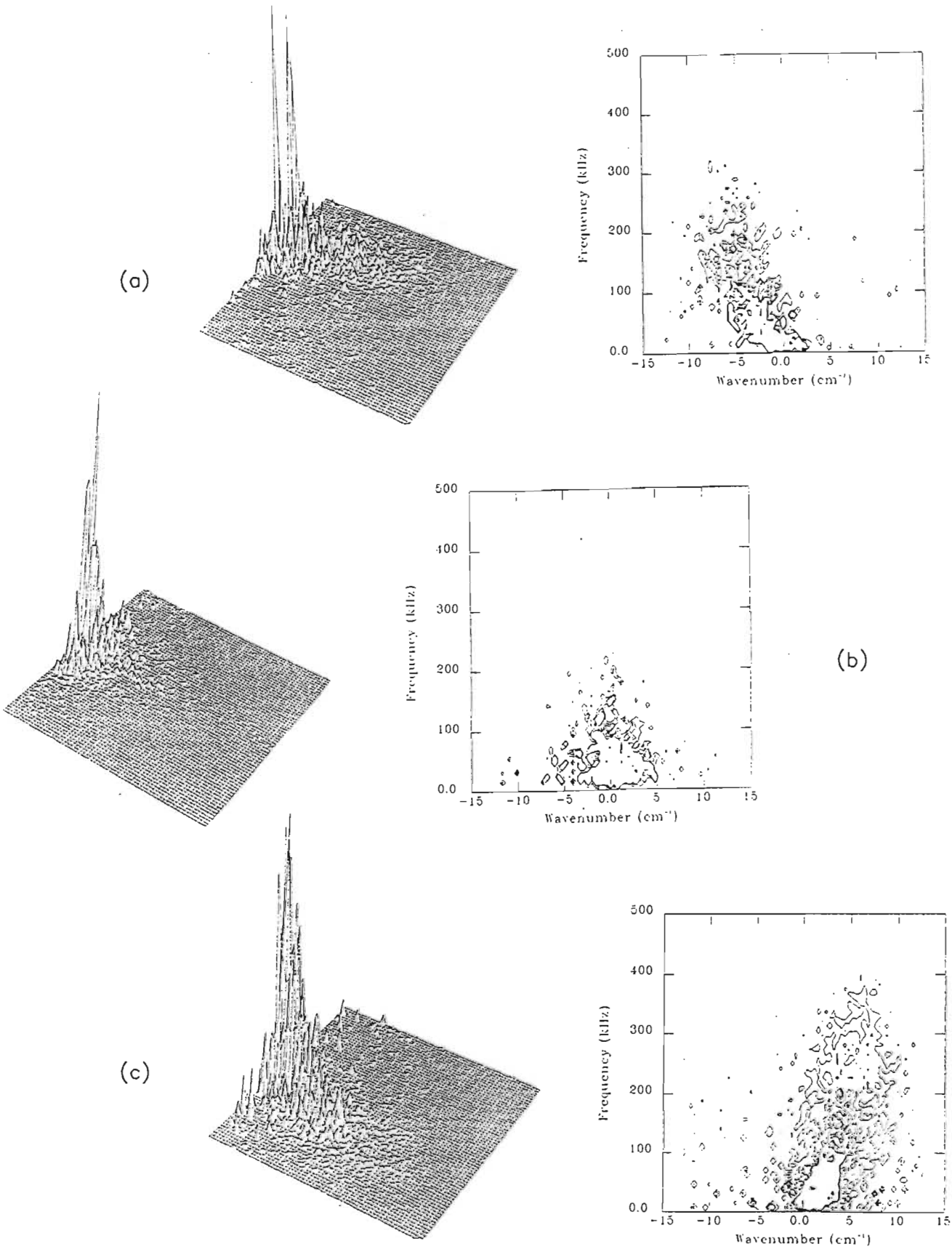

Figure 4.20: $S(\omega, k_\theta)$ spectra and contour plots of $\tilde{i}_{\mathbf{sat}}$ at $\rho =$ (a) 0.95 (bulk plasma), (b) 1.00 (limiter position), and (c) 1.04 (limiter shadow).

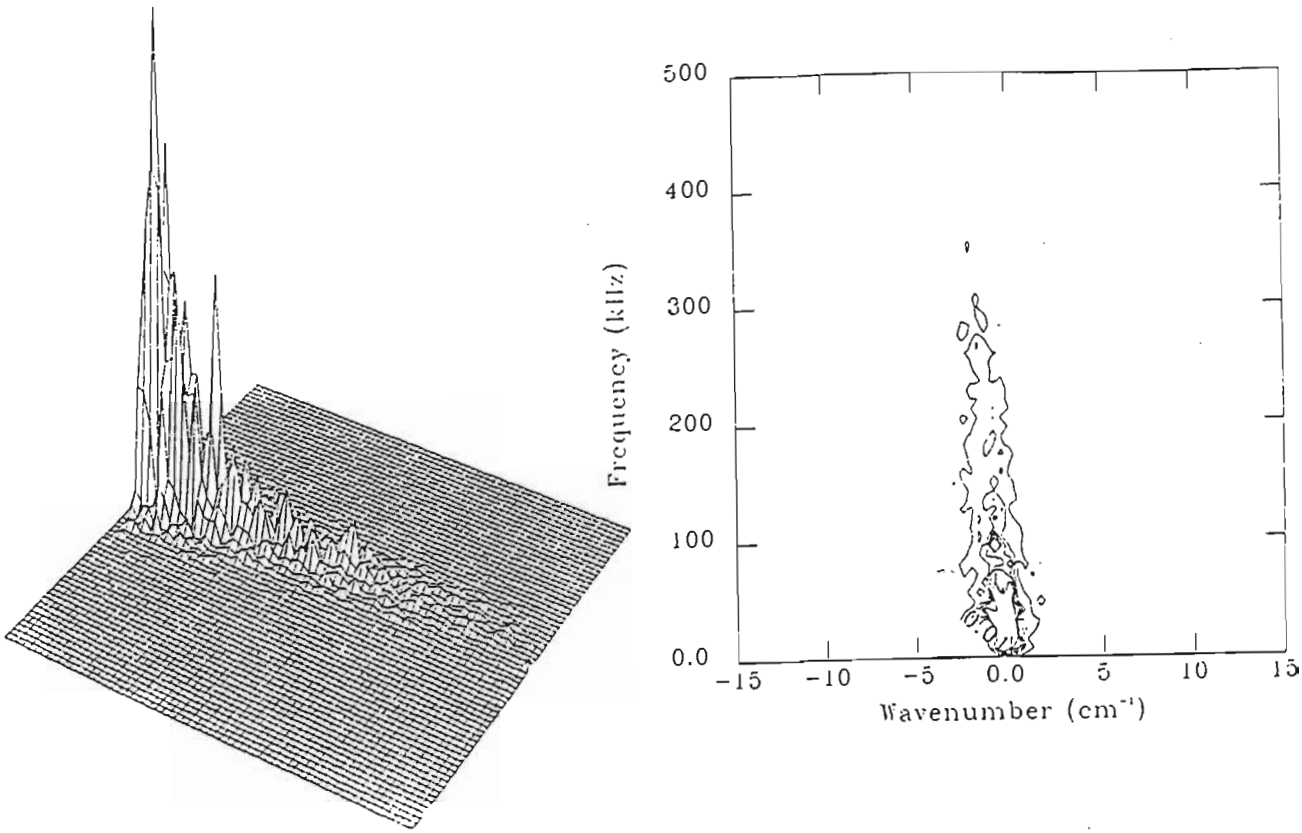

Figure 4.21: $S(\omega, k_\phi)$ spectrum and contour plot at $\rho = 0.93$, showing a high toroidal propagation velocity between $\tilde{\phi}_f$ fluctuations.

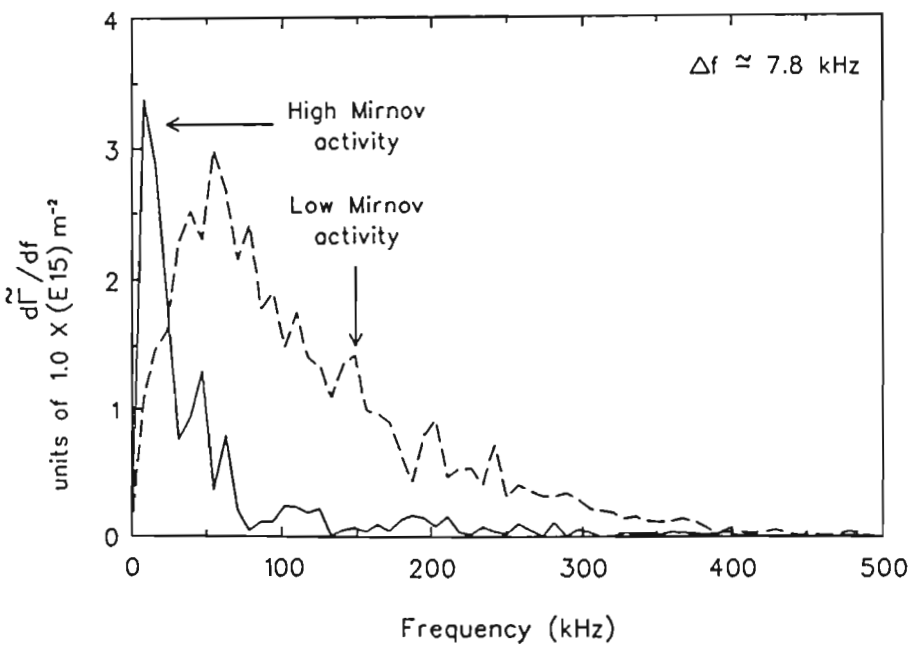

Figure 4.22: $\tilde{\Gamma}$ spectrum taken at $\rho = 0.93$ during a 5 ms period of high Mirnov activity and 5 ms during a low period of Mirnov activity. $\Delta f = 7.81$ kHz is the frequency resolution.

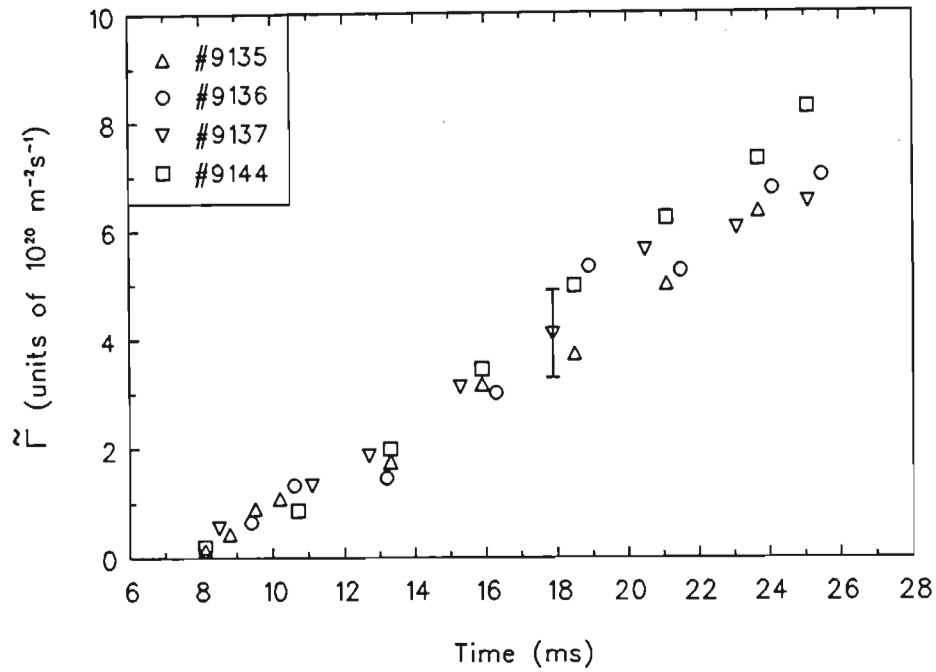

Figure 4.23: $\tilde{\Gamma}(t)$ taken at $\rho = 0.93$ using 2 ms sampling periods during high and low Mirnov activity.

of strong gas puffing and is unaffected by the smooth transition of high into low Mirnov activity later in the shot. The shots used here were separated by several weeks in some cases and they show very small scatter indicating a high level of reproducibility of results on *Tokoloshe*.

The measured radial dependence of particle flux in *Tokoloshe*, $\tilde{\Gamma}$, is shown in Figure 4.24 measured using ≈ 2 ms time intervals (16×128 μs) from $t = 8 \rightarrow 15$ ms during the period of high Mirnov activity. The flux peaks at a radial position about 1.5 cm ($\rho = 0.93$) into the bulk plasma in a region where both $\tilde{\phi}_p/T_e$ and ϕ_p are a maximum (see Figures 4.8 and 4.6, respectively). The flux increases very rapidly from limiter shadow to limiter and then drops off again further into the bulk plasma. Figure 4.25 shows a surface plot of $\tilde{\Gamma}(t, \rho)$. Peak flux is clearly at $\rho = 0.93$ and increases almost linearly throughout the duration of the discharge. For $\rho > 0.97$, $\tilde{\Gamma}(t, \rho)$ is very small, if not negligible. Closer in to the center of the minor cross section of the tokamak, ($\rho < 0.91$) the flux falls off rapidly again.

RITZ *et al* (19) obtained a similarly peaked $\tilde{\Gamma}(\rho)$ profile on TEXT and pointed out that in order to maintain continuity along the plasma cross section an additional convection mechanism must be invoked. Possible mechanisms invoked to maintain this continuity were (e.g.) radial flow or toroidal/poloidal convection of particles due to asymmetries.

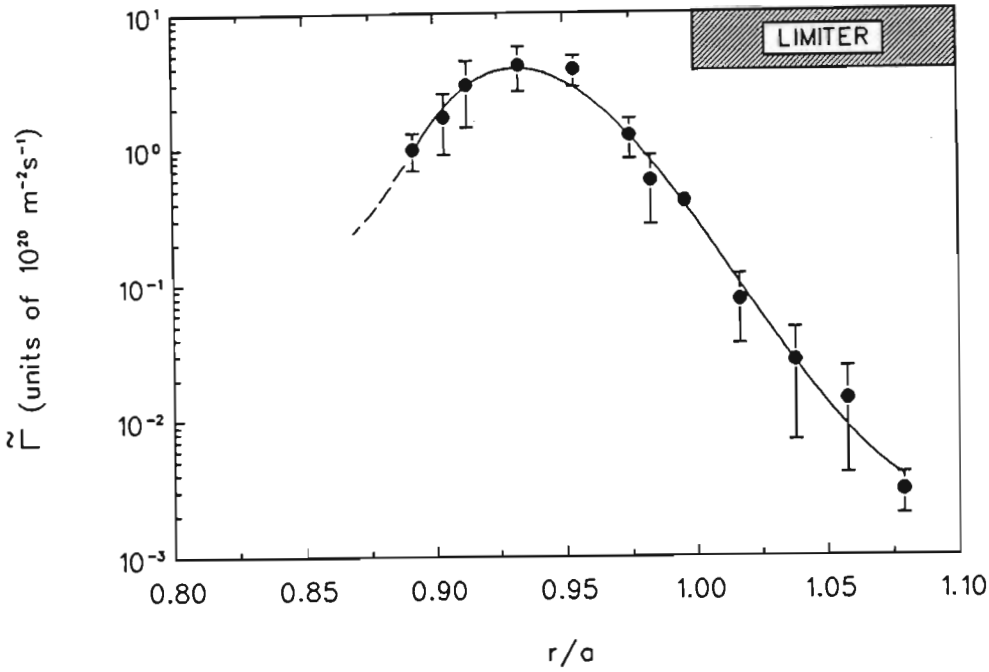

Figure 4.24: $\tilde{\Gamma}(\rho)$ profile on a log scale using 4 ms sampling periods during high Mirnov activity. Peak transport is at $\rho \simeq 0.93$.

The observations described above are also consistent with a large neutral source, S_{neutral}, in the edge plasma which balances the radial particle flux (RHODES (1989)). This can be seen using the continuity equation for the edge plasma

$$\nabla\Gamma = \nabla_r\tilde{\Gamma} = S_{\text{neutral}}$$

where $\nabla_{\|}\Gamma_{\|}$ is negligible. In the scrape-off layer, there is parallel flow to the limiter, $v_{\|} = \Gamma_{\|}/n$ as well as the large source S_{neutral} which enter the continuity equation

$$\nabla_r\tilde{\Gamma} + \nabla_{\|}\Gamma_{\|} = S$$

and cause $\tilde{\Gamma}$ to decrease in the scrape-off layer. For a more accurate comparison of these quantities, a better knowledge of both the $\tilde{T}_e$ level (VAYAKIS (1991)) and the sources and sinks of the particles is required.

LIN (1991) observed strong turbulent enhancement of radial particle flux during Mirnov ($m/n = 2/1, 3/1$) oscillations on TEXT and HOWLING (1986), who also found $\tilde{\Gamma}$ to be affected by Mirnov oscillations on TOSCA,attributed these changes to large fluctuations in T_e. Using Langmuir probes, RHODES (1989) observed turbulent enhancement during *sawtooth* oscillations in the far edge TEXT plasma with no accompanying changes in local gradients. Simple transport models could not explain these observations.

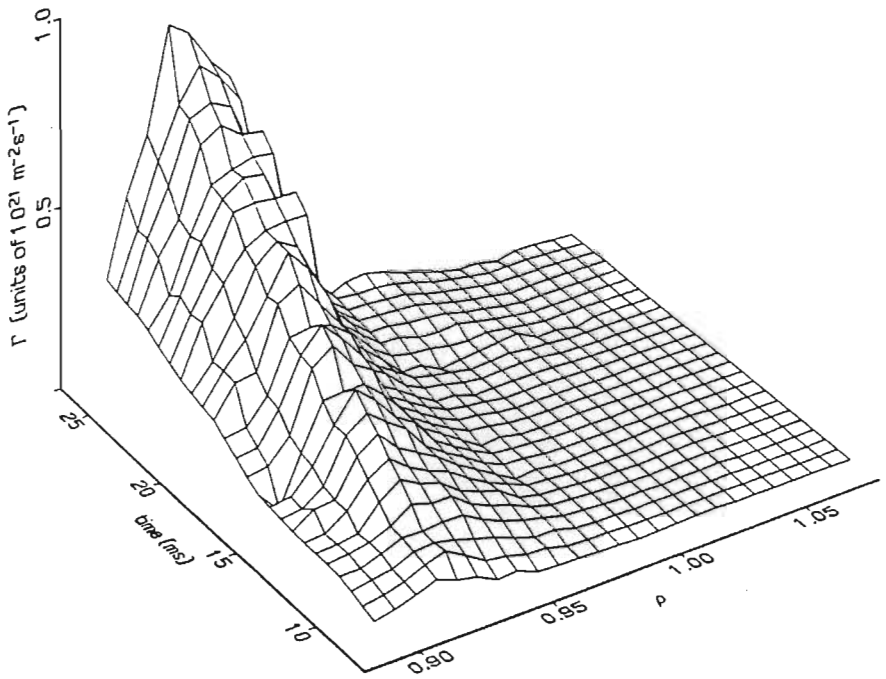

Figure 4.25: 2D plot of $\tilde{\Gamma}(\rho, t)$ on a linear scale using 2 ms sampling periods during high ($0 \leq t \leq 12$ ms) and low ($12 \leq t \leq 28$ ms) Mirnov activity. For clarity, time is shown increasing into the page.

Diffusion Coefficients

The effective diffusion coefficient, D_{eff}, is obtained from

$$D_{\text{eff}} = \frac{-\tilde{\Gamma}}{\nabla n_e},$$

and the (phenomenological) Bohm diffusion coefficient given by

$$D_{\text{Bohm}} = \frac{T_e}{16 B_\phi}. \tag{4.1}$$

A comparison of these values is at the five radial positions where T_e was measured is given in Table 4.2. The use of an effective diffusion coefficient (D_{eff}) is not necessarily valid since Ficks Law may not hold in the turbulent edge region. Also, stochastic fields for example or radial field components can greatly enhance D_{eff}.

4.2.2 Double Probe Results

The Langmuir probe array was configured as a double probe for all of the results presented in this Section. The current flowing between the two tips was sampled every 1 μs for

Table 4.2: Comparison of Bohm diffusion coefficient and D_{eff}.

COEFFICIENT	ρ				
(m^2s^{-1})	**0.93**	**0.95**	**0.98**	**1.00**	**1.02**
Bohm	1.88	1.78	1.58	1.34	1.17
Effective	19.66	18.32	5.87	0.63	0.17

32 ms during the flat top of the plasma current. Data segments of 5 ms duration, during both high and low Mirnov activity, were selected and the mean of these data calculated. These values, at each value of the probe bias, yielded a time averaged characteristic which was then used as the data from which T_e was extracted. Probe bias was varied between -80 V and $+80$ V in units of 10 V.

Edge Electron Temperatures

Figures 4.26(a) through (e) shows the i vs V_{bias} curves for the five different radial positions chosen from $\rho = 0.93$ to 1.02. The error bars are an indication of shot-to-shot scatter as well as the variation of $\bar{i}$ over five 1000 μs blocks within the 5 ms sample. Data for Figure 4.26 were obtained during the high Mirnov phase. Very little difference was observed between the these values and data recorded during low Mirnov activity (about 15% between the parameters returned by the program, which is smaller than the experimental uncertainty.)

The results in Figure 4.27 show that the edge electron temperature is decreasing from the bulk plasma towards the wall. The temperature drops from 18.0 V to 11.3 eV over a radial distance of 2 cm with no discontinuity in this trend at the limiter. These results are in good agreement with values obtained on *Tokoloshe* by ROBERTS (1986) using a single Langmuir probe. The value of ∇T_e from Figure 4.27 is 3.7 ± 1.0 eV cm^{-1} giving an effective L_{T_e} of 3.5 ± 1.5 cm at the limiter.

The uncertainty in T_e of 20% was estimated by assuming a random distribution of errors within 2σ of the actual data points, where σ is the standard deviation of the errors on all points. A difference of only 2.8 eV was recorded between high and low Mirnov activity electron temperatures, well within the uncertainty of measurement. The goodness of fit parameter, χ, defined by $\chi^2 = \sum [y(x_i) - \mathcal{F}(x_i, a)]^2$ where $y(x_i)$ are the actual data points and $\mathcal{F}(x_i, a)$ is the fitted curve, was calculated and found to be small (less than

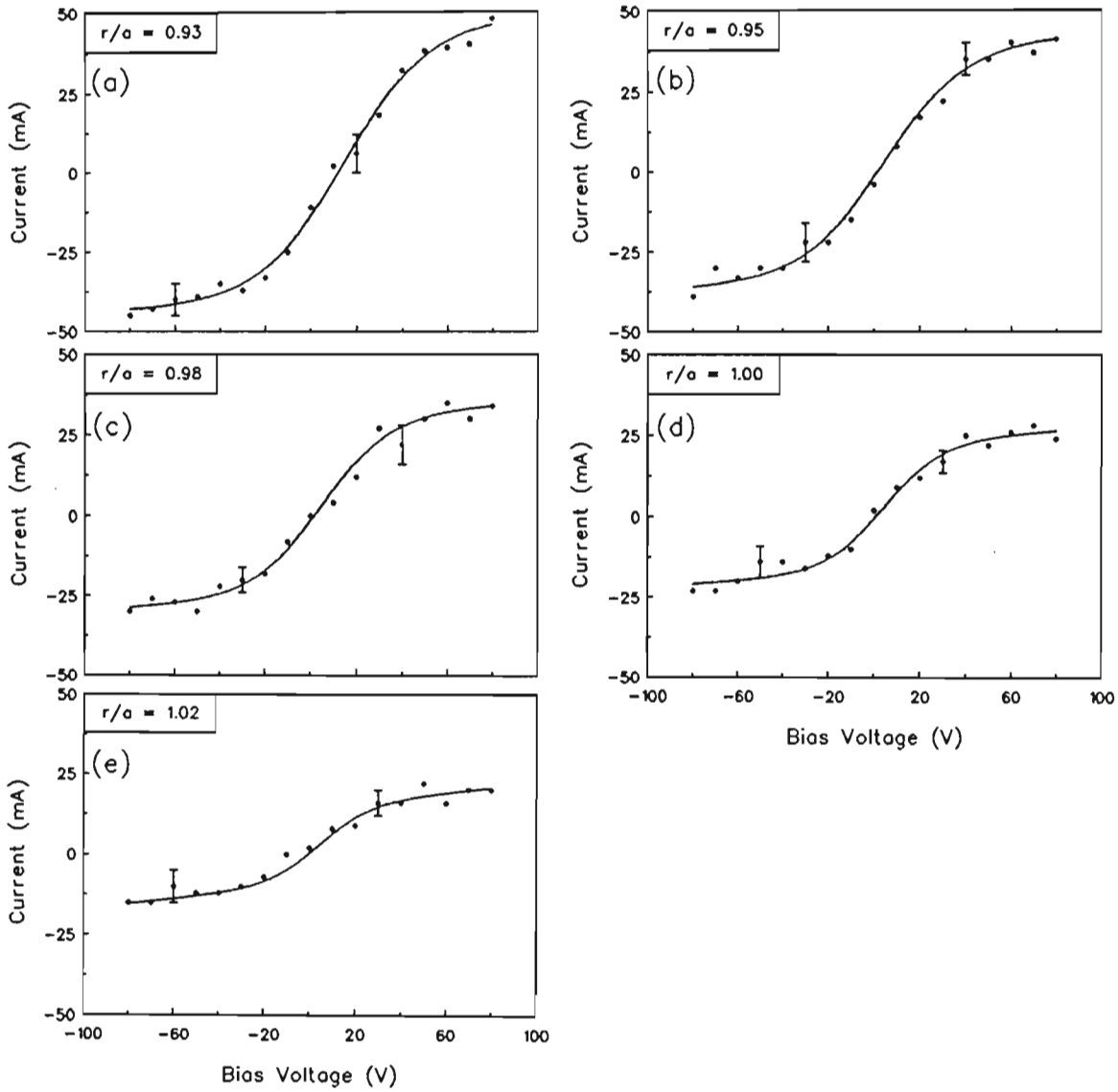

Figure 4.26: Double probe i vs V_{bias} voltage characteristics for five radial positions, taken during 5 ms of high Mirnov activity. Error bars here indicate both the shot-to-shot scatter as well as $\langle i \rangle$, i.e., variation of $\bar{i}$ over five 1000 μs blocks.

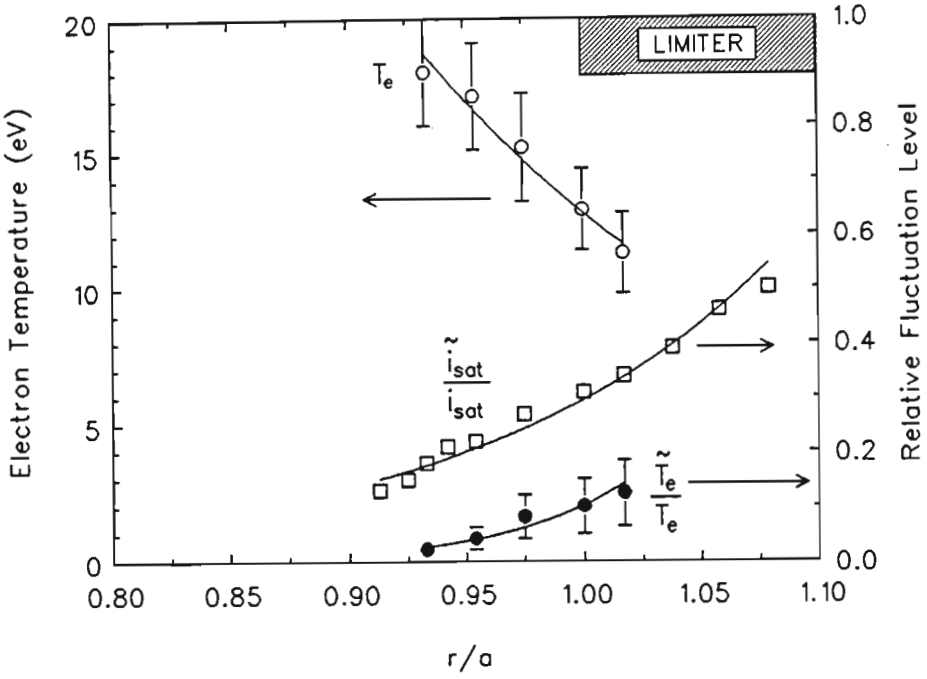

Figure 4.27: Radial profiles of T_e, $\tilde{T}_e/T_e$ and $\tilde{i}_{sat}/i_{sat}$ during high Mirnov activity.

1.0×10^{-3}) for each curve. The ion saturated current decreases from positions in the bulk plasma to those in the limiter shadow from 42 mA at $\rho = 0.93$ to 12 mA at $\rho = 1.02$. Both V_{offset} and i_{offset} were small ($< 20\%$) relative to the electron temperature (in eV) and saturated ion current respectively, at each radius.

The values of V_{offset} and T_e, returned by the ASYST program (Chapter 3), are now used in the second curve-fitting program to calculate the fluctuation coefficients discussed in Section 3.4.

Electron Temperature Fluctuations

The results of the fluctuation data analysis are shown in Figures 4.28(a) through (e) for five radial positions, viz., $\rho = 0.93, 0.95, 0.98, 1.00$ and 1.02 averaged over the frequency range $0 < f < 500\,\text{kHz}$. Thick solid lines represent the best fit through the data values comprising contributions from $\tilde{n}_e/n_e$, $\tilde{\phi}_p/T_e$ and $\tilde{T}_e/T_e$ in (i) and the cross-correlation terms viz., $\langle \tilde{n}_e \tilde{T}_e \rangle / n_e T_e$, $\langle \tilde{n}_e \tilde{\phi}_p \rangle / n_e T_e$ and $\langle \tilde{\phi}_p \tilde{T}_e \rangle / T_e^2$ in (ii). Because many terms contribute to the best fit curve of the data, even a slight change in data values could, in principle, give rise to potentially large variations in the returned parameters. In order to investigate this, the standard deviation, σ, of the existing errors was found (i.e. $\sigma = \sqrt{[y(x_i)^2 - \mathcal{F}(x_i, a)^2]\,/N}$). A new set of data were generated by assuming that the old data values exhibited a range of errors ($< 2\sigma$). Also, assuming these errors obey

a Guassian-type distribution function $P(y) = \sqrt{\pi\sigma}\int_{-\infty}^{\infty}\exp(-y^2/\sigma^2)dy$ where $P(y)$ is the probability of the error having value y. Random numbers were chosen for $P(y)$ and the corresponding (random) value of y returned and added or subtracted from the old data. Using this new set of data, the ASYST program was used again and the returned parameters compared to those returned by the old set, giving an estimate of the errors involved in the calculation of these values (see Table 4.3).

All the returned parameters from Figures 4.28(a) through (e) were from data taken during high Mirnov activity. Comparison with the low Mirnov activity phase data ($t \gtrsim 15 \rightarrow 30$ ms) showed that again, all returned parameters agreed within 15% (which was usually less than the error bars) with the high Mirnov data (taken between $t \gtrsim 7 \rightarrow 15$ ms). Significantly, $\tilde{T}_e/T_e$ for the two cases agreed within about 10%.

Electron temperature fluctuations increase from $\tilde{T}_e/T_e = 0.023$ at $\rho = 0.93$ to 0.125 at $\rho = 1.02$ as shown in Figure 4.27. The estimated errors associated with $\tilde{T}_e/T_e$ are large and approach 50% for these data. Clearly, this parameter is very sensitive to even very small variations in the data. Comparison of fluctuation levels at these radii gives a range of $\tilde{T}_e/T_e \approx 0.2 \pm 0.1\tilde{n}_e/n_e$ with the fraction increasing from bulk plasma to limiter shadow. This suggests that neglecting the fluctuations in electron temperature in the calculation of $\tilde{\Gamma}$ is not a bad assumption, at least for the reference plasmas (see also next Subsection). The value of χ^2 decreases from bulk plasma towards the wall by as much as $\approx 10\times$ over 2 cm.

The double probe results contain no *direct* spectral information of any of the fluctuating quantities so it is impossible to estimate the overall effect on $\tilde{\Gamma}$ or in what frequency range these fluctuations exhibit peak power. However, an estimate can be obtained from the auto-power spectra of $\tilde{i}$. An approximation is made by determining the fraction of the total power in any specified spectral band. The errors involved in this method are potentially large but this is compensated for in some way by taking sufficiently large frequency ranges (i.e. minimum $\approx$ 50 kHz). The three ranges investigated here were: $0 \rightarrow 500$ kHz, $0 \rightarrow 100$ kHz and $25 \rightarrow 75$ kHz. Results from the first case appear in Figure 4.28. Between 85 and 95% of the power was observed in the frequency range $0 \rightarrow 100$ kHz and about $65 \rightarrow 85$% of the power in the $\tilde{n}_e/n_e$ and $\tilde{\phi}_p/T_e$ spectra were observed in the $25 \rightarrow 75$ kHz range. By contrast, only between 20 and 30% of the spectral power was observed in this range for $\tilde{T}_e/T_e$ and the cross-correlation term, $\langle\tilde{\phi}_p\tilde{T}_e\rangle/T_e^2$, indicating that these fluctuations exhibit the bulk of their power at low frequencies, below 25 kHz.

TSUI *et al*, (1992c), using the extended triple probe technique, which measures the power

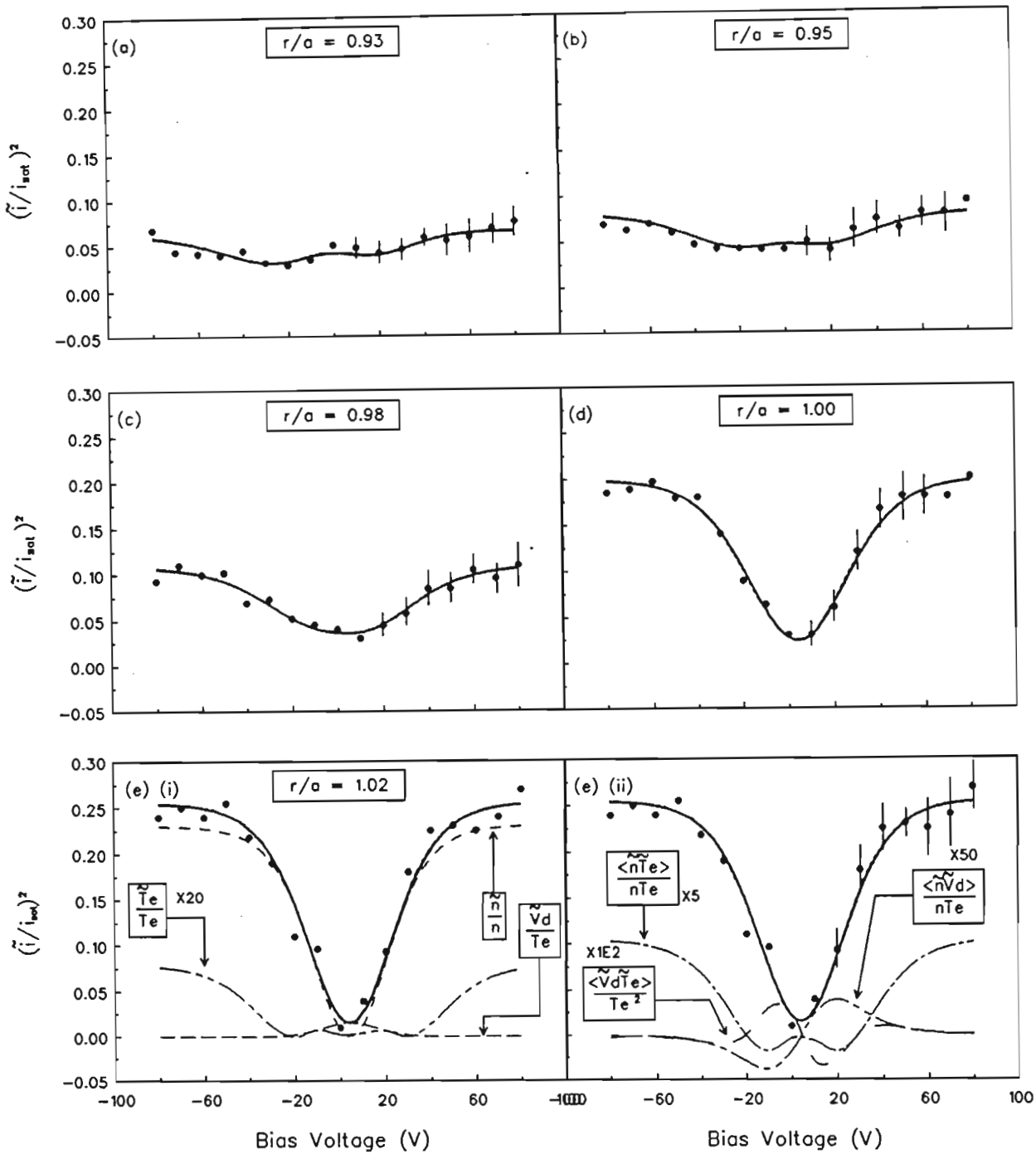

Figure 4.28: (a) — (e) $(\tilde{i}/i_{\rm sat})^2$ vs. $V_{\rm bias}$ at 5 radial positions during high MHD. (e)(i) shows contributions from $\tilde{n}_e/n_e$, $\tilde{V}_d/T_e$ and $\tilde{T}_e/T_e$ and (e)(ii) the cross-correlation terms: $\langle\tilde{n}_e\tilde{T}_e\rangle/n_eT_e$, $\langle\tilde{n}_e\tilde{V}_d\rangle/n_eT_e$ and $\langle\tilde{V}_d\tilde{T}_e\rangle/T_e^2$. Note that scaling factors for various quantities are only to illustrate the shapes of the curves.

spectrum of $\tilde{T}_e$ directly, found that the power spectra of $\tilde{T}_e$, $\tilde{\phi}_f$ and $\tilde{i}_{\rm sat}$ were very similar, suggesting a single driving source for the turbulent fluctuations.

Other Fluctuating Quantities

The results show that the level of density fluctuations rises monotonically from $\tilde{n}_e/n_e = 0.25$ at $\rho = 0.93$ to about 0.49 at $\rho = 1.02$ (see Table 4.3). With an estimated uncertainty of only 10%, $\tilde{n}_e/n_e$ is certainly increasing from the bulk plasma into the limiter shadow region. Comparison of these results with Figure 4.8, obtained using single probe measurements, shows fair agreement (with the assumption that $\tilde{n}_e/n_e \approx \tilde{i}_{\rm sat}/i_{\rm sat}$), both in absolute values and trend, and well within all estimated errors and uncertainty in measurements. From $i_{\rm sat} = \alpha n_e \sqrt{T_e}$, it can be shown that

$$\frac{\tilde{n}_e}{n_e} = \left\{ \frac{\tilde{i}_{\rm sat}}{i_{\rm sat}} - \frac{1}{4}\left(\frac{\tilde{T}_e}{T_e}\right)^2 - \frac{1}{2}\frac{\langle \tilde{n}_e \tilde{T}_e \rangle}{n_e T_e} \right\}^{\frac{1}{2}} . \tag{4.2}$$

Using values of these quantities obtained from *Tokoloshe* reference plasmas the error in using $\tilde{i}_{\rm sat}/i_{\rm sat}$ instead of $\tilde{n}_e/n_e$ is between 4 and 10%.

The cross-correlation term, $\langle \tilde{n}_e \tilde{T}_e \rangle / n_e T_e$, is very small (i.e between 0.2% and 2%) at all five positions with an estimated error of $\approx 30\%$. This value increases from plasma interior towards the wall but the values are not large enough to ascertain this for certain.

The asymmetric cross-correlation term, $\langle \tilde{V}_d \tilde{T}_e \rangle / T_e^2$, is small ($\lesssim 0.05$) and has a large associated error of about 50%. Within the error bars, this value is decreasing over the radial range under investigation from plasma interior towards the wall. The particle transport term, $\langle \tilde{n}_e \tilde{V}_d \rangle / n_e T_e$, exhibits an error of $\approx 40\%$ and the value of this term decreases within its error bars for increasing ρ for all radial positions from a value of ≈ 0.04 to 0.002. At these positions using Figure 4.4 and 4.27 the density and temperature may be substituted into Equation 3.23 (with $B_\phi = 0.6\,\mathrm{T}$ and $d = 0.004\,\mathrm{m}$). The value of $\tilde{\Gamma}$ calculated in this way is found, in each case, to be in very good agreement with the values obtained under the same conditions but using the spectral analysis technique (Figure 4.24).

The normalised coherence of the correlation terms discussed above is defined as $\gamma^2_{\tilde{x}\tilde{y}} = \langle \tilde{x}\tilde{y} \rangle / (\tilde{x}\tilde{y})$ with an upper limit of 1 but having no sign information. The usual definition of correlation involves complex quantities but these values are real so no direct phase angle measurements between fluctuating quantities is available. However, this is a convenient form for understanding these terms and it may be important in theoretical models of

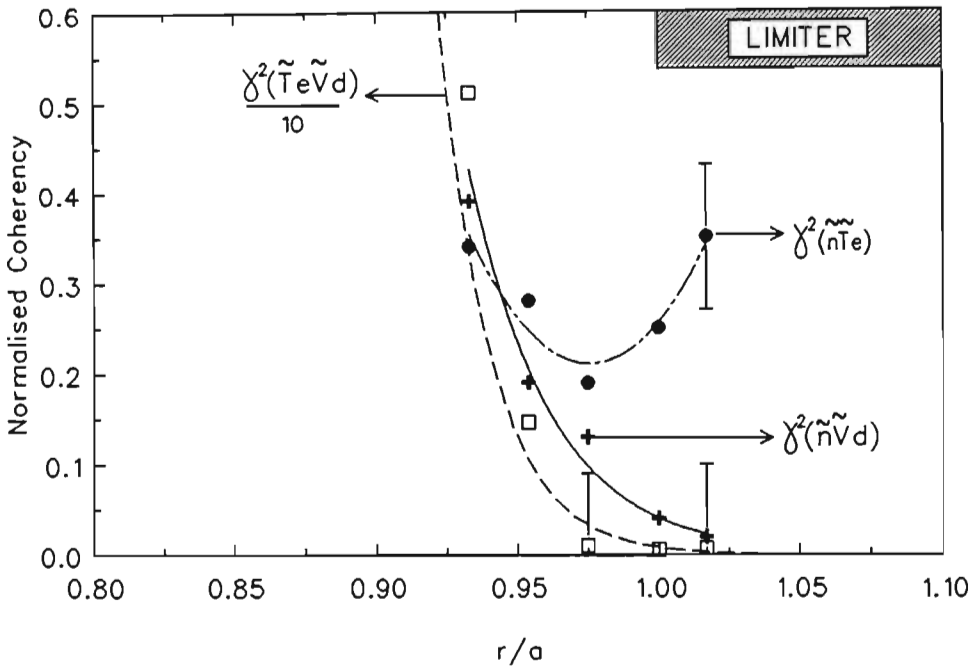

Figure 4.29: Radial profiles of the normalised coherency between the fluctuating quantities: $\langle \tilde{n}_e \tilde{T}_e \rangle / (\tilde{n}_e \tilde{T}_e)$, $\langle \tilde{n}_e \tilde{V}_d \rangle / (\tilde{n}_e \tilde{T}_e)$ and $\langle \tilde{T}_e \tilde{V}_d \rangle / (\tilde{T}_e \tilde{V}_d)$.

plasma microturbulence. Figure 4.29 shows the normalised coherence of $\langle \tilde{n}_e \tilde{T}_e \rangle$, $\langle \tilde{T}_e \tilde{V}_d \rangle$ and $\langle \tilde{n}_e \tilde{V}_d \rangle$ as functions of the radial position. The values of $\gamma^2_{\tilde{n}_e \tilde{V}_d}$ are fairly low and decreasing from ≈ 0.4 at $\rho = 0.93$ to 0.02 at $\rho = 1.02$. The normalised coherence, $\gamma^2_{\tilde{n}_e \tilde{T}_e}$, is also relatively low and constant within the error bars at $\approx 0.25 \pm 0.1$. The normalised coherence of $\langle \tilde{T}_e \tilde{V}_d \rangle$, $\gamma^2_{\tilde{T}_e \tilde{V}_d}$, is *very* high in the plasma interior and above 1.0 for $\rho < 0.95$. In Figure 4.29 this quantity has been divided by 10.0 to show the trend from bulk plasma towards the wall.

The excessive levels of coherence call the basis of this analysis into question, at least for the smaller terms (e.g. $\langle \tilde{T}_e \tilde{V}_d \rangle / \tilde{T}_e \tilde{V}_d$ which are small compared with, say, $\langle \tilde{T}_e \tilde{n}_e \rangle / \tilde{T}_e \tilde{n}_e$), but the theory may still hold for the more significant terms. Without more complete data (e.g. a full radial scan which would allow a more thorough investigation of the uncertainties involved as well as an intensive study of other possible errors and reliability of estimates) the results should be considered preliminary until this effect has been adequately explained.

Energy Fluxes

The energy fluxes given by Equations 3.21 and 3.22 may be calculated using the normalised correlation parameters $\langle \tilde{n}_e \tilde{E}_\theta \rangle$ and $\langle \tilde{T}_e \tilde{E}_\theta \rangle$. Using these Equations (i.e. 3.21 and 3.22), the ratio of $q^{\tilde{E}}_{\rm conv}$ to $q^{\tilde{E}}_{\rm cond}$ may be written

$$\frac{q^{\tilde{E}}_{\rm conv}}{q^{\tilde{E}}_{\rm cond}} = \left[\frac{\frac{5}{2}\langle \tilde{n}_e \tilde{V}_d \rangle / n_e T_e}{\frac{3}{2}\langle \tilde{T}_e \tilde{V}_d \rangle / T_e^2 - \langle \tilde{n}_e \tilde{V}_d \rangle / n_e T_e} \right]. \tag{4.3}$$

With the large error bars involved in the estimation of $\langle \tilde{T}_e \tilde{V}_d \rangle / T_e^2$ it is possible, at least mathematically, that $\langle \tilde{T}_e \tilde{V}_d \rangle / T_e^2 = 0$. A nonzero correlation of (e.g.) $\langle \tilde{T}_e \tilde{V}_d \rangle$, however, is related to the asymmetry of the i vs $V_{\rm bias}$ curves in Figure 4.28—physically equivalent to the assumption that the plasma is homogenous. If this were the case, all parameters which depend on $\tilde{E}_\theta$ (and hence $\tilde{V}_d$) must be ignored. LIN (1991) attempted a curve-fit to the data obtained on TEXT with the above assumption and found that the curve-fit was significantly worse than id $\langle \tilde{T}_e \tilde{V}_d \rangle / T_e^2 \rangle \neq 0$. This is also partly because the model (Equation 3.15) then *demands* symmetry about $V_{\rm bias} = 0$; an effect that is not observed. LIN (1991) argued that, since these odd terms ($\langle \tilde{T}_e \tilde{V}_d \rangle / T_e^2$ and $\langle \tilde{n}_e \tilde{V}_d \rangle / n_e T_e$) were related to the fluctuation induced particle and energy transport terms, they could not be 0 in the edge of a tokamak plasma.

Figure 4.30 shows that both the conducted and convected fluctuation induced energy fluxes are decreasing from the plasma interior outwards towards the wall with the convected flux larger than the conducted component at each radial position. At $\rho = 0.93$ the ratio of $q^{\tilde{E}}_{\rm conv}/q^{\tilde{E}}_{\rm cond}$ is about 3 and it increases monotonically to ≈ 50 at $\rho = 1.02$, indicating that $q^{\tilde{E}}_{\rm cond}$ is decreasing towards the wall at a faster rate than $q^{\tilde{E}}_{\rm conv}$. Power balance shows that the power lost by convection and conduction contribute a total of about 10% of the total power loss. The problem of establishing whether or not fluctuation related energy transport can account for the edge heat losses is even more difficult than establishing this for particle transport.

The electron thermal diffusivity coefficient, χ_e, may be calculated using ∇T_e and other parameters from *Tokoloshe*. The total electron heat flux at the limiter radius, $Q_e(a)$, may be written

$$Q_e(a) = n_e(a)\chi_e(a)\nabla T_e + \frac{3}{2} T_e(a)\tilde{\Gamma}(a). \tag{4.4}$$

Substituting measured values from *Tokoloshe*, i.e., $Q_e(a)(= q^{\tilde{E}}_{\rm cond} + q^{\tilde{E}}_{\rm conv}), = 210\,{\rm Jm^{-2}s^{-1}}$ (Figure 4.30), $T_e(a) = 12.9\,{\rm eV}$ (Figure 4.26), $\nabla T_e(a) = 370\,{\rm eV\,m^{-1}}$ (Figure 4.26), $n_e(a) = 0.93 \times 10^{18}\,{\rm m^{-3}}$ (Figure 4.4) and $\tilde{\Gamma}(a) = 0.4 \times 10^{20}$ (Figure 4.24), $\chi_e(a)$ is found to be $\simeq 1.0 \pm 0.4\,{\rm m^2 s^{-1}}$. This value is roughly 2 orders of magnitude higher than the neoclassical

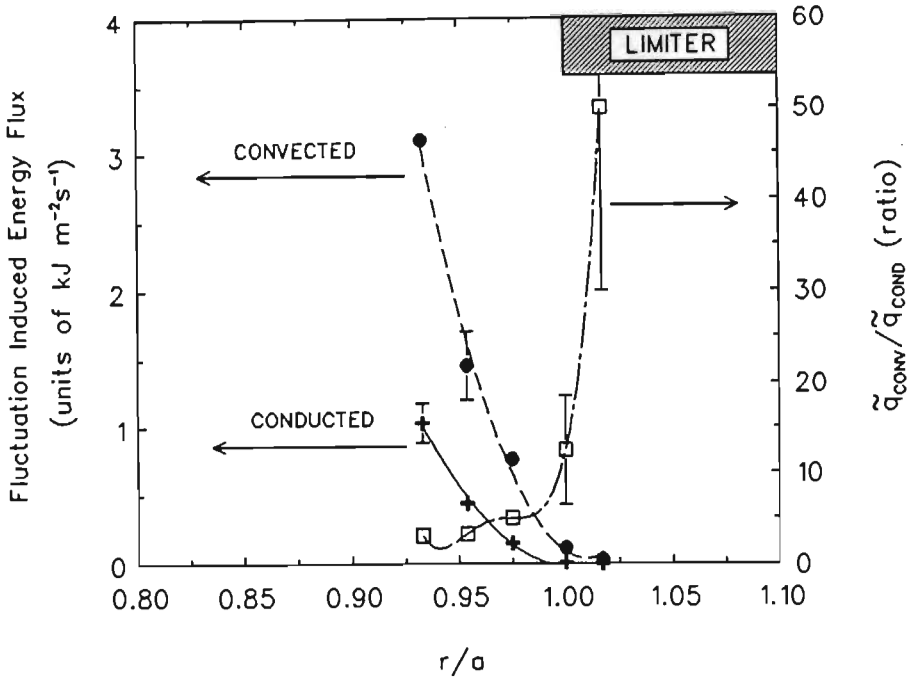

Figure 4.30: Radial profiles of the fluctuation induced energy flux (convected and conducted) and the quotient of these quantities, $q^{\tilde{E}}_{\rm conv}/q^{\tilde{E}}_{\rm cond}$.

prediction of ≈ 0.01 m^{2}s^{-1} but of much the same size as found on other machines.

HOWLING (1986) found that thermal transport cannot alone account for heat loss from the plasma core even if the anomalously large convection and conduction coefficients in the measured edge gradients are taken into account. This is because of the low thermal conductance and diffuse nature of the edge plasma in comparison with the central plasma region: the central plasma thermal energy cannot be sufficiently rapidly transported to the edge. A possible explanation was that radiative loss was responsible for the low energy confinement time measured, since this loss mechanism does not rely on transport in the boundary plasma medium. Electron energy may be lost by bremsstrahlung radiation and excitation (plus ionization) of impurities from the walls. Ionization of hydrogen (as the working gas in *Tokoloshe*) is another source of electron energy depletion. The outward convective particle flux (which recombines at the wall) must be balanced by neutral hydrogen ionization from gas-puffing or recycling. MCCRACKEN *et al*, (1979) showed that in the low temperature regions of the edge plasma, dissociation by electron impact and ionization processes dominate over ion charge exchange interactions. These processes have a strong cooling effect on the boundary plasma electrons and can effectively triple the heat loss derived from convection alone. These considerations of radiative losses and atomic processes show that the outward convection of heat via fluctuations through the edge plasma need only account for a fraction of the total heat loss from the plasma core

Table 4.3: Parameters deduced for double probe measurements.

	ρ					ERROR
QUANTITY	**0.93**	**0.95**	**0.97**	**1.00**	**1.02**	±(%)
i_{sat} (mA)	42	35	28	20	12	5
T_e (eV)	18.0	17.1	15.2	12.9	11.3	20
$\tilde{n}_e/n_e$	0.25	0.28	0.32	0.43	0.49	10
$\tilde{V}_d/T_e$	0.41	0.43	0.38	0.31	0.24	25
$\tilde{T}_e/T_e$	0.023	0.043	0.082	0.101	0.125	50
$\langle\tilde{n}_e\tilde{V}_d\rangle/n_eT_e$	0.040	0.023	0.016	0.005	0.002	40
$\langle\tilde{T}_e\tilde{V}_d\rangle/T_e^2$	0.048	0.027	0.016	0.004	0.0014	50
$\langle\tilde{n}_e\tilde{T}_e\rangle/n_eT_e$	0.002	0.003	0.005	0.012	0.021	30
$\chi^2(\times10^{-4})$	78	31	11	9.2	8.5	
$\tilde{E}_\theta/T_e$ (cm^{-1})	1.03	1.08	0.95	0.78	0.60	50
$\langle\tilde{n}_e\tilde{E}_\theta\rangle/n_eT_e$ (cm^{-1})	0.10	0.06	0.04	0.01	~0.00	40
$\langle\tilde{T}_e\tilde{E}_\theta\rangle/T_e^2$ (cm^{-1})	0.12	0.07	0.04	0.01	~0.00	50

to the wall. Any discrepancies that may remain between estimated and measured values of τ_E could be resolved by assuming toroidal and poloidal asymmetries in the fluxes.

WOOTTON (1988) reported that more than half of the experimental heat flux could be accounted for by the fluctuation-driven energy convection and the fluctuation-driven conduction flux could account for up to 20%. In view of the experimental uncertainties and possible asymmetries involved, the edge energy flux could be all fluctuation-driven. However, at lower densities, the fluctuation-driven heat transport is significantly smaller than that measured, leading to the conclusion that the measured fluctuations could fully explain edge *particle* transport, but not the heat transport. Also, STANGEBY *et al*, (1990) reported that ion heat conduction may be more important than originally assumed. Measured energy flux may not, therefore, be simply related to $q_{\text{conv, cond}}$ even if radiation, etc., is ignored. Finally, much more information as regards fluctuation measurements is required for energy transport than particle transport (e.g. more cross correlation terms etc.)

Fluctuating quantities and cross correlation terms, returned by the ASYST program, are shown as a summary in Table 4.3.

Particle and Energy Confinement

It is interesting to know how large the fluctuation induced particle and energy loss terms are compared with the total particle and energy loss terms. The power losses due to electrostatic fluctuation driven energy fluxes may be determined using the power balance equation,

$$\begin{aligned} \int_V \frac{dW}{dt} dV &= P_{\text{in}} - P_{\text{out}} \\ &= P_{\text{in}} - (\tilde{P} + P_{\text{other}}). \end{aligned} \tag{4.5}$$

Here, W is the thermal energy given by $\frac{3}{2}(n_e T_e + n_i T_i)$ and $T_i \simeq 0.3 T_e$, $n_i \approx n_e$ and $T_{\text{impurities}} \ll T_e$. P_{in} is the total power input ($= V_{\text{loop}} \times I_p$) and P_{out} the total power output. This quantity may be written as $P_{\text{out}} = \tilde{P} + P_{\text{other}}$ where $\tilde{P}$ is the power losses due to electrostatic fluctuation contributions and P_{other} the power losses from other mechanisms (e.g. radiation, charge exchange, etc.).

The electron density has a linear time dependence of the form $\alpha + \beta t$ where β is the rate of increase of n_e in the centre of the tokamak between $t = 10$ and 15 ms when the measurements were taken. The value of β deduced from interferometer studies (FLETCHER (1992)) is $\beta \approx 1.3 \times 10^{21}\,\text{m}^{-3}\text{s}^{-1}$. A parabolic radial profile of the form $n_e(t)(1 - r^2/a^2)$ is assumed. The electron temperature has a squared parabolic radial profile of the form $T_{e0}(1 - r^2/a^2)^2$ and it is assumed that $T_e \neq T_e(t)$. Using these values, the left hand side of Equation 4.5 above becomes

$$\int_V \frac{d}{dt}\left(\frac{3 n_e T_e}{2}\right) dV = 3\pi R_o \int_r \frac{d}{dt}(\alpha + \beta t)\left(1 - \frac{r^2}{a^2}\right) T_{e0}\left(1 - \frac{r^2}{a^2}\right)^2 2\pi r dr. \tag{4.6}$$

Integration yields $\int_V (dW/dt)\, dV \approx 20\,\text{kW}$.

The total input power, P_{in}, is $\approx 240\,\text{kW}$ using peak plasma current of $I_p \simeq 120\,\text{kA}$ and loop voltage of about 2 V (resistivity terms, inductance and the change of plasma resistance with temperature are neglected). The fluctuation-induced component of the total energy losses at the edge is determined using the values of $q^{\tilde{E}}_{\text{conv}}$ and $q^{\tilde{E}}_{\text{cond}}$. Assuming these energy fluxes are poloidally and toroidally symmetric, $\tilde{P} = (q^{\tilde{E}}_{\text{conv}} + q^{\tilde{E}}_{\text{cond}}) \times A|_{\rho=0.93}$, where $A|\rho = 0.93$ is the area of the toroidal surface at $\rho = 0.93$. This value is found to be about 20 kW and thus, $P_{\text{other}} \simeq 200\,\text{kW}$. $\tilde{P}$, therefore, contributes only 10% of the total power loss at the edge (75% of this value being a *convective* power loss) at $\rho = 0.93$. Closer in towards the limiter and into the shadow these values fall off rapidly and are negligible for $\rho > 0.98$.

The particle confinement time could not be measured directly as the required spectroscopic equipment was not available. However, τ_p at the limiter radius may be *estimated*

by first determining the contribution to the total particle flux by the fluctuation-induced particle flux. This may be calculated using the particle balance equation,

$$\frac{dn_e}{dt} = S - L, \tag{4.7}$$

where S is the particle source term and L represents particle losses, all terms being functions of both time and minor radius. The source term is assumed to have an exponential radial profile, decaying from a maximum at the edge region—where the temperature is relatively low and many particles are not ionized—to zero at the center of the tokamak where T_e is high and all particles are assumed to be fully ionized. The particle losses from the confinement region, L, may be written as $\nabla\cdot(\Gamma_{\text{total}})$. This quantity represents the total particle losses comprising $\tilde{\Gamma}$, the fluctuation induced particle flux, and Γ_{other}, the flux due to other mechanisms. The electron density has a time dependence of the form $\alpha+\beta t$ with $\beta \approx 1.3\times10^{21}\,\text{m}^{-3}\text{s}^{-1}$ and a parabolic radial profile of the form $n_e(t)(1-r^2/a^2)$, discussed earlier. Integrating Equation 4.7 over the entire plasma volume gives

$$\begin{aligned}
\int_V \left(\frac{dn_e}{dt}\right) dV &= \int_V S\,dV - \int_V \nabla\cdot(\tilde{\Gamma}+\Gamma_{\text{other}})\,dV,\\
\text{i.e. } 4\pi^2 R_0 \int_r \frac{d}{dt}[\alpha+\beta t]\left(1-\frac{r^2}{a^2}\right) r\,dr &= \int_V S\,dV - \int_A (\tilde{\Gamma}+\Gamma_{\text{other}})\,dA,\\
\text{or } \pi^2 R_0\, a^2\,\beta &= \int_V S\,dV - (\tilde{\Gamma}+\Gamma_{\text{other}})A|_{\text{limiter}}.
\end{aligned}$$

The volume integrated source term has been independently estimated by FLETCHER *et al*, (1992) from the gas puff and found to be $\approx 1.2\times10^{21}\text{s}^{-1}$. Using parameters obtained from *Tokoloshe* and the measured $\tilde{\Gamma}$ at the limiter ($\simeq 0.4\times10^{20}\text{m}^2\text{s}^{-1}$), $\Gamma_{\text{other}} \simeq 1.27\times10^{20}\text{m}^2\text{s}^{-1}$. $\tilde{\Gamma}$ therefore contributes roughly $25\pm15\%$ of the total particle flux at the limiter and is therefore a non-negligible component of these particle losses, as found on many tokamaks.

Having an estimate of Γ_{total}, the global particle confinement time, τ_p, may be calculated using

$$\tau_p = \frac{N_e}{\Gamma A}, \tag{4.8}$$

where N_e is the total number of electrons, A is $= 2\pi R_0 \times 2\pi r$ with r the radial position and Γ_{total} the total particle flux out of A. Using Γ_{total} above, τ_p is found to be $\approx 12\pm6$ ms.

The energy confinement time may be calculated from

$$\tau_E = \frac{W}{\frac{5}{2}T_e\,(\Gamma_{\text{total}})\,(A|_{\text{limiter}})}, \tag{4.9}$$

where $W = \int_V \frac{3}{2} n_e(r,t)T_e(r)dV$ is the total, volume integrated, thermal energy of the plasma discussed above, $A|_{\text{limiter}}$ is the area of the last closed flux surface (assuming

this is at the limiter radius) and T_e is the edge electron temperature, also measured in eV. Using the values obtained from *Tokoloshe* at the limiter, $\tau_E \simeq 140 \pm 35$ ms. This estimate is about 40 × larger than the value of 2.5 → 3.5 ms obtained by ROBERTS *et al*, (1991b). The latter value, however, refers to the *total* electron energy confinement time, τ_E, whilst the present estimate refers to energy lost only by fluctuation induced particle transport. The large difference, therefore, implies that radiation and other energy losses are very important. This is consistent with the fact that, at least at the higher densities, radiative collapse of the plasma column occurs, implying that $P_{\rm rad}/P_{\rm in} = 1$.

It is important to note that τ_E calculated here contains the inherent assumption that energy losses from the plasma occurs only via particles, i.e. radiation losses etc., are ignored. RITZ *et al*, (1987b) compared the power balance energy flux with fluctuation induced energy flux in the TEXT tokamak. Since only the electron component was examined in the estimation of the power balance at the edge, the discrepancy between these two values was found to be unacceptably large—except for the lowest densities—since both T_e and T_i are not known accurately enough. ROWAN *et al* (1987) and RITZ *et al*, (1989) examined the problem of fluctuation induced heat flux and particle flux respectively and compared these to the total losses of these quantities at the edge. Both were found to account for a major (if not all) of the total fluxes in the far edge (i.e. $\rho \sim 1$).

4.3 Discussion

4.3.1 Comparison With Other Tokamaks

MACROTOR

Plasma parameters: $R = 0.90$ m, $a = 0.45$ m, $B_\phi = 0.2 - 0.3$ T, $I_p = 60$ kA, $T_e(0) = 100$ eV, $T_e(a) = 30$ eV, $n_e(0) = 10^{12} - 10^{13}$ cm^{-3}.
ZWEBEN *et al*, (1979, 1981) measured broadband density fluctuations in the frequency range 10 — 100 kHz using Langmuir probes on Macrotor. The relative level of the density fluctuations was found to be large with $\tilde{n}_e/n_e \simeq 0.2 - 0.4$ at the wall and the density and potential fluctuations satisfied $\tilde{n}_e/n_e \sim \tilde{\phi}_p/T_e$ in magnitude. These results are similar to the values from *Tokoloshe* where $\tilde{n}_e/n_e$ was found to be between 0.1 and 0.5 (Figure 4.8) and $\tilde{n}_e/n_e \sim \tilde{\phi}_p/T_e$ in magnitude. ZWEBEN *et al*, (1983) found partial correlation between $\tilde{n}_e$ and $\tilde{\phi}_p$ but neither was correlated with the magnetic fluctuations,

later explained by WALTZ (1985). The energy confinement time was $\tau_E \simeq 1\,\mathrm{ms}$ for $n_e(0) \simeq 4 \times 10^{12}\,\mathrm{cm}^{-3}$.

CALTECH RESEARCH TOKAMAK

Plasma parameters: $R = 0.46\,\mathrm{m}$, $a = 0.15\,\mathrm{m}$, $B_\phi = 0.5\,\mathrm{T}$, $I_p = 30\,\mathrm{kA}$, $T_e(0) = 100$ — $200\,\mathrm{eV}$, $T_e(a) = 30\,\mathrm{eV}$, $n_e(0) = 10^{12} - 10^{13}\,\mathrm{cm}^{-3}$.
HEDEMANN *et al*, (1980), found broadband turbulence in the density and potential fluctuations with $\tilde{n}_e/n_e$ between 0.1 — 0.8 and maximum $\tilde{n}_e/n_e$ at the wall, slightly larger than the range of $\tilde{n}_e/n_e \simeq 0.1 - 0.5$ observed on *Tokoloshe*. A radial scan of density fluctuations gave a scaling $\tilde{n}_e/n_e \simeq (3-5)r_s/L_n$ whilst on *Tokoloshe* $\tilde{n}_e/n_e \simeq (1-2)\sqrt{r_s/L_n}$ (Figure 4.33) was found. The relative level of $\tilde{n}_e/n_e$ and spectra were also found to be independent of poloidal position, the presence of a limiter or whether the limiter was grounded or floating. This poloidal symmetry was not observed on *Tokoloshe* and will be addressed in the next Chapter. Triple probe measurements allowed simultaneous correlation between $\tilde{n}_e$ and $\tilde{\phi}_p$ to give a direct measurement of $\tilde{\Gamma}$. The lower frequency fluctuations (i.e. $0 \leq f \leq 200\,\mathrm{kHz}$) made the largest contribution to the fluctuation induced particle flux. Results from *Tokoloshe* show that the largest contribution to $\tilde{\Gamma}$ come from frequencies below 150 kHz (Figure 4.22). Radial profiles of n_e and T_e showed that both decreased linearly outwards, similar to results from *Tokoloshe* (Figure's 4.4 and 4.27, respectively).

Poloidal electric field fluctuation level (ZWEBEN *et al*, (1983)) was $\tilde{E}_\theta \simeq 10\,\mathrm{Vcm}^{-1}$, very similar to the value of $12\,\mathrm{Vcm}^{-1}$ measured on *Tokoloshe*. The maximum v_{phase} was measured as $\simeq 3 \times 10^3\,\mathrm{ms}^{-1}$ whilst on *Tokoloshe* maximum $v_{\mathrm{phase}} \simeq 4 \times 10^3\,\mathrm{ms}^{-1}$ measured just inside the limiter shadow. The particle flux was always outwards (c.f. Figure 4.24) with most of the flux due to fluctuations below $f \leq 200\,\mathrm{kHz}$. For these frequencies, $\alpha_{n\phi}$ was in the range 0° to 60° or 0 — $\pi/3$ and not $\pi/2$ as expected for weakly unstable linear drift waves. The range of phase angle on *Tokoloshe* was between $0.3 - 0.8\pi$. Measured $\tilde{\Gamma} \simeq 10^{20}\,\mathrm{m}^{-2}\mathrm{s}^{-1}$ at the limiter gave a particle confinement time comparable to the global energy confinement time, $\tau_E \simeq 1\,\mathrm{ms}$. This value is of the same order as that measured on *Tokoloshe* of about $1.5 \times 10^{20}\,\mathrm{m}^{-2}\mathrm{s}^{-1}$ at the limiter radius.

A 2D 8×8 Langmuir probe array (ZWEBEN *et al*, (1985)) indicated the presence of localised regions of increased density ('blobs') of spatial extent 0.5 — 2.0 cm, moving irregularly both radially and poloidally through the edge region. The lifetime of these 'blobs' was $\simeq 2\tau_c$ where τ_c is the poloidal correlation time of the turbulence (5 — 10 μs). Note, however, that the determination of this time is dependant on the relationship be-

tween the cross-correlation function, $R(t)$, and t. In this case $R(t)$ is assumed to decrease exponentially with t. The filaments of increased H_α observed on ASDEX (NIEDERMEYER *et al*, (1991)) have been suggested as the being the same phenomenon as these 'blobs'. FLETCHER (1991) observed similar filaments using framing camera studies on *Tokoloshe*. The wavenumber spectrum, $S(k_\theta)$, was found to peak in the region $k_\theta = 0.5 - 1.0\,\mathrm{cm}^{-1}$ giving an effective $\overline{k}_\theta r_s \simeq 0.10 - 0.15$. On *Tokoloshe* $S(k_\theta)$ peaks at $\approx 2 - 4\,\mathrm{cm}^{-1}$ giving $\overline{k}_\theta r_s \simeq 0.15 - 0.25$. LIEWER *et al*, (1986) measured the electron temperature fluctuations using a double probe and reported $\tilde{T}_e/T_e \leq 0.5\tilde{n}_e/n_e$. Maximum $\tilde{T}_e/T_e$ on *Tokoloshe* was about $0.25\tilde{n}_e/n_e$ measured at $\rho = 1.02$.

TFTR

Plasma parameters: $R = 2.4\,\mathrm{m}$, $a = 0.8\,\mathrm{m}$, $B_\phi = 5.0\,\mathrm{T}$, $I_p = 2.2\,\mathrm{MA}$, $T_e(0) \lesssim 1\,\mathrm{keV}$, $T_e(a) = 5 - 50\,\mathrm{eV}$, $n_e(0) = 2 \times 10^{13}\,\mathrm{cm}^{-3}$.
Fluctuations in the plasma density, plasma potential and magnetic field were measured by ZWEBEN *et al*, (1987) and found to be incoherent and strongest in the frequency range from 0 to 200 kHz. Power law dependence for these fluctuations was $P(f) \propto f^{-1.0\pm0.5}$ and the spatial scale range was 0.1 — 10 cm. Power law dependence of fluctuations on *Tokoloshe* are higher and between 1 and 3 (Figure 4.11). Typical fluctuation levels of $\tilde{n}_e/n_e = 0.3 - 0.5$ and $\tilde{\phi}_p/T_e \simeq 0.1$ measured by Langmuir probes. Floating potential fluctuation levels on *Tokoloshe* are much higher and between 0.4 and 0.6 in the bulk plasma (Figure 4.8). Short poloidal wavelengths of $\tilde{n}_e$ and $\tilde{B}_\theta$ were found, in the range corresponding to $m-$numbers $\gtrsim 15$, i.e. small scale compared with machine dimensions. The range of $m-$ numbers of *Tokoloshe* are between 20 and 40. Filaments such as those observed on ASDEX (RUDYJ *et al*, (1990)) and the Caltech Research Tokamak (ZWEBEN *et al*, (1985)) were also observed on TFTR ZWEBEN *et al*, (1987) and see FLETCHER *et al*, (1991).

PRETEXT

Plasma parameters: $R = 0.53\,\mathrm{m}$, $a = 0.14\,\mathrm{m}$, $B_\phi = 0.8\,\mathrm{T}$, $I_p = 40\,\mathrm{kA}$, $T_e(0) = 200\,\mathrm{eV}$, $T_e(a) = 18\,\mathrm{eV}$, $n_e(0) = 5 \times 10^{12}\,\mathrm{cm}^{-3}$, $Z_{\mathrm{eff}} \simeq 2.5 - 3$.
Broadband turbulence was found predominantly between 10 and 1000 kHz. Measured $S(k_\theta)$ gave a peak at $k_\theta \simeq 1\,\mathrm{cm}^{-1}$ giving $\overline{k}_\theta r_s \lesssim 0.05$, much less than the values on *Tokoloshe* of between 0.15 and 0.25. The fluctuation phase velocity was in the ion diamagnetic drift direction, apparently not caused by $E \times B$ rotation, in contrast to

the results from *Tokoloshe* where $E \times B$ rotation is required to explain the observed change in direction of the poloidal phase velocity on either side of the limiter. The array of four Langmuir probes allowed simultaneous measurement of $\tilde{n}_e$ and $\tilde{\phi}_p$ and hence, direct measurement of $\tilde{\Gamma}$. The particle flux was large and dominated by low frequency fluctuations ($0 \leq f \leq 50\,\mathrm{kHz}$). In magnitude, $\tilde{\Gamma}$ was $\simeq 2 \times 10^{19}\,\mathrm{m^{-2}s^{-1}}$, slightly smaller than the value on *Tokoloshe* of $\simeq 1.5 \times 10^{20}\,\mathrm{m^{-2}s^{-1}}$ at the limiter. The measured value of $\tilde{\Gamma}$ on PRETEXT gave $\tau_p (\simeq \tau_E)$ comparable to estimates of this quantity using spectroscopic techniques. LEVINSON *et al*, (1984) found $\tilde{n}_e/n_e \sim \tilde{\phi}_p/T_e \simeq 0.3 - 0.8$, but the scaling for the two quantities was opposite as a function of radius (c.f. Figure 4.8). This deviation suggested that a non-adiabatic response may play a significant role in edge turbulence.

TOSCA

Plasma parameters: $R = 0.53\,\mathrm{m}$, $a = 0.14\,\mathrm{m}$, $B_\phi = 0.8\,\mathrm{T}$, $I_p = 40\,\mathrm{kA}$, $T_e(0) = 200\,\mathrm{eV}$, $T_e(a) = 18\,\mathrm{eV}$, $n_e(0) = 5 \times 10^{12}\,\mathrm{cm^{-3}}$, $Z_{\mathrm{eff}} \simeq 2.5 - 3$.
HOWLING (1986) reported broadband fluctuations for both $\tilde{n}_e$ and $\tilde{\phi}_p$ with power law $P(f) \propto f^{-2.0}$. Using Langmuir probes, high coherency ($0.9 - 0.7$) for $f \leq 200\,\mathrm{kHz}$ (c.f. Figure 4.12) and short ($\approx 5\,\mu\mathrm{s}$) correlation times were found between the fluctuating quantities at the limiter (c.f. Figure 4.10). Radial profiles of both the density and potential decreased exponentially towards the edge whilst those of $\tilde{n}_e/n_e$ and $\tilde{\phi}_p/T_e$ had opposite scaling, the former increasing and the latter decreasing monotonically outwards (c.f. Figure 4.8). VAYAKIS (1989) suggested that this departure could be due to temperature fluctuations. It can be shown from $n_e \simeq i_{\mathrm{sat}}\sqrt{m_i}/(Ae\sqrt{T_e})$ (where A is the probe area) that

$$\frac{\tilde{n}_e}{n_e} = \left\{ \left(\frac{\tilde{i}_{\mathrm{sat}}}{i_{\mathrm{sat}}}\right)^2 - \frac{1}{4}\left(\frac{\tilde{T}_e}{T_e}\right)^2 - \frac{1}{2}\frac{\langle \tilde{n}_e \tilde{T}_e \rangle}{n_e T_e} \right\}^{\frac{1}{2}} . \tag{4.10}$$

Both $\tilde{T}_e/T_e$ and $\langle \tilde{n}_e \tilde{T}_e \rangle/(n_e T_e)$ are small at all radii on *Tokoloshe* as are their coherency's so it can be safely concluded that these values are too small to account for this non-Boltzmann behavior in *Tokoloshe* reference discharges.

A large variation in the poloidal electric field ($\tilde{E}_\theta \simeq 10\,\mathrm{Vcm^{-1}}$) was also measured on TOSCA, similar to the value of $\simeq 12\,\mathrm{Vcm^{-1}}$ measured on *Tokoloshe*. The phase angle, $\alpha_{n\phi}$, was $-100°$ (c.f. Figure 5.15) and a high phase velocity of $\approx 3.5 \times 10^3\,\mathrm{ms^{-1}}$ in the electron diamagnetic drift direction was measured at the limiter. The sign of v_{phase} reversed behind the limiter, changing to the ion diamagnetic direction (c.f. Figure 4.16). The fluctuation induced particle flux was always directed outwards with the bulk of the flux coming from fluctuations below 200 kHz. Temperature fluctuations were also

measured and found $\tilde{T}_e/T_e \leq 5\%$ during low Mirnov activity using toroidally separated probes and neglecting transport terms. HOWLING (1986) found that, for transport during the high Mirnov phase of the discharge, the transport was large but *negative* at and below the Mirnov frequency. For higher frequencies the transport spectrum looked very similar to that observed during the low Mirnov activity phase. The sine of the phase angle between $\tilde{i}_{\rm sat}$ and $\tilde{\phi}_f$ was found to change sign (i.e. between $\alpha_{n\phi} \approx 3\pi/2$ and $\pi/2$) at and below the Mirnov frequency but resembled the phase spectrum of the low Mirnov case at higher frequencies. This sign change of the phase angle altered the transport at these low frequencies and high levels of electron temperature fluctuations were invoked to describe these observations.

Temperature fluctuations on *Tokoloshe* have been shown to be small during both high and low Mirnov activity phases with very little difference (if any, since both measurements are within mutual error bars) between them. The electron thermal diffusivity of TOSCA was also measured and found to be $\approx 2.0\,\mathrm{m^2 s^{-1}}$. Figure 4.31(a) shows that the phase angle on *Tokoloshe* during low Mirnov activity is negative and between $-\pi/3$ and $-\pi/2$ for frequencies between 0 and 100 kHz. At higher frequencies it is roughly $-\pi/3$ but the coherency is very low in this regime. During the high Mirnov phase, the sine of this angle changes sign (since the angle itself changes sign) and is about $+\pi/3$ below 50 kHz. Above 50 kHz it becomes negative and, for frequencies above 100 kHz it is very similar to the spectrum obtained during low Mirnov activity. This change of sign in phase angle alone should change the sign of the transport at these frequencies but Figure 4.31(b) shows that the sign of the poloidal wavenumber, k_θ, *also* changes sign over the frequency range where $\alpha_{n\phi}$ is positive. Whilst the k_θ values (between two probes separated poloidally and measuring k_θ for $\tilde{\phi}_f$) are negative at all frequencies in the low Mirnov phase, they are positive between 0 and 50 kHz and negative elsewhere in the high Mirnov case. Above 100 kHz the relations look very similar. The combination of the sign changes for both $\alpha_{n\phi}$ and k_θ between 0 and 50 kHz ensures that $\tilde{\Gamma}$ is positive (outwards) at all frequencies.

Edge fluctuations were identified as being responsible for anomalously large edge transport coefficients by HOWLING (1985), (1986) who found that neoclassical electron diffusion coefficients were about two orders of magnitude higher than the Bohm coefficient, the latter being deduced from particle balance considerations in the edge regions of the tokamak.

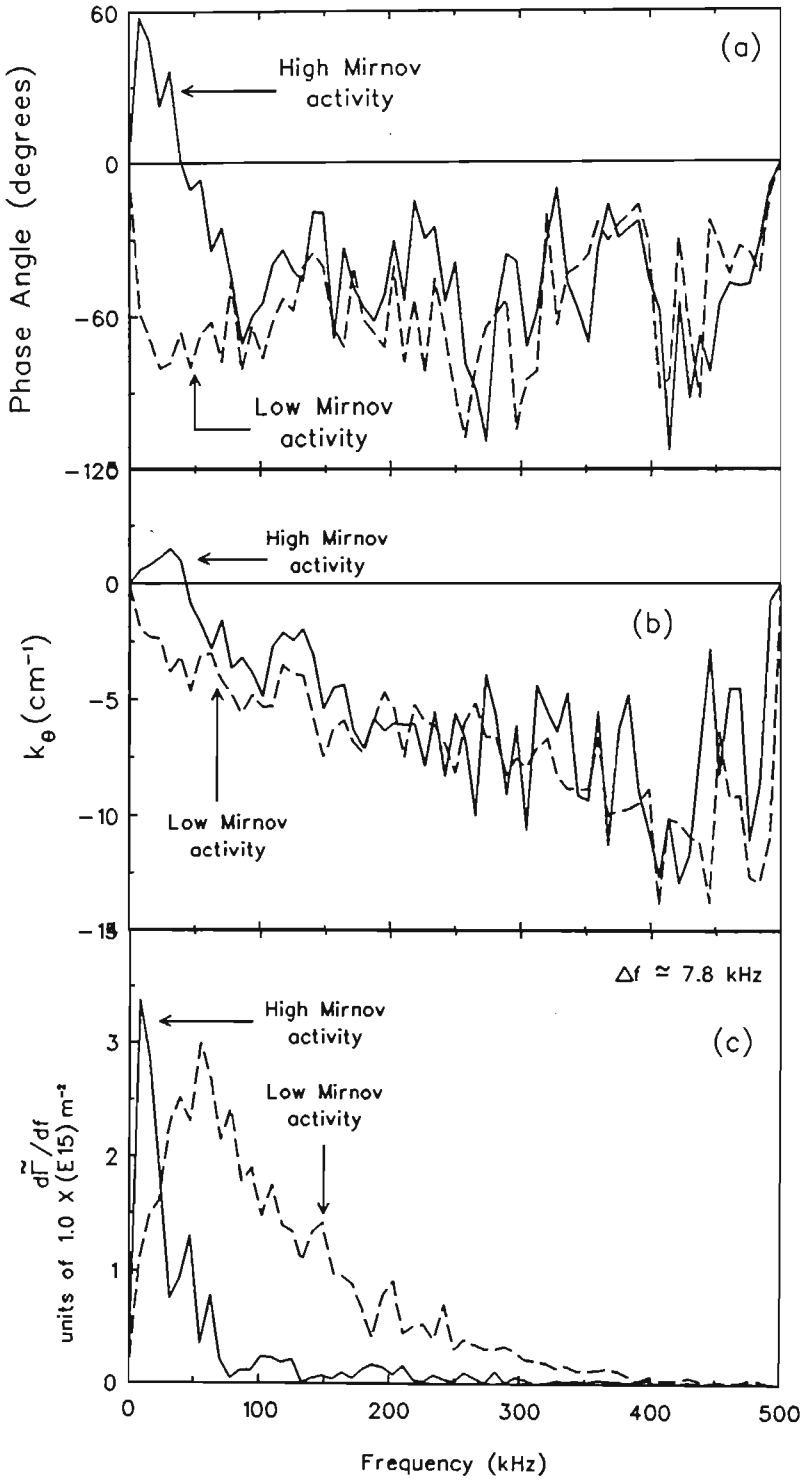

Figure 4.31: Comparison of spectra for (a) $\alpha_{n\phi}$, (b) k_θ between poloidally separated probes measuring $\tilde{\phi}_f$ and (c) $\tilde{\Gamma}$ taken at $\rho = 0.93$ during periods of both high and low Mirnov activity.

TEXT

Plasma parameters: $R = 1.00\,\mathrm{m}$, $a = 0.27\,\mathrm{m}$, $B_\phi = 2.8\,\mathrm{T}$, $I_p = 300\,\mathrm{kA}$, $T_e(0) = 950\,\mathrm{eV}$, $T_e(0) \simeq 20 - 30\,\mathrm{eV}$, $T_i(0) = 600\,\mathrm{eV}$, $n_e(0) = 3.5 \times 10^{13}\,\mathrm{cm}^{-3}$, $Z_{\mathrm{eff}} \simeq 2$.
Probe measurements of the edge turbulence in TEXT showed an increase in $\tilde{n}_e/n_e$ with radius from 0.1 — 0.5 (RITZ *et al*, (1984)). The $\tilde{\phi}_p/T_e$ showed a peaked profile (maximum at $\rho = 0.98$) and opposite scaling with radius to $\tilde{n}_e/n_e$ very similar to the results presented in Figure 4.8. The phase velocity of the fluctuations was in the electron diamagnetic drift direction at the leading edge of the limiter and in the ion diamagnetic drift direction behind the limiter, changing continuously with radial position, again, similar to the results obtained on *Tokoloshe*, shown in Figure 4.16. In the region of maximum velocity shear, the turbulence changed character, with $S(\omega, k_\theta)$ becoming broader and the k_θ spectra more isotropic. A velocity shear-driven instability was suggested. Measured spectra were broad with $\Delta k_\theta/k_\theta \simeq \Delta\omega/\omega \simeq 1.0$. The value of $\overline{k}_\theta r_s$ was $\approx 0.05 - 0.1$. WOOTTON (1989) found $\alpha_{n\phi}$ was found to be $0.2 — 0.5\pi$ in the limiter shadow. On *Tokoloshe* the range of $\alpha_{n\phi}$ is between $0.3 - 0.8\pi$.

The measured particle flux was found to be large and always positive with peak $\tilde{\Gamma}$ of $\simeq 6.0 \times 10^{20}\,\mathrm{m}^{-2}\mathrm{s}^{-1}$ at $\rho \simeq 0.96$. The $\tilde{\Gamma}(\rho)$ has been measured in many ohmically heated plasmas (WOOTTON *et al*, (1990a)). A simple model, used to obtain the total perpendicular component, $\Gamma_\perp$ of the parallel flow to the limiter, gives approximate agreement with the measured flux[3]. This demonstrates that the measured turbulent flux accounts for a significant part (if not all) of the total particle flux in the edge of TEXT. Similar conclusions have been drawn for Stellarators (WOOTTON (1990b)). FILIPPAS *et al*, (1991) found coherent structures in the TEXT edge plasma.

Energy fluxes were found to decrease from bulk plasma to limiter shadow with $q^{\tilde{E}}_{\mathrm{conv}} \simeq 1.0 \rightarrow 0.0\,\mathrm{Wcm}^{-2}$ and $q^{\tilde{E}}_{\mathrm{cond}} \simeq 0.2 \rightarrow 0.0\,\mathrm{Wcm}^{-2}$ at all radii. Electron temperature fluctuations were measured by LIN (1989) found $\tilde{T}_e/T_e = 0.4^{+0.2}_{-0.3}\tilde{n}_e/n_e$. These values were found to be independent of frequency range investigated, unlike the results from *Tokoloshe*. A scaling of temperature fluctuations with density fluctuations was found, suggesting the possibility of the same driving mechanism. (BENGTSON *et al*, (1990) measured ($\tilde{T}_e/T_e \sim \tilde{n}_e/n_e$) on ASDEX, and HIDALGO *et al*, (1990) on the ATF stellarator:

[3]The particle balance expression is given by

$$\Gamma_\parallel \simeq \frac{1}{2} n_e c_s d^2 = \Gamma_\perp,$$

where n_e is the electron density, d the probe separation and $c_s \approx \sqrt{k(T_e + T_i)/m_i}$ the ion acoustic velocity.

$0.5\tilde{n}_e/n_e \leq \tilde{T}_e/T_e \leq 2\tilde{n}_e/n_e$). The energy confinement time was measured as $\tau_E \simeq 12\,\text{ms}$. LEVINSON *et al*, (1984) found D_{eff} of the order of $10 \times D_{\text{Bohm}}$.

Summary

From the preceding discussion it is clear, in general, that the results from *Tokoloshe* are very similar to the results obtained on other machines operating with both similar and very different physical parameters. However, as WOOTTON (1989) reported, to every set of results from which a general conclusion can be drawn, there are exceptions, and the results from *Tokoloshe* are no different.

The basic operating parameters (n_e, T_e, ϕ_p, etc.) are similar to many machines although B_ϕ and the aspect ratio $R/a = 2.17$ of *Tokoloshe* are unusually low. Fluctuation levels of all relevant quantities are very similar to other results as well as other observations about these values e.g., non-Boltzmann behavior between $\tilde{n}_e/n_e$ and $\tilde{\phi}_p/T_e$. Values of (e.g.) $v_{\text{phase}}(\rho)$ the width of the shear layer, $k_\theta(\omega)$, $\tilde{\Gamma}(\omega)$, $\tilde{\Gamma}_{\text{max}}$ and so on, are all comparable to other results. Although some machines may exhibit behavior contrary to the results described here, in each case at least one other machine has produced results similar to those observed on *Tokoloshe*.

On the other hand, the simultaneous reversal of $k_\theta(\omega)$ and $\alpha_{n\phi}(\omega)$ (Figure 4.31) has not yet been reported and requires explanation. Also, the shift of the main peak in the $d\tilde{\Gamma}/df$ spectrum and the broadening of the width of this peak are both new results and are, as yet, unexplained. The modulation of ϕ_f and the (apparent) modulation of the fluctuation amplitudes of $\tilde{i}_{\text{sat}}(t)/i_{\text{sat}}$ and $\tilde{\phi}_f(t)/T_e$ by the Mirnov oscillation amplitude have also not been reported and the observed rapid decrease of $\tilde{\Gamma}$ from bulk plasma to limiter shadow region—whilst not a new result—is certainly rare.

4.3.2 Comparison with Theoretical Predictions

Comparison of results obtained from *Tokoloshe* with those predicted by the two main theoretical models, namely drift waves (collisional ∇n driven) and rippling modes ($\nabla\eta$ driven model), are summarized in Table 4.4.

Each of the ∇n models were examined and the salient, persistent predictions used in the Table. One of the problems for the ∇n models is the failure to predict the non-Boltzmann-like behavior, i.e., $\tilde{n}_e/n_e \neq \tilde{\phi}_p/T_e$, at the edge, although the $\tilde{n}_e/n_e$ fluctuations do scale in proportion to $\beta(r_s/L_n)^{\frac{1}{2}}$ as predicted by the HASEGAWA-WAKATINI

Table 4.4: Comparison between experimentally measured parameters of the edge plasma with theoretical predictions.

	OBSERVED TOKOLOSHE	**COLLISIONAL ∇n MODELS**	**$\nabla\eta$ MODELS**
$\tilde{n}_e/n_e$	$(0.1 \rightarrow 0.5)$	Saturates at 'mixing length' $\simeq 3r_s/L_n$ $\simeq 0.1 \rightarrow 0.2\%$	$\simeq 20\%$. Scales as $\sim n_e^{1/3}q/T_e^{5/6}B_\phi^{1/3}$
$\tilde{\phi}_p/T_e$	$0.4 \rightarrow 0.6 \rightarrow 0.1$ Non-Boltzmann	$\simeq \tilde{n}_e/n_e$ $(\simeq 1/(k_\theta L_n))$ from 2 pt renormalised collisional DWT	Non-Boltzmann & same magnitude as $\tilde{n}_e/n_e$
$\tilde{T}_e/T_e$	$(0.1 \rightarrow 0.3)\tilde{n}_e/n_e$	$\simeq 0$	$0.3\ (\tilde{n}_e/n_e)(L_n/L_{T_e})$ $(0.1 \rightarrow 0.3)\tilde{n}_e/n_e$
$\alpha_{n\phi}$	$\lvert\alpha_{n\phi}\rvert \sim 0.3 \rightarrow 0.8\pi$	$\simeq -\pi$	Large and > 0
$\overline{k}_\theta$	$(1 \rightarrow 2)\text{cm}^{-1}$	$(2 \rightarrow 3)\text{cm}^{-1}$	$\simeq \overline{m}/r \simeq 2\text{cm}^{-1}$
$\overline{m}-$range	$20 \rightarrow 40$	$40 \rightarrow 60$	≤ 20
$\Delta\omega/\omega$	≈ 0.5	Narrow: ≈ 0.1	
D $(\text{m}^2\text{s}^{-1})$	$1.5 \rightarrow 5$	≈ 1.0 $(\propto T_e^{1/6}n_e^{1/3})$	~ 81
$\tilde{\Gamma}$ $(\text{m}^{-2}\text{s}^{-1})$	Peak: $\approx 5 \times 10^{20}$	Order of Bohm diffusion, $D_{\text{Bohm}}\nabla n_e$ Peak: $\approx 4 \times 10^{19}$	5×10^{22}

(1983) model (see Figure 4.33). Some of the predictions by the ∇n models may be satisfied deeper into the plasma but no information on this region is available. It must be emphasised that this study does not rule out more complicated dependencies of $\tilde{n}_e/n_e$ or $\tilde{\phi}_f/T_e$ upon these gradients or upon other unmeasured parameters. The average poloidal wavenumber, $\overline{k}_\theta$, scaled approximately as th ion gyroradius, r_s, in agreement with several drift wave theories (WALTZ *et al*, (1983) and TERRY, *et al* (1985)) but with a magnitude 10 $\times$ smaller than predicted. No simple relationship between the gradients and the particle flux were found in this study. These theories support a simple relationship between the gradients and $\tilde{\Gamma}$ are thus not substantiated by the data presented here.

Whilst the $\nabla\eta$ model is more accurate in some of its predictions, it does fail to predict the high $\overline{m}$ values observed on some tokamaks (e.g. TEXT). Even though the $\overline{m}$ range observed on *Tokoloshe* and the predicted value of the $\nabla\eta$ model are in good agreement, unless the value of $\overline{m}$ is ≈ 5 in this model, the predicted fluxes are too small (RITZ *et al*, (1987b)). A local maximum of $\tilde{\phi}_f$ near $\rho = 1$ has been observed in the edge plasma of many tokamaks. This gives rise to a more complicated radial behavior of $\tilde{\phi}_f/T_e$ than the $\tilde{n}_e/n_e$ radial profile. Neither the drift wave theories nor the mixing length arguments predict this. However, this is not inconsistent with impurity radiation driven turbulence (which depends strongly on L_z, the edge impurity scale length, and the radiation rate) where low ionization states of carbon and oxygen impurities peak near the edge. Also, in $\nabla\eta$ turbulence theories, the impurity radiation rate $I_z(T_e)$ can be a complicated function of T_e. These theories predict complicated dependencies of $\tilde{\Gamma}$ on other parameters which are not necessarily constant. As a result, nothing can be said about the validity of these theories on the basis of gradient drive scalings alone.

In this comparison, while the mixing length prediction of $\tilde{n}_e/n_e \sim 1/k_{\rm rms}L_n$ is too small by a factor of only 2–5, it does fail to have the required L_n dependence. The review by SURKO (1987) found that data from many different tokamaks, under many different plasma conditions, roughly followed a $\tilde{n}_e/n_e \sim 1/k_{\rm rms}L_n$ type relation. The findings in this thesis are different from the findings given by SURKO *et al* (1987) but could perhaps be reconciled on the basis of measurements in different plasma regimes, all of which cannot be described by one generic theory.

It is important to note that *no* model can reproduce *all* of the observed parameters defining the edge plasma.

SCOTT (1990) used the linear theory developed by HASSAM *et al*, (1983) to investigate the rippling instability and found a 'regime boundary' between the two types of turbulence (viz., ∇n and $\nabla\eta$ driven turbulence). The linear parameter space discussed by

SCOTT (1992) is defined by the collisionality parameter, C, and the rippling parameter, R. C is the ratio of the nominal electron and ion widths and is defined as

$$C \equiv \frac{\Delta_D^2}{r_s^2}$$

where Δ_D^2 is the hydrodynamic layer width. The collisional regime is defined by $C \gtrsim 1$. The rippling parameter, R, is defined as

$$R \equiv \frac{j_o}{n_e c_s}\left(\frac{L_n}{L_s}\right)$$

where c_s is the ion acoustic speed and L_s is the magnetic shear scale length. The region to the left of the line $RC = 1$ is the so-called 'drift wave' regime and the region to the right of this line, the so-called 'rippling' regime. The asymptotic boundary for the linear stability transition was found by HASSAM *et al* (1983) to lie on this line, i.e., $RC = 1$ where 'asymptotic' here means small R and large C.

The operating parameter space of ASDEX and TFTR were found to be well within the 'drift wave regime' (SCOTT (1992)) leading to the conclusion that the resistivity gradient has no relevance to present or future tokamak experiments. A similar study shows that the parameter space of *Tokoloshe* is also well within the drift wave regime as are some similar sized machines (Figure 4.32). Because a wide range of edge n_e—both as function of time and space—was studied on *Tokoloshe* it was possible to investigate the relationship between $\tilde{n}_e/n_e$ and r_s/L_n. The results, shown in Figure 4.33, seem to indicate that it is the drift wave (and not the resistivity gradient) that is responsible for the turbulence in *Tokoloshe*.

It is important to note that correlations between observed interior fluctuating amplitudes and plasma transport coefficients need not be automatic. Geometric asymmetries play a large role in measurements and WOOTTON (1989) pointed out that neither point nor line of sight measurements of fluctuating quantities is adequate. Also, choice of applicable turbulence regime (e.g. $\tilde{\Gamma} \propto (\tilde{n}/n)^0$, $(\tilde{n}/n)^1$, $(\tilde{n}/n)^2$ in quasilinear, strong turbulence and stochastic regimes respectively) could affect results. Finally, some plasma parameters (e.g. T_e) appear in relationships between fluctuation levels. Since these parameters are often themselves varying, errors can be large.

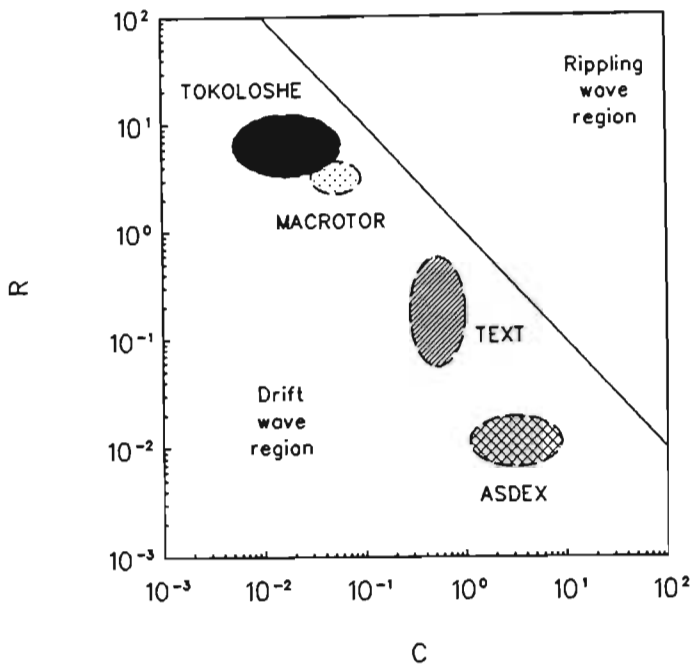

Figure 4.32: Rippling mode versus drift wave parameter space for four machines, viz., *Tokoloshe*, ASDEX, MACROTOR and TEXT, all well within the drift wave regime.

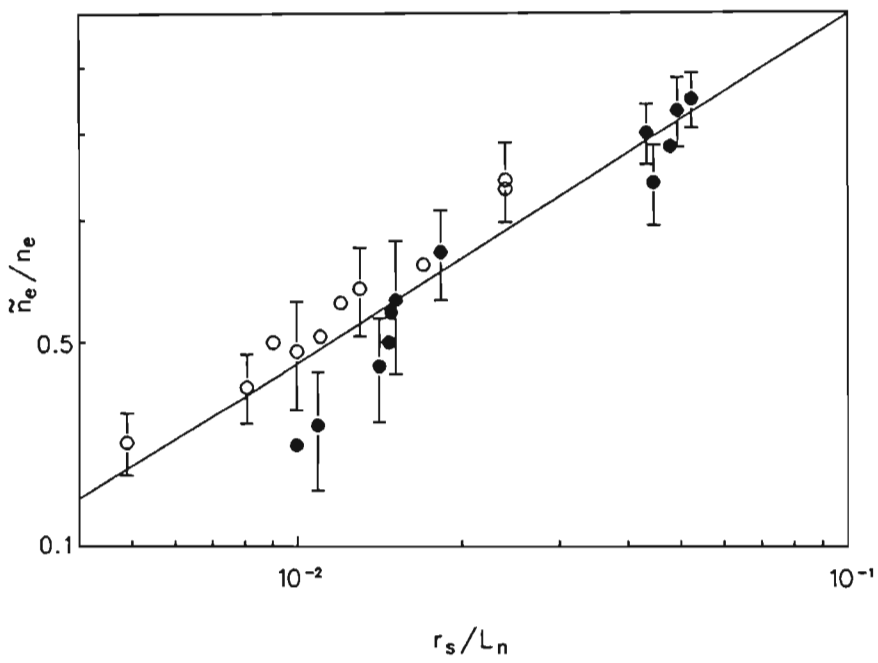

Figure 4.33: $\tilde{n}_e/n_e$ vs r_s/L_n on a logarithmic scale showing a linear dependence of these quantities in both time (open circles) and space (closed circles). The best fit curve indicates that $\tilde{n}_e/n_e \simeq 3(r_s/L_n)^{\frac{1}{2}}$ (c.f. HASEGAWA *et al*, (1983)). Points used are from Figures 4.7 and 4.8.

Chapter 5

Locked Plasmas

The edge region of reference plasmas have been characterised in the previous Chapter. They have been found to be strongly turbulent with high levels of fluctuations in many edge parameters. Strong radial electric fields give rise to a shear layer which, in turn, modifies edge parameters and defines a strongly turbulent region in the shear layer. No obvious effects of the high amplitude, low frequency Mirnov oscillations were found on the fluctuation induced energy and particle transport.

The toroidally rotating plasma is now locked by magnetic fields produced by currents in the external helical coils. The Mirnov oscillations are produced by the toroidal rotation of the saturated tearing modes. The current in the external coils produces magnetic fields to which these modes align themselves and eventually 'lock'. The results presented here are for the case where the tearing mode islands (already present in the plasma) are smaller than the islands generated by the external field. The resultant island structure is thus expected to be dominated by the external coils. The suppression of the Mirnov signal, $\tilde{B}_\theta$, by the external coils is due to a slowing down of rotation, leading to mode locking, $\partial/\partial t \rightarrow 0$, rather than to suppression of the mode, $\tilde{B}_\theta \rightarrow 0$. A more detailed description of the mechanisms involved in locking and the locking procedure is described by ROBERTS *et al* (1991b).

The edge plasma under these locked conditions is characterised in this Chapter and compared with results presented in Chapter 4.

5.1 Locked Discharges

The type of discharge required for the coils to lock the toroidally rotating plasma must possess very specific characteristics. The discharge parameters may still be described by Table 4.1. As with the reference plasmas, these plasmas must exhibit a period of high Mirnov activity for at least 10 — 14 ms from the start of the shot. If the amplitude is too high, the plasma locks to a naturally occurring stray edge field *before* the coils are energised or results in a major disruption. If the amplitude is too low or has already decreased significantly into a low-amplitude Mirnov phase, the edge field produced by the coils will not be large enough to slow or lock the rotating plasma. Also, as will be shown later, minor disruptions alter edge parameters significantly so cases where these were present were omitted from the bulk of this study. A separate discussion on the effects of minor disruptions on the *Tokoloshe* plasma is given at the end of this Chapter.

The results presented in this Chapter consist mainly of those taken during discharges in which the plasma was locked by the $\ell = 2$ and $\ell = 3$ coil in the resonant configuration. That is, the total plasma field, produced by the combination of plasma current, I_p, and toroidal magnetic field, B_ϕ, has the same helicity as the field produced by the coils. The current in the coils can also be reversed. This changes the orientation of the magnetic islands produced by the coils as shown in Figure 5.1 for the $\ell = 2$ coil. The two configurations will henceforth be referred to as the '$--+2$' (or '$--+3$') and '$---2$' (or '$---3$') configurations, as shown in the diagram. The first three characters in the brackets refer to the direction of B_ϕ, I_p and I_{ell} respectively and the fourth character refers to the mode, as described by ROBERTS *et al*, (1991). Results from $\ell = 3$-coil-locked plasmas (with the same convention adopted as in the $\ell = 2$ case) are also discussed, in less detail, at the end of the Chapter.

The coils, discussed in Chapter 3, are energised at a prescribed time, usually $t \approx 10$ ms after the start of the shot. One of three capacitor banks discharges at this stage, driving the coil current from 0 kA to ≈ 1.5 kA in about 1 ms. A second bank discharges at peak current (i.e. after ≈ 1 ms from the first bank discharging) to maintain this current and the third bank discharges at a prescribed time after that. With this arrangement the current in the coils may be controlled to give either a 'short' current pulse (usually about ≈ 3 ms) in which the third bank discharges after the user-specified time to bring the coil current to zero, or a 'long' current pulse in which the third bank is *not* charged and the current in the coil either decays over several ms to zero or until the major disruption, whichever comes first.

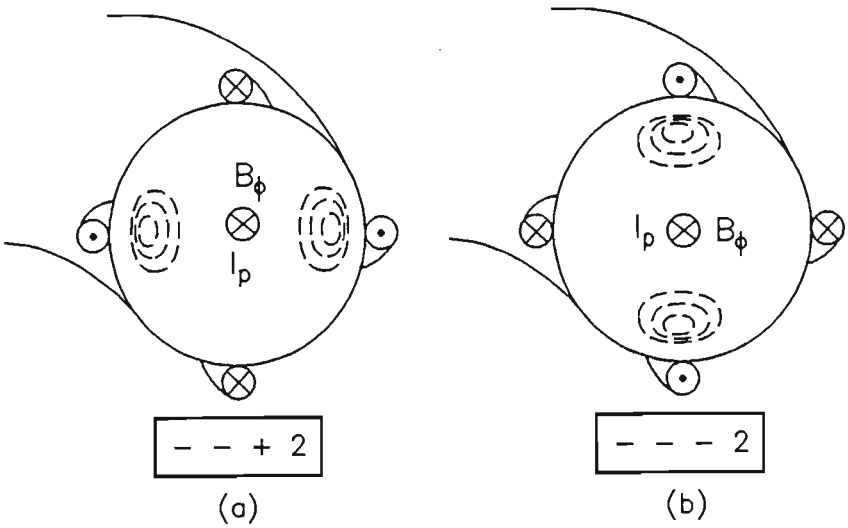

Figure 5.1: Schematic representation of the $\ell = 2$ helical coils on *Tokoloshe* showing imposed island positions for the (a) '$--+2$' non-resonant and (b) '$---2$' resonant configurations, at $\phi = 0$.

A puncture plot ('Poincaré plot') of the total magnetic field is shown in Figure 5.2 for the case shown in Figure 5.1(b). The field includes the effects of the perturbing field due to the $\ell = 2$ helical coils and is calculated at the same toroidal position as the Langmuir probe. In each case, I_ℓ, the current in the helical $\ell = 2$ coils, is about 1.5 kA. The islands shown represent those produced by the $\ell = 2$ coils and show the position at which the rotating $m = 2$ island is expected to lock. The island positions are those expected for the long pulses only. For the short current pulse, the effect of the $\ell = 2$ coils is expected only to slow the rotation velocity sufficiently to allow a stray edge field to lock the plasma completely. It was thus expected that the final locking orientation of the islands for both coil current directions for short pulses would be approximately the same. FLETCHER (1991), using framing camera studies, found that the locking orientation was independent of the sense of the helical coil current, possibly because the plasma locks to the coil field, unlocks and rerotates to lock on a stray field. Indeed, as will be seen, results for the above two cases are very similar. The position of the Langmuir probe is shown to scale, at the position of maximum insertion into the bulk plasma. Whilst the Poincaré plots are intended only to illustrate the approximate widths, poloidal extents and radial positions of the induced islands, it is clear that the probe array lies well within the stochastic edge region and at no stage encounters even the outer magnetic surfaces

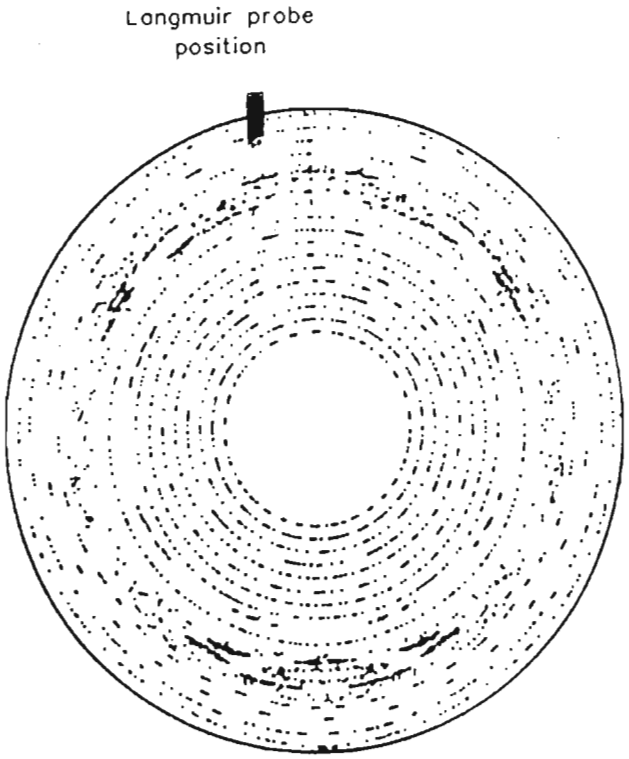

Figure 5.2: Poincaré puncture plot for the $\ell = 2$ coil island positions for the $---2$ configuration.

of the induced islands.

Unless otherwise specified, the results presented in this Chapter were taken from discharges in which the plasma was locked by the fields produced by a short ($\approx 3\,\mathrm{ms}$) current pulse. The current in the coils was arranged as shown in Figure 5.1(b) with a maximum coil current of $\approx 1.5\,\mathrm{kA}$.

Figure 5.3 shows typical traces from four diagnostics on *Tokoloshe,* before, during and after locking of the plasma. Figure 5.3(a) shows the $\tilde{B}_\theta(m = 3)$ signal, locking at the same time as the $m = 2$ islands and then decreasing in amplitude before unlocking, (b) the amplitude of the $\tilde{B}_\theta(m = 2)$ signal on the same timescale, locking at $t \simeq 12\,\mathrm{ms}$ and unlocking at $t \simeq 18\,\mathrm{ms}$, (c) the current in the $\ell = 2$ coil switching on at $t \approx 10\,\mathrm{ms}$ and off at $t \approx 13.5\,\mathrm{ms}$ and (d) the plasma current, I_p, from the start of the shot until the major disruption.

Studies of the force required to lock the plasma show that prior to locking the bulk plasma is rotating as a solid body at the Mirnov frequency ($f_{\mathrm{Mirnov}} = 8 \rightarrow 15\,\mathrm{kHz}$), (ROBERTS *et al*, (1992)). This corresponds to a toroidal rotation velocity of between 35 and 60 $\times 10^3\,\mathrm{ms}^{-1}$ or between 8 and 14 times the maximum observed poloidal velocity. The $\tilde{B}_\theta$ signals show that the bulk plasma slows down shortly after the coil is switched on and then locks for a few ms before rotating again. In most discharges, however,

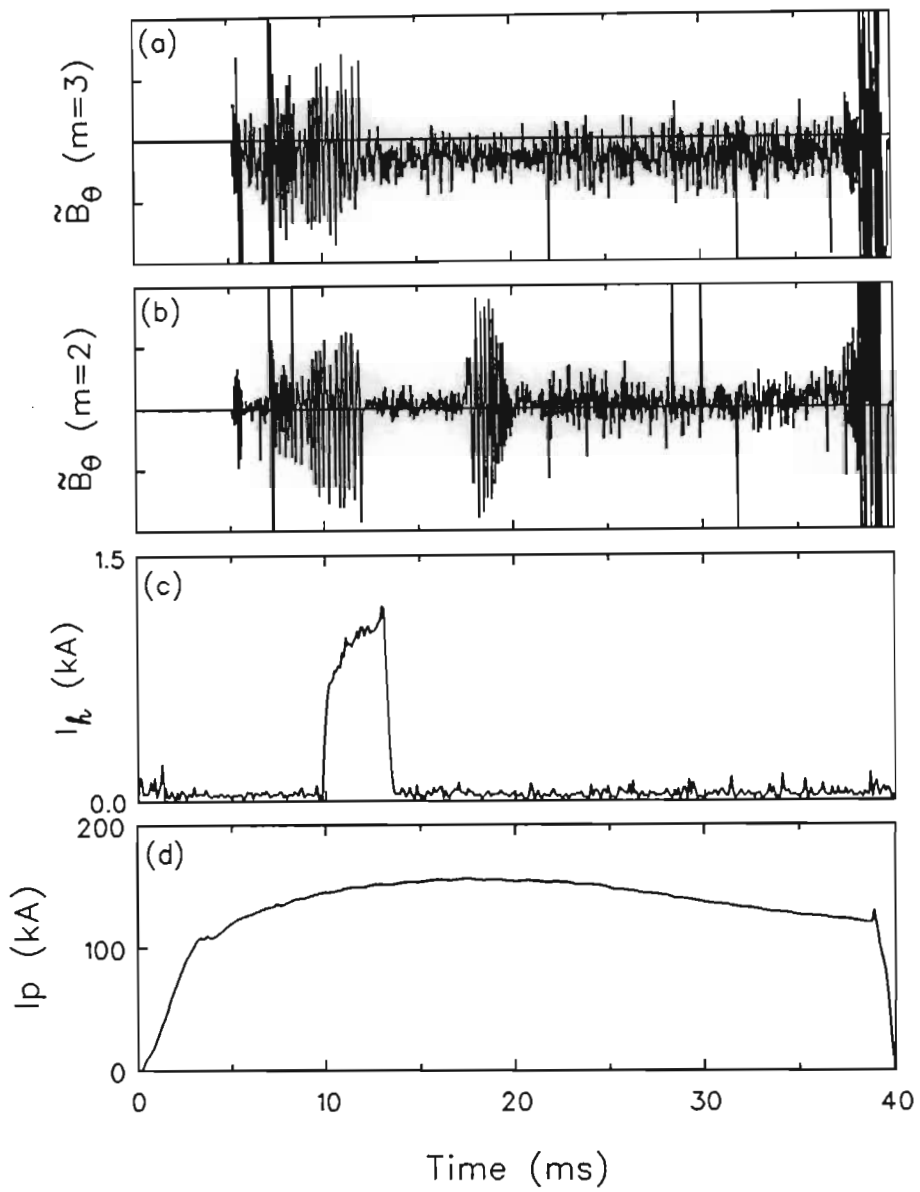

Figure 5.3: Typical traces from 4 diagnostics on *Tokoloshe*. (a) $\tilde{B}_\theta(m = 3)$, (b) $\tilde{B}_\theta(m = 2)$, (c) $I_{\ell=2}$, the helical coil current in the $\ell = 2$ coil and (d) the plasma current, I_p with maximum of ≈ 160 kA. Both the $\tilde{B}_\theta(m = 3)$ and the $\tilde{B}_\theta(m = 2)$ modes are locked by the coil but only the latter has sufficiently high amplitude at $t \simeq 18$ ms to show unlocking and rerotation.

the plasma *did not* rerotate and remained locked to disruption. The locked plasma is less stable than its rotating counterpart and invariably disrupts earlier ($t_{\text{rotating}} \approx 30 - 40\,\text{ms}, t_{\text{locked}} \approx 15 - 20\,\text{ms}$); hence the lack of data for $t > 20\,\text{ms}$ in many cases. The $m = 2$ mode amplitude remained almost unchanged throughout a locked phase of up to $3\tau_e$ in duration (ROBERTS *et al*, (1991a)). On the other hand, the $m = 3$ mode amplitude often decreased during locking so that, if the plasma does unlock and rerotate, this was only observed on the $\tilde{B}_\theta(m = 2)$ signal: the $\tilde{B}_\theta(m = 3)$ mode amplitude is small, the mode having passed into the low Mirnov activity phase during the locked phase. No minor disruption occurred for any of these shots after locking.

5.2 $\ell = 2$ Coil Results

5.2.1 Single Probe Results

Edge Density, Potential & Electric Field

Figure 5.4 shows the edge electron density for three discharges as a function of time, measured with the probe at $\rho = 0.93$. Points are raw data averages, taken over every $500\,\mu\text{s}$. In each case, the coil was switched on at $t \simeq 10\,\text{ms}$ and locking occurred within 2 ms after that. In the case of shot #9157, the plasma unlocked at $t \simeq 17.5\,\text{ms}$ and rerotated with its previous frequency (of $\approx 5\,\text{kHz}$) and amplitude. The mode amplitude rapidly decreases after unlocking and after $\approx 2.5\,\text{ms}$ had passed into the low Mirnov activity phase. In the case of shots #9161 and #9162 the $m = 2$ mode remains locked to disruption ($t \simeq 23\,\text{ms}$).

The density rises at a rate comparable to that observed in the reference case for all three shots until the time the plasma locks, i.e. $t \simeq 12\,\text{ms}$. At this stage the rate of increase in edge density drops to zero. Throughout the period in which the plasma is locked the density does not increase and actually decreases slightly for some shots, e.g. #9161 and #9162. For shot #9157, the density increases again at $t \approx 20\,\text{ms}$, some 2 ms after the plasma has started rotating again at the onset of the low Mirnov activity phase. FLETCHER *et al*, (1992) observed similar behavior for $\overline{n}_e$ (i.e. $d\overline{n}_e/dt$ decreases during the locked phase) using $\mu-$wave interferometer studies. These changes are much more modest than the changes in the observed $\tilde{\Gamma}$. These results suggested a change in the source term.

The radial profile of the edge density during locking is shown in Figure 5.5 with the

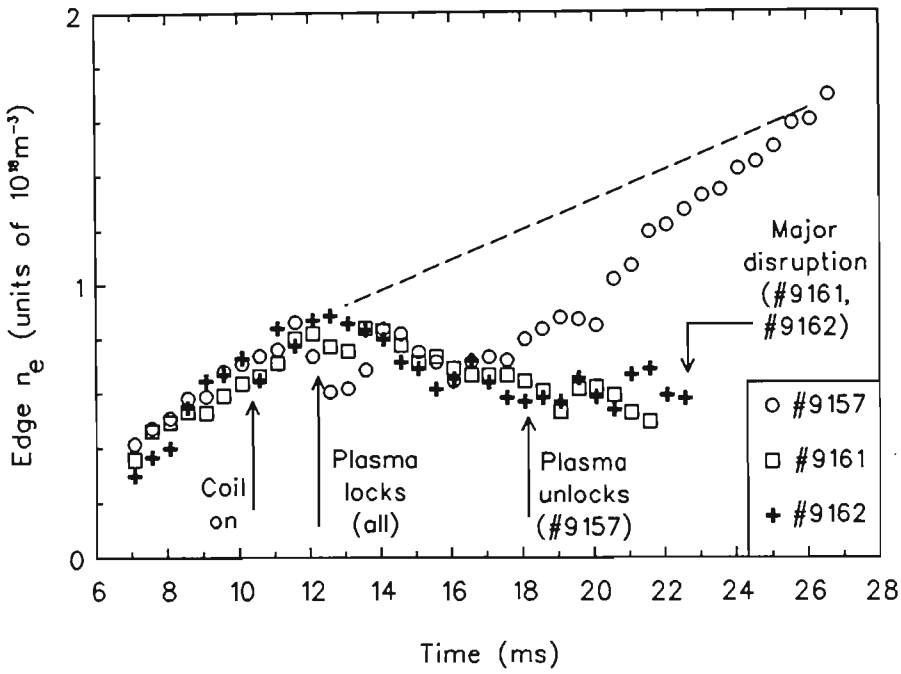

Figure 5.4: Edge electron density as a function of time at $\rho = 0.93$. The modes lock and unlock at the times indicated in the Figure. In this Figure—and henceforth—the dashed line/curve represents the reference results on the same scale as the locked results for comparison.

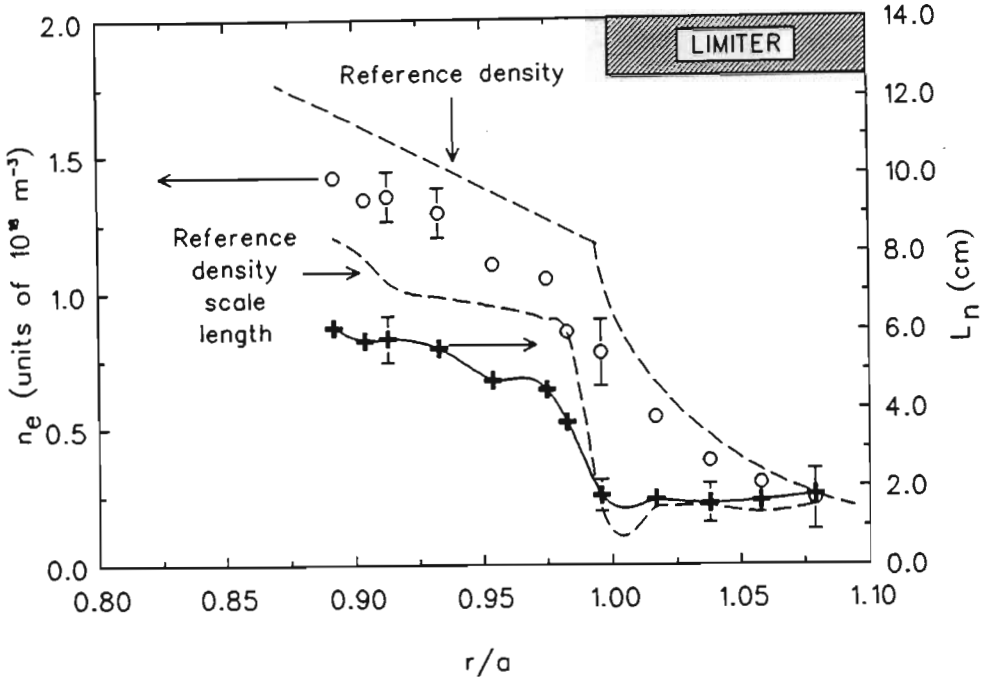

Figure 5.5: Edge electron density profile with points representing time averages of n_e from $t = 13$ — 18 ms during the locked phase.

reference edge density and density scale length shown as dashed lines for comparison. These values are again the average of n_e taken from $t \simeq 13$ — 18 ms for each shot. For $\rho \lesssim 1.0$, i.e. from bulk plasma up to the limiter, the density decreases linearly within the error bars as it did in the reference cases. At each value of ρ, however, the density is lower than the reference values by a factor of $\approx 30\%$. For larger values of ρ the density is very similar to the reference cases in both trend and magnitude, dropping off exponentially closer to the wall. The radial scale length in the bulk plasma is $L_n \simeq 7.7$ cm and at the limiter, where a local estimate is required because ∇n_e is changing by a large amount with ρ, $L_n \simeq 1.8$ cm. For larger values of ρ, L_n remains roughly constant at ≈ 1.5 cm, similar to the reference value.

Figures 5.6(a) and (b) show the floating potential as functions of time with the probe at $\rho = 0.93$ in both cases. The Mirnov activity depicted in (a) is that taken from shot #9157 and (b), from shot #9161 (see Figure 5.4). In (a) the floating potential remains roughly constant during the high Mirnov activity phase at $\phi_f \simeq 20$ V. At locking, the potential rapidly increases by $\pm 20\%$ to $\simeq 25$ V and remains roughly constant at this value throughout the locked phase. As the plasma unlocks, the potential decreases by some $60 \rightarrow 70\%$ to $\phi_f \simeq 8$ V and remains at this value to disruption.

The floating potential for the shot represented in (b) increases throughout the period in

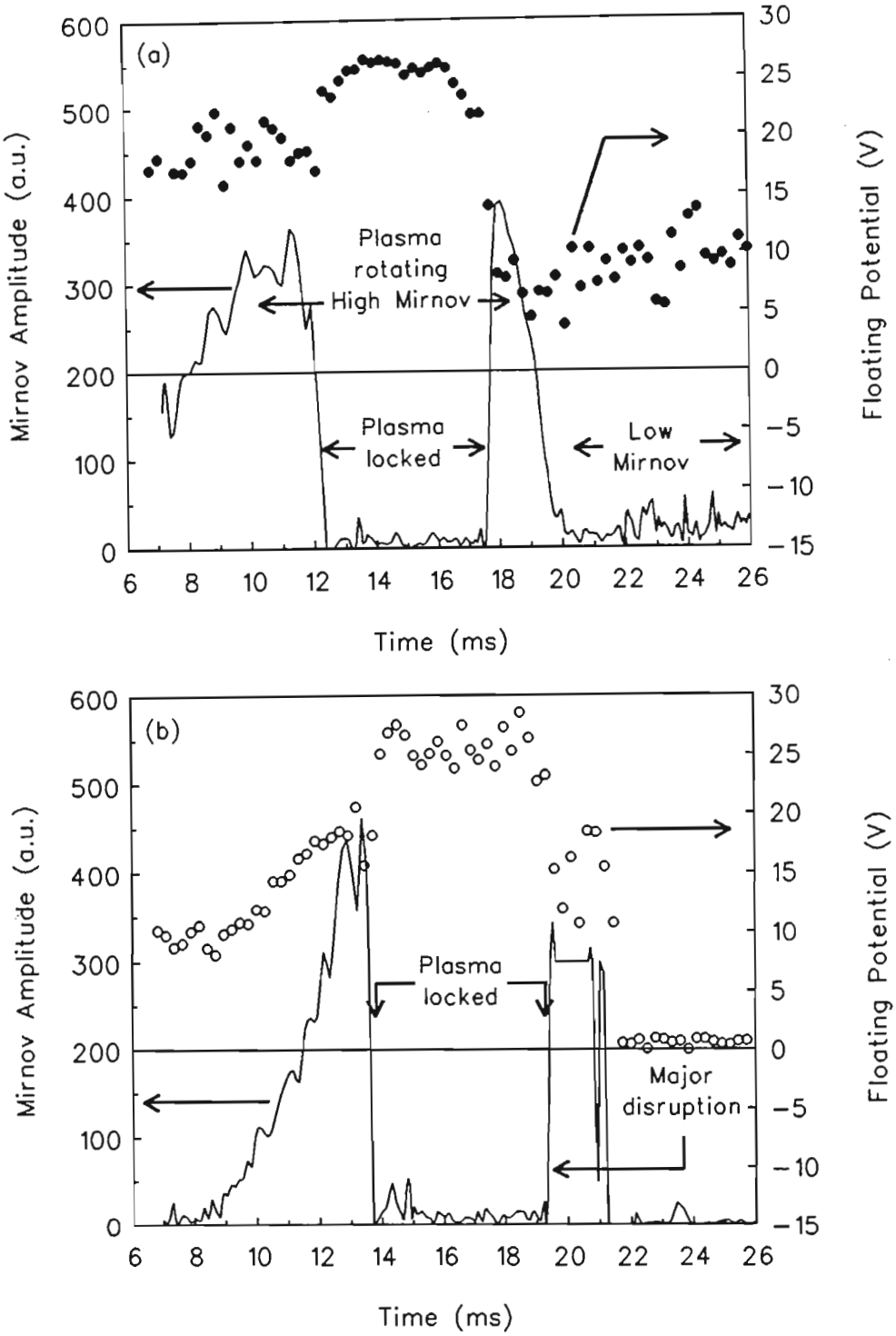

Figure 5.6: Floating potential before, during and after a locked phase, measured at $\rho = 0.93$. Also shown on the same time scale are Mirnov, $\tilde{B}_\theta(m = 2)$ mode amplitudes for shot (a) #9157 and (b) #9161.

which the Mirnov amplitude is increasing from $\phi_f \approx 10\,\mathrm{V}$ to $\approx 20\,\mathrm{V}$. At $t \approx 14\,\mathrm{ms}$—when the plasma locks—the potential again increases to $\phi_f \simeq 25\,\mathrm{V}$ and remains at this value throughout the locked phase until the major disruption at which stage it drops rapidly to zero. The change in the magnetic fields at the edge as the plasma locks could change the probe sheath size and the collection length which will alter, in turn, the ion saturation current and the local floating potential.

The radial profile of the plasma potential profile is shown in Figure 5.7 with points calculated from $\phi_p = \phi_f + 3.6T_e$ using averages of ϕ_f, calculated between $t \approx 12$ and $t \approx 18\,\mathrm{ms}$ (i.e., the locked phase), and the electron temperature calculated during this phase (see later). Also shown is the radial electric field from $-\nabla\phi_p$. Finally, the plasma potential and electric field profiles for the reference case are shown on the same graph as dashed lines for comparison. The plasma potential profile has much the same shape during locking as during the reference discharges but is higher by a factor of ≈ 0.3 for $\rho \sim 0.88$ and ≈ 0.1 for $\rho \gtrsim 0.88$. At larger values of ρ, the potential is approximately the same or slightly lower than that measured during the reference cases. This gives a more peaked profile with a maximum potential at $\rho \approx 0.92$ of some 90 V. This in turn leads to a more peaked radial electric field profile with a maximum $\vec{E}_r$ at $\rho \simeq 1.02$ of $16\,\mathrm{V\,cm^{-1}}$ and zero $\vec{E}_r$ at $\rho \simeq 0.92$ (c.f. $\vec{E}_r = 0$ at $\rho \simeq 0.94$ in the reference cases). The radial electric field is larger at each radial position than the field measured in the reference plasmas, giving rise to an L_E during locking of $\approx 2.4\,\mathrm{cm}$ and $L_E/r_s \approx 26$.

Fluctuation Levels

Relative fluctuation levels of the ion saturation current and the floating potential as a function of time are shown in Figure 5.8 for the three shots used in Figure 5.4. The probe was inserted 1.5 cm into the bulk plasma and points are determined using $\tilde{x} = \langle \sum (x - \overline{x})^2 \rangle^{\frac{1}{2}}$ (where x is the fluctuating parameter) for blocks of 500 μs.

As with the reference case, both fluctuation levels increase with time during the period of high Mirnov activity up to locking. At locking, $\tilde{i}_{\mathrm{sat}}/i_{\mathrm{sat}}$ decreases abruptly in all three cases from 0.25 to about 0.15 or by a factor of ≈ 0.6. During the locked phase the level is roughly constant at ≈ 0.15. For shot #9157, where the plasma began rotating again at $t \simeq 18\,\mathrm{ms}$, this level increases abruptly to ≈ 0.25 where it remains to disruption.

The floating potential fluctuation levels also drop sharply at locking from 0.7 ± 0.1 to about 0.43 — again a factor of about 0.6. Throughout the locked phase this level increases slightly until the discharge ends in a major disruption. For shot #9157, at

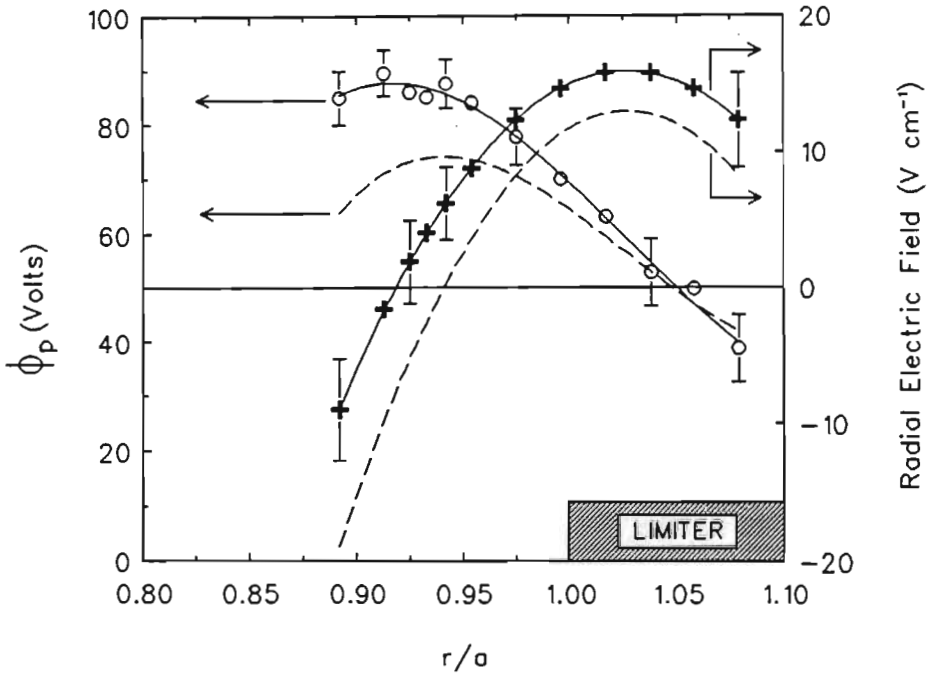

Figure 5.7: Radial edge profile of ϕ_p during the locked phase. Points are time averages taken during the locked phase ($t \approx 13 \rightarrow 18\,\mathrm{ms}$). Also shown is E_r, calculated from $\vec{E}_r = -\nabla\phi_p$.

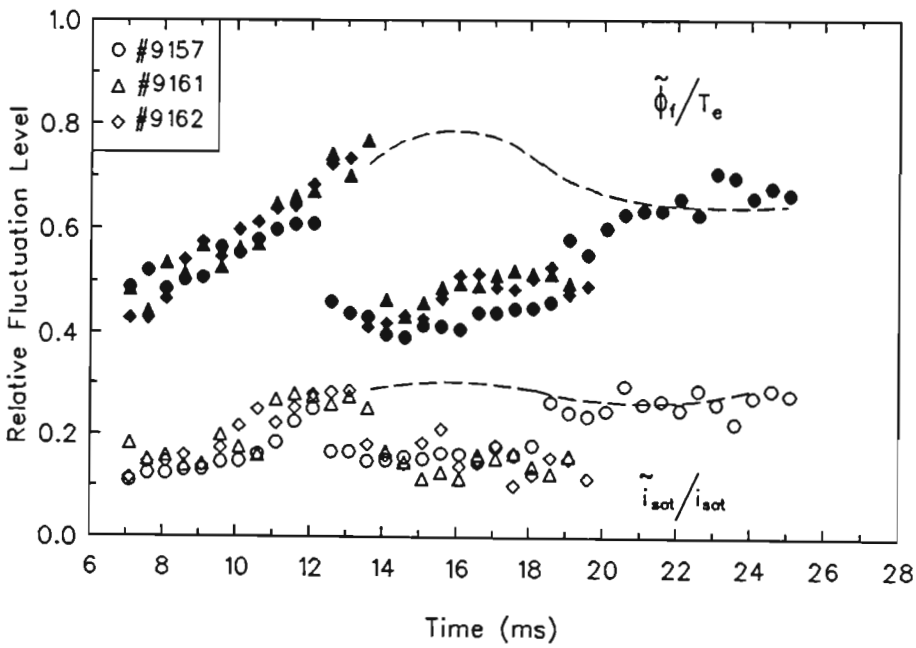

Figure 5.8: Typical fluctuation levels of $\tilde{\phi}_f(t)/T_e$ and $\tilde{i}_{sat}(t)/i_{sat}$ taken at $\rho = 0.93$ during the locked phase. Locking occurred at $t \simeq 12\,\mathrm{ms}$.

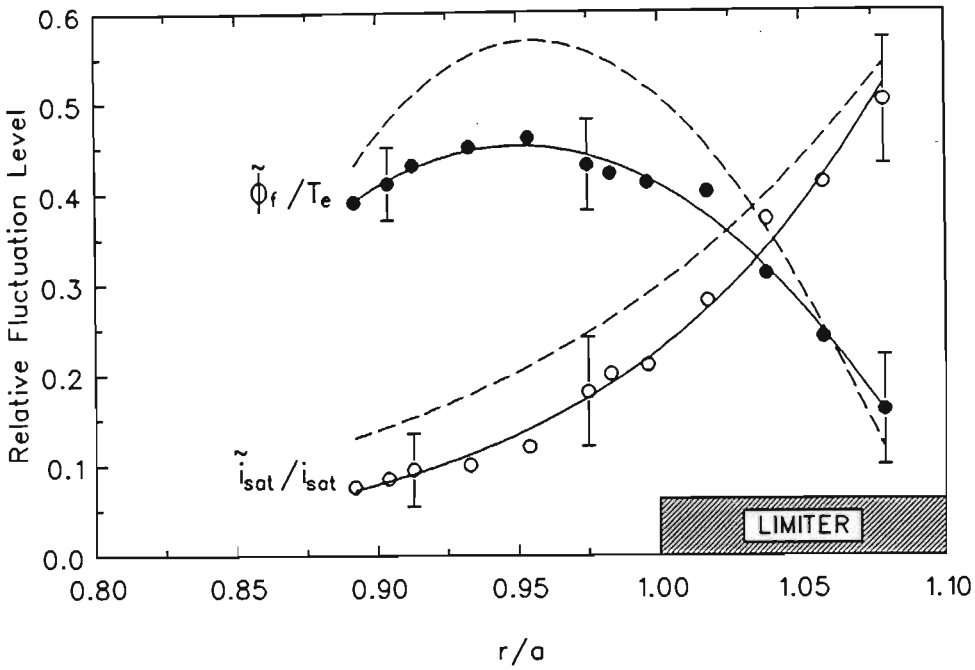

Figure 5.9: Radial profiles of $\tilde{\phi}_f/T_e$ and $\tilde{i}_{\rm sat}/i_{\rm sat}$, averaged over about 5 ms (between $t = 13$ — 18 ms) during the locked phase. Dashed curves are for the reference (rotating) plasmas.

$t \simeq 18$ ms the level jumps to ≈ 0.62 where it remains until the end of the shot with no change as the Mirnov activity passes from the high into the low phase.

Figure 5.9 shows the radial profile of the current and potential fluctuations. Points were obtained by calculating $\tilde{x}$ as above during the locked phase. The duration of the locked phase varied from shot to shot but was usually about 4 ms in length (i.e. 4 000 points).

At each position in the bulk plasma ($0.89 \leq \rho \leq 1.00$) the relative level of current fluctuations is lower than during the reference shots. At the limiter and closer to the wall ($\rho \geq 1.00$) the levels are approximately the same or slightly lower, with the value of $\tilde{i}_{\rm sat}/i_{\rm sat}$ increasing monotonically from bulk plasma to limiter shadow. The floating potential fluctuations have a peaked profile with a maximum of $\tilde{\phi}_f/T_e$ at 0.94 ± 0.2. The profile during the locked phase is less peaked than during the reference cases with $\tilde{\phi}_f$ being less during locking than during reference cases at each radial position. In the limiter shadow the levels are approximately the same.

Power Spectra

Figure 5.10 shows the power spectrum of $\tilde{\phi}_f$ during the 5.4 ms of locking for shot #9157. The Langmuir probe is positioned at $\rho = 0.93$ and $42 \times 128\,\mu$s blocks were used to generate the spectrum. As with the reference (rotating plasma) case (shown as a dashed curve in the figure) there are no reproducible peaks and the spectrum is broadband over the entire frequency range. The highest peak in the power spectrum occurs at $f \simeq 50\,$kHz (c.f. the low Mirnov case, Figure 4.9) and the power is greater than that measured during the low Mirnov phase and lower than during the high Mirnov activity phase at all frequencies. As expected, the Mirnov peak at $\sim 10\,$kHz is absent on the power spectrum for the locked phase. Shorter correlation times are measured between signals separated in the toroidal direction and much the same τ_c in the poloidal direction as the reference cases (c.f. Figure 4.10), shown in Figure 5.11. The explanation used to describe the difference in these quantities during the rotating phase may be used again here. The toroidal phase velocity of the fluctuations is closely correlated with the bulk plasma toroidal velocity, i.e. $v_{\text{phase, TOROIDAL}} \rightarrow 0$ as the rotation frequency $\rightarrow 0$. Toroidal elongation (or distortion) of plasma 'blobs' is, therefore, no longer expected and toroidal correlation times are expected to be shorter than those measured during the rotating phase. On the other hand, the poloidal elongation of the 'blobs' should remain roughly the same since $v_{\text{phase, POLOIDAL}}$ does not change very much between the rotating and the locked phase. Both of the above effects are observed.

On a logarithmic scale (Figure 5.12), the power $P(f) \propto f^{-1.0\pm0.2}$ for frequencies less than 200 kHz and $\propto f^{-2.5\pm0.1}$ for $200 \lesssim f \lesssim 500\,$kHz. The $\tilde{\phi}_f$ power spectrum, measured during the rotating phase, is also shown in the Figure for comparison (c.f. Figure 4.11).

Coherency & Coherence Length

The coherency between the fluctuating quantities is shown in Figure 5.13 with the dashed line at $\gamma = 0.2$ indicating the significance level. The dashed curve is the typical coherency spectrum obtained between these quantities during a reference (rotating plasma) discharge, during the rotating phase (Figure 4.12). In both cases, the probe is inserted 1.5 cm into the bulk plasma with $\rho = 0.93$. The coherency between $\tilde{i}_{\text{sat}}$ and $\tilde{\phi}_f$ is higher at all frequencies during the locked phase than during a reference discharge except for very low frequencies, i.e. $\lesssim 30\,$kHz. The main peak is located at $f \approx 50\,$kHz with $\gamma_{n\phi} \simeq 0.82$ and the coherency drops below the significance level for $f \geq 250\,$kHz.

The poloidal coherence length between signals is longer for most frequencies during

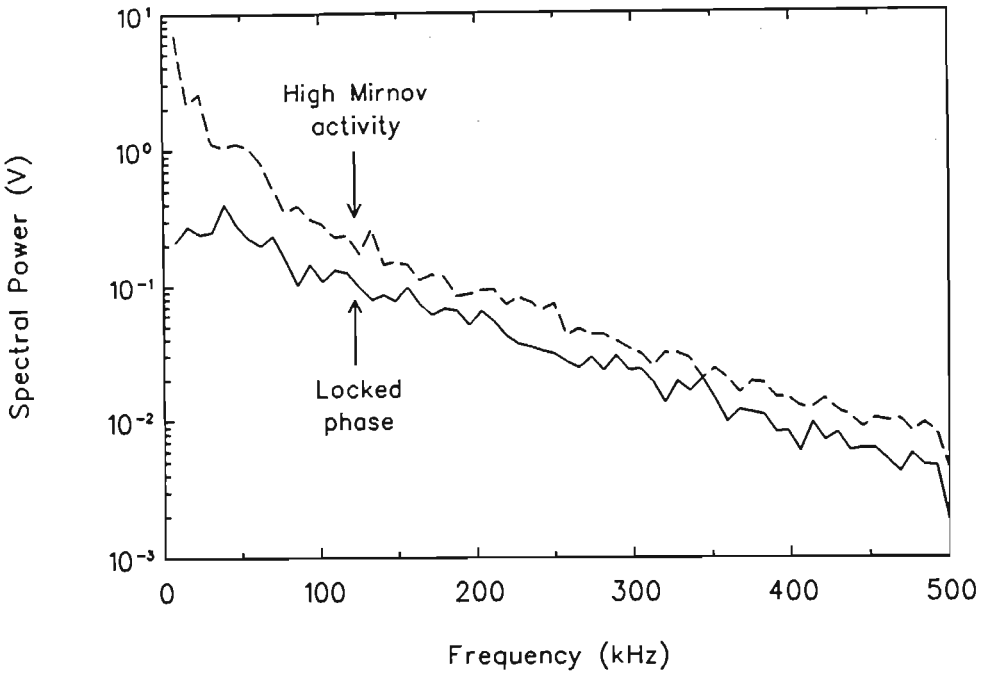

Figure 5.10: Power spectrum of $\tilde{\phi}_f$ during the locked phase with $\tilde{\phi}(f)$ during the rotating phase also shown for comparison. The interval sampled was ≈ 5 ms in duration, i.e. 39 $\times 128\,\mu$s.

the locked phase than during a reference shot as seen in Figure 5.14, again except for frequencies below about 30 kHz. The dashed line is the significance level and the dashed curve, the coherency spectrum obtained during the rotating phase for comparison. For frequencies between $0 \leq f \leq 100$ kHz, $L_{\text{coher}} \simeq 1.0$ cm, except at peak coherency ($\simeq$ 50 kHz) where it is ≈ 2.5 cm, and between $100 \leq f \leq 250$ kHz it is $\simeq 0.7 \pm 0.2$ cm. Above 250 kHz the coherence length is not well defined, being below the significance level.

Phase Angle & Dispersion Relation

The phase angle between $\tilde{i}_{\text{sat}}$ and $\tilde{\phi}_f$ at the same three radial positions used in the reference cases ($\rho = 0.95, 1.00$ and 1.04) is shown in Figure 5.15. In the bulk plasma, at $\rho = 0.95$, $\alpha_{n\phi}$ is negative and in the range $-45° < \alpha_{n\phi} < -90°$ or roughly $-\pi/3$ for frequencies below 200 kHz where the coherency between these signals is highest. At the limiter, $\alpha_{n\phi}$ is positive and roughly $+\pi/4$ for $f \leq 200$ kHz. In the limiter shadow region where $\rho = 1.04$, $\alpha_{n\phi}$ is still positive and $\approx +\pi/3$, at least for lower frequencies (c.f. Figure 4.14).

The k_θ spectrum is shown in Figure 5.16, measured at the radial positions mentioned

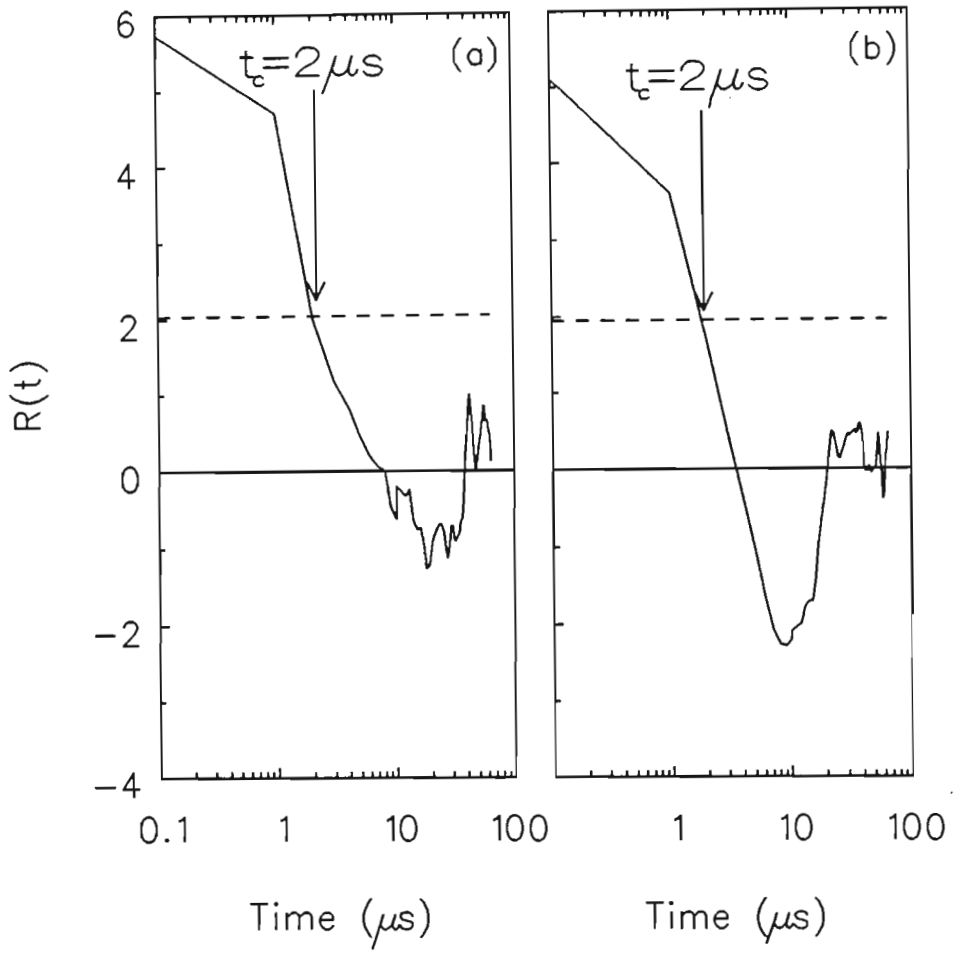

Figure 5.11: Correlation times between $\tilde{\phi}_f$ signals separated by 4 mm (probe separation) in the (a) poloidal direction and (b) toroidal direction during about 4 ms of the locked phase. Corresponding times for the rotating phase are 2 μs and 7 μs respectively. Dashed lines are $1/e$ levels of $R(t)|_{\max}$.

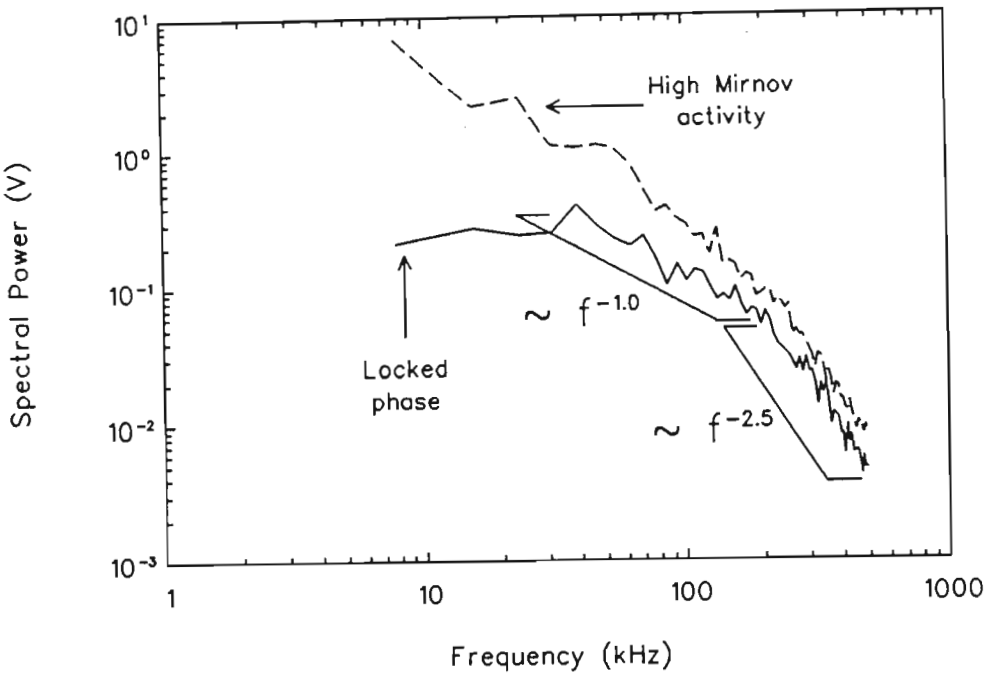

Figure 5.12: Power spectrum of $\tilde{\phi}_f$ during a period of about 5 ms of locking at $\rho = 0.93$ with both axes on a logarithmic scale and $\tilde{\phi}(f)$ during the rotating phase also shown for comparison. The time interval was the same as that used in the previous Figure.

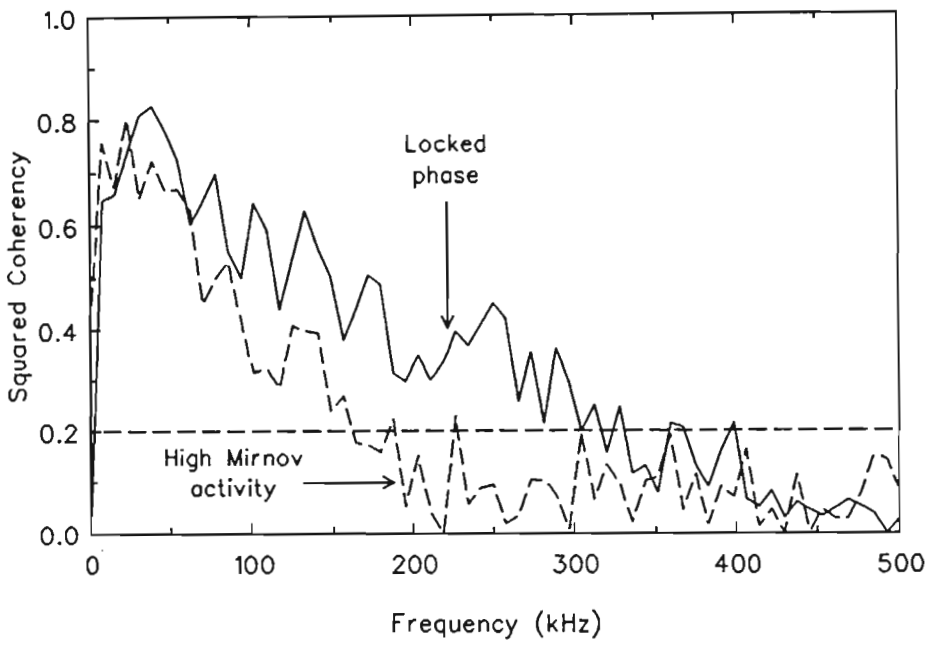

Figure 5.13: Coherency spectrum, $\gamma_{n\phi}$, between adjacent, poloidally separated probes during the locked phase. Also shown (dashed curve) is $\gamma_{n\phi}$ measured during the rotating phase for comparison. The straight dashed line is the significance level.

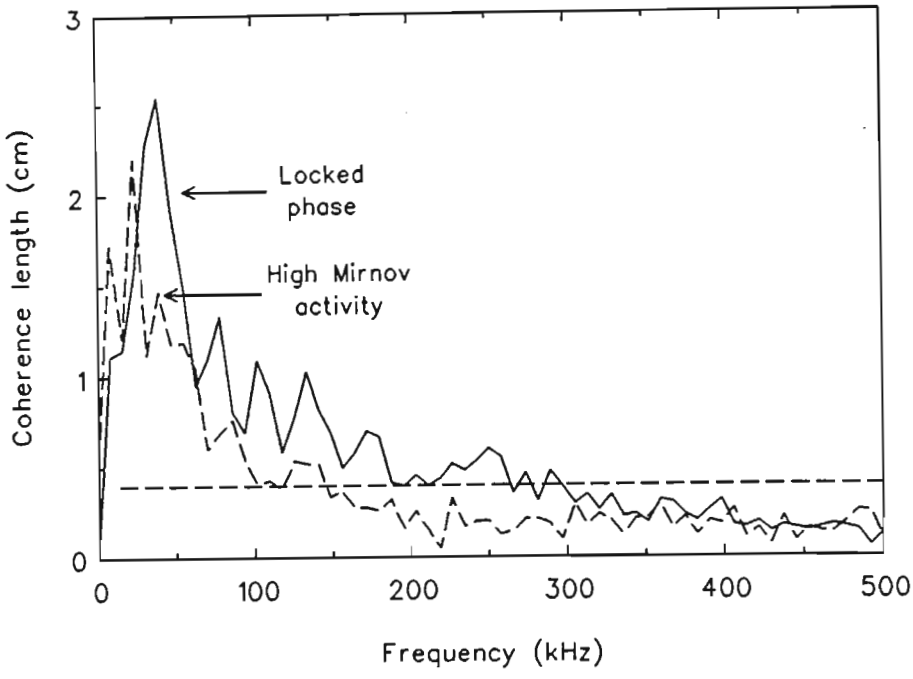

Figure 5.14: Poloidal coherence length spectrum between signals during the same interval of locked phase used in the previous Figure. L_{coher} for measurements taken during the rotating phase is also shown (dashed curve) for comparison. The straight dashed line indicates the significance level.

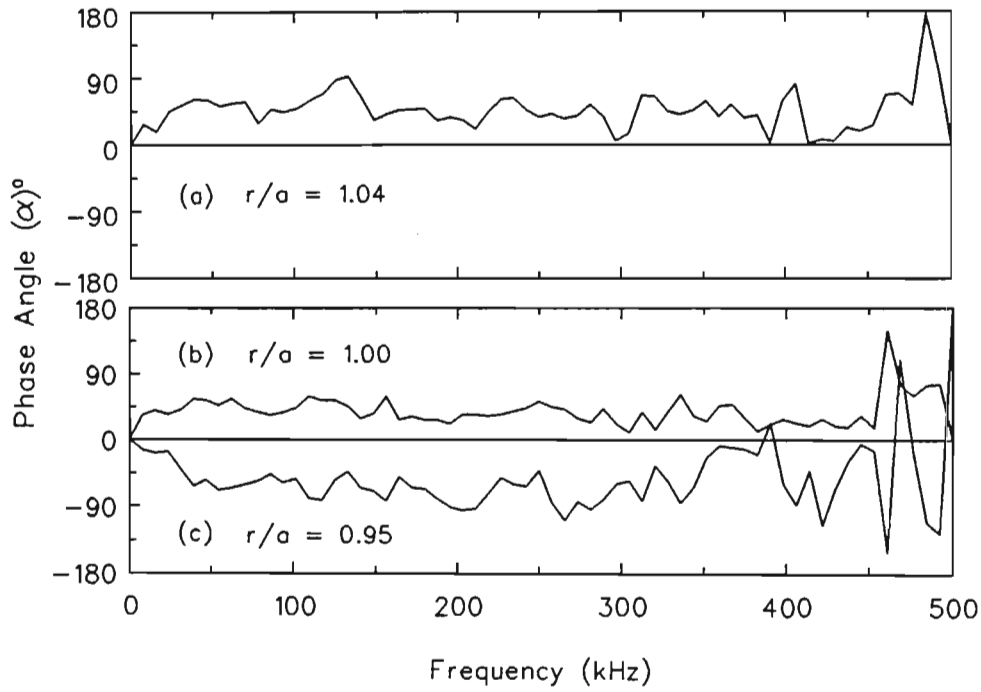

Figure 5.15: Phase angle between $\tilde{i}_{sat}(f)$ and $\tilde{\phi}_f(f)$ during locking at $\rho =$ (a) 1.04, (b) 1.00 and (c) 0.95, showing a sign change near the limiter.

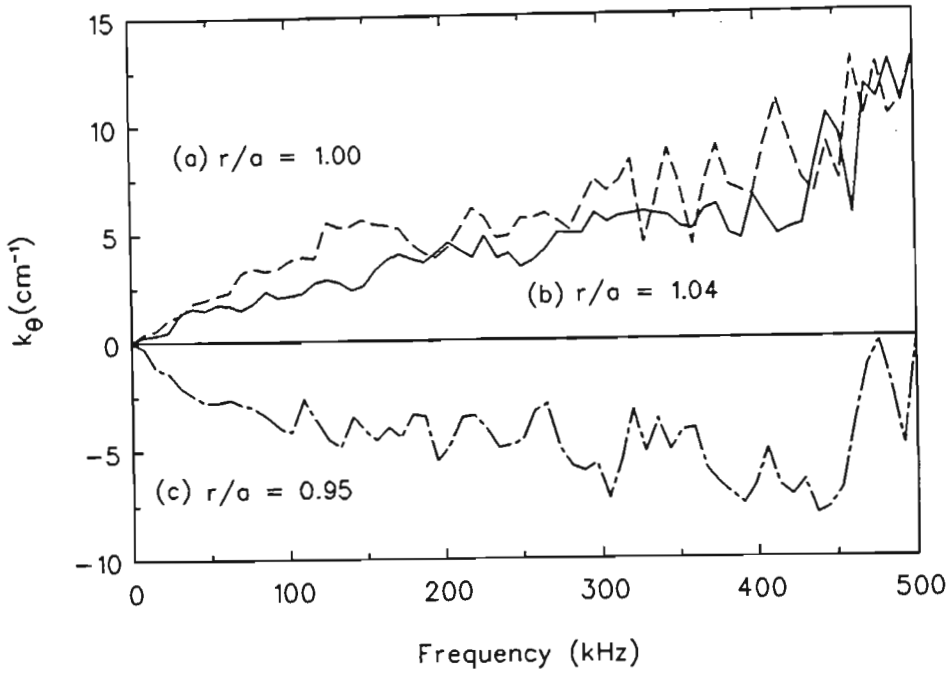

Figure 5.16: Dispersion relation between measurements of $\tilde{\phi}_f$ taken by probe tips separated in the poloidal direction, during locking, at the same radial positions as in the previous Figure, viz., ρ = (a) 1.04, (b) 1.00 and (c) 0.95 showing reversal of propagation direction.

above. In the bulk plasma k_θ is negative at all frequencies and has a gradient of $-1.76 \times 10^3\,\mathrm{ms}^{-1}$, whilst at the limiter ($+1.56 \times 10^3\,\mathrm{ms}^{-1}$) and further into the shadow ($+2.91 \times 10^3\,\mathrm{ms}^{-1}$) the gradient is positive for all frequencies showing a change in propagation direction between $\rho = 0.95$ and 1.00 (c.f. Figure 4.15).

Phase Velocity

The poloidal phase velocity of $\tilde{\phi}_f$ as a function of minor radius is shown in Figure 5.17, measured during the locked phase. In the bulk plasma the phase velocity is lower than that measured during the reference cases with a maximum of $1.8 \times 10^3\,\mathrm{ms}^{-1}$ in the electron diamagnetic drift direction. At $\rho = 0.93$ the measured phase velocity changes sign and increases to a maximum of about $2.2 \times 10^3\,\mathrm{ms}^{-1}$ in the ion diamagnetic direction. The profile is also not as strongly peaked as the reference profile.

At this point it should be stressed that 'locking' refers to a *toroidal* cessation of rotation, rather than an overall 'freezing' of the plasma in the vacuum vessel. Thus, it is still possible for the edge regions to experience turbulent fluctuations, poloidal velocity

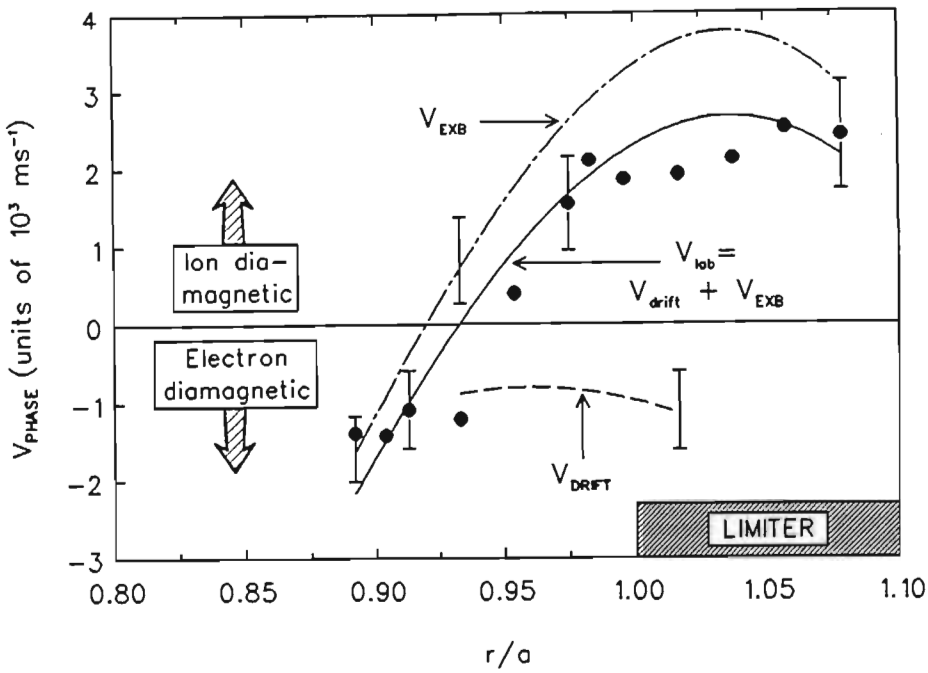

Figure 5.17: Phase velocity profile of $\tilde{\phi}_f$ during a period of about 5 ms of locking. Also shown are $v_{E\times B}$ (dot-dash curve) and $v_{\rm phase}$ (plasma) = $v_{\rm drift}$ (dashed curve).

variations, etc. It is therefore not unreasonable to observe a similar radial $v_{\rm phase}$ profile of (e.g.) $\tilde{\phi}_p$ to the rotating case, since the poloidal and toroidal motion of the plasma may not be very closely connected. Fluctuations may therefore still propagate poloidally, giving the results shown in Figure 5.17.

The velocity shear, $dv_{\rm phase}/dr$, is shown in Figure 5.18 with $v_{\rm phase}$ shown on the same radial scale. The width of the shear layer present during locking ($\simeq$ 2.4 cm) is broader than the reference layer ($\simeq$ 1.7 cm) by roughly 40%. The maximum shear ($1.5 \times 10^5 {\rm s}^{-1}$) is about 60% lower than the reference maximum (dashed curve) and the position of this maximum ($\rho = 0.95$) is shifted inwards, relative to the reference case, which has maximum shear at $\rho = 0.98$. Since the locked phase leads to a *decrease* in the velocity shear, a degradation in the momentum confinement is expected.

The absolute fluctuation levels of $i_{\rm sat}$ and ϕ_f are shown in Figure 5.19 with the shear layer also shown on the same radial scale. The fluctuation levels of $i_{\rm sat}$ drop sharply from $\rho = 0.97$ to all smaller values of ρ, i.e. where the shear is high, indicating a strong reduction in turbulence in this quantity in this range. The absolute fluctuation level of ϕ_f increases from limiter shadow to about $\rho = 0.97$ and then flattens off over the shear layer region (c.f. Figure 4.18).

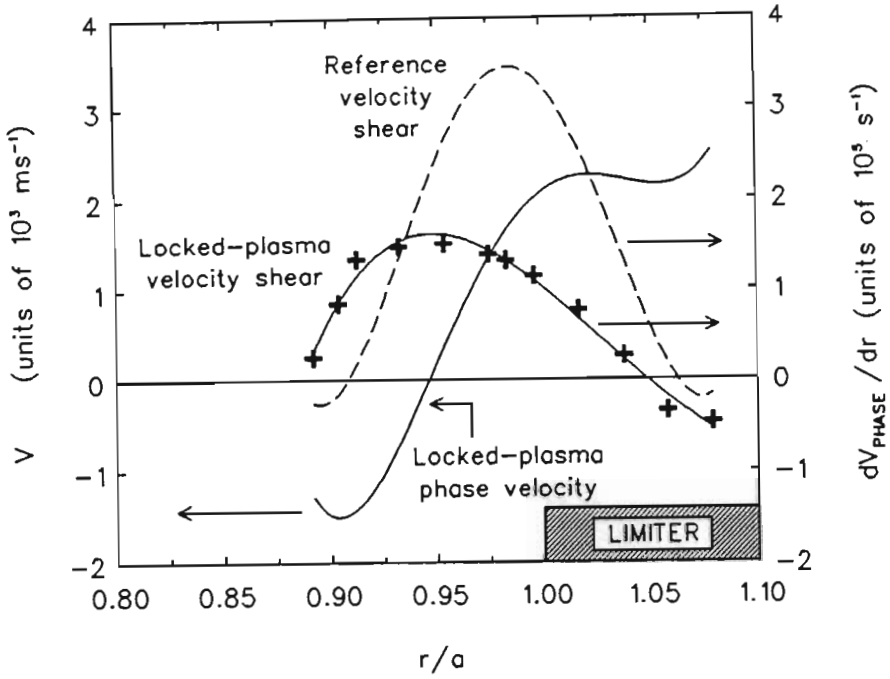

Figure 5.18: Velocity shear profile during locking. The phase velocity is also shown for comparison with the position of maximum shear.

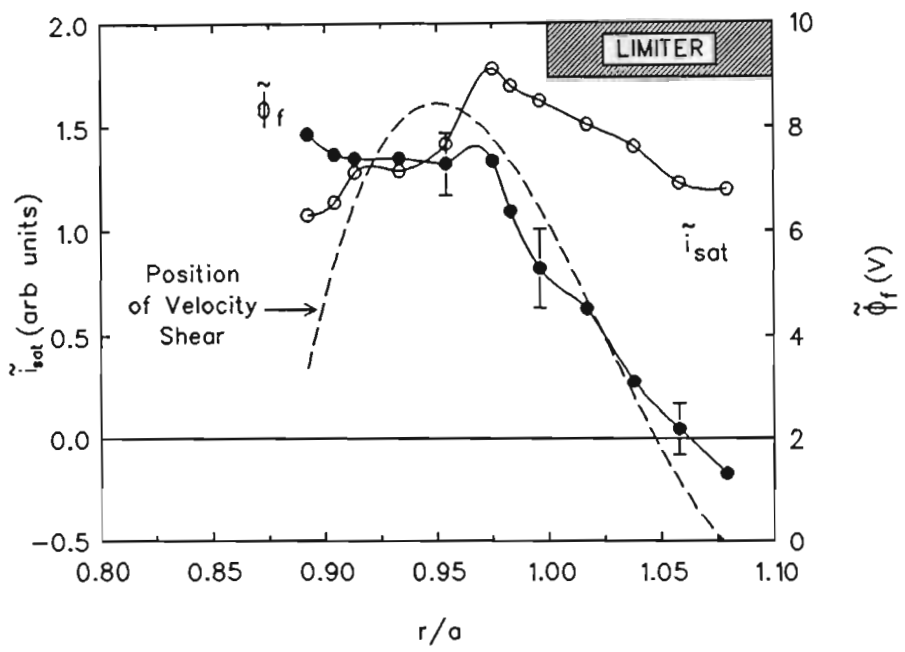

Figure 5.19: Absolute fluctuation levels of $\tilde{i}_{sat}$ and $\tilde{\phi}_f$ with the velocity shear layer shown as a dashed curve during the locked phase. At the position of maximum shear, $\tilde{i}_{sat}$ drops significantly whilst $\tilde{\phi}_f$ remains constant.

$S(\omega, k_\theta)$ Spectra

$S(\omega, k_\theta)$ spectra and their associated contour plots are shown in Figures 5.20(a) through (c) for the saturated ion current fluctuations at the three radial positions discussed earlier ($\rho = 0.95, 1.00$ and 1.04). The $S(\omega, k_\theta)$ spectra for the floating potential are practically identical to those shown here for $\tilde{i}_{\mathrm{sat}}$. As in the reference case (Figure 4.20), the spectra are peaked but broad with $\Delta\omega/\omega \approx \Delta k_\theta/k_\theta \approx 0.5$. There is a clear change in the propagation direction from bulk plasma to limiter shadow region and, at the limiter, the $S(\omega, k_\theta)$ spectrum is broader than the spectra obtained 1 cm either side of it with $\Delta k_\theta \simeq 5\,\mathrm{cm}^{-1}$.

The $S(k_\theta)$ spectrum exhibits a broad peak at $k_\theta \approx 3\,\mathrm{cm}^{-1}(k_\theta r_s \simeq 0.30)$ with a fall off proportional to $k_\theta^{-3\pm1}$ for larger wavenumbers as shown in Figure 5.21, measured at $\rho = 0.93$. The ion gyroradius is 0.10 cm at $\rho = 0.93$ and 0.01 cm in the limiter shadow. As in the reference case, the poloidal wavenumber spectrum indicates that k_θ does not vary much between $0.89 \leq \rho \leq 1.05$ and remains at about $1.5\,\mathrm{cm}^{-1}$ at each radial position. This gives a value of $\overline{k}_\theta r_s$ of between 0.13 and 0.15.

Radial Particle Flux

Figure 5.22 shows the frequency resolved, fluctuation induced particle flux measured at $\rho = 0.93$ during the locked phase. The data sample used was $\simeq 5.4$ ms in duration, comprising 42 $\times 128\,\mu$s blocks. The dashed curve is the transport spectrum during a reference discharge (rotating plasma) with the probe in the same position.

The spectrum is positive at all frequencies with the bulk of the flux ($= \int \tilde{\Gamma}(f)df$) being below 200 kHz. Above this frequency, the transport spectrum is small but still positive. At each frequency above about 30 kHz, the spectrum obtained during the locked phase is higher than that obtained during the high Mirnov (rotating plasma) activity case. Compared with the rotating phase the spectrum is distinctly broader with peak power at a higher frequency of about 50 kHz than about 20 kHz measured for the rotating phase.

The particle flux at $\rho = 0.93$ is shown in Figure 5.23 for several discharges as a function of time. Locking occurred at the times indicated in the figure since it is not always exactly the same time for each shot. In most cases, the locked phase persisted to an early major disruption but in shots #9157, #9341 and #9346 the plasma rerotated after a period of locking as indicated in the Figure. During the period of the rotating phase the particle flux increases in all cases almost linearly as it does during the reference cases

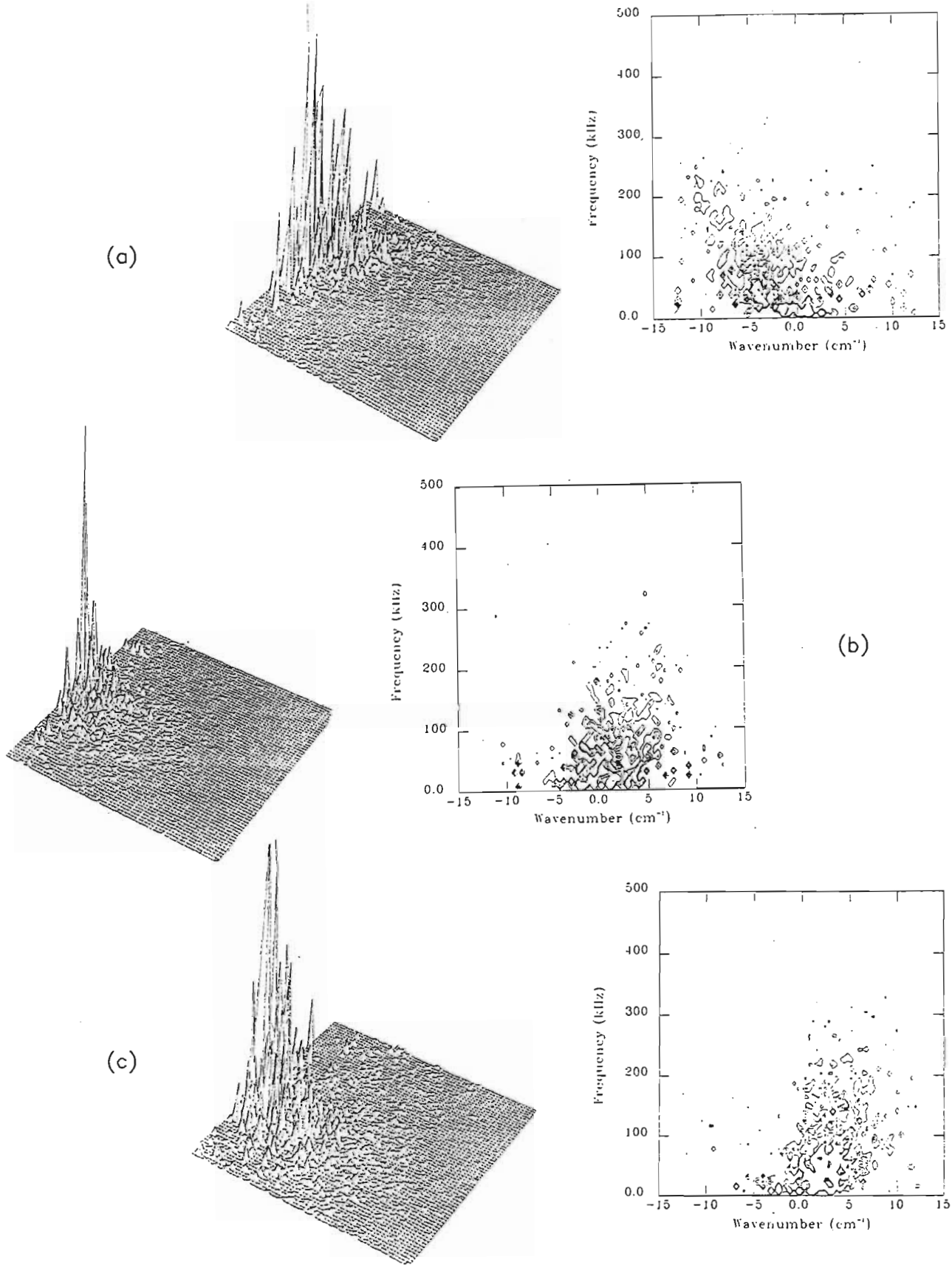

Figure 5.20: $S(\omega, k_\theta)$ spectrum and contour plot of $\tilde{i}_{\mathrm{sat}}$ at $\rho =$ (a) 0.95, (b) 1.00, and (c) 1.04 during a 5 ms period of the locked phase.

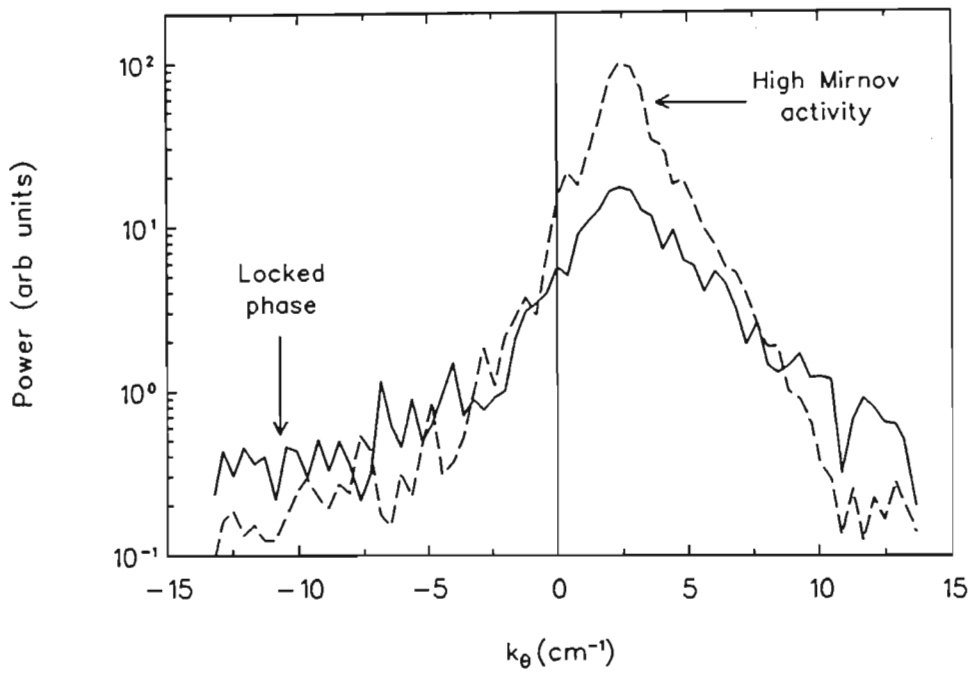

Figure 5.21: Power spectrum as a function of wavenumber, $S(k_\theta)$, for $\tilde{\phi}_f$ measured at $\rho = 0.93$ during about 5 ms of locked phase.

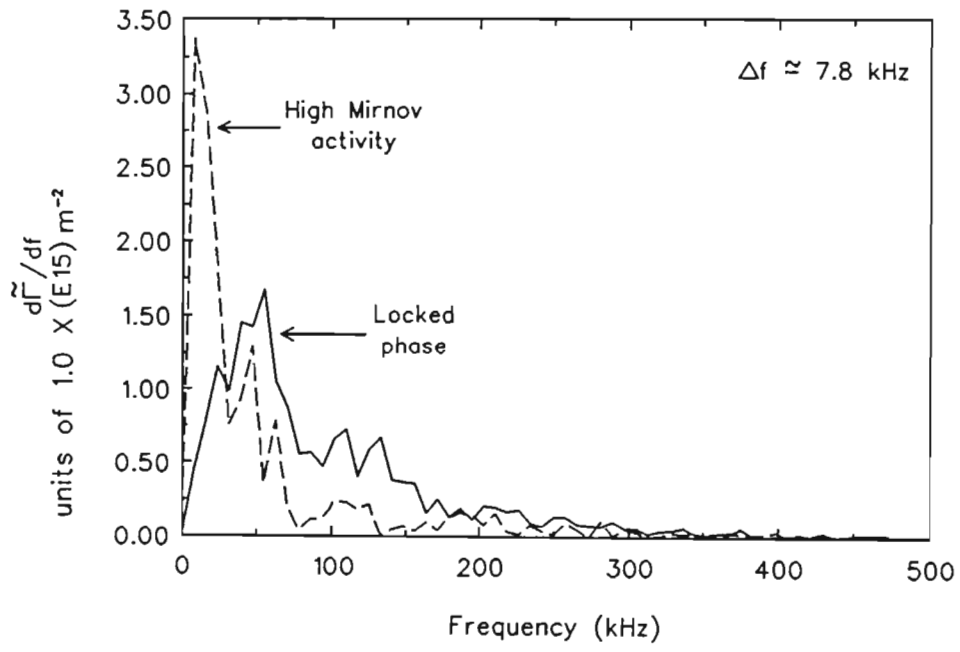

Figure 5.22: $\tilde{\Gamma}$ spectrum taken at $\rho = 0.93$ during a 5 ms period of locking.

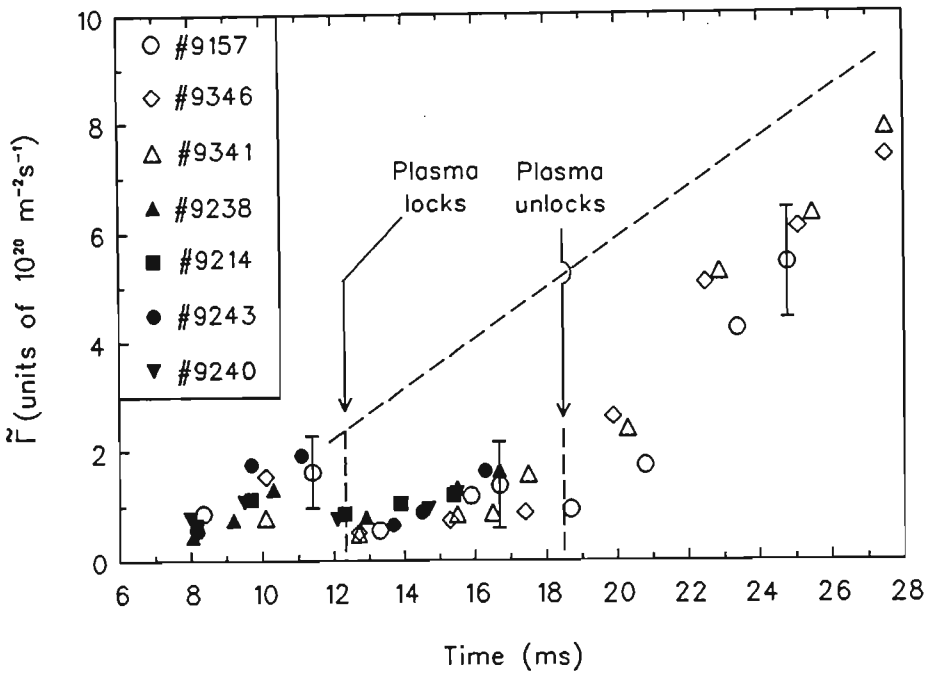

Figure 5.23: $\tilde{\Gamma}(t)$ taken at $\rho = 0.93$ using 2 ms sampling periods during locking. Rotating case $\tilde{\Gamma}$ is shown as a dashed curve.

(as expected: see Figure 4.23) at a rate of $\approx 4.8 \times 10^{22}\,\mathrm{m^{-2}s^{-2}}$. At locking the value of $\tilde{\Gamma}$ decreases somewhat, by about 50% within the error bars. Also the rate of increase of $d\tilde{\Gamma}/dt$ drops abruptly to zero and throughout the locked phase the flux remains constant until the major disruption. For shots #9157, #9341 and #9346 the rate of increase again changes abruptly as the plasma unlocks and continues to increase at a rate greater than that prior to locking with $d\tilde{\Gamma}/dt \approx 5.8 \times 10^{22}\,\mathrm{m^{-2}s^{-2}}$. The tendency is to reach the same flux as the rotating case but with a delay of several τ_E.

The particle flux as a function of minor radius is shown in Figure 5.24. Points were obtained using 23 data ensembles of 128 μs duration ($\approx$ 3 ms) during the locked phase of several shots at each radial position. The dashed curve is the flux measured during reference discharges for comparison.

A rapid increase in $\tilde{\Gamma}(\rho)$ is observed from limiter shadow into bulk plasma. For $\rho \gtrsim 1.02$ the value of $\tilde{\Gamma}(\rho)$ [locked] and $\tilde{\Gamma}(\rho)$ [reference] are very similar. At values of $\rho \lesssim 1.02$ the flux continues to increase but not as rapidly as during the reference case. The profile is broad with peak transport at $\rho \approx 0.92 \pm 0.02$ of $\approx 1.5 \times 10^{20}\,\mathrm{m^{-2}s^{-1}}$ where, as with the reference case, ϕ_p (Figure 5.7) and $\tilde{\phi}_p$ (Figure 5.9) are a maximum. At values of $\rho \lesssim 0.9$ the transport either decreases slightly or remains constant but, since these values are within the error bars and since the probe could not reach smaller values of ρ (due to the

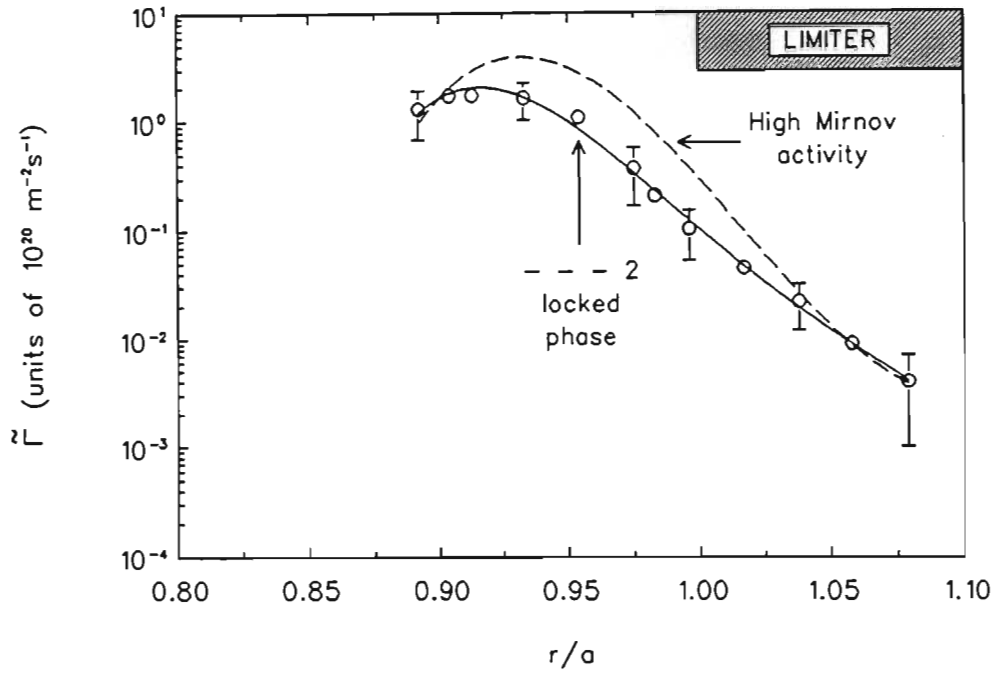

Figure 5.24: $\tilde{\Gamma}(\rho)$ profile using 4 ms sampling periods during the locked phase. Peak transport is at $\rho \simeq 0.92$.

presence of the probe precipitating a major disruption), this could not be ascertained accurately.

Changes in particle transport upon mode locking take place over a transport time-scale rather than the MHD time-scale, subsequently altering plasma profiles (usually in a destabilizing manner). The variation in the edge physics that resonant magnetic perturbations (RMP) create could also explain much of the variability and complexity of the results of many RMP experiments (TODD (1992)).

The 2D-profile of $\tilde{\Gamma}(\rho, t)$ is shown in Figure 5.25 showing the features discussed above. Peak transport is at 0.92 ± 0.02, the profile is broader in space than during the reference case (Figure 4.25) and for $\rho \gtrsim 1.02$ the flux is very low.

Diffusion Coefficients

The effective diffusion coefficient, D_{eff}, and the measured phenomenological Bohm coefficient, D_{Bohm}, are compared at the five radial positions where T_e was measured is given in Table 5.1. Whilst, as may be expected, D_{Bohm} is roughly the same as during reference shots (Table 4.3), D_{eff} is smaller at each radius.

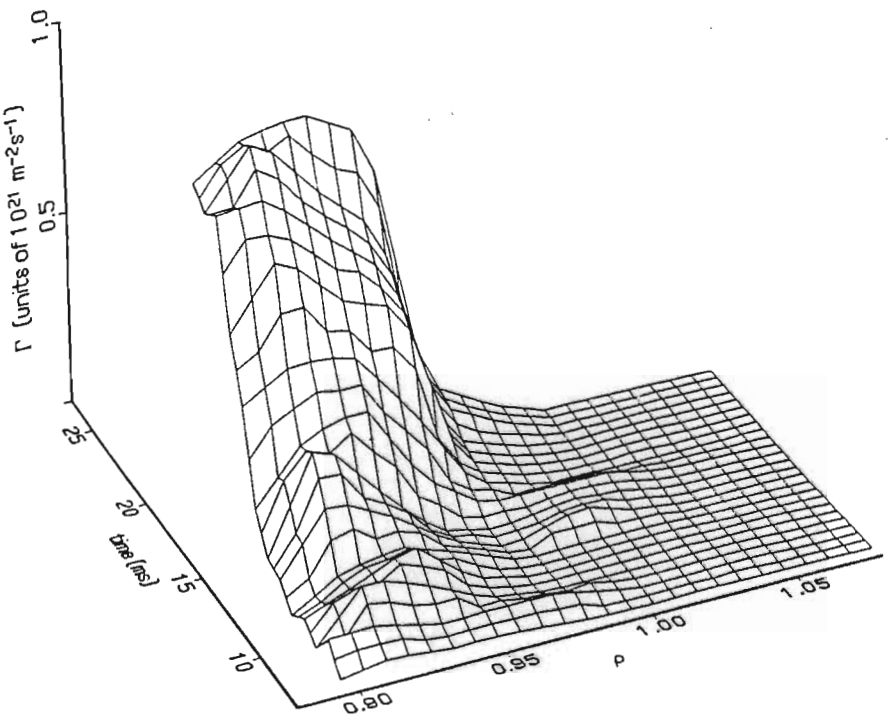

Figure 5.25: 2D plot of $\tilde{\Gamma}(\rho, t)$ using 2 ms sampling periods during high ($0 \leq t \leq 12$ ms) Mirnov activity, the locked phase ($12 \leq t \leq 18$ ms) and the low Mirnov activity ($18 \leq t \leq 24$ ms).

Table 5.1: Comparison of Bohm diffusion coefficient and D_{eff} during the locked phase.

COEFFICIENT	ρ				
$(\text{m}^2\text{s}^{-1})$	**0.93**	**0.95**	**0.97**	**1.00**	**1.02**
Bohm	1.70	1.54	1.46	1.27	1.11
Effective	6.95	4.59	1.59	0.24	0.14

5.2.2 Double Probe Results

For the results presented in this Section, the tips were again configured as a double probe. Probe current flowing between the tips was sampled every 1 μs for the duration of the discharge (usually $\simeq$ 25 ms) and the locked phase data later extracted.

Edge Electron Temperatures

The i vs V_{bias} curves for the five different radial positions chosen are shown in Figure 5.26. The positions are the same as those chosen in the reference discharges (Figure 4.26), i.e. between $0.93 \leq \rho \leq 1.02$. Error bars are again an indication of shot-to-shot scatter and the variation of $\bar{i}$ over equal sized segments within the blocks of locked-plasma data.

The temperatures at each radial position are lower during the locked phase than during the reference shots (dashed curve) as shown in Figure 5.27 whilst exhibiting the same trend, i.e. decreasing monotonically from bulk plasma to limiter shadow (Figure 4.27). The goodness of fit parameter, χ, was calculated and again found to be small ($\lesssim 1.0 \times 10^{-3}$) for each curve but greater by about 4$\times$ the value of χ for the reference cases. The ion saturated current decreases from positions in the bulk plasma to those in the limiter shadow from 37 mA at $\rho = 0.93$ to 12 mA at $\rho = 1.02$. Both V_{offset} and i_{offset} were again small ($< 15\%$) relative to the electron temperature (in eV) and saturated ion current, respectively, at each radius.

The electron temperature decreases from 16.3 eV to 10.7 eV over 2 cm giving a range of ∇T_e of $\simeq 3.3 \pm 0.8\,\text{eV cm}^{-1}$. This gives an effective L_{T_e} of 5.1 $\pm$ 2 cm at the limiter and a radial range of L_{T_e} of 4.6 $\pm$ 2 cm. The electron thermal diffusivity coefficient may be calculated during the locked phase using Equation 4.4 and is found to be $\chi_e \approx 2.5 \pm 0.7\,\text{m}^2\text{s}^{-1}$ or $2\frac{1}{2}\times$ larger than during the rotating plasma phase The values of V_{offset} and T_e, returned by the ASYST program, are again used in the second curve-fitting program to calculate the fluctuation terms discussed in the previous Chapter.

Electron Temperature Fluctuations

The results of the fluctuation data analysis are shown in Figures 5.28(a) through (e) for the same five radial positions as those used in the previous Chapter. The bold faced line again represents the best fit through the data values comprising contributions from $\tilde{n}_e/n_e$, $\tilde{V}_d/T_e$ and $\tilde{T}_e/T_e$ in (i) and the cross-correlation terms viz., $\langle \tilde{n}_e \tilde{T}_e \rangle / n_e T_e$, $\langle \tilde{n}_e \tilde{V}_d \rangle / n_e T_e$ and $\langle \tilde{V}_d \tilde{T}_e \rangle / T_e^2$ in (ii).

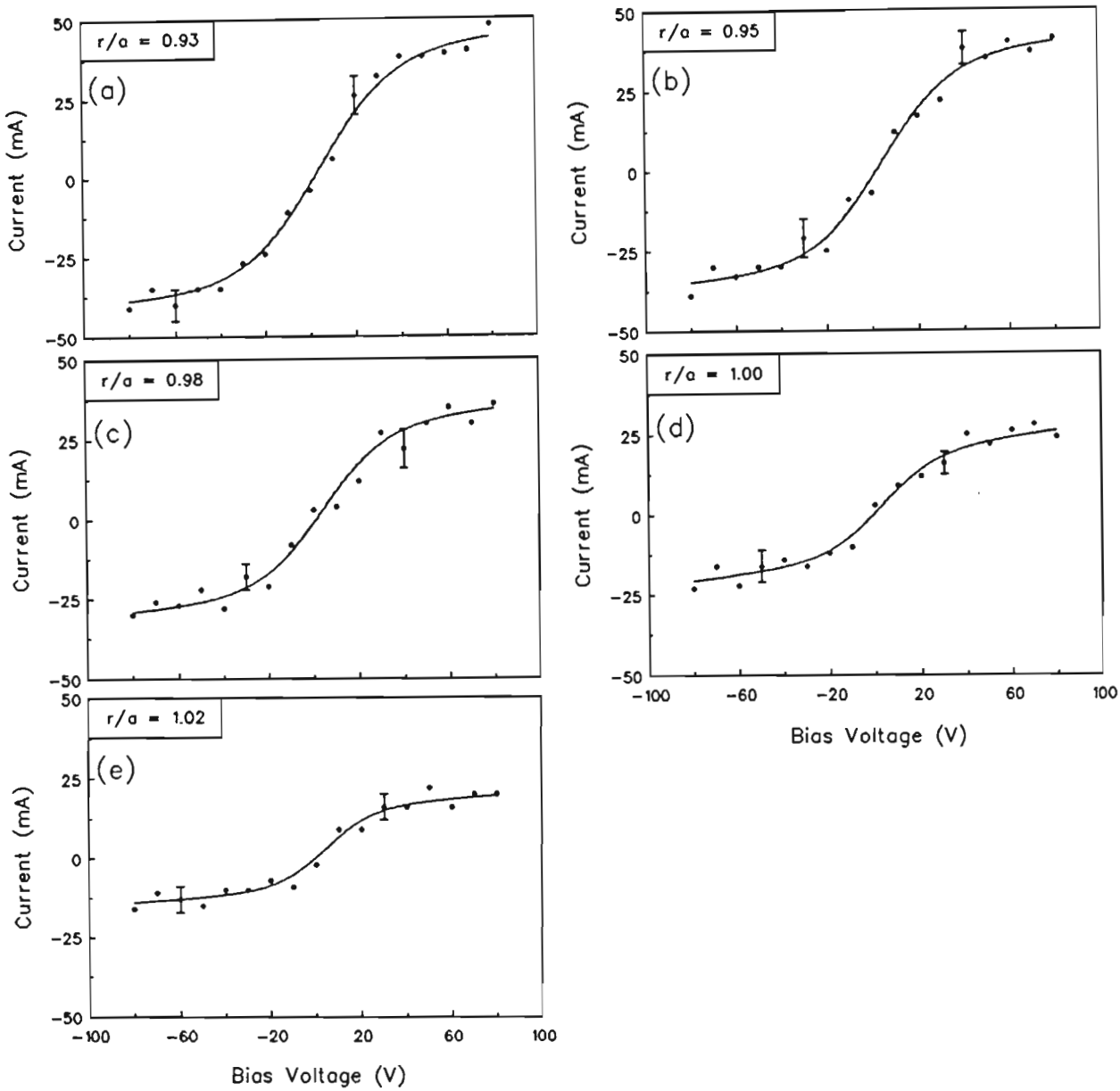

Figure 5.26: i vs V_{bias} characteristics for five radial positions, indicated in the text during 5 ms of locking. Error bars indicate shot-to-shot scatter as well as $\langle i \rangle$, i.e. variation of $\bar{i}$ over five 1000 μs blocks within the 5 ms sample used.

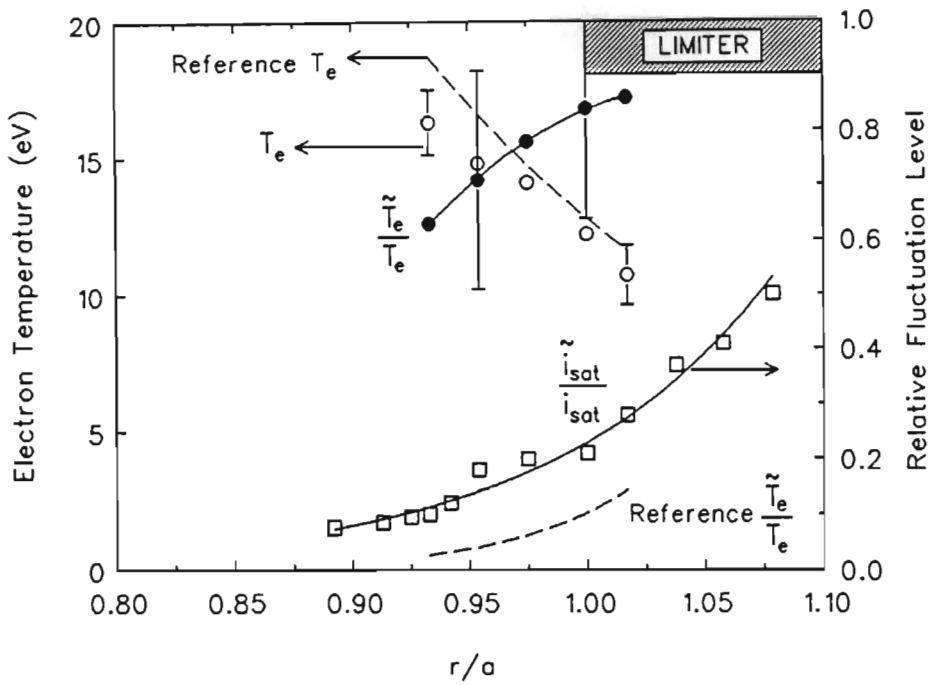

Figure 5.27: Radial profiles of T_e, $\tilde{T}_e/T_e$ and $\tilde{i}_{sat}/i_{sat}$ (for comparison) during locking.

Electron temperature fluctuations during the locked phase are very much higher than those measured during the reference plasmas, increasing from 0.63 at $\rho = 0.93$ to 0.86 at $\rho = 1.02$ (Figure 5.27). This represents an increase in $\tilde{T}_e/T_e$ during locking of about 27 $\times$ that during the rotating phase (Figure 4.27). Comparison of fluctuation levels at these radii gives a range of $\tilde{T}_e/T_e \approx (3.0 \pm 1.0)\tilde{n}_e/n_e$ with this value decreasing from bulk plasma to limiter shadow, as T_e increases. This high level is not completely ruled out by some thermally driven turbulence models (e.g. LEBOEUF *et al*, (1991)).

As in the reference case, an estimate of the *spectral* power of the fluctuation components can be obtained from the auto-power spectra of $\tilde{i}$, the approximation made by determining the fraction of the total power in the specified spectral band. The three ranges investigated here were again, $0 \rightarrow 500$ kHz, $0 \rightarrow 100$ kHz and $25 \rightarrow 75$ kHz. Results from the first case appear in Figure 5.28. Between 90 and 100% of the power was observed in the frequency range $0 \rightarrow 100$ kHz and about $75 \rightarrow 90\%$ of the power in the $\tilde{n}_e/n_e$ and $\tilde{V}_d/T_e$ spectra were observed in the $25 \rightarrow 75$ kHz range. In contrast to the reference value of power, over 80% of the spectral power was observed in this range for $\tilde{T}_e/T_e$ and the cross-correlation term, $\langle \tilde{V}_d \tilde{T}_e \rangle / T_e^2$ during locking, indicating that these fluctuations now exhibit the bulk of their power at higher frequencies, *above* 25 kHz. This observation could have some consequences for the high frequency magnetic mode, observed during locking, discussed later.

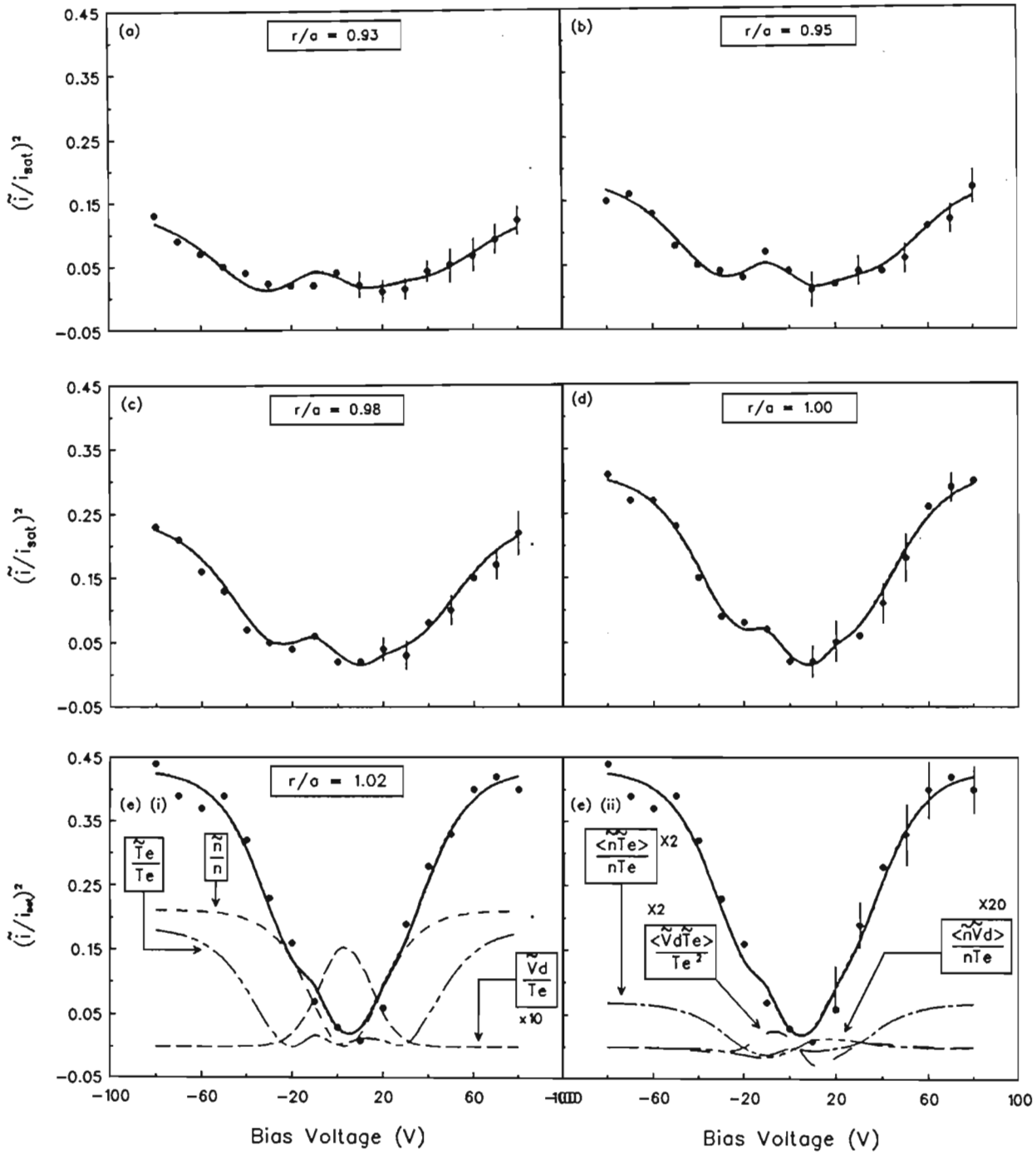

Figure 5.28: (a) — (e) $(\tilde{i}/i_{\rm sat})^2$ vs $V_{\rm bias}$ at 5 radial positions during locking. (e)(i) shows the contributions to the fitted curve from $\tilde{n}_e/n_e$, $\tilde{V}_d/T_e$ and $\tilde{T}_e/T_e$ and (e)(ii) the cross-correlation terms: $\langle \tilde{n}_e\tilde{T}_e \rangle/n_eT_e$, $\langle \tilde{n}_e\tilde{V}_d \rangle/n_eT_e$ and $\langle \tilde{V}_d\tilde{T}_e \rangle/T_e^2$.

The change in $d\tilde{\Gamma}/dt$ is consistent with the observed change in $\overline{n}_e(t)$ (FLETCHER *et al*, (1992)) and $n_e(t)$ (Figure 5.4). However, $\tilde{i}_{\rm sat}/i_{\rm sat}$ and $\tilde{\phi}_f/T_e$ are used in the calculation of $\tilde{\Gamma}$ instead of the electron density and plasma potential. Since both quantities depend strongly on the level of $\tilde{T}_e/T_e$ and since this quantity is very high during the locked phase, the estimation of $\tilde{\Gamma}$ is seriously affected. Aspects of this problem were addressed by FILIPPAS (1991) who examined the commonly used signal processing methods based on computer simulations as well as higher order correlation function analysis and problems such as conditional sampling. TSUI *et al*, (1991), using the triple probe technique, found measurements of $\tilde{T}_e$ to be in approximate agreement with the double probe technique and discussed possible sources of errors. The results obtained indicated that the plasma tends to become *less* electrostatic toward the hotter interior.

Other Fluctuating Quantities

As can be seen from Figure 5.27 the fluctuation level of $\tilde{i}_{\rm sat}/i_{\rm sat}$ rises monotonically from 0.18 at $\rho = 0.93$ to about 0.46 at $\rho = 1.02$. This may be correlated with $\tilde{n}_e/n_e$ as discussed in Chapter 4. The estimated uncertainty is only about 10% for this quantity, so $\tilde{n}_e/n_e$ is certainly increasing from the bulk plasma into the limiter shadow region. Comparison of these results with Figure 5.9 shows good agreement—in both absolute values and trend—and is well within all estimated errors and uncertainty in measurements. Using Equation 4.2, because of the large value of $\tilde{T}_e/T_e$, the error using $\tilde{i}/i_{\rm sat}$ instead of $\tilde{n}_e/n_e$ is now between 25 and 50%, depending on the sign of $\langle\tilde{n}_e\tilde{T}_e\rangle/n_eT_e$.

The cross correlation term, $\langle\tilde{n}_e\tilde{T}_e\rangle/n_eT_e$, is relatively small but about 5× larger at each radial position than that measured during the reference cases. This level increases, within the error bars, from bulk plasma into limiter shadow. The values of $\langle\tilde{V}_d\tilde{T}_e\rangle/T_e^2$ are also small (< 0.1 at all positions) but again about 3× larger at each radius than the reference values. This value decreases monotonically from bulk plasma into limiter shadow. The particle transport term, $\langle\tilde{n}_e\tilde{V}_d\rangle/n_eT_e$, is about 20% lower than the values obtained for the reference case but the trend is very similar in the two cases. At larger values of ρ, the terms are approximately the same. A comparison of $\tilde{\Gamma}$, calculated using these values in Equation 3.23 with density from Figure 5.5 and temperature from Figure 5.27, with the spectral analysis technique shows that, in each case, the values agreed very well within the error bars in both magnitude and trend.

The normalised coherence of the correlation terms discussed above is shown in Figure 5.29(a) through (c). In each graph the values obtained for the reference cases are shown as dashed lines for comparison.

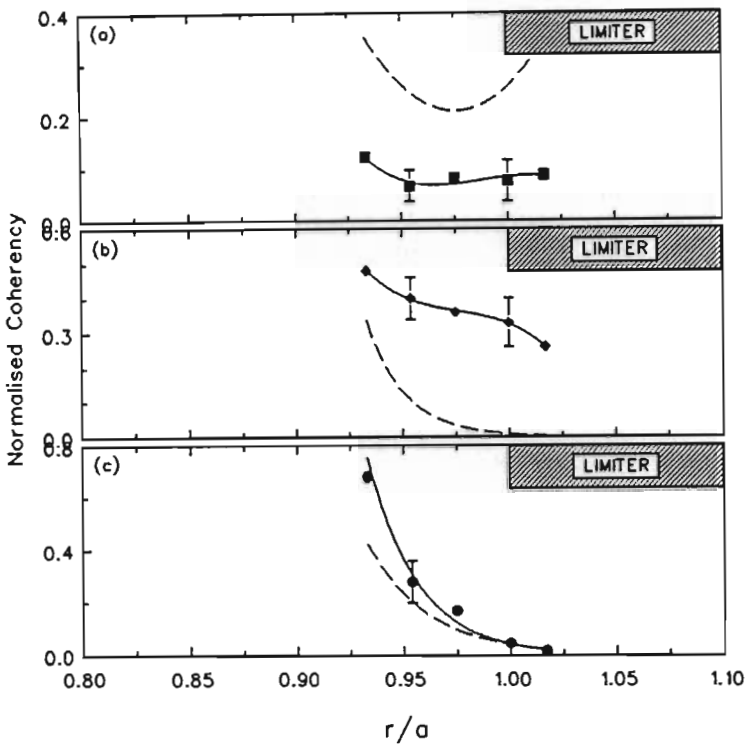

Figure 5.29: Radial profiles of the normalised coherency between the fluctuating quantities during locking: (a) $\langle \tilde{n}_e \tilde{T}_e \rangle / (\tilde{n}_e \tilde{T}_e), (b) \langle \tilde{n}_e \tilde{V}_d \rangle / (\tilde{n}_e \tilde{V}_d)$ and (c) $\langle \tilde{V}_d \tilde{T}_e \rangle / (\tilde{T}_e \tilde{V}_d)$. The dashed curves show the same quantities during the rotating phase.

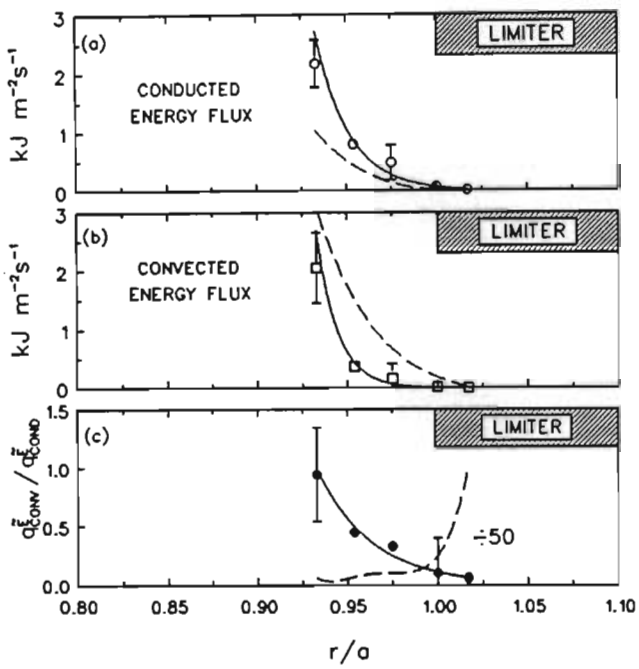

Figure 5.30: Radial profiles of the fluctuation induced (a) conducted and (b) convected energy flux and (c) the quotient of these quantities, $q^{\tilde{E}}_{\text{conv}}/q^{\tilde{E}}_{\text{cond}}$, during locking.

Energy Fluxes

The ratio of the convected and conducted energy fluxes given by Equation 5.30(c) is significantly lower than for the reference value at each radial position as shown in Figure 5.30(a). The trend is also reversed; the ratio decreases exponentially from bulk plasma to limiter shadow in contrast to the exponential *increase* observed during the rotating-plasma phase. At $\rho = 0.93$ the ratio is $\simeq 1.0$ so the energy fluxes are approximately the same at this position. At the same radius for the reference case, this ratio is $\simeq 3.0$. In the shadow region at $\rho = 1.02$, $q^{\tilde{E}}_{\text{conv}}/q^{\tilde{E}}_{\text{cond}} \approx 0.06$, whilst during the rotating phase, $q^{\tilde{E}}_{\text{conv}}$ is $\simeq 50 \times q^{\tilde{E}}_{\text{cond}}$.

Figures 5.30(b) and (c) show that whilst both energy fluxes show the same trend during the locked phase as they do during reference shots, the conducted energy flux is larger and the convected energy flux smaller at each radial position.

The fluctuating quantities and cross correlation terms, returned by the ASYST program, as well as associated (calculated errors) are shown as a summary in Table 5.2.

Table 5.2: Parameters deduced for double probe measurements during the locked phase.

	$\rho =$					ERROR
QUANTITY	**0.93**	**0.95**	**0.97**	**1.00**	**1.02**	±(%)
i_{sat} (mA)	37	32	26	16	12	5
T_e (eV)	16.3	14.8	14.1	12.2	10.7	20
$\tilde{n}_e/n_e$	0.18	0.23	0.28	0.34	0.46	10
$\tilde{V}_d/T_e$	0.31	0.31	0.29	0.26	0.25	25
$\tilde{T}_e/T_e$	0.63	0.71	0.78	0.84	0.86	50
$\langle\tilde{n}_e\tilde{V}_d\rangle/n_eT_e$	0.038	0.020	0.014	0.004	0.002	40
$\langle\tilde{T}_e\tilde{V}_d\rangle/T_e^2$	0.093	0.087	0.081	0.072	0.056	50
$\langle\tilde{n}_e\tilde{T}_e\rangle/n_eT_e$	0.014	0.011	0.018	0.022	0.035	30
$\chi^2(\times10^{-4})$	102	65	41	29.6	16.5	
$\tilde{E}_\theta/T_e$ (cm^{-1})	0.78	0.78	0.73	0.65	0.63	50
$\langle\tilde{n}_e\tilde{E}_\theta\rangle/n_eT_e$ (cm^{-1})	0.10	0.05	0.04	0.01	~0.00	40
$\langle\tilde{T}_e\tilde{E}_\theta\rangle/T_e^2$ (cm^{-1})	0.23	0.22	0.20	0.18	0.14	50

Particle and Energy Confinement

Power losses during the locked phase due to electrostatic fluctuation driven energy fluxes may be determined using the power balance equation (Equation 4.5). It should be pointed out, however, that all fluxes here are determined from measurements at one point. Since tearing mode theory inherently involves distorted flux surfaces it is difficult to verify the assumption that these results are representative of global parameters.

The value of β (Equation 4.6) during the locked phase was also calculated by FLETCHER *et al*, (1992) and found to be $\approx 1.0 \times 10^{21}$ m^{-3}s^{-1}. Using this value in the power balance equation, $\int_V (dW/dt)dV$ is about 15 kW. Total input power, P_{in}, is again ≈ 240 kW using 120 kA peak current and $V_{\text{loop}} = 2$ V. Assuming poloidal and toroidal symmetry for $q^{\tilde{E}}_{\text{conv}}$ and $q^{\tilde{E}}_{\text{cond}}$, the fluctuation induced power losses, $\tilde{P}$, ($= [q^{\tilde{E}}_{\text{conv}} + q^{\tilde{E}}_{\text{cond}}] \times A|_{\rho=0.93}$) are about 22 kW. The power lost by other mechanisms, P_{other}, is therefore roughly 200 kW, the same as estimated for the reference case, indicating that the contribution to total power loss by $\tilde{P}$ is only about 10%, of which $q^{\tilde{E}}_{\text{conv}}$ and $q^{\tilde{E}}_{\text{cond}}$ contribute about 50% each at $\rho = 0.93$.

The particle confinement time could again be estimated by first determining the contribu-

tion to the total flux by $\tilde{\Gamma}$. Using $\beta \approx 1.0 \times 10^{21}\,\mathrm{m^{-3}s^{-1}}$, the value of $S(\approx 1.2 \times 10^{21}\,\mathrm{s^{-1}})$ and $\tilde{\Gamma}$ at the limiter $(= 0.103 \times 10^{20}\,\mathrm{m^{-2}s^{-1}})$ in Equation 4.7, Γ_{other} was found to be $\approx 1.73 \times 10^{20}\,\mathrm{m^{-2}s^{-1}}$ or about 16 times larger than $\tilde{\Gamma}$. Substituting these values into Equation 4.8, $\tau_p \simeq 11 \pm 4\,\mathrm{ms}$—very similar to the particle confinement measured for the reference cases.

The energy confinement time (Equation 4.9) was found to be $\tau_E \approx 60 \pm 20\,\mathrm{ms}$ or about $\frac{1}{2}$ that estimated for the reference cases and 16× that estimated by ROBERTS *et al*, (1991b). As with the reference case the τ_E measured in the above way makes the assumption that all energy losses occur via particles. Other loss mechanisms (e.g. radiation) were ignored in this calculation but included in the results obtained by ROBERTS *et al*, (1991b).

5.2.3 Comparison with other Results

Many experiments have been done on machines involving resonant magnetic perturbations (RMP's) e.g. PULSATOR (PULSATOR TEAM (1985)), TOSCA (ELLIS *et al*, (1984)), TEXT (OHYABU (1985)) and TEXTOR (NICOLAI *et al* (1985)) and COMPASS (MORRIS *et al*, (1990a, 1991)). In most of these cases, however, the main objective for the installation of the helical coils was to control disruptive instabilities via the influence of certain magnetic surfaces in the plasma. In the case of limiter coils the aim was mainly to study plasma-limiter interactions.

MORRIS *et al*, (1990b) reported that, on COMPASS, $m/n = 2/1$ RMP's led to a partial stabilisation of $m = 2$ modes, but otherwise had no effect even when the islands from the vacuum field calculations were predicted to be large (i.e. $W/a = 10 \rightarrow 15\%$). The effects that were observed were plausibly attributed to changes in the plasma boundary, such as recycling, due to sidebands of the primary RMP. Larger RMP currents were applied to COMPASS and the results (MORRIS *et al*, (1990a)) were

- the appearance of a large, stationary $n = 1$ structure in the plasma
- suppression of the sawteeth after a delay of 1—2 ms while the 2/1 field penetrates (but see also NOTHNAGEL (1991))
- a marked change in the toroidal impurity rotation velocity
- a reduction in τ_E ($\lesssim 30\%$), T_e ($\lesssim 20\%$), T_i ($\lesssim 10\%$), n_e ($\lesssim 10\%$) and
- a substantial variation in the edge potential and $\tilde{\phi}_f$ and reversal in the direction of propagation of edge fluctuations.

When the RMP was removed, a large rotating $m/2 = 2/1$ mode appeared transiently with a modest $m = 1$ component in the plasma core. This was interpreted as the stationary mode accelerating: the plasma velocity rapidly increased to its former value. Also, it was possible on COMPASS to rotate the RMP structure slowly in the toroidal direction (at $\sim 25\,\mathrm{kHz}$). When this was done the fluctuation level at a fixed Langmuir probe position was strongly modulated, as was the edge temperature, density, hard X-ray flux and ϕ_f, confirming that localised changes in the plasma edge did occur, similar to the results from *Tokoloshe*.

To date, however, no studies of mode locking on fluctuation induced particle transport have been done, so no meaningful comparisons with other results can be done at this stage.

5.2.4 $--+2$ Coil-Locked Results

Measurements from discharges in which the plasma was locked by the $--+2$ coils were very similar to those shown here for the $---2$ coil-locked plasmas. Complete radial scans of all parameters were made and all showed remarkable similarities to each other in trends and magnitudes and all were within the error bars or experimental uncertainties. The particle flux as a function of time is shown in Figure 5.31 measured at $\rho = 0.93$ for discharges in which the plasma was locked by the $--+2$ coils. The flux again increases linearly with time during the rotating phase to $t \approx 12\,\mathrm{ms}$ when the rotating plasma locked to the imposed field (or was slowed down by the imposed field and locked to a stray field). At this stage, as with the $---2$ case (Figure 5.23), the rate of increase of $\tilde{\Gamma}$ drops to zero and the flux remains constant in time, at $\tilde{\Gamma} = 2.2 \times 10^{20}\,\mathrm{m^{-2}s^{-1}}$. The rapid decrease in $\tilde{\Gamma}$ between the rotating phase and early locked phase, observed for the $---2$ case is also observed for the $--+2$ case but the decrease is not as great in the latter. The decrease for $---2$ is $\approx 50\%$ and for $--+2$, $\approx 33\%$. No shots were available for this case of duration $t \gtrsim 20\,\mathrm{ms}$: all ended with a major disruption earlier than this time. Also, no shots were recorded where the plasma unlocked and rerotated.

Note that $\tilde{\Gamma}$ is measured with the probe array at the toroidal position $\theta = 120°$, i.e. nearer to an imposed magnetic island in the $---$ case than in the $--+$ case, which could, in principle, affect these results in the island width were large enough.

The radial profile of the flux, measured during $--+2$ coil-locked discharges is shown in Figure 5.32. The values are very similar to and within the error bars of the data obtained for the $---2$ case, as shown in the Figure.

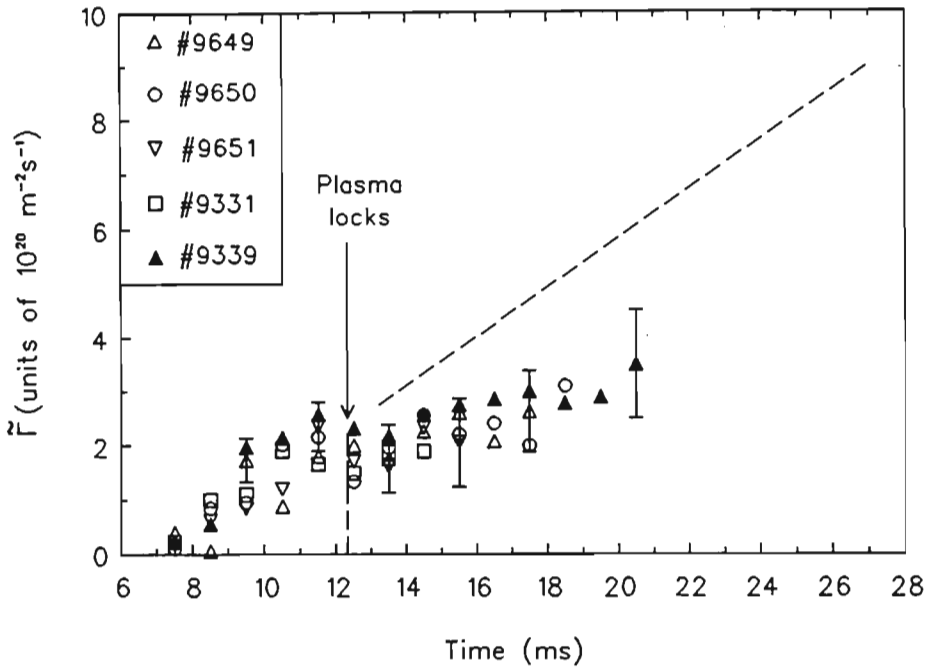

Figure 5.31: $\tilde{\Gamma}(t)$ for plasmas locked by the $--+2$ configuration at $\rho = 0.93$. Data for $t \geq 20$ ms were not available since the discharges ended in early disruptions.

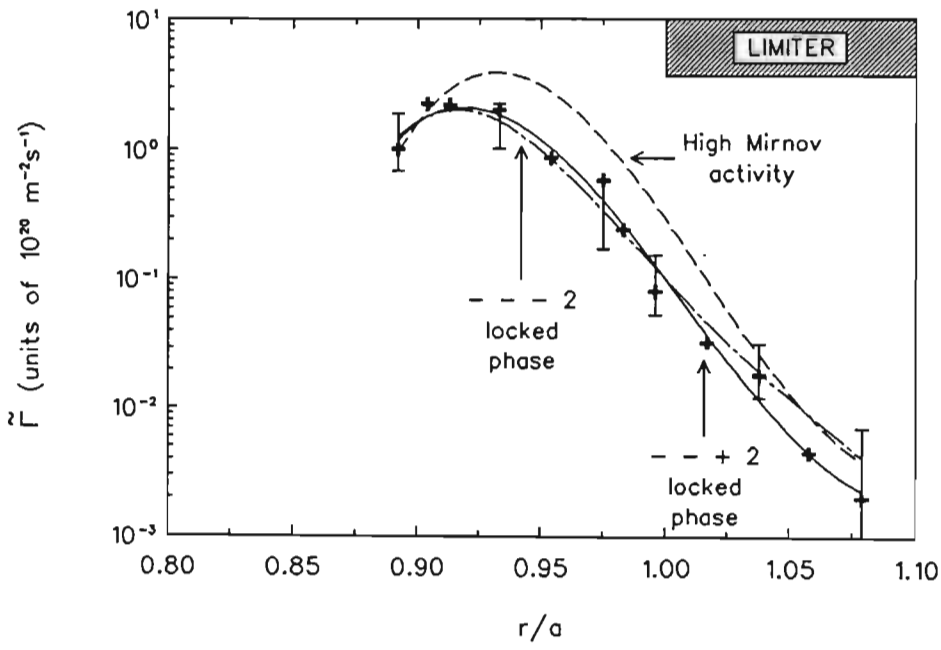

Figure 5.32: $\tilde{\Gamma}(\rho)$ for plasmas locked by the $--+2$ configuration during ≈ 4 ms of locked phase. Also shown are similar profiles for the $---2$ and reference cases.

In both cases, a short current pulse was applied to the coils of duration $\simeq 2\,\mathrm{ms}$. The similarity in results could be explained by the fact that, after the coil was switched off (and the external applied field $\rightarrow 0$), the plasma, though stationary, may be in an unstable position. With effectively no forces to restrain the stationary plasma, it can rotate until it is locked by the force arising from a stray edge field. Since this stray field, by definition, is unchanged by the helical coil current direction, the plasma will lock in the same position regardless of whether the $--{-}2$ or $--{+}2$ configuration is used. FLETCHER (1991) reported a similar conclusion based on high-speed photographic observations of the plasma column. It is also possible, however, that the probe is always in the magnetic stochastic region, even at $\rho = 0.93$ (1.5 cm into the plasma) and therefore no significant differences were detected between the $---2$ and $--+2$ cases, even though the locked magnetic islands may have been in different positions.

Furthermore, in a separate study a 2 mm single channel, vertically viewing $\mu-$wave interferometer was used to study $\overline{n}_e$ (FLETCHER *et al*, (1992)). Results showed the same behavior of $\overline{n}_e$ and $\tilde{\Gamma}$ as found here, i.e. reduction in $d\overline{n}_e/dt$ and $d\tilde{\Gamma}/dt$ during the locked phase(s) and it was suggested that the main effect of locking was to change the source function.

5.2.5 Minor Disruptions

All plasmas locked by the $--{+}2$ coils experienced a minor disruption shortly after locking. The minor disruption is accompanied by an expansion of the plasma column, a loss in I_p and a rapid loss of particles to the wall. The severity of the minor disruption was found to have a marked effect on most edge parameters, especially the measured particle flux as shown in Figures 5.31 and 5.33. Figure 5.31 shows $\tilde{\Gamma}(t)$ measured at $\rho = 0.93$ for several discharges locked by the $\ell = 2$ coil which experienced a minor disruption accompanied by a 2% or less loss of plasma current. Figure 5.33, at the same radius, shows $\tilde{\Gamma}(t)$ for several discharges which experienced a 4% or greater loss of plasma current following the minor disruption. At locking the flux starts decreasing as in Figure 5.31. After the minor disruption, the rate of increase of $\tilde{\Gamma}$ changes rapidly from $\approx 4.3 \times 10^{22}\,\mathrm{m^{-2}s^{-2}}$ to about $20.0 \times 10^{22}\,\mathrm{m^{-2}s^{-2}}$ or roughly $5\times$ the rate prior to the minor disruption. All such shots are relatively short in duration ($t \approx 17\,\mathrm{ms}$), ending with an early major disruption. The transport spectrum measured immediately after a minor disruption is shown in Figure 5.34 at $\rho = 0.93$ using 23 blocks of 128 μs duration. The time dependence of the plasma current is shown in Figure 5.35 with (a) showing a 4% and (b) a 1.5% loss of I_p.

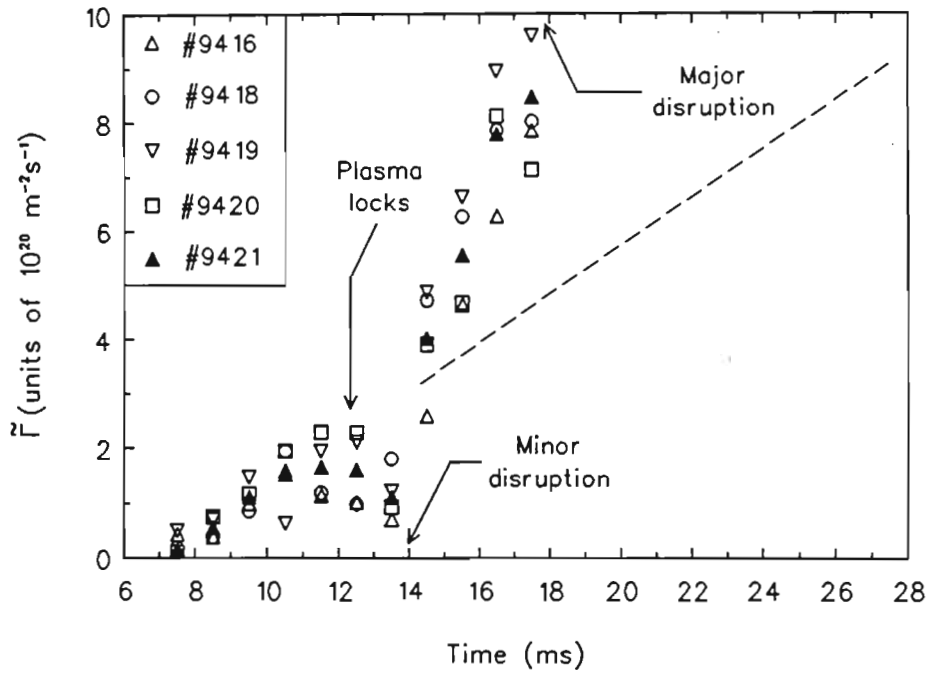

Figure 5.33: $\tilde{\Gamma}(t)$ for plasmas locked by the $--+2$ configuration, at $\rho = 0.93$, which experienced a minor disruption about 300 μs after locking. Also shown is $\tilde{\Gamma}$ during the rotating phase for comparison.

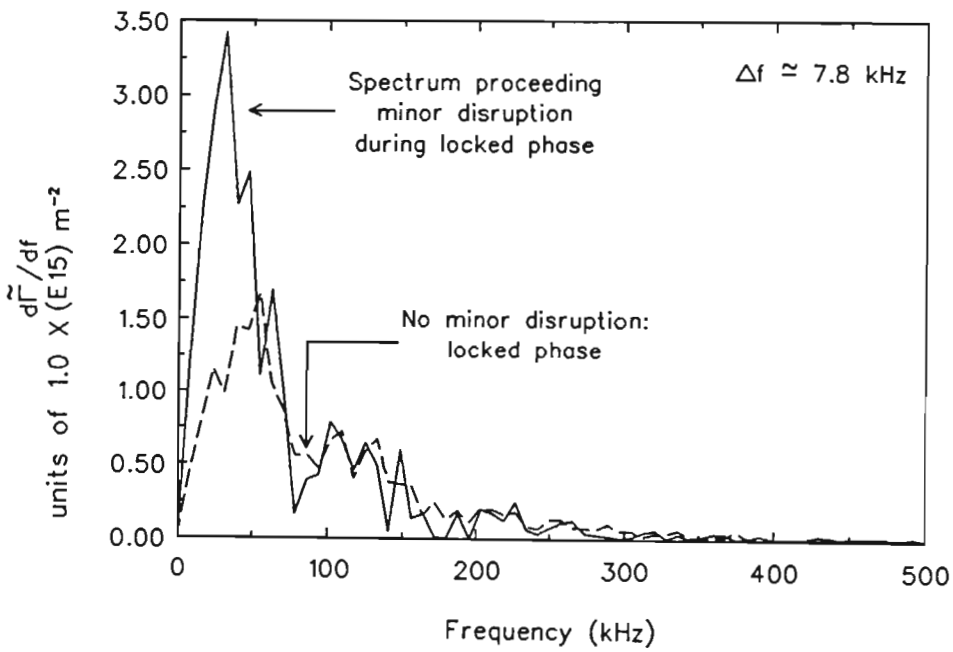

Figure 5.34: $\tilde{\Gamma}(f)$ for plasmas locked by the $--+2$ configuration, at $\rho = 0.93$, which experienced a minor disruption about 300 μs after locking.

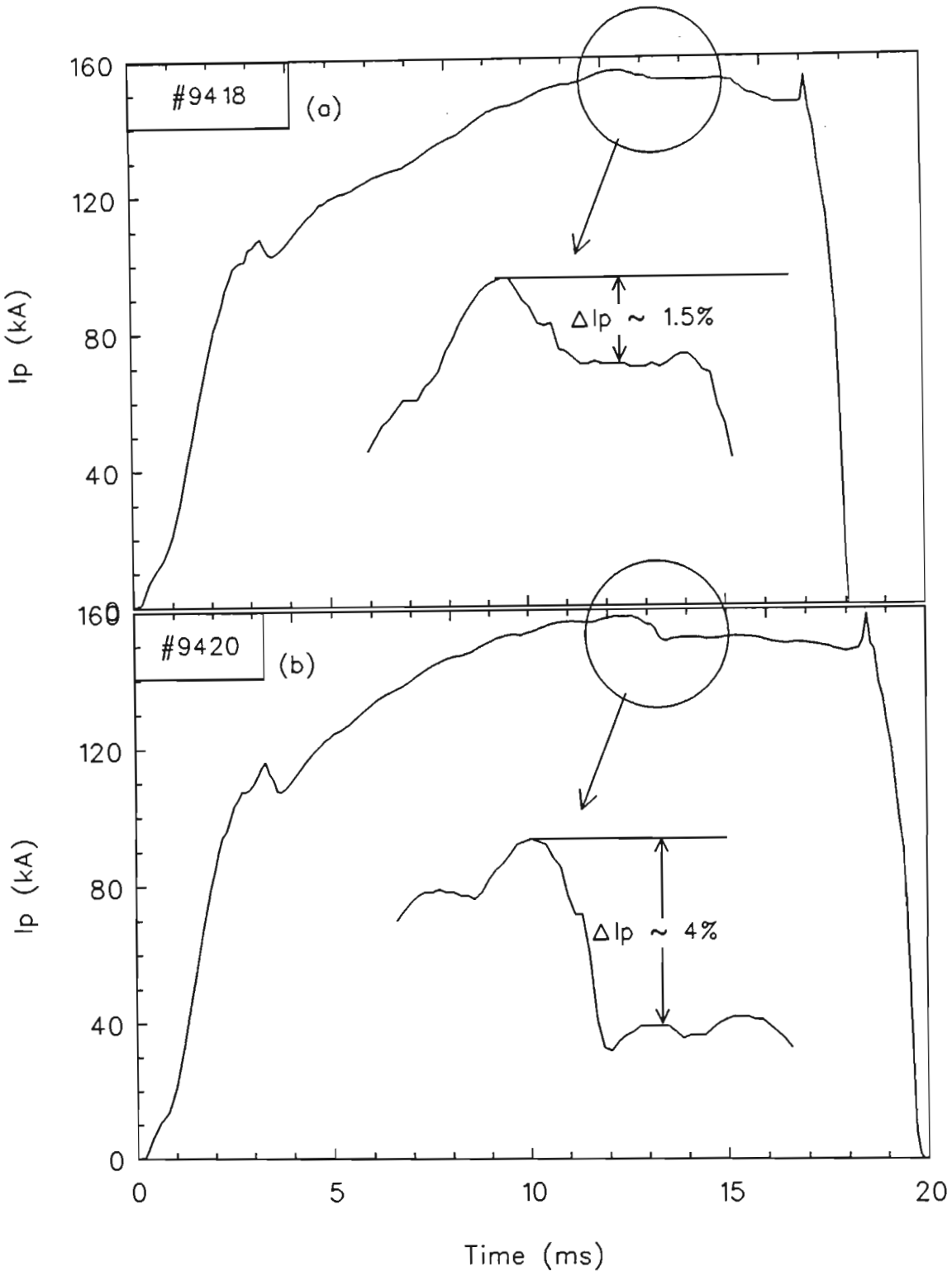

Figure 5.35: Plasma current for two shots showing different degree of minor disruption (enlarged). (a) has a minor disruption in which $\Delta I_p/I_p \approx 1.5\%$ and (b) $\Delta I_p/I_p \approx 4\%$.

The observed rapid increase in particle flux following a minor disruption is consistent with the results of ROBERTS *et al*, (1991a) in which the minor disruption was found to be signaled by the rapid ($\ll 200\,\mu$s) growth of the $m = 3$ mode, often starting within $t \ll \tau_E$ of locking. The $m/n = 3/1$ mode amplitude due to the coil was predicted to be increased by nearly a factor of 3 and appeared to be the cause of the minor disruption. It was also shown that ΔI_p was approximately that amount of I_p in an annulus of the width of a 3/1 island, overlapping with the limiter.

5.3 $\ell = 3$ Coil Results

The type of shot required for the $\ell = 3$ coils to lock the rotating plasma was identical to that required for the $\ell = 2$ coil, i.e. high amplitude Mirnov activity at the coil switch-on time. The coils were again switched on at $t \simeq 10\,$ms and locking invariably occurred roughly 2 ms after this. Results presented here again consist only of those taken from plasmas locked by the $\ell = 3$ coil in the resonant configuration. The only *physical* difference between the plasma under consideration in this Section and that investigated in the previous Section is the toroidal, locked position of the plasma.

Most of the results obtained from plasmas locked by these coils were very similar to the $\ell = 2$ coil results. Consequently, only Figures from those results that differed from the $\ell = 2$ results will be presented.

5.3.1 Similarities

Prior to locking the edge density increases linearly as a function of time, flattening off at locking and either remaining constant or decreasing slightly throughout the locked phase. The radial profile of the edge density shows a linear decrease radially outwards with an exponentially decreasing trend further out, in the limiter shadow. The range of L_n is $\approx 6.0 - 8.0\,$cm in the bulk plasma and $\approx 2\,$cm in the limiter shadow.

The floating potential as a function of time is modulated by the high Mirnov activity, abruptly increasing by up to 20% at locking and remaining elevated throughout the locked period until the major disruption. The radial electric field peaks just inside the limiter with maximum $E_r \approx 19\,\mathrm{V\,cm^{-1}}$ at $\rho \simeq 1.03$. The plasma potential peaks at $\rho \simeq 0.93 - 0.94$ with $\phi_p|_{\max} \approx 80 - 90\,$V, assuming $T_e(\rho)_{\ell=3} = T_e(\rho)_{\ell=2}$.

Fluctuation levels of both fluctuating quantities ($\tilde{i}_{\mathrm{sat}}$ and $\tilde{\phi}_f$) increase during the rotating

phase and then drop sharply (by about $40-50\%$) as the plasma locks, remaining at this value or slightly increasing during locking.

Radial profiles of the relative fluctuation levels indicate an exponential increase in $\tilde{i}_{\rm sat}/i_{\rm sat}$ radially outwards and a parabolic profile of $\tilde{\phi}_f/T_e$ at $\rho \simeq 0.93-0.95$. The values of $T_e(\rho)|_{\ell=3}$ are again assumed to be the same as $T_e(\rho)|_{\ell=2}$.

Power spectra of both quantities have a fairly small peak at $f \simeq 50\,\mathrm{kHz}$ but are otherwise broadband with a fall-off in power of the form $P(f) \propto f^{-2.0\pm0.5}$. Correlation times are below $10\,\mu\mathrm{s}$, with $\tau_{c\,\mathrm{TOROIDAL}} \simeq 3\,\mu\mathrm{s}$ and $\tau_{c\,\mathrm{POLOIDAL}} \simeq 6\,\mu\mathrm{s}$.

The power weighted poloidal phase velocity reverses direction between $\rho \simeq 0.93-0.94$. In the bulk plasma the direction of propagation is in the electron diamagnetic direction (with a maximum of about $1.3\times10^3\,\mathrm{ms}^{-1}$) and in the limiter shadow it is in the ion diamagnetic direction (maximum $1.8\times10^3\,\mathrm{ms}^{-1}$). The resulting shear layer is peaked (maximum shear $\approx 1.2\times10^5\,\mathrm{s}^{-1}$) and broad with a width of $\approx 2.7\,\mathrm{cm}$ at $\rho \simeq 0.97-0.98$. Absolute fluctuation levels in this region are significantly reduced.

$S(\omega, k_\theta)$ spectra are broad, with $\Delta\omega/\omega \approx \Delta k_\theta/k_\theta \approx 0.4-0.6$ and peak $S(k_\theta)$ at about $1-3\,\mathrm{cm}^{-1}$ at most radii giving a value of $\overline{k}_\theta r_s \approx 0.2$.

The dispersion relation measured at radii in the bulk plasma and in the limiter shadow for the $\tilde{\phi}_f$ signals is shown in Figures 5.36(a) and (b) measured over periods of about 4 ms of the locked phase. Whilst the power weighted poloidal phase velocity is slightly smaller at each radius than for the $\ell = 2$ case, the dispersion relation shows an identical trend, i.e. positive in the limiter shadow and up to $\rho \simeq 0.94$, changing sign at this radius and then negative in the bulk plasma.

5.3.2 Differences

For all figures shown in this section, solid lines are results from $\ell = 3$ locked plasmas whilst dashed lines indicate the results from the $\ell = 2$ cases under identical conditions.

The coherency between the fluctuating quantities is high for the lower frequency range ($0 \le f \le 150\,\mathrm{kHz}$), usually between 0.8 and 0.9 as shown in Figure 5.37. At higher frequencies, the coherency decreases significantly and above 300 kHz falls below the significance level. This results in a coherence length of about 3.5 cm or roughly 1 cm longer than the $\ell = 2$ coherence lengths, as shown in Figure 5.38.

The phase angle between $\tilde{i}_{\rm sat}$ and $\tilde{\phi}_f$ shows opposite behavior to that observed in the

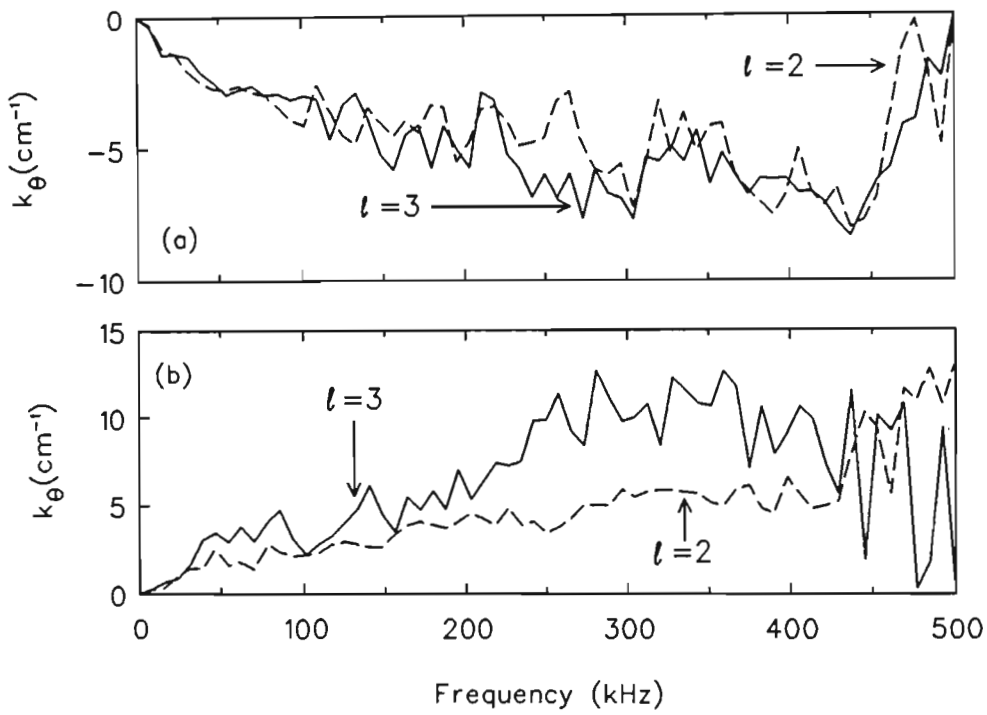

Figure 5.36: $k_\theta(\omega)$ between poloidally separated $\tilde{\phi}_f$ signals measured at $\rho =$ (a) 0.93 and (b) 1.04 during 4.1 ms period of an $\ell = 3$ locked phase. The dashed curve represents results for $k_\theta(\omega)$ during a similar period of an $\ell = 2$ locked phase under the same conditions.

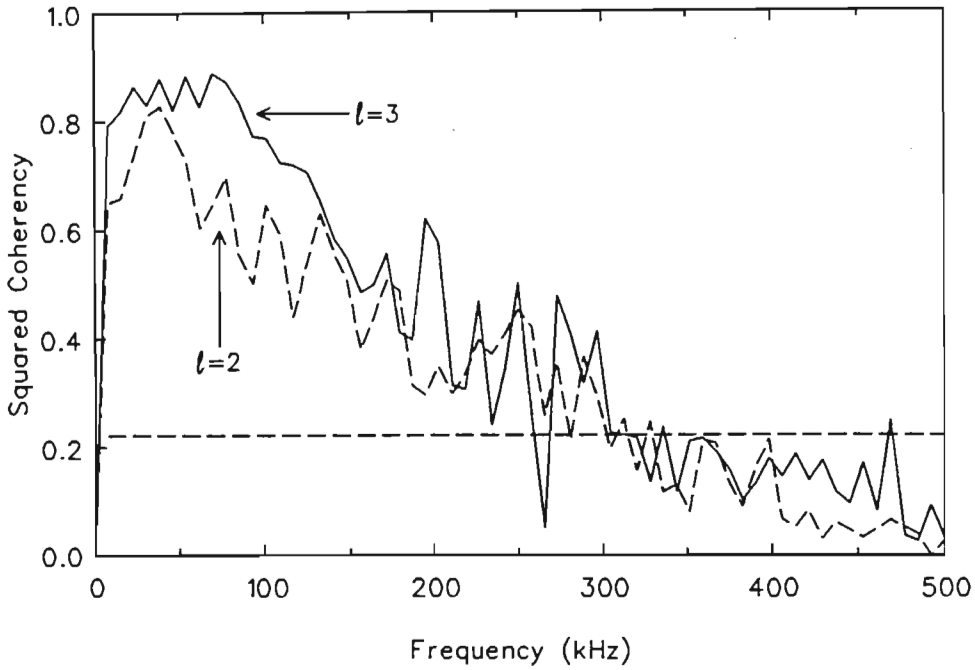

Figure 5.37: $\gamma_{n\phi}$ during about 4 ms of an $\ell = 3$ locked phase at $\rho = 0.93$. $\gamma_{n\phi}$ during a similar period of an $\ell = 2$ locked phase, at the same radial position, is also shown as a dashed curve for comparison. The straight dashed line is the significance level.

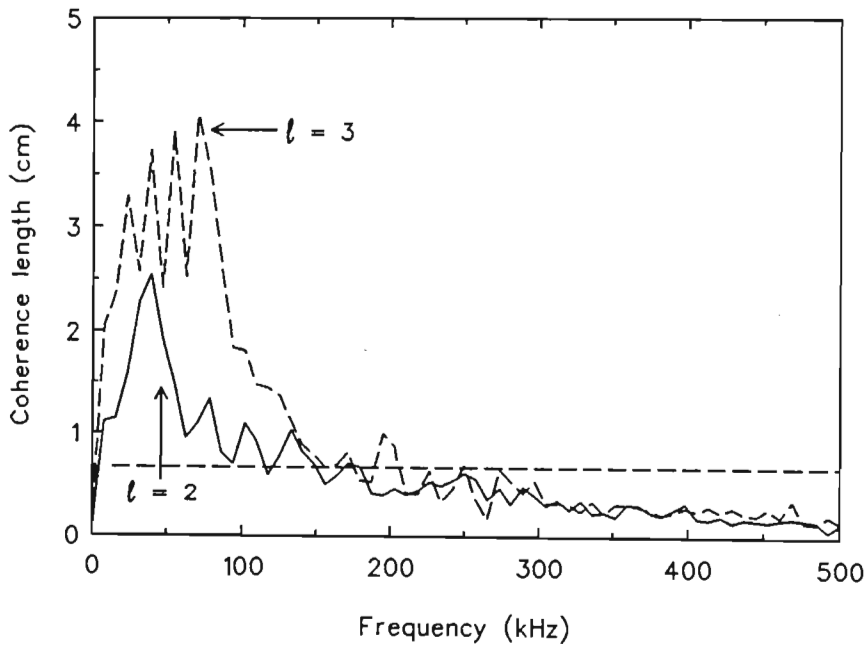

Figure 5.38: Coherence lengths associated with $\gamma_{n\phi}$ from the previous Figure.

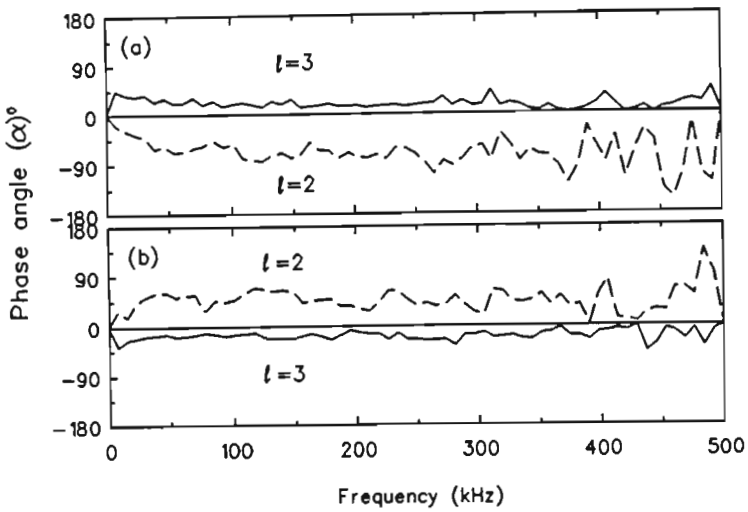

Figure 5.39: Phase angle between $\tilde{i}_{sat}$ and $\tilde{\phi}_f$ at the same radii as (a) and (b) above. during the same time intervals for the $\ell = 3$ locked phase, showing opposite behavior to measurements taken during the $\ell = 2$ locked phase (dashed lines).

reference and $\ell = 2$ cases. For plasmas locked by the $\ell = 2$ coil, $\alpha_{n\phi}$ is large and negative ($-45° \leq \alpha_{n\phi} \leq -90°$) in the bulk plasma for $\rho \lesssim 0.96$. At this radius $\alpha_{n\phi}$ changes sign and is fairly large and positive ($45° \leq \alpha_{n\phi} \leq 60°$) for $\rho \leq 0.96$. During an $\ell = 3$ locked phase, however, $\alpha_{n\phi}$ is small and *positive* ($15° \leq \alpha_{n\phi} \leq 20°$) for all frequencies for $\rho \leq 0.94$ and, at all larger values of ρ, it is small and *negative* ($-15° \leq \alpha_{n\phi} \leq -25°$) at all frequencies, shown in Figures 5.39(a) and (b).

The effect of this behavior is most marked on the fluctuation induced particle flux. In the equation,

$$\tilde{\Gamma}(\omega) = \frac{\tilde{n}_e(\omega)\tilde{V}_d(\omega)k_\theta(\omega)\gamma_{n\phi}(\omega)\sin[\alpha_{n\phi}(\omega)]}{B_\phi},$$

only the $k_\theta(\omega)$ and $\sin[\alpha_{n\phi}(\omega)]$ terms govern the direction of particle flux, i.e. either radially inwards or outwards. In the reference and $\ell = 2$ cases both quantities are either *simultaneously* positive or *simultaneously* negative, resulting in 'positive' (i.e. outward) flux of particles at all radii, for all frequencies, ω.

In the $\ell = 3$ case, $k_\theta(\omega)$ and $\sin[\alpha_{n\phi}(\omega)]$ have *opposite* signs at each frequency, at each radius, both changing signs at the same radius, i.e. $\rho \simeq 0.94$. The resulting $\tilde{\Gamma}$ is *negative* (i.e. inwards) at each radius as shown in Figure 5.40. Whilst the magnitude is smaller—

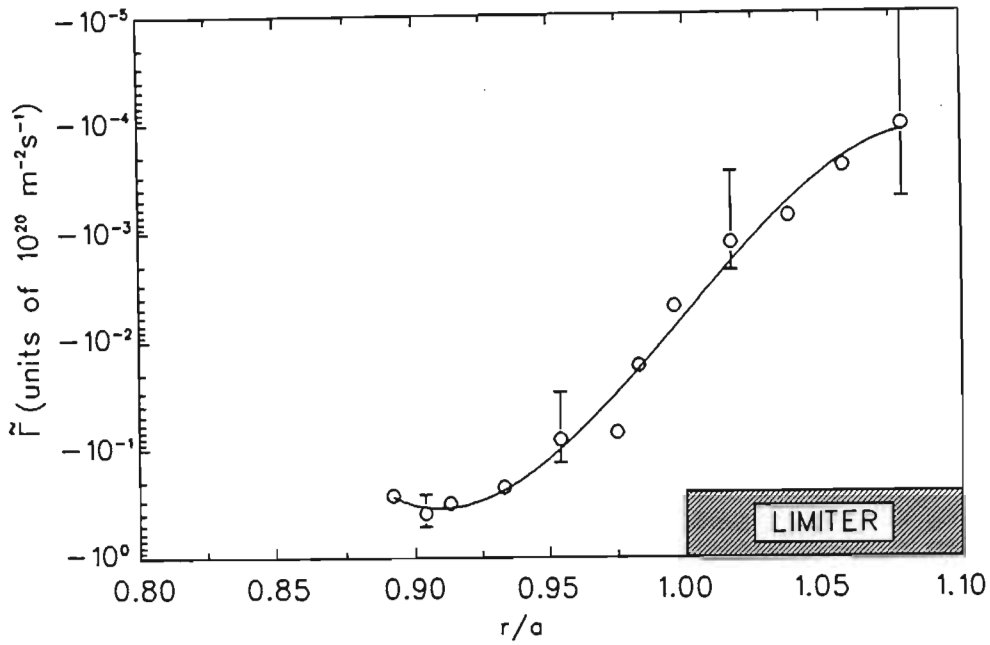

Figure 5.40: $\tilde{\Gamma}(\rho)$ during periods of about 4.1 ms of the $\ell = 3$ locked phase. Error bars are an indication of shot to shot scatter.

for all ρ—than values measured during the $\ell = 2$ locked phase the trend is very similar with peak $\tilde{\Gamma}$ of $0.35 \times 10^{20} m^{-2}s^{-1}$ at $\rho \simeq 0.93$ or roughly the same radius at which $\tilde{\phi}_f$ and ϕ_p have their maximum values.

The temporal behavior of $\tilde{\Gamma}$ is shown in Figures 5.41(a) and (b) for the $--+3$ and $--3$ cases respectively. Before locking, the flux increases with time—in (a) and (b)—at a rate very similar (during the same time interval) to both the reference and the $\ell = 2$ cases, as expected. At locking, the particle flux for the $--+3$ case abruptly changes from $\approx +3.5 \times 10^{20}\, m^{-2}s^{-1}$ to $\approx -2.0 \times 10^{20}\, m^{-2}s^{-1}$ and remains at this constant, negative value throughout locking. Discharges in which the plasma rerotated again after a period of locking were unobtainable: all shots experienced a major disruption after about 18 ms from the start of the shot. The transport characteristics after unlocking in these cases could prove to be an interesting result. In Figure 5.41(b), the $--3$ case, the flux changes at locking, such that the rate of *decrease* of $\tilde{\Gamma}$ after locking is approximately the same as the rate of *increase* of $\tilde{\Gamma}$ prior to locking. After $\approx$ 2 ms the flux has decreased to $0.0\, m^{-2}s^{-1}$ and thereafter becomes negative, now increasingly negative indicating an increasing flux, radially *in*wards, reaching a maximum inward flux of about $6.5 \times 10^{20} m^{-2}s^{-1}$ at the end of the discharges, immediately before the major disruption.

These observations could be explained by the large temperature fluctuations observed during the locked phases. These fluctuations affect the measurement of $\tilde{\phi}_f$ in such a way as to change the sign of the phase angle between the fluctuating quantities. This, in turn, affects both the magnitude and the sign of the particle flux during locking. The particle flux spectrum for a $---3$ locked plasma during about 4 ms of the locked phase, is shown in Figure 5.42, negative at all frequencies at two different radii. No conclusive information was available to determine whether the probe was located at an X or an O point for these measurements. It seems unlikely, however, that the probe was located at an O point, since it would be difficult to explain how $\tilde{\Gamma}$ could be inwards here. It is far more likely that the plasma is locked with an X point at the probe position and that, locally at least, there is an inward flux of particles.

Whilst these measurements suggest an inward flux of particles it must be emphasized again that these are local, point measurements of $\tilde{\Gamma}$. It is still possible that the poloidally averaged $\tilde{\Gamma}$ is outwards and that the local radial direction of $\tilde{\Gamma}$ is dependent on whether the probe measures this quantity at (e.g.) an O or an X point in the plasma.

Double probe measurements were not made during the $\ell = 3$ locked phase.

5.4 The High Frequency Magnetic Mode

Power spectra of $\tilde{B}_\theta$ measurements show two distinct peaks superimposed on an otherwise broadband spectrum. One of these peaks is due to the tearing modes present in the plasma ($m/n = 3/1$ and $2/1$) which give rise to strong Mirnov activity. Another magnetic feature—superimposed on the Mirnov signals and more easily seen during the locked phase—is present and this gives rise to the second peak in the spectrum. The Mirnov signals are high amplitude ($\tilde{B}_\theta/B_\theta > 1\%$), low frequency ($8 \leq f_{\text{Mirnov}} \leq 15\,\text{kHz}$), coherent modes and can be slowed down and stopped by currents in the helical coils (see previous Section). The high frequency mode is, on the other hand, observed to be low amplitude ($\tilde{B}_\theta/B_\theta > 0.03\%$), high frequency ($40 \leq f_{\text{HF}} \leq 70\,\text{kHz}$) and is present during both the rotating phase and after the mode has been locked by the coils. Since the transport spectrum also peaks in this higher frequency regime, measurements were performed to investigate the physical connection (if any) of these two processes.

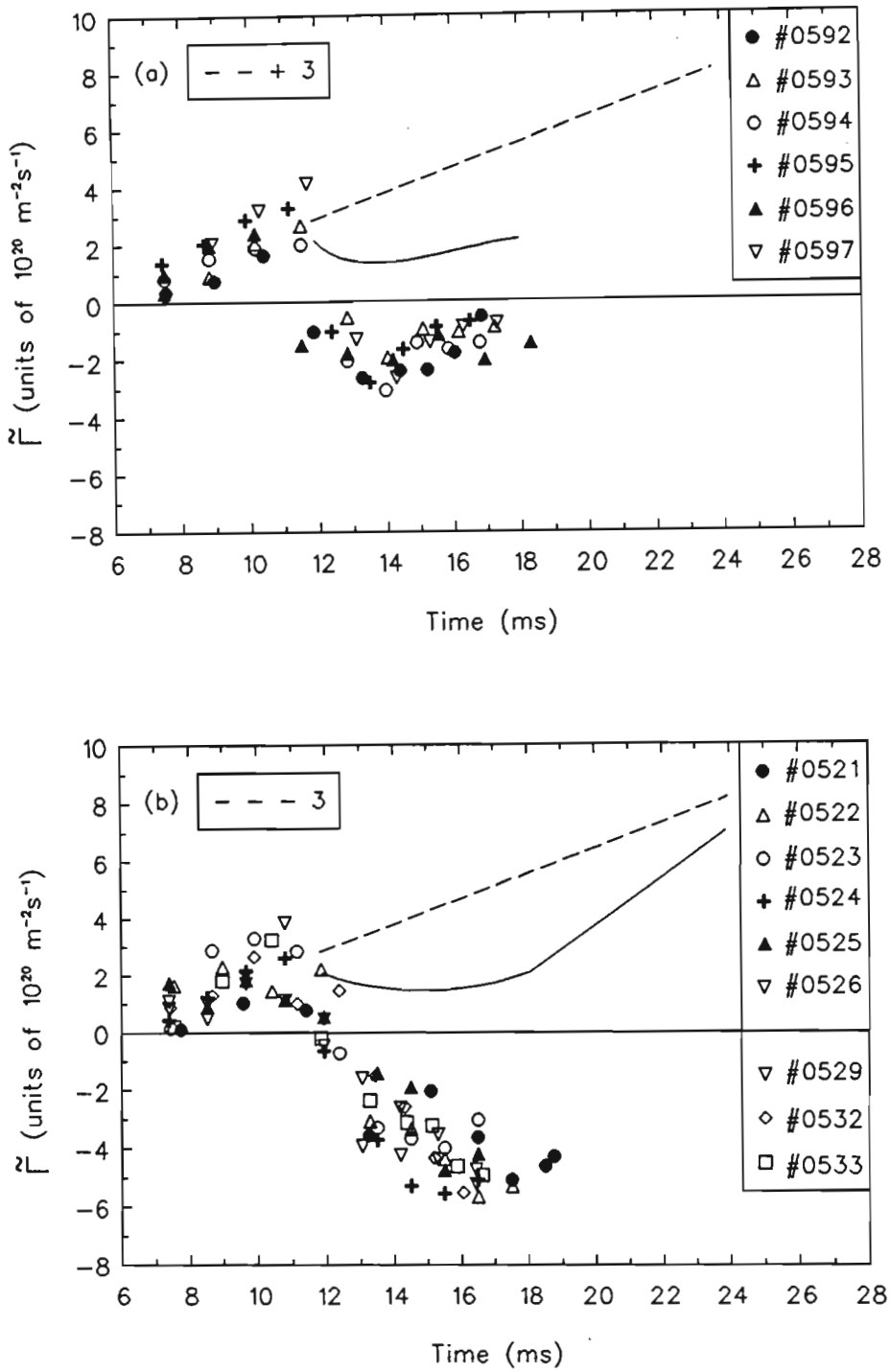

Figure 5.41: $\tilde{\Gamma}(t)$ at $\rho = 0.93$ for the locked phase of the (a) $--+3$ and (b) $---3$ configurations. Data segments were $\approx$ 1 ms long ($8 \times 128\,\mu$s). The dashed curve is reference $\tilde{\Gamma}$ and the solid line $\tilde{\Gamma}_{\ell=2}$ $(--+2)$ at $\rho = 0.93$ in (a) and $\tilde{\Gamma}_{\ell=2}$ $(---2)$ at $\rho = 0.93$ in (b).

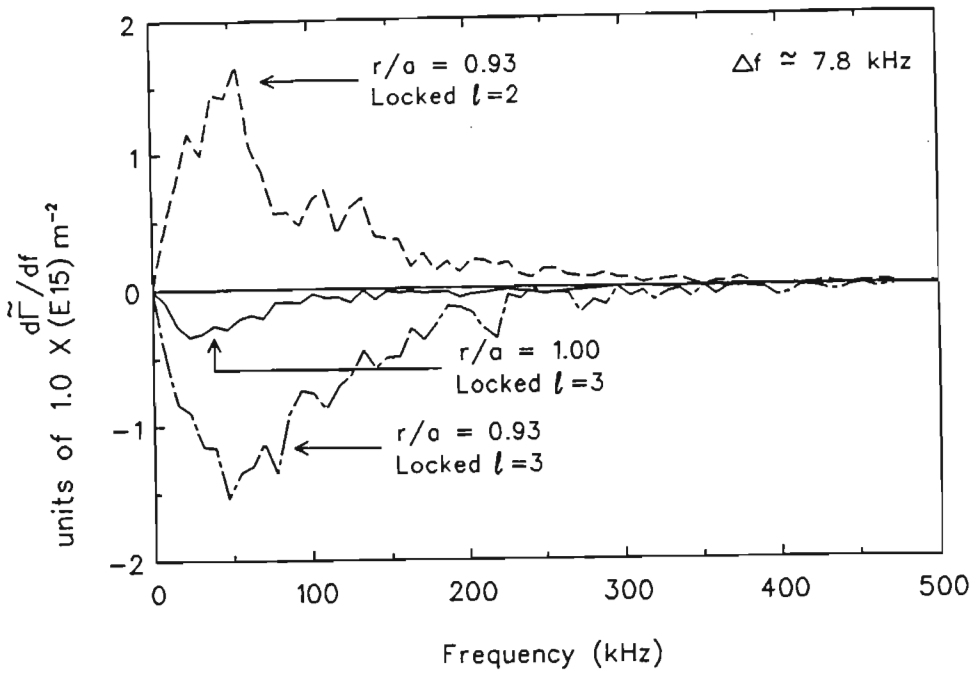

Figure 5.42: $\tilde{\Gamma}(\omega)$, using $25 \times 128\,\mu$s blocks, measured at $\rho = 0.93$ (solid line) and $\rho = 1.00$ (dash-dot line) and the $\tilde{\Gamma}(\omega)$ spectrum for the $\ell = 2$ ($---2$) case, measured at $\rho = 0.93$ for comparison.

5.4.1 Results

Magnetic Measurements

The measurements for this Section were taken during high Mirnov activity with both $m/n = 3/1$ and $2/1$ tearing modes present and $q_\psi(a) \simeq 3.3$. Twelve coils, arranged poloidally, measured $\dot{\tilde{B}}_\theta$ and could be moved to one of two toroidal locations. A set of eight coils—with closer poloidal spacing of $\Delta\theta = 10.4°$—and a single, radially moveable, $\dot{\tilde{B}}_\theta$ coil were also used. All data were recorded with a 1 MHz sampling rate.

Typical traces from four $\dot{\tilde{B}}_\theta$ coils are shown in Figure 5.43 for different poloidal positions, labelled BT5 through BT8 as indicated in Figure 5.44. They show a period of high Mirnov activity, slowing of the mode due to locking by helically induced fields and finally a period during which the plasma is locked. Also shown is an expanded time segment of $\sim 300\,\mu$s during the locked phase, showing clear $\dot{\tilde{B}}_\theta$ at a frequency of ~ 60 kHz. The amplitude of the high frequency component has a maximum near $\theta \approx \pi$, unlike the Mirnov amplitude which peaks near $\theta \simeq 0$. Measurements taken at two toroidal positions suggest that these $m = 1$ shifts are not helical ($n = 0$). The Mirnov activity and the high frequency mode have an $m = 3$ structure distorted by the low aspect ratio toroidicity. The high

frequency mode is also non-propagating, unlike the Mirnov oscillation (ROBERTS *et al*, (1991c)).

Power spectra from a 7 ms ($55 \times 128\,\mu$s) period of locked phase of two adjacent signals (labelled BT5 and BT6 in Figure 5.44) are shown, are shown in Figure 5.45, clearly peaked at $f \simeq 70$ kHz. Otherwise the spectra are broadband except at $f \simeq 210$ kHz where another peak is seen on both signals. Coherency between these signals is high (i.e. well above the significance level) at $f \simeq 70$ kHz and again at 210 kHz (Figure 5.46). Elsewhere the coherency is below the significance level. These two peaks appear between all combinations of $\dot{\tilde{B}}_\theta$ signals (i.e. BT5 $\rightarrow$ 6,7,8 or BT6 $\rightarrow$ 7,8 or BT7 $\rightarrow$ 8) with the stronger of the two peaks being at the lower frequency in each case. The general picture is to have a high frequency mode at $f \approx 40 - 70$ kHz whose frequency may change within a shot and from shot to shot within this frequency range. Often $2 \times f$ and $3 \times f$ are observed as well.

Power spectra of the same two adjacent signals (BT5 and BT6) are shown in Figure 5.47. These spectra were generated from $6 \times 128\,\mu$s blocks from 0.77 ms just before locking. They are broadband with $P(f) \propto f^{-n} (n \simeq 3)$ and only one significant peak at $f \simeq 7 - 15$ kHz, i.e. the Mirnov frequency. The coherency between these signals is very high at the Mirnov frequency and also at about 50 kHz (Figure 5.48) indicating that the high frequency magnetic mode is present during the rotating plasma phase as well as during the locked phase.

Probe Measurements

With the Langmuir probe array in the same poloidal and toroidal position as that indicated in previous Sections, $\tilde{i}_{sat}$ and $\tilde{\phi}_f$ were measured during the locked phase (in these cases, always the $- - -2$ locked phase) to ascertain the degree of correlation between these signals and the high frequency magnetic variations. In all experiments in this Section the probes were situated at $\rho = 0.93$ where the particle flux is known to be a maximum and where the probe signals themselves are strongly modulated by the $m = 2$ Mirnov signals.

Figure 5.49 shows the power spectra of $\dot{\tilde{B}}_\theta$ at BT5, $\tilde{i}_{sat}$ and $\tilde{\phi}_f$ for 7 ms of locked phase. The $\tilde{i}_{sat}$ and $\tilde{\phi}_f$ power spectra are broadband with no major peaks, as found previously. The coherency between these two signals, shown in Figure 5.50, is high with highest coherency below 500 kHz. Very low coherency (well below even the significance level) is observed between [$\tilde{i}_{sat}$ and $\dot{\tilde{B}}_\theta$ at BT5] and [$\tilde{\phi}_f$ and $\dot{\tilde{B}}_\theta$ at BT5].

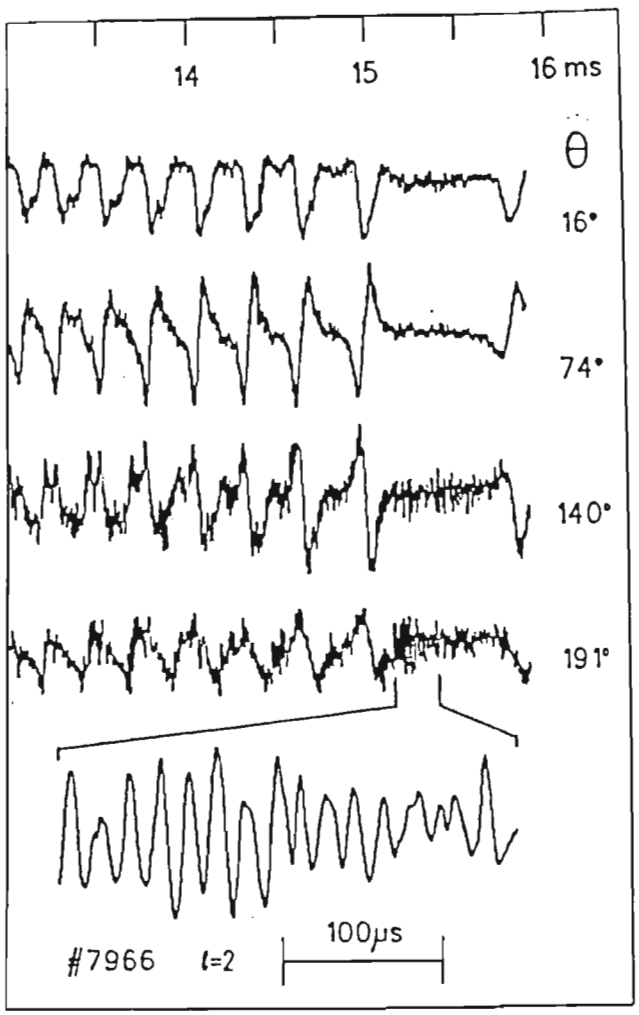

Figure 5.43: Typical traces from four $\dot{\tilde{B}}_\theta$ coils from four different poloidal positions indicated in the next Figure. The expanded region clearly shows the high frequency mode during the locked phase, oscillating at a frequency of $\approx 60\,\mathrm{kHz}$.

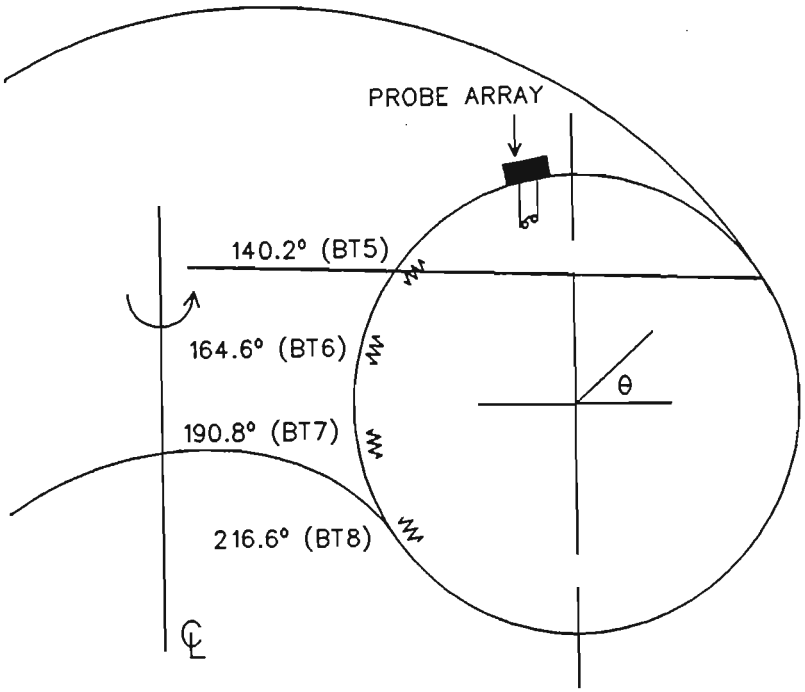

Figure 5.44: Position of the four main $\dot{\tilde{B}}_\theta$ coils situated at (a) 140.2° (BT5), (b) 164.6° (BT6), (c) 190.8° (BT7) and (d) 216.6° (BT8).

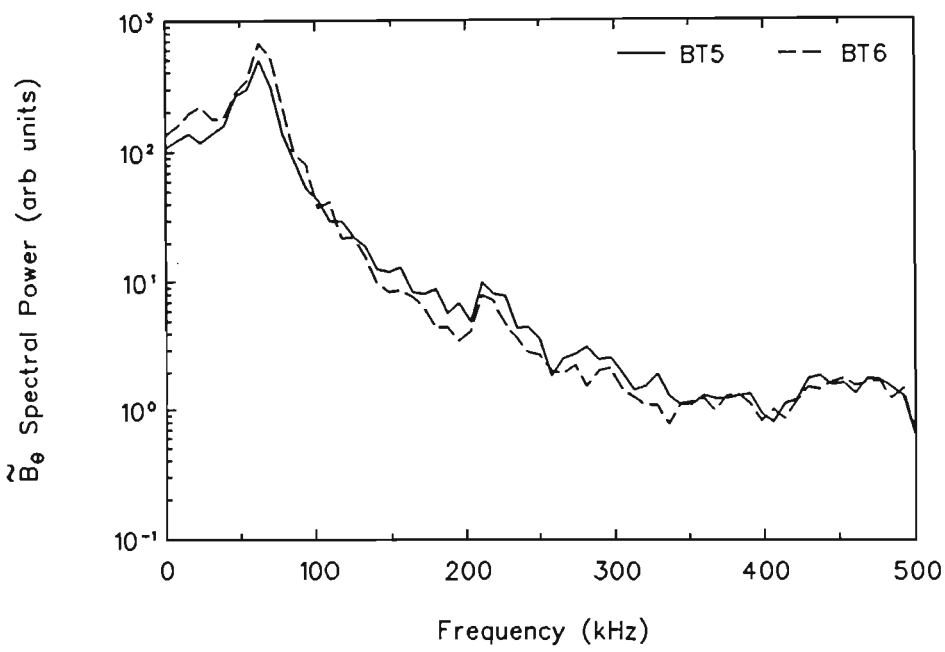

Figure 5.45: Power spectra of $\dot{\tilde{B}}_\theta$ measured at two adjacent coils, BT5 and BT6, as in the previous Figure, during 7 ms of locked phase. Prominent peaks at $f \simeq 70$ kHz and $f \simeq 210$ kHz are present.

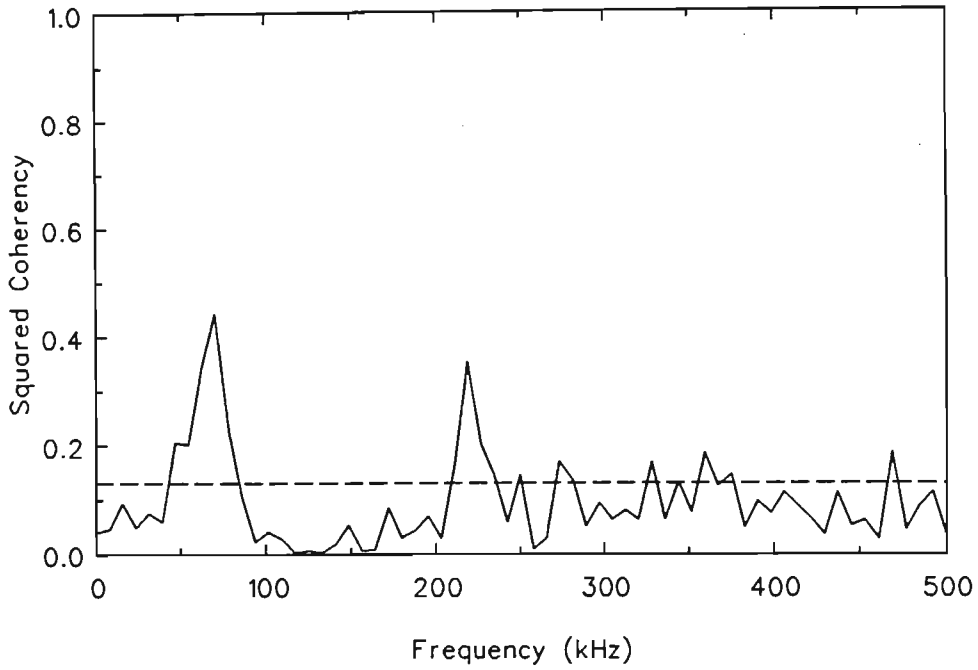

Figure 5.46: Coherency between $\dot{\tilde{B}}_\theta$ from adjacent coils, BT5 and BT6, measured during the 7 ms locked phase, indicated above. Two peaks are again evident: one at $f \simeq 70$ kHz and $f \simeq 210$ kHz.

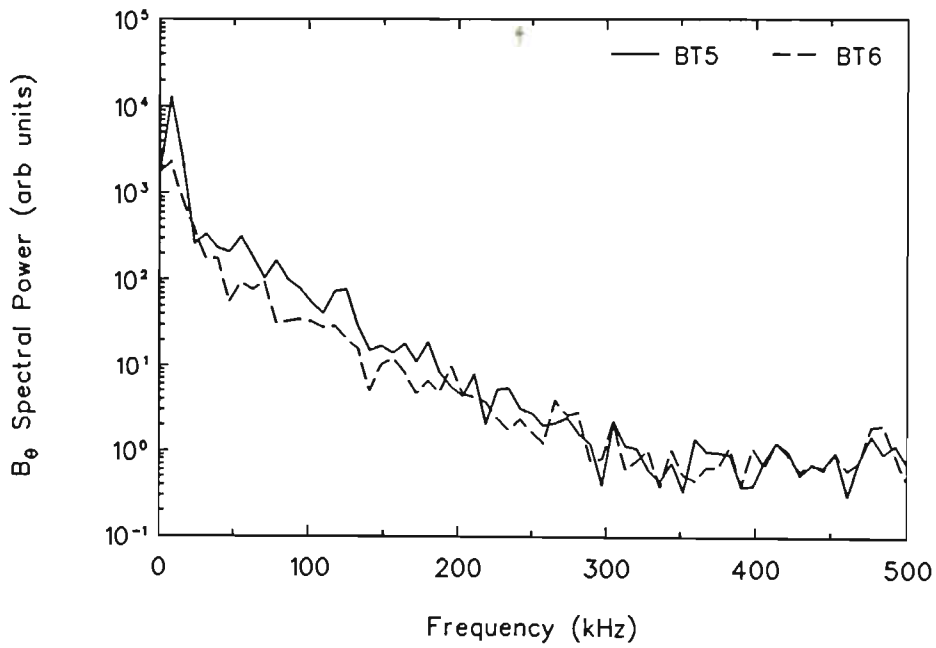

Figure 5.47: Power spectra of $\dot{\tilde{B}}_\theta$ from two adjacent coils, BT5 and BT6, during about 0.8 ms of the rotating phase. The only major peak is at $f \simeq 7 - 15$ kHz.

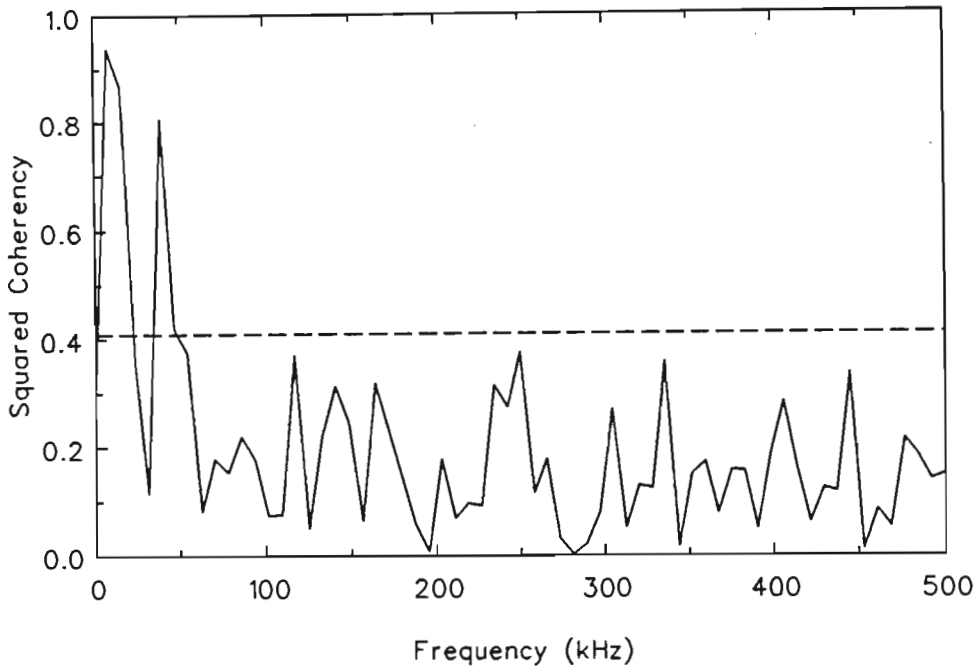

Figure 5.48: Coherency between $\dot{\tilde{B}}_\theta$ from adjacent coils, BT5 and BT6, measured during the rotating phase. Two peaks are evident: one at $f \simeq 7 - 15\,\mathrm{kHz}$ (i.e. Mirnov) and $f \simeq 50\,\mathrm{kHz}$, i.e. (high frequency mode).

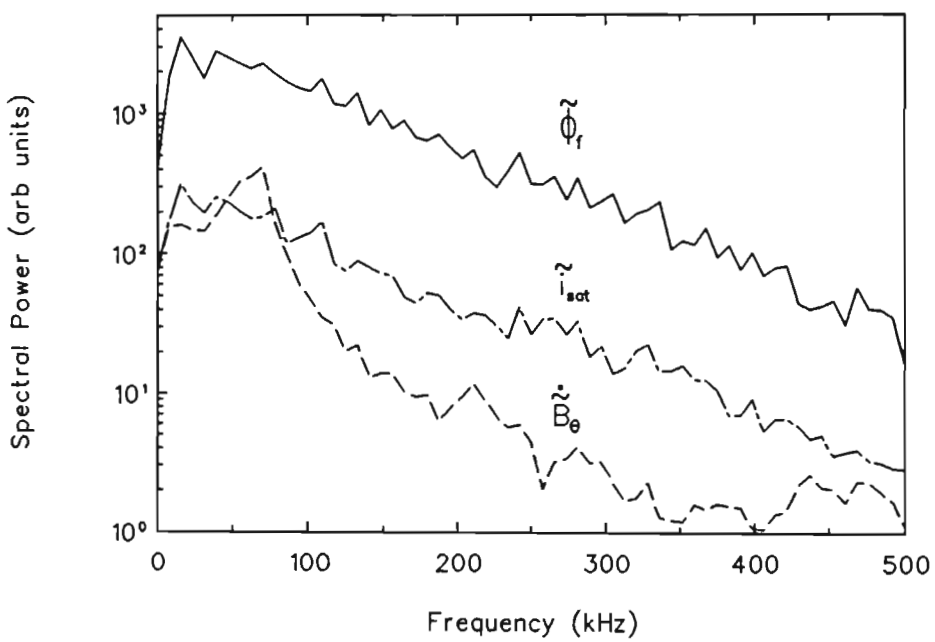

Figure 5.49: Power spectra of $\dot{\tilde{B}}_\theta$ from BT5 (showing the high frequency peak at $f \simeq 70\,\mathrm{kHz}$), $\tilde{i}_{\mathrm{sat}}$ and $\tilde{\phi}_f$, all showing broadband characteristics.

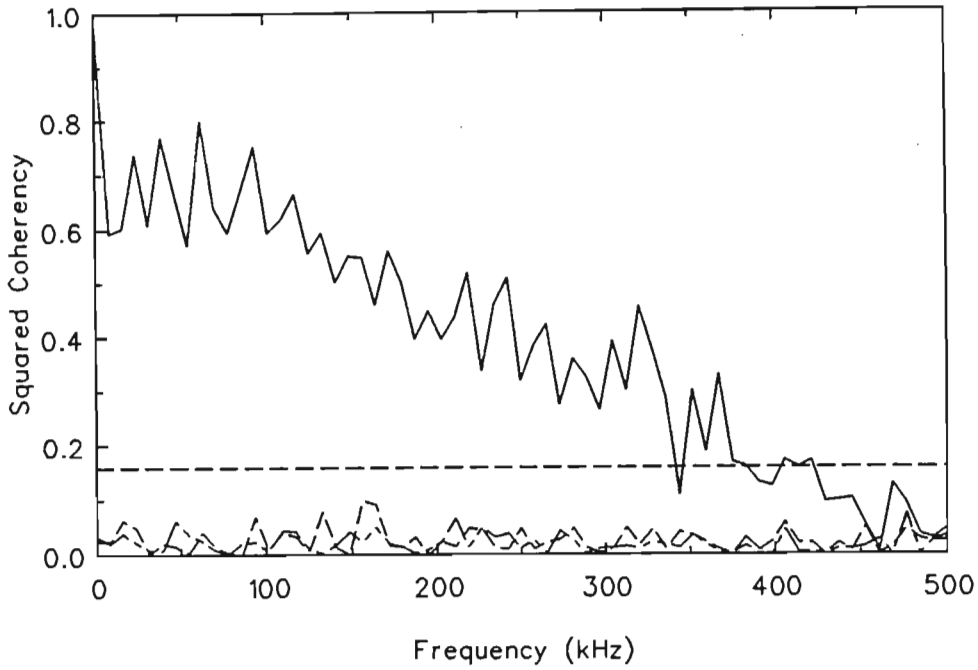

Figure 5.50: Coherency between (i) $\tilde{i}_{\rm sat}$ and $\tilde{\phi}_f$ (solid line), (ii) $\tilde{i}_{\rm sat}$ and $\dot{\tilde{B}}_\theta$ at BT5 (dash-dot line) and (iii) $\tilde{\phi}_f$ and $\dot{\tilde{B}}_\theta$ at BT5 (dash-dot-dash line), during a 7 ms period of locked phase.

Correlation between signals from adjacent coils is fairly high but falls off rapidly for alternate (and further apart) coils, e.g. BT5 with BT7, suggesting a poloidal correlation length ($a\Delta\theta$) of between $\simeq$ 10 cm and 21 cm. The position of these coils varies between 50° and 127° away from the poloidal position of the probe array, i.e. between 21 and 53 cm, so it is not entirely surprising that no correlation was found. It is possible that some degree of correlation *does* exist, but the probes would have to be moved to the inside of the torus (i.e. $\theta = 180°$) where the hf mode is known to be most prominent before this could be ascertained. It is interesting to note that the high level of temperature fluctuations observed during the locked phase exhibit bulk power in roughly the same frequency range of this magnetic mode, i.e. 30 - 70 kHz.

Magnetic oscillations during locked modes have been observed on other tokamaks. DUPERREX (1988) observed a high level of coherent magnetic fluctuations in the frequency range 8 $\rightarrow$ 13 kHz superimposed on the locked mode. These coherent oscillations were found to be stationary (standing modes) and had $m/n = 4/1$ with the same helicity as the equilibrium magnetic field. The mode amplitude was modulated by the $m = 2, n = 1$ locked mode. These results suggested a kink or tearing mode located on the $q_\psi(r) = 4$ surface. KIM (1989b) found a broadband spectrum for $\tilde{B}_\theta$ with a broad peak near

$80 \leq f_{HF} \leq 100\,\text{kHz}$ which correlated well with both the density and potential fluctuations in this frequency range. These measurements were taken inside the limiter during a period of low Mirnov activity. OHYABU *et al*, (1987) found a correlation between magnetic fluctuations and edge energy transport in the DOUBLET II tokamak. TAKAMURA *et al*, (1986) reported a direct observation of anomalous edge electron diffusion due to small scale magnetic turbulence in CSTN–II.

Chapter 6

Summary, Conclusions and Future Work

The tokamak edge was studied with a Langmuir probe array. Measurements of many edge parameters were taken to elucidate the character, nature and effect on transport of the electrostatic fluctuations in the edge. The toroidally rotating plasma was then locked and edge parameters again measured. These results were compared with the reference plasma results and found to exhibit some similarities but also some significant differences depending on factors such as coil current direction, duration of locked phase, presence or absence of minor disruptions, helicity of coil used to lock the plasma, etc. Finally, an attempt was made to determine if there was any correlation between the high frequency magnetic mode and the particle transport.

6.1 Summary

6.1.1 Reference Plasmas

Reference plasmas show a high level of turbulence in the edge region ($0.89 \leq \rho \leq 1.08$) and are characterised by the following features. The edge density increases linearly with time due to strong gas puffing in the edge. Density decreases linearly with increasing minor radius up to the limiter where it drops off exponentially. Edge potential decreases with time as the Mirnov ($m = 2$) amplitude passes from high Mirnov activity to low Mirnov activity. The radial profile is peaked a few mm into bulk plasma. The edge radial electric field peaks a few mm behind the limiter.

In time, the fluctuation levels of both quantities increase slightly during the high Mirnov activity phase and remain constant at their maximum levels even after the amplitude of the $m = 2$ mode has decreased. In radius, the fluctuating edge density increases exponentially outwards whilst fluctuating plasma potential is again peaked a few mm inside the bulk plasma. Power spectra of both quantities are broadband with no reproducible or persistent peaks present. Most power is in the lower frequency range, i.e. below 100 kHz. Correlation times are short with $\tau_{c,\,\mathrm{TOROIDAL}} \simeq 2\tau_{c,\,\mathrm{POLOIDAL}}$.

Measured poloidal phase velocity changes from the electron diamagnetic drift direction in bulk plasma to the ion diamagnetic drift direction in the shadow, changing sign a few mm outside the limiter. This gives rise to a shear layer of width of order ≈ 1 cm. Absolute fluctuation levels are reduced in this layer. Coherency between $\tilde{n}_e$ and $\tilde{\phi}_p$ is about 0.6 for frequencies below 100 kHz and below the significance level for higher frequencies.

Wavenumber spectra are dominated by broadband fluctuations with $\Delta\omega/\omega \approx \Delta k_\theta/k_\theta \approx 0.5 - 0.8$. The phase angle changes sign at the same position that the k_θ spectrum changes sign which results in radially outward fluctuation induced particle transport at all radii. The flux is peaked in minor radius at the same radial position that both the floating potential and floating potential fluctuations are peaked. In time, $\tilde{\Gamma}$ increases more or less linearly throughout the discharge. Spectra show most of the fluctuating power is at frequencies below 100 kHz. The particle transport spectrum is peaked at $f < 20$ kHz for $0 \lesssim t \lesssim 12$ ms. For $t \gtrsim 12$ ms the spectrum broadens and the peak shifts to higher frequencies, $f \approx 50 - 70$ kHz.

Edge electron temperatures decrease by a few eV over the radial range investigated. Temperature fluctuations are small and increase with minor radius. The fluctuation induced heat flux is dominated by convection processes with $q^{\tilde{E}}_{\mathrm{conv}}/q^{\tilde{E}}_{\mathrm{cond}}$ being about 3 at the limiter and 50 further out. Particle and energy balance considerations show that electrostatic fluctuations account for 25% of the total outward transport of particles (but the error bars are large so this could be as high as 100%) and about 10% of the heat transport.

6.1.2 $\ell = 2$ Locked Plasmas

Plasmas locked by the $\ell = 2$ coil are overall less turbulent in character. The increase in edge density with time is suppressed during locking and the radial profile shows a 20–40% decrease compared with the reference case. The floating potential increases somewhat during locking and the radial profile is again peaked but a few mm further

into bulk plasma compared with the reference case. The edge electric field is larger at each radial position and is again peaked at the same radius as the reference.

The power spectra are again broad with no major peaks. Fluctuation levels of ion saturation current and floating potential decrease significantly during locking by up to 60% in both cases. The radial profiles are similar to the reference case but both values are smaller at each radius. Coherency between fluctuating quantities is higher during locking than during the rotating phase, $\gamma_{n\phi}$ being about 0.8 for the lower $f \leq 100\,\mathrm{kHz}$. Correlation times remain short but whilst $\tau_{c,\,\mathrm{TOROIDAL}}$ is about $\frac{1}{2}$ its reference value, the value of $\tau_{c,\,\mathrm{POLOIDAL}}$ remains roughly constant.

The $S(\omega, k_\theta)$ spectra are broader than their reference counterparts with $\Delta\omega/\omega \approx \Delta k_\theta/k_\theta \approx 1.0$. The phase velocity is smaller at each radius, still changing direction on either side of the limiter, but a few mm further into the bulk plasma than was measured for the reference case. The shear layer is broader and absolute fluctuation levels are again reduced in this region of maximum shear. The phase angle changes sign at the radius where the k_θ spectrum changes sign so the fluctuation induced particle flux is again outwards at all radii. The flux increases from limiter to bulk plasma, peaking a few mm further in than the maximum of $\tilde{\Gamma}$ for the reference case. In time, the linear increase in $\tilde{\Gamma}$ is suppressed during the locked phase.

Edge temperatures are slightly lower during a period of locking and fluctuation levels of $\tilde{T}_e/T_e$ are *much* higher, leading to the conclusion that $\tilde{i}_{\mathrm{sat}}/i_{\mathrm{sat}} \approx \tilde{n}_e/n_e$ and $\tilde{\phi}_f/T_e \approx \tilde{\phi}_p/T_e$ are not valid assumptions, at least, not during the locked phase. The validity of this assumption has consequences for all the above results.

The overall electrostatic, fluctuation induced heat flux is slightly enhanced during the locked phase with the dominant contribution from the *conducted* heat flux. In bulk plasma $q^{\tilde{E}}_{\mathrm{cond}}/q^{\tilde{E}}_{\mathrm{conv}}$ is about 1 whilst further out it is about 17. The fluctuation induced components of the particle and heat fluxes account for only about 6% of the total particle flux (again, the error bars are large) and about 10% of the total heat flux, respectively.

6.1.3 $\ell = 3$ Locked Plasmas

The plasmas locked by these coils showed very different behavior from reference plasmas and plasmas locked by the $\ell = 2$ coils. Whilst most parameters remain the same as those measured in other cases (e.g. density and potential profiles, power spectra, correlation times, etc.), the phase angle and hence particle flux of these locked plasma were very different. The dispersion relation was similar at all radii to those measured in previous

cases but the phase angle changed sign immediately after locking, causing radially *in*ward transport. For cases in the limiter shadow the phase *angle* changed sign after locking with no accompanying change in poloidal phase velocity. The poloidal, power weighted, phase velocity was very similar in both magnitude and trend to the profile measured in the $\ell = 2$ locked case. The shear layer was also similar in magnitude and width.

Coherency between $\tilde{i}_{\mathrm{sat}}$ and $\tilde{\phi}_f$ were generally higher for these plasmas but decreased sharply for frequencies above 250 kHz. $S(\omega, k_\theta)$ spectra showed similar features to those measured in the $\ell = 2$ case.

The radial transport decreased after locking at a rate equal to the *increase* prior to locking in the $--{-}3$ case and changed abruptly to a constant, negative value after locking in the $--{+}3$ case. The radial profile of $\tilde{\Gamma}$ has a very similar shape to that found for $\ell = 2$ locked plasmas, but is negative at each radial position and smaller in absolute magnitude by a factor of $\simeq 6$. The transport spectrum shows that $\tilde{\Gamma}$ is negative at all frequencies, maximum power being below 150 kHz. Electron temperatures and associated fluctuation levels of the $\ell = 3$ locked plasmas were not measured.

6.1.4 High Frequency Magnetic Mode

No correlation was found between the fluctuating parameters that contribute to $\tilde{\Gamma}$ and $\dot{\tilde{B}}_\theta$. This could be due to the short poloidal correlation lengths and the relatively large poloidal separation between the Langmuir probe array and the magnetic coils.

6.2 Conclusions

The conclusions from this study may be summarized as follows:

- The tokamak edge is a strongly turbulent environment with large fluctuations in edge density and plasma potential and broad electrostatic spectra.
- The formation of the shear layer near the edge results in a local decrease in the level of turbulence in both fluctuating quantities measured.
- Edge particle and heat fluctuation driven fluxes may account for only a small fraction of the total fluxes of the edge transport.

- Although the parameter space within which *Tokoloshe* operates is quite different from other machines of similar size (e.g. ASDEX, TEXT, MACROTOR), it is still well within the drift wave, turbulence-driven regime. Also, some relationships (e.g. $\tilde{n}_e/n_e \simeq 3\,r_s/L_n$)—predicted by drift wave models—are satisfied on *Tokoloshe*. These facts confirm earlier conclusions that resistivity gradient driven model(s) do not accurately describe tokamak turbulence.

- Edge temperature fluctuations during the $\ell = 2$ locked plasma cases invalidate the assumptions $\tilde{i}_{\rm sat}/i_{\rm sat} \simeq \tilde{n}_e/n_e$ and $\tilde{\phi}_f/T_e \simeq \tilde{\phi}_p/T_e$.

- $\ell = 2$ locked plasma fluctuation driven particle flux is reduced during locking due to a reduction in the edge density and large reduction in the fluctuation levels of both $\tilde{i}_{\rm sat}/i_{\rm sat}$ and $\tilde{\phi}_f/T_e$. The extent to which this is a *local* effect due to a change in the outer flux surface is not yet clear.

- $\ell = 3$ locked plasma fluctuation driven particle flux decreases during locking and then becomes negative due to a reversal of the phase angle between the fluctuating quantities immediately after locking. Although temperature fluctuation levels were not measured for these discharges, it is possible that they are also large in this case and affect the measurement of $\tilde{\phi}_f$ to such a degree as to alter the phase angle between it and $\tilde{i}_{\rm sat}$.

- The assumption of toroidal and poloidal symmetry in the tokamak edge is invalid, at least during locked plasmas as indicated by the significant differences in edge properties measured for different positions of the locked plasma.

- The high frequency mode *appears* to be uncorrelated with the edge density and plasma potential, perhaps because of the short poloidal correlation lengths and the large poloidal separation of the diagnostics measuring these quantities.

6.3 Future Work

Several points arise in the conclusions which suggest additional experimental work to resolve questions.

One of the main issues that requires further investigation is that of large temperature fluctuations. The results presented in this thesis did not include fluctuating gradients in electron temperature and density. As a result, the level of $\tilde{T}_e/T_e$ could not be unambiguously deduced so it is difficult to ascertain whether the high observed values were,

in fact, due only to temperature fluctuations. A direct measurement of $\tilde{T}_e$ is clearly needed as a function of both ρ and t. Knowledge of $\tilde{T}_e/T_e$ is useful for theoretical models and would help in solving the (largely unresolved) problem of power flows in the edge region. By using the new technique of TSUI *et al*, (1992c), the power spectrum of $\tilde{T}_e$ may be measured directly and could yield important information on both the amplitude and frequency of the temperature fluctuations during the locked modes.

A problem that has been largely ignored is that of poloidal and toroidal asymmetry. Results from the toroidally stationary plasma show very distinct poloidal asymmetries when different coils are used to lock the plasma in different positions. Problems of access restrict the work that could be accomplished in this region. Ideally, probes at several toroidal and poloidal locations would be required, simultaneously measuring various parameters. The heavy ion beam probe may be a useful diagnostic to determine the degree of poloidal asymmetry.

Locking of the plasma by the $\ell = 3$ coil is another area of research that could be further investigated. The differences in fluctuation induced particle flux between reference, $\ell = 2$ and $\ell = 3$ locked plasmas are large. The (apparent) inward transport of particles for the $\ell = 3$ case requires explanation. Changing the locked position with long coil pulses and a mixture of $\ell = 2$ and $\ell = 3$ coils currents could help in elucidating these results. The temperature, temperature fluctuation levels and heat flows during locking by the $\ell = 3$ coils were not measured. Double probe measurements during such a locked period could yield interesting results on the heat flows during this time and inward particle flux could have significant consequences for particle and energy confinement times.

The high frequency magnetic mode and its correlation (or lack thereof) with fluctuating parameters has not been exhaustively investigated. An array of probes, situated at $\theta = 180°$ (i.e. the inside, where the high frequency mode is most prominent) may indeed yield an as yet undetected correlation between these parameters.

References

BEALL, J.M., KIM, Y.C., POWERS, E.J., J Applied Physics, **53**, 3933 (1982).

BENGTSON, R.D., BESSENRODT-WEBERPALS, M., CARLSON, A., *et al*, Proc 17th EPS Conf on Contr Fusion and Plasma Phys, Amsterdam, **14 B**, 1460 (1990).

BICKERTON, Nucl Fusion, **13**, 290 (1973).

BURRELL, K.H., *et al*, Pl Physics and Contr Fusion, **31**, 1649 (1989)

CARLSON, A., RUDYJ, A., NIEDERMEYER, H., Workshop on Electrostatic Turbulence, Cadarache, September (1989).

CARLSON, A., RUDYJ, A., *et al*, Proc 17th EPS Conf on Contr Fusion and Plasma Phys, Amsterdam, **14 B**, 1676 (1990).

CHEN, S., SEKIGUCHI, T., J Applied Physics, **36**, 2363 (1963).

CHEN, F.F., in Plasma Diagnostic Techniques, edited by R. Hudleston $ S. Leonard, 113 (Academic Press (1965)).

CHIUEH, T., TERRY, P.W., DIAMOND, P.H., & SEDLAK, J.E., Phys Fluids, **29**, (1), 231 (1986).

COOLEY, J.W., LEWIS, P.A.W., and WELCH, P.D, Historical notes on the Fast Fourier Transform, IEEE Trans. Audio Electroacoustics, **AU-15**, 76 (1967).

DIAMOND, P.H., Comments Pl Phys & Contr Fusion, **10**, 271 (1987).

DIAMOND, P.H., & KIM, Y.B., Phys Fluids, **B 3**, 1626 (1991).

DÜCHS, D.F., Jet Report JET-R(89) 13 (1989).

DUPERREX, P.A., PhD Thesis, (1988).

ELLIS, J.J., *et al*, Proc 10th Int Conf on Contr Fusion and Plasma Phys, London, **I**, 363 (1984).

EMMERT, WIELAND, MENSE, DAVIDSON, Phys Fluids, **23**, (4), 803 (1980).

FILIPPAS, A. V., RITZ, Ch. P., KONIGES, A. E., *et al*, Proc 18th EPS Conf on Contr Fusion and Plasma Phys, Berlin, **15 C**, I-309 (1991).

FLETCHER, J. D., ROBERTS, D. E., SHERWELL, D., *et al*, Proc 18th EPS Conf. on Contr Fusion and Plasma Phys, Berlin, **15 C**, A-74 (1991).

FLETCHER, J. D., ROBERTS, D. E., SHERWELL, D., *et al* Proc 19th EPS Conf on Contr Fusion and Plasma Phys, Innsbruck, , (1992).

GARBET, X., LAURENT, J. P., ROUBIN, J. P., SAMAIN, A., Cadarache, Internal Report, EUR-CEA-FC-1398, June (1990).

GENTLE, K. W., KIM, Y. J., RITZ, Ch. P. and RHODES, J. L., Proc 14th EPS Conf on Contr Fusion and Plasma Phys, Madrid, **1**, 133 (1984).

GRAESSLE, D. E., PhD Thesis, University of Wisonsin, (1989).

HAAS, THYAGARAJA & COOK, Pl Phys, **23**, 1027 (1981).

HAHM, T. S., DIAMOND, P. H., TERRY, P. W., *et al*, Phys Fluids, **30**, 1452 (1987).

HASEGAWA, A., WAKATANI, M., Phys Rev Lett, **50**, 682 (1983).

HASSAM, A. B., DRAKE, J. F., Phys Fluids, **26** 1, 133 (1983).

HASSAM, A. B., ANTONSEN, T. M, DRAKE, J. F., & LIU, C. S., Phys Rev Lett, **66**, 309 (1991).

HAZELTINE, R. D., Phys Fluids, **B 1**, 2031 (1989).

HEDEMANN, M. A., GOULD, R. W., *em al*, Bull Am Phys Soc., **25**, 975 (1980).

HEDEMANN, M., PhD thesis, California Institute of Technology, (1981).

HIDALGO, C., UCKAN, T., BELL, J. H., *et al*, Proc 17th EPS Conf. on Contr Fusion and Plasma Phys, Amsterdam, **14 B**, 1353 (1990).

HINTON, F. L., Phys Fluids, **B 3**, 696 (1991).

HORTON, C. W., LIU, J., University of Texas at Austin, Report #IFSR–111 (1984).

HOWLING, A. A., COTÉ, A., DOYLE, E. J., *et al*, Proc. 12th EPS Conf on Contr Fusion and Plasma Phys, Budapest, **9 F**, 311 (1985).

HOWLING, A. A., PhD Thesis, University of Oxford, (1986).

HOWLING, A. A., ROBINSON, D. C., Pl Phys and Contr Fusion, **30**, 1863 (1988).

JET TEAM, Nucl Fusion, **32**, 2, 187 (1992).

JOHNSON, MALTER, Phys Rev **80**, (1), 58 (1950).

KIM, Y. C., and POWERS, E. J., IEEE, Trans Pl Sci, **PS-5**, 31 (1977).

KIM, Y. J., GENTLE, K. W., RITZ, Ch. P., *et al*, Nucl Fusion, **29**, 1 (1989a).

KIM, Y. J. PhD Thesis, University of Texas at Austin, (1989b).

LANGMUIR, MOTT-SMITH, Gen Elec Rev, **27**, 449 (1924).

LEBOEUF, J. N., LEE, D. K., CARRERAS, B. A., *et al*, Phys Fluids, **B 3**, 2291 (1991).

LEVINSON, S. J., BEALL, J. M., *et al*, Nucl Fusion, **24**, 5, 527 (1984).

LIEWER, P. C., Nucl Fusion, **25**, 5, 543 (1985).

LIEWER, P. C., McCHESNEY, J. M., ZWEBEN, S. J., & GOULD, R. W., Phys Fluids, **29**, 309 (1986).

LIN, H., BENGSTON D., RITZ, Ch.P., Phys Fluids, **B 1**, 2027 (1989).

LIN, H., PhD Thesis, University of Texas at Austin, (1991).

LIN, H., XI, G. X., BENGTSON, R. D., University of Texas at Austin, Internal Report #414, April (1992).

MALACARNE, M., DUPERREX, P. A., Nucl Fusion, **27**, 2113 (1987).

MANHEIMER, COOK, Comment Pl Phys, **5**, 9 (1979).

McCRACKEN, G. M., SCOTT, P. E., Nucl Fusion, **19**, 889 (1979).

MORRIS A. W., FITZPATRICK, R., *et al*, Proc 17th EPS Conf on Contr Fusion and Plasma Phys, Amsterdam, **14 B**, 379 (1990a).

MORRIS A. W., *et al*, Plasma Phys and Contr Nucl Fus Research (Proc 13th Int Conf), Washington, IAEA CN-53/E-3-8 (1990b).

MORRIS A. W., FITZPATRICK, R., *et al*, Proc 18th EPS Conf. on Controlled Fusion and Plasma Heating, Berlin, **15 C**, II-61 (1991).

MOTLEY, Nucl Fusion, **21**, 1541 (1981).

NICOLAI, N., *et al*, Plasma Physics, **27**, 1479 (1985).

NIEDERMEYER H., CARLSON, A., *et al*, Proc 18th EPS Conf. on Controlled Fusion and Plasma Heating, Berlin, **15 C**, I-301 (1991).

NOTHNAGEL, G., PhD Thesis, University of Stellenbosch, (1991).

OHYABU, N., *et al* Nucl Fusion, **25**, 1684 (1985).

OHYABU, N., JAHNS, G. L., STAMBAUGH, R. D., STRAIT, E. J., Phys Rev Lett, **58**, 2 (1987).

OREN, L., TAYLOR, R. J., Nucl Fusion, **17**, 1143 (1977).

POWERS, E. J., Nucl Fusion, **14**, 749 (1974).

PRESS, W. H., FLANNERY, B. P., *et al*, Numerical Recipes, Cambridge University Press, (1986).

PULSATOR TEAM, Nucl Fusion, **25**, 1059 (1985).

RHODES, T. L., PhD Thesis, University of Texas at Austin, (1989).

RITZ, Ch. P., BENGTSON R. D., *et al*, Phys Fluids, **27**, 2956 (1984).

RITZ, Ch. P., BROWER, D. L., RHODES, T. L., *et al*, Nuc Fusion, **27**, 7, 1125 (1987).

RITZ, Ch. P., BRAVENEC, R. V., BENGTSON, R. D., *et al*, J Nucl Mater, **145–147**, 241 (1987).

RITZ, Ch. P., BRAVENEC, R. V., SCHOCH, P. M., *et al*, Phys Rev Lett., **62**, 6, 1844 (1989).

RITZ, Ch. P., LIN, H., RHODES, T. L., *et al*, Phys Rev Lett, **65**, 2543 (1990a).

RITZ, Ch. P., LIN, H., BENGTSON, R. D., *et al*, Proc 17th EPS Conf on Contr Fusion and Plamsa Phys, Amsterdam, **14 B**, 1456 (1990b).

ROBERTS, D. E., DE VILLIERS, J. A. M., FLETCHER, J. D., *et al*, Nucl Fusion, **26**, (6), 785 (1986).

ROBERTS, D. E., SHERWELL, D., FLETCHER, J. D., NOTHNAGEL, G., de VILLIERS, J. A. M., Nucl Fusion, **31**, #2, 319 (1991a).

ROBERTS, D. E., FLETCHER, J. D., NOTHNAGEL, G., *et al*, Phys Rev Lett, **66**, 22, 2875 (1991b).

ROBERTS, D. E., VAN VUUREN, G. W., FLETCHER, J. D., *et al*, Proc 18th EPS Conf on Contr Fusion and Plasma Phys, Berlin, **15 C**, A-66 (1991c).

ROBERTS, D. E., Private Communication, (1992).

ROBINSON, D. C., RUSBRIDGE, M. G., Pl Phys., **11**, 73 (1969).

ROSS, D. W., *et al*, University of Texas at Austin, FRCR #295, (1987).

ROSS, D. W., *et al*, Comments on Pl Phys & Contr Fusion, **XII**, 155 (1989).

ROWAN, W. L., KLEPPER, C. C., RITZ, Ch. P., *et al* Nucl Fusion, **27**, 1105 (1987).

RUDYJ, A., *et al*, Proc 16th EPS Conf on Contr Fusion and Pl Physics, Venice, **13B**, 27 (1989).

RUDYJ, A., *et al*, Proc 17th EPS Conf on Contr Fusion and Pl Physics, Amsterdam, **14B**, 81 (1990).

SCOTT, B. D., Phys Rev Lett, **65**, 26, 3289 (1990).

SCOTT, B. D., Nucl Fusion, **32**, 5, 873 (1992).

SHAING, K. S., CRUME, E. C., & HOULBERG, W. A., Phys Fluids, **B2**, 1492 (1990).

STANGEBY, P. C., Phys Fluids, **27**, (3), 682 (1984).

STANGEBY, P. C., McCRACKEN, G. M., Nucl Fusion, **30**, 7, 1225 (1990).

SUGAWARA, M., HATTA, Y., J Phys Soc Japan, **19**, 1908 (1964).

SURKO, C. M., in Turbulence and Anomalous Transport in Magnetized Plasmas, edited by D. Gresillon and M. Dubois, — Editions de Physique, Orsay, 93 (1987).

SWIFT, SCHWAR, 'Electrical Probes for Plasma Diagnostics', Iliffe Books (1970).

TAKAMURA, S., OHNISHI, N., IWAI, K., OKUDA, T., Phys Rev Lett, **56**, 19 (1986).

TERRY, P., DIAMOND, P. H., University of Texas at Austin, Report #IFSR–143, (1984).

TERRY, P. W., DIAMOND, P. H., Phys Fluids, **28**, 1419 (1985).

THAYER, D. R., DIAMOND, P. H., Phys Fluids, **30**, 3724 (1987).

TODD, T. N., J. de Physique (Supplement to No. 7) **40**, C7–841, (1979).

TODD, T. N. Nucl Fusion, **32**, 6, 1071 (1992).

TSUI, H. Y. W., RITZ, Ch. P., LIN, H., *et al* Proc 18th EPS Conf on Contr Fusion and Plasma Phys, Berlin, **15 C**, I-297 (1991).

TSUI, H. Y. W., University of Texas at Austin, Internal Report, FRCR #406, January, (1992).

VAYAKIS, G., ROBINSON, D. C., Proc 17th EPS Conf on Contr Fusion and Plasma Phys, Amsterdam, **14 B**, 211 (1990).

VAYAKIS, G., PhD Thesis, University of Oxford, (1991).

WAGNER, F., BECKER, G., BEHRINGER, K., *et al* Proc 9th Conf on Pl Physics and Contr Nucl Fus Research, Baltimore (1982).

WALTZ, R. E., Phys Fluids, **28**, 577 (1985).

WALTZ R. E., DOMINGUEZ, R. R., Phys Fluids, **30**, 1452 (1987).

WESSON, J., *Tokamaks*, Clarendon Press, Oxford (1987).

WOOTTON, A. J., *et al* Pl Phys and Contr Fusion, **30**, 1479 (1988).

WOOTTON, A. J., University of Texas at Austin, Internal Report, FRCR #6/27/89, August, (1989).

WOOTTON, A. J., CARRERAS, B. A., MATSUMOTO, H., *et al*, Phys Fluids, **B2**, 2879 (1990a).

WOOTTON, A. J., 9th Int. Conf. on Plasma Surface Interactions in Controlled Nuclear Devices, Bournemouth, FRCR #371, June (1990b).

WOOTTON, A. J., University of Texas at Austin, Internal Report, FRCR #393, August, (1991).

ZUSHI, H., MIZUUCHI, O., MOTOJIMA, M., *et al*, Nucl Fusion, **28**, 433 (1988).

ZWEBEN, S. J., MENYUK, C. R., *et al*, Phys Rev Lett, **42**, 1270 (1979).

ZWEBEN, S. J., TAYLOR, R. J., *et al*, Nucl Fusion, **21**, 193 (1981).

ZWEBEN, S. J., LIEWER, P. C., GOULD, R. W., *et al*, J Nucl Mater, **111—112**, 39 (1982).

ZWEBEN, S. J., TAYLOR, R. J., Nucl Fusion, **23**, 513 (1983).

ZWEBEN, S. J., and GOULD, R. W., Nucl Fusion, **25**, 2, 171 (1985).

ZWEBEN, S. J., MANOS, D., J Nuc Mater, **145 - 147**, 250 (1987).